IPP-Report

Max-Planck-Institut
für Plasmaphysik

Florian Martin Laggner

Inter-ELM pedestal structure development in ASDEX Upgrade

IPP 2017-02
Juni, 2017

TECHNISCHE
UNIVERSITÄT
WIEN

DISSERTATION

Inter-ELM pedestal structure development in ASDEX Upgrade

ausgefürt zum Zwecke der Erlangung des akademischen
Grades eines Doktors der technischen Wissenschaften
unter der Leitung von

Univ.Prof. Dr. Friedrich Aumayr
Institut für Angewandte Physik

Univ.Doz. Dr. Elisabeth Wolfrum
Max-Planck-Institut für Plasmaphysik

eingereicht an der Technischen Universität Wien
Fakultät für Physik

von

Dipl.-Ing. Florian Martin Laggner
Sittich 8a
9560 Feldkirchen

Wien, 2017

Kurzfassung

Die Leistungsfähigkeit eines magnetisch eingeschlossenen Fusionsplasmas hängt stark vom Plasmarand ab, der die Grenze zwischen dem heißen, eingeschlossenen Plasma und der Reaktorwand darstellt. In einem Tokamak, der eine toroidale, axialsymmetrische Magnetfeldkonfiguration besitzt, wurde ein Regime mit verbessertem Plasmaeinschluss, die High Confinement Mode (H-Mode), beobachtet. Der verbesserte Einschluss wird durch eine Randtransportbarriere (ETB) bedingt, welche mit der Formierung von steilen Gradienten des Plasmadrucks einhergeht, die als Pedestal bezeichnet werden. Das maximal erreichbare Pedestal, d.h. der maximale Druckgradient, ist normalerweise durch ein magnetohydrodynamisches Limit begrenzt, dessen Überschreitung zu sogenannten Edge Localised Modes (ELMs) führt. ELMs sind Instabilitäten, die das Pedestal abflachen und zu einem Verlust von rund 10 % der im Plasma gespeicherten Energie führen. Die Mechanismen, die die Pedestalstruktur vor einem ELM Ausbruch bestimmen, sind nicht vollständig verstanden. Es wird erwartet, dass mikroturbulente Instabilitäten, z.B. Kinetische Ballooning Moden (KBMs), hierbei eine wichtige Rolle spielen.

Die vorgelegte Dissertation untersucht die zeitliche Entwicklung der Dichte- und Temperaturprofile des Pedestals zwischen ELM Ausbrüchen am ASDEX Upgrade Tokamak. Die Ziele waren Vergleiche von unterschiedlichen Plasmabedingungen, wie der Kollisionalität (ν^*) des Plasmas, verschiedenen Hauptionenspezies und unterschiedlichen Plasmaformen. Weiters wurde der Einfluss der Bedingungen außerhalb des eingeschlossenen Plasmas auf die Pedestalentwicklung untersucht. Die umfassende Studie dieser Parameter resultierte in einer Schlüsselbeobachtung: Das Pedestal baut sich in unterschiedlichen Phasen zwischen ELM Ausbrüchen auf, deren Abfolge immer gleich ist. Unmittelbar nach dem ELM Ausbruch wird das Elektronendichtepedestal hergestellt, anschließend das Elektronentemperaturpedestal. Abschließend tritt eine Phase mit konstanten Druckgradienten auf, die unterschiedlich lange andauern kann.

Über einen weiten Bereich von ν^* wurde beobachtet, dass das Einsetzen von Magnetfeldfluktuationen mit Frequenzen über 200 kHz mit einer Stagnation des Elektronendruckgradienten im Pedestal korreliert. Wenn diese Fluktuationen vorhanden sind, steigen die Gradienten von Elektronendichte und -temperatur nicht weiter an und sind stabil gegen einen ELM Ausbruch. Die Fluktuationen sind Signatur von Mikroinstabilitäten, die sich im Pedestal befinden. Ihre Frequenz, die an der Außenseite, der

Niederfeldseite (LFS), detektiert wird, korreliert linear mit der neoklassischen Approximation der Hintergrundgeschwindigkeit am Plasmarand, was indiziert, dass sich die Instabilität mit der Hintergrundgeschwindigkeit des Plasmas bewegt. Darüber hinaus konnte den Fluktuationen eine globale Modenstruktur mit toroidalen Modenzahlen im Bereich von 11 zugeordnet werden. Die Fluktuationen sind auch auf der Innenseite, der Hochfeldseite (HFS), des Tokamaks mit signifikanter Amplitude messbar, was für eine KBM nicht erwartet wird, deren dominante Amplitude auf der LFS liegen sollte.

Ein Vergleich von Wasserstoff (H), Deuterium (D) und Helium (^{4}He) Plasmen wurde durchgeführt, um die inter-ELM Entwicklung der Pedestalstruktur in Plasmen mit verschiedenen Hauptionenspezies zu untersuchen. Die Pedestalstabilität aller Plasmen stimmt mit der „Peeling-Ballooning“ (PB) Theorie überein, die unabhängig von der Hauptionenspeziesmasse ist. Die inter-ELM Pedestalentwicklung zeigt dieselbe Phasensequenz im Pedestalaufbau für alle Hauptionenspezies. Weiters wurde eine ähnliche inter-ELM Signatur der magnetischen Fluktuationen sowie gleiche zugehörige toroidale Modenstrukturen gemessen.

Zusätzlich zum Abflachen des Pedestals beeinflussen ELMs das Plasma im Divertor und in der Abschälschicht (SOL). Der Einfluss der geänderten Bedingungen außerhalb des eingeschlossenen Plasmas auf die inter-ELM Pedestalentwicklung wurde untersucht, wobei der Fokus auf der Entwicklung der Elektronendichte lag. Die Teilchen- und Leistungsflüsse, die durch den ELM ausgestoßen werden, führen zu einem „Re-Attachment“ des Plasmas im inneren Divertor. Nach dem ELM Ausstoß geht der äußere Divertor in ein Regime mit hohem Neutralenrecycling über, welches eine hohe Elektronendichte vor den Divertorkacheln bedingt. Auf ähnlichen Zeitskalen hebt sich das Plasma vollständig vom inneren Divertor ab („Detachment“) und eine Hochfeldseitenhochdichteregion (HFSHD) formiert sich, die bis zur Mittelebene auf der HFS ausgedehnt ist. Weder die Zeitskala der Formation der HFSHD noch der Anstieg der Neutralenflüsse in der Hauptkammer weisen dieselbe Zeitskala wie das Elektronendichtepedestal auf, das sich schneller aufbaut. Es wurde beobachtet, dass der Aufbau des Elektronendichtepedestals mit der magnetischen Aktivität an der LFS Mittelebene verknüpft ist, deren Amplitude während des schnellen Aufbaus des Elektronendichtepedestals stark reduziert ist.

Die Form des Plasmas, beziehungsweise die Triangularität, beeinflusst die Stabilität des Pedestals. In dedizierten Experimenten wurde beobachtet, dass die erhöhte Elektronendichte, die in hochtriangulären Plasmen auftritt, bereits während der Phase des Elektronendichteaufbaus erreicht wird. Die Erniedrigung der ELM Frequenz bei größerer Triangularität ist mit längeren Aufbauphasen des Pedestals verbunden. In sämtlichen untersuchten Entladungsintervallen befanden sich die pre-ELM Pedestalprofile in Übereinstimmung mit der PB Theorie.

Die detaillierte Untersuchung der einzelnen Phasen des Wiederaufbaus der Randgradienten nach einem ELM zeigte erstmals, dass die Phasensequenz unabhängig von Hauptionenspezies, Kollisionalität und Form des Plasmas immer gleich abläuft, bis die Stabilitätsgrenze, die gut mit der PB Theorie beschrieben werden kann, erreicht ist. Außerdem konnte gezeigt werden, dass der schnelle Anstieg des Elektronendichtepedestals nicht von der Dynamik der Neutralen im Divertor oder Hauptraum dominiert wird, da er auf schnelleren Zeitskalen erfolgt. Die magnetischen Fluktuationen, die in der Phase vor dem ELM auftreten, in der sich der Druckgradient nicht mehr ändert, konnten erstmals genauer charakterisiert werden. Es wurde gezeigt, dass die zugrundeliegende Instabilität im Minimum des radialen elektrischen Feldes lokalisiert ist, eine toroidale Modenzahl von 11 aufweist und auch auf der HFS messbar ist, was für einen signifikanten „Peeling“-Anteil spricht.

Abstract

The performance of a magnetically confined, fusion plasma is strongly impacted by the plasma edge, which is the boundary between the hot, confined plasma and the reactor walls. In a tokamak, which uses a toroidally axis-symmetric magnetic field configuration, a regime of improved plasma confinement, the high confinement mode (H-mode), has been observed. The confinement improvement originates from an edge transport barrier (ETB), which is accompanied by steep gradients of the plasma pressure, named pedestal. The maximum sustainable pedestal, i.e. the maximum pressure gradient, is usually set by an ideal magnetohydrodynamic limit, which if exceeded is leading to edge localised modes (ELMs). ELMs are instabilities that relax the pedestal and lead to a loss of the order of 10 % from the plasma stored energy. The mechanisms, which set the pedestal structure before an ELM crash, keeping the pedestal stable up to this point, are not fully understood. Here, microturbulent instabilities, e.g. kinetic ballooning modes (KBMs), are expected to play an important role.

The presented PhD thesis investigates the temporal development of the pedestal density and temperature profiles in between ELM crashes at the ASDEX Upgrade tokamak. The aims were comparisons of different plasma conditions, i.e. plasma collisionality (ν^*), main isotope species and plasma shapes. Further, the impact of the conditions outside the confined plasma on the pedestal development was investigated. The extensive study of these parameters resulted in one key observation: The pedestal recovers in distinct phases in between ELM crashes with always the same sequence. Immediately after the ELM crash, the electron density (n_e) pedestal is established, followed by the electron temperature (T_e) pedestal. Finally, a period with constant pressure gradient appears, which can vary in duration.

For a large range of ν^* it has been found that the onset of radial magnetic fluctuations with frequencies above 200 kHz correlates with the stagnation of the electron pressure gradient in the pedestal. When these fluctuations are present, the gradients of the edge n_e and T_e are clamped and stable against an ELM onset. These fluctuations are signatures of microinstabilities which act in the pedestal. Their frequency, that is detected on the outboard, low field side (LFS), linearly correlates with the neoclassical estimate of the plasma edge background velocity, indicating that the instability propagates with the background flow. Furthermore, it has been found that the fluctuations have a global mode structure with toroidal mode numbers in the region of

11. The fluctuations are also observable on the inboard, high field side (HFS) of the tokamak with significant amplitude, which is not expected for a KBM that should have its dominant amplitude on the LFS.

The comparison of hydrogen (H), deuterium (D) and helium (^{4}He) plasmas has been performed to investigate the inter-ELM evolution of the pedestal structure in plasmas with different main ion species. The pedestal stability of all plasmas is in agreement with peeling-ballooning (PB) theory, which is independent of the main ion species mass. The inter-ELM pedestal evolution has the same sequence of recovery phases for all main ion species. Further, similar evolution of the inter-ELM magnetic signature as well as similar corresponding toroidal mode structures are found.

In addition to the relaxation of the pedestal, ELMs introduce changes to the divertor and scrape-off layer (SOL) conditions. Their impact on the inter-ELM pedestal recovery was investigated with emphasis on the evolution of the n_e pedestal. The particle and power fluxes expelled by the ELM crash lead to a re-attachment of the inner target plasma. After the ELM crash, the outer divertor target moves into a high recycling regime with high n_e in front of the plate. On similar timescales, the inner target fully detaches and the high field side high density region (HFSHD) is formed reaching up to the HFS midplane. Neither the timescale of the appearance of the HFSHD nor the increase of the main chamber neutral fluxes fit the timescale of the n_e pedestal, which is faster. It is found that the recovery phase of the n_e pedestal is linked to the magnetic activity at the LFS midplane. The fluctuation amplitude is strongly reduced during the re-establishment of the n_e pedestal.

The plasma shape, respectively triangularity (δ), impacts on the pedestal stability. In dedicated experiments it was found that the higher pedestal top n_e, which is observed at high δ, is already established in the n_e pedestal recovery phase. The lowering of the ELM repetition frequency (f_ELM) with increasing δ is related to longer pedestal recovery phases. In all investigated discharge intervals, the pre-ELM pedestal profiles are in agreement with PB theory.

The detailed investigation of the pedestal recovery phases after an ELM crash showed for the first time that the sequence of recovery phases evolves independently of main ion species, plasma collisionality and plasma shape till the stability limit, which is well described by PB theory, is reached. Furthermore, it was evidenced that the fast increase of the n_e pedestal is not dominated by the neutral dynamics in the divertor or main chamber because it occurs on faster timescales. The magnetic fluctuations, occurring in the pre-ELM phase with constant pressure gradient, were characterised in detail for the first time. It has been shown that the underlying instability is located close to the minimum of the radial electric field, exhibits a toroidal mode number of 11 and is also detectable on the HFS, indicating a significant peeling contribution.

List of publications

Parts of this thesis have already been published, are accepted for publication or are in preparation for publication.

Publications in Scientific Journals as first author

- **F. M. Laggner**, E. Wolfrum, M. Cavedon, F. Mink, M. Bernert, M. G. Dunne, P. A. Schneider, A. Kappatou, G. Birkenmeier, R. Fischer, M. Willensdorfer, F. Aumayr, the EUROfusion MST1 Team and the ASDEX Upgrade Team
  "Pedestal structure and inter-ELM evolution for different main ion species in ASDEX Upgrade"; Physics of Plasmas, **24**, 5 (2017)
- **F. M. Laggner**, E. Wolfrum, M. Cavedon, F. Mink, E. Viezzer, M. G. Dunne, P. Manz, H. Doerk, G. Birkenmeier, R. Fischer, S. Fietz, M. Maraschek, M. Willensdorfer, F. Aumayr, the EUROfusion MST1 Team and the ASDEX Upgrade Team
  "High frequency magnetic fluctuations correlated with the inter-ELM pedestal evolution in ASDEX Upgrade"; Plasma Physics and Controlled Fusion, **58**, 6 (2016)

Publications in Scientific Journals as co-author

- M. Cavedon, T. Pütterich, E. Viezzer, **F. M. Laggner**, A. Burckhart, M. G. Dunne, R. Fischer, A. Lebschy, F. Mink, U. Stroth, M. Willensdorfer, E. Wolfrum and the ASDEX Upgrade Team
  "Pedestal and E_r profile evolution during an edge localized mode cycle at ASDEX Upgrade"; Submitted to Plasma Physics and Controlled Fusion (2017)
- D. Carralero, J. Madsen, S. Artene, M. Bernert, G. Birkenmeier, T. Eich, G. Fuchert, **F. M. Laggner**, V. Naulin, P. Manz, N. Vianello, E. Wolfrum, the EUROfusion MST1 team and the ASDEX Upgrade Team
  "A study on the density shoulder formation in the SOL of H-mode plasmas"; In press, Nuclear Materials and Energy (2017)

- M. G. Dunne, L. Frassinetti, M. N. A. Beurskens, M. Cavedon, S. Fietz, R. Fischer, L. Giannone, G. T. A. Huijsmans, B. Kurzan, **F. M. Laggner**, P. J. McCarthy, R. M. McDermott, G. Tardini, E. Viezzer, M. Willensdorfer, E. Wolfrum, the EUROfusion MST1 Team and the ASDEX Upgrade Team
  "Global performance enhancements via pedestal optimisation on ASDEX Upgrade"; Plasma Physics and Controlled Fusion **59**, 2, (2017)

- P. T. Lang, R. Maingi, D. K. Mansfield, R. M. McDermott, R. Neu, E. Wolfrum, R. Arredondo Parra, M. Bernert, G. Birkenmeier, A. Diallo, M. G. Dunne, E. Fable, R. Fischer, B. Geiger, A. Hakola, V. Nikolaeva, A. Kappatou, **F. M. Laggner**, M. Oberkofler, B. Ploeckl, S. Potzel, T. Pütterich, B. Sieglin, T. Szepesi and the ASDEX Upgrade Team
  "Impact of lithium pellets on plasma performance in the ASDEX Upgrade all-metal-wall tokamak"; Nuclear Fusion **57**, 1, (2017)

- M. G. Dunne, S. Potzel, F. Reimold, M. Wischmeier, E. Wolfrum, L. Frassinetti, M. Beurskens, P. Bilkova, M. Cavedon, R. Fischer, B. Kurzan, **F. M. Laggner**, R. M. McDermott, G. Tardini, E. Trier, E. Viezzer, M. Willensdorfer, the EUROfusion MST1 team and the ASDEX Upgrade Team
  "The role of the density profile in the ASDEX-Upgrade pedestal structure"; Plasma Physics and Controlled Fusion **59**, 1, (2017)

- L. Frassinetti, M. G. Dunne, M. Beurskens, E. Wolfrum, A. Bogomolov, D. Carralero, M. Cavedon, R. Fischer, **F. M. Laggner**, R. M. McDermott, H. Meyer, G. Tardini, E. Viezzer, the EUROfusion MST1 Team and the ASDEX Upgrade Team
  "ELM behavior in ASDEX Upgrade with and without nitrogen seeding"; Nuclear Fusion **57**, 2, (2017)

- E. Viezzer, E. Fable, M. Cavedon, C. Angioni, R. Dux, **F. M. Laggner**, M. Bernert, A. Burckhart, R. M. McDermott, T. Pütterich, F. Ryter, M. Willensdorfer, E. Wolfrum, the ASDEX Upgrade Team and the EUROfusion MST1 Team
  "Investigation of inter-ELM ion heat transport in the H-mode pedestal of ASDEX Upgrade plasmas"; Nuclear Fusion **57**, 2 (2017)

- M. Cavedon, T. Pütterich, E. Viezzer, G. Birkenmeier, T. Happel, **F. M. Laggner**, P. Manz, F. Ryter, U. Stroth and the ASDEX Upgrade Team
  "Interplay between turbulence, neoclassical and zonal flows during the transition from low to high confinement mode at ASDEX Upgrade"; Nuclear Fusion **57**, 1 (2017)

- F. Mink, E. Wolfrum, M. Maraschek, H. Zohm, L. Horváth, **F. M. Laggner**, P. Manz, E. Viezzer, U. Stroth and the ASDEX Upgrade Team

"Toroidal mode number determination of ELM associated phenomena on ASDEX Upgrade" Plasma Physics and Controlled Fusion **58**, 12, (2016)

- M. Willensdorfer, S. S. Denk, E. Strumberger, W. Suttrop, B. Vanovac, D. Brida, M. Cavedon, I. Classen, M. Dunne, S. Fietz, R. Fischer, A. Kirk, **F. M. Laggner**, Y. Q. Liu, T. Ostrčil, D. A. Ryan, E. Viezzer, H. Zohm, I. C. Luhmann, the ASDEX Upgrade Team and the EUROfusion MST1 Team
  "Plasma response measurements of magnetic perturbations using electron cyclotron emission and comparison to 3D ideal MHD equilibrium"; Plasma Physics and Controlled Fusion, **58**, 11 (2016)

- G. Birkenmeier, M. Cavedon, G. D. Conway, P. Manz, U. Stroth, R. Fischer, G. Fuchert, T. Happel, **F. M. Laggner**, M. Maraschek, A. Medvedeva, V. Nikolaeva, D. Prisiazhniuk, T. Pütterich, F. Ryter, L. M. Shao, M. Willensdorfer, E. Wolfrum, H. Zohm and the ASDEX Ugrade Team
  "Magnetic structure and frequency scaling of limit-cycle oscillations close to L-to H-mode transitions"; Nuclear Fusion, **56**, 8 (2016)

- R. Arredondo Parra, R. Moreno Quicios, B. Ploeckl, G. Birkenmeier, A. Herrmann, G. Kocsis, **F. M. Laggner**, P. T. Lang, T. Lunt, R. Macian-Juan, V. Rohde, G. Sellmair, T. Szepesi, E. Wolfrum, W. Zeidner, R. Neu and the ASDEX Upgrade Team
  "A Compact Lithium Pellet Injector for Tokamak Pedestal Studies"; Review of Scientific Instruments **87**, 2 (2016)

- L. Shao, E. Wolfrum, F. Ryter, G. Birkenmeier, **F. M. Laggner**, E. Viezzer, R. Fischer, M. Willensdorfer, B. Kurzan and the ASDEX Upgrade Team
  "On the role of the edge density profile for the L-H transition power threshold in ASDEX Upgrade"; Plasma Physics and Controlled Fusion, **58**, 2 (2016)

- E. Viezzer, E. Fable, T. Pütterich, A. Bergmann, M. Cavedon, R. Dux, R. M. McDermott, C. Angioni, R. M. Churchill, M. G. Dunne, **F. M. Laggner**, B. Lipschultz, U. Stroth, E. Wolfrum and the ASDEX Upgrade Team
  "Collisionality dependence of edge rotation and in-out impurity asymmetries in ASDEX Upgrade H-mode plasmas"; Nuclear Fusion **55**, 12 (2015)

- G. Birkenmeier, P. Manz, D. Carralero, **F. M. Laggner**, G. Fuchert, K. Krieger, H. Maier, F. Reimold, K. Schmid, R. Dux, T. Pütterich, M. Willensdorfer, E. Wolfrum and the ASDEX Upgrade Team
  "Filament transport, warm ions and erosion in ASDEX Upgrade L-modes"; Nuclear Fusion, **55**, 3 (2015)

- T. Kobayashi, G. Birkenmeier, E. Wolfrum, **F. M. Laggner**, M. Willensdorfer, U. Stroth, S. Inagaki, S.-I. Itoh, K. Itoh and the ASDEX Upgrade Team
  "Method for estimating the propagation direction of a coherent plasma structure

using a one-dimensional diagnostic array"; Review of Scientific Instruments, **85**, 8 (2014)

- G. Birkenmeier, **F. M. Laggner**, M. Willensdorfer, T. Kobayashi, P. Manz, E. Wolfrum, D. Carralero, R. Fischer, B. Sieglin, G. Fuchert, U. Stroth and the ASDEX Upgrade Team
  "Magnetic field dependence of the blob dynamics in the edge of ASDEX Upgrade L-mode plasmas"; Plasma Physics and Controlled Fusion, **56**, 7 (2014)

- M. Willensdorfer, G. Birkenmeier, R. Fischer, **F. M. Laggner**, E. Wolfrum, G. Veres, F. Aumayr, D. Carralero, L. Guimarais, B. Kurzan and the ASDEX Upgrade Team
  "Characterization of the lithium beam emission spectroscopy at ASDEX Upgrade"; Plasma Physics and Controlled Fusion, **56**, 2 (2014)

Conference and workshop contributions as first author

Invited Talks

- **F. M. Laggner**, E. Wolfrum, M. Cavedon, M. G. Dunne, F. Mink, G. Birkenmeier, R. Fischer, E. Viezzer, M. Willensdorfer, F. Aumayr, the ASDEX Upgrade Team and the EUROfusion MST1 Team
  "Inter-ELM pedestal evolution: High frequency magnetic fluctuations correlated with the clamping of the pressure gradient"; 24^{th} European Fusion Physics Workshop, Zakopane, Poland (2016)

- **F. M. Laggner**
  "Pedestal shape, stability and inter-ELM evolution for different main ion species in ASDEX Upgrade"; 58^{th} Annual Meeting of the APS Division of Plasma Physics, San Jose, California, GI2.00001 (2016)

Talks

- **F. M. Laggner**, E. Wolfrum, M. Cavedon, M. G. Dunne, F. Mink, G. Birkenmeier, R. Fischer, E. Viezzer, M. Willensdorfer, F. Aumayr, the ASDEX Upgrade Team and the EUROfusion MST1 Team
  "Inter-ELM pedestal evolution in ASDEX Upgrade: Magnetic activity correlated with the recovery of the edge profiles"; NSTX-U Physics Meeting, Princeton, New Jersey (2016)

- **F. M. Laggner**, E. Wolfrum, M. Bernert, M. Cavedon, M. G. Dunne, P. A. Schneider, F. Mink, G. Birkenmeier, R. Fischer, M. Willensdorfer, F. Aumayr, the EUROfusion MST1 Team and the ASDEX Upgrade Team
  "Pedestal structure and stability for different main ion species"; E2M Programme Seminar, Kreuth, Germany (2016)

- **F. M. Laggner**, E. Wolfrum, F. Mink, M. Cavedon, M. G. Dunne, P. Manz, G. Birkenmeier, R. Fischer, M. Maraschek, E. Viezzer, M. Willensdorfer, F. Aumayr, the ASDEX Upgrade Team and the EUROfusion MST1 Team
  "Inter-ELM pedestal evolution: High frequency magnetic fluctuations correlated with the clamping of the pressure gradient"; 43rd EPS Conference on Plasma Physics, Leuven, Belgium; Proceedings: Europhys. Conf. Abstracts, **40A**, 4.119 (2016)

- **F. M. Laggner**, E. Wolfrum, F. Mink, M. Cavedon, M. G. Dunne, G. Birkenmeier, F. Aumayr, the ASDEX Upgrade Team and the EUROfusion MST1 Team
  "High frequency magnetic fluctuations correlated with the inter-ELM pedestal recovery"; DPG Frühjahrstagung, Hannover, Germany, P 1.4 (2016)

- **F. M. Laggner**, E. Wolfrum, M. Cavedon, F. Mink, E. Viezzer, M. G. Dunne, P. Manz, H. Doerk, G. Birkenmeier, R. Fischer, S. Fietz, M. Maraschek, M. Willensdorfer, F. Aumayr, the EUROfusion MST1 Team and the ASDEX Upgrade Team
  "High frequency magnetic fluctuations correlated with the inter-ELM pedestal evolution in ASDEX Upgrade"; MST1 Task Force Meeting, Garching, Germany (2015)

- **F. M. Laggner**, E. Wolfrum, M. Cavedon, F.Mink, E. Viezzer, M. G. Dunne, P. Manz, H, Doerk, G. Birkenmeier, R. Fischer, S. Fietz, M. Maraschek, M. Willensdorfer, the EUROfusion MST1 Team and the ASDEX Upgrade Team
  "Inter-ELM pedestal evolution correlated to high frequency magnetic fluctuations"; ASDEX Upgrade Programme Seminar, Kreuth, Germany (2015)

- **F. M. Laggner**, E. Wolfrum, H. Doerk, M. Cavedon, E. Viezzer, F. Aumayr, G. Birkenmeier, M. Willensdorfer and the ASDEX Upgrade Team
  "Inter-ELM pedestal recovery in ASDEX Upgrade"; HEPP Seminar, Garching, Germany (2015)

- **F. M. Laggner**, F. Aumayr, G. Birkenmeier, M. Cavedon, M.G. Dunne, R. Fischer, L. Guimarais, P. Manz, A. Medvedeva, V. Nikolaeva, E. Viezzer, M. Willensdorfer, E. Wolfrum and the ASDEX Upgrade Team
  "KBM turbulence prior to the ELM onset"; E2M Kochel Seminar, Kochel am See, Germany (2015)

- **F. M. Laggner**, F. Aumayr, G. Birkenmeier, R. Fischer, M. Willensdorfer, E. Wolfrum and the ASDEX Upgrade Team
"Experimental investigation of the inter-ELM pedestal build-up"; 1. Fusionstag, Graz, Austria (2014)
- **F. M. Laggner**, G. Birkenmeier, M. Willensdorfer, E. Wolfrum, P. Manz, D. Carralero, F. Aumayr and the ASDEX Upgrade Team
"Lithium beam emission spectroscopy as a tool for tokamak edge electron density fluctuation measurements"; EFTSOMP Workshop, Berlin, Germany (2014)
- **F. M. Laggner**, F. Aumayr, G. Birkenmeier, R. Fischer, M. Willensdorfer, E. Wolfrum and the ASDEX Upgrade Team
"Inter-ELM pedestal profile development"; ASDEX Upgrade Programme Seminar, Kreuth, Germany (2014)
- **F. M. Laggner**, G. Birkenmeier, M. Willensdorfer, E. Wolfrum, F. Aumayr and the ASDEX Upgrade Team
"Determination of electron density perturbations with the Lithium beam diagnostic"; Edge Physics Forum, Max Planck Institute for Plasma Physics, Garching, Germany; (2014)

Posters

- **F. M. Laggner**, E. Wolfrum, M. G. Dunne, M. Cavedon, P. Manz, G. Birkenmeier, R. Fischer, E. Viezzer, M. Willensdorfer, F. Aumayr the EUROfusion MST1 Team and the ASDEX Upgrade Team
"The effects of triangularity and main ion species on the inter-ELM profile evolution in ASDEX Upgrade"; 42$^{\text{nd}}$ EPS Conference on Plasma Physics, Lisbon, Portugal; Proceedings: Europhys. Conf. Abstracts, **39E**, 1.147 (2015)
- **F. M. Laggner**, G. Birkenmeier, M. G. Dunne, R. Fischer, E. Viezzer, M. Willensdorfer, E. Wolfrum, F. Aumayr and the ASDEX Upgrade Team
"Comparison of the inter-ELM pedestal profile recovery in plasmas with different main ion species"; DPG Frühjahrstagung, Bochum, Germany, P16.1 (2015)
- **F. M. Laggner**, E. Wolfrum, M. Willensdorfer, G. Birkenmeier, T. Kobayashi, F. Aumayr and the ASDEX Upgrade Team
"Reconstruction of electron density perturbations using lithium beam emission spectroscopy"; DPG Frühjahrstagung, Jena, Germany, P10.5 (2013)

Contents

1 Background and Motivation

Electric power is one of the main bases for technological, economical and social progress. For this reason, the demand for electricity has been steadily increasing for several decades. But currently it is mainly met by non-renewable sources [1], which have the drawback that energy production is not sustainable on long time scales. Today, the majority of conventional power plant concepts rely on burning fossil fuels, emitting huge amounts of green house gas, most prominently carbon dioxide. These are proven to cause global warming [2] and therefore, are responsible for the world's climate change with all its unratable consequences. To curtail the impact of power generation on the environment, i.e. green house gas emission, by simultaneously meeting an increasing demand, alternatives to common power plant technology are required. This pushes research towards the realisation of novel methods for electric power generation.

Several renewable energy sources without green house gas emission like solar power or wind energy have been developed and promoted within the last years. Their major drawback is a non-reliable power production in the sense that they cannot cover the grid base load. Here, large power plants that continuously produce electrical power by nuclear fusion reactions could help to cover the base load in future.

1.1 Thermonuclear Fusion

In a nuclear fusion reaction two light atomic nuclei are combined, forming a heavier one. Since the reaction leads to a loss of total mass, i.e. the sum of the starting nuclei masses is larger than the total mass of the products, energy is released. Nuclear fusion reactions have been the energy source of the sun for several billions of years. This illustrates the enormous potential that underlies fusion reactions. However, the sun is huge in dimension and consists of many particles. Therefore, it is not possible to continuously reproduce similar conditions on earth. Especially, the high particle densities at the required temperatures to enable fusion reactions cannot be achieved simultaneously.

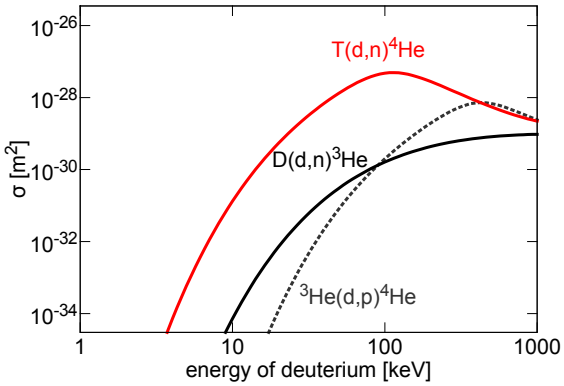

Figure 1.1: Cross sections for several fusion reactions: The D-T fusion reaction (T(d,n)^{4}He) has a significantly higher cross section at low energies than the D-D (D(d,n)^{3}He) or D-^{3}He (^{3}He(d,n)^{4}He) reaction. Curves taken from [3, 4].

The last decades of fusion research aimed at using the energy source from nuclear fusion reactions for electric power production. A more efficient fusion reaction than in the sun has to be used:

$$\mathrm{D} + \mathrm{T} \longrightarrow {}^4\mathrm{He} + \mathrm{n} + 17.6\,\mathrm{MeV}. \tag{1.1}$$

This is the so-called deuterium-tritium (D-T) reaction: Two isotope nuclei of hydrogen, deuterium (D) and tritium (T), fuse to helium (^{4}He) and a neutron (n), while 17.6 MeV of kinetic energy are released to the fusion products. Since a ^{4}He nucleus is almost four times heavier than a neutron, 3.5 MeV of energy are given to ^{4}He and 14.1 MeV to the neutron due to kinematics. The D-T reaction is the most efficient one because it has the largest cross section in comparison to other fusion reactions at the achievable temperatures. Figure 1.1 presents a comparison of the cross sections (σ) for different nuclear fusion reactions in dependency of the energy of an impinging D nucleus. At relatively low energies of roughly 100 keV, σ of the D-T reaction is approximately two orders of magnitude larger than for the D-D or D-^{3}He reaction. It has to be stressed that 1 keV corresponds to a temperature of roughly $1.1 \cdot 10^7$ K. Matter heated-up to such temperatures is in the aggregate state of plasma.

A plasma is an ionised gas, meaning that the electrons are not bound to the atomic nuclei. To fuse positively charged nuclei, the counteracting process of Coulomb repulsion has to be exceeded. Since σ for the Coulomb repulsion is higher than σ for fusion reactions, on average the nuclei in the plasma have to collide roughly 50 times till a fusion reaction happens. Therefore, it is required that the plasma is well confined in the reactive volume.

The threshold for self-sustaining D-T fusion reactions is given by the so-called Lawson criterion [5]. It is based on power balance considerations and yields that the product of plasma density, energy confinement time and temperature has to be higher than $5 \cdot 10^{21}\,\mathrm{m}^{-3}\,\mathrm{keV\,s}$ for a D-T plasma.

Within the last decades of research two main approaches were considered to fulfil the criterion. The first one is to increase the density by compression, while the energy confinement time is automatically reduced owing to the Coulomb repulsion. The plasma confinement is solely sustained by the inertia of the particles, therefore, this approach is called inertial confinement fusion [6]. Usually, frozen D-T pellets are compressed with laser or ion beams, to achieve fusion. The second approach is to enlarge the confinement time by applying electromagnetic fields, which is bound to operate at lower plasma densities. This approach is utilized in magnetic confinement fusion [7].

1.2 Magnetic Plasma Confinement

Since the plasma particles are charged, they interact with electric and magnetic fields according to the Lorentz force. In a magnetic field a charged particle with a velocity component perpendicular to the magnetic field lines is forced on a gyro-orbit. In a certain sense, this confines the charged particle in the perpendicular direction to the magnetic field, whereas the particle does not experience any repelling force by motion in parallel direction. Therefore, in a first order approach a magnetic field with self-contained field lines is desired, which can be realised in toroidal geometry. However, this is not sufficient to confine a plasma since drifts occur, which lead to charge separation and loss of confinement. To sustain confinement a superimposition of a toroidal and poloidal magnetic field is required. The poloidal field can either be externally introduced by application of a helical current component around the toroidal magnetic field, which is the concept of a stellarator. Or it can be achieved by driving a large current in the plasma, which is the concept of the tokamak. Both concepts are currently expected to be applicable to power plant requirements. Recently, a new stellarator experiment Wendelstein 7-X (W7-X) has been taken into operation. It already demonstrated that the achieved magnetic field geometry agreed with the designed one with an accuracy better than 10^{-5} [8], which is an enormous advance for design and optimisation of stellarators. A large tokamak experiment, ITER (the Latin word for ‘the way’) is currently constructed in southern France. It should demonstrate the production of several times more thermal power from fusion reactions than required for the heating of the plasma [9] and the feasibility to build a fusion power plant, named DEMO (DEMOnstration power station).

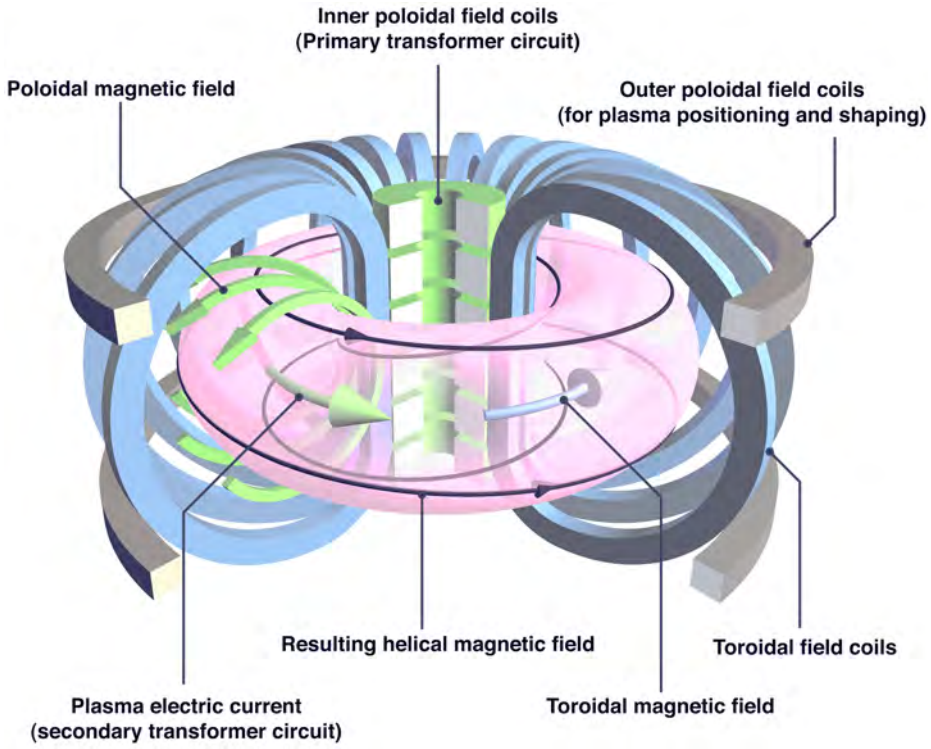

Figure 1.2: Magnetic coils and field lines in a tokamak: The magnetic field produced by the toroidally assembled coils (blue) is superimposed by the field produced by the current that is induced in the plasma (green arrow) resulting in helically twisted field lines (dark blue). Figure taken from [10].

1.2.1 Tokamak

In the early 1950s this concept was developed in the former Soviet Union. Its main components are illustrated in figure 1.2. Toroidally assembled magnetic field coils (blue coils, figure 1.2) create the toroidal component of the magnetic field. The required poloidal field component (green arrows, figure 1.2) is established by induction of an electric current (of the order of MA) in the plasma, which is done with the inner poloidal field coils (green, figure 1.2). These coils represent the primary circuit of a transformer with the plasma as secondary circuit. The superimposition of the toroidal and poloidal magnetic fields results in helically twisted field lines (dark blue arrow, figure 1.2), which can sustainably confine the plasma particles. The requirement of an induced current is one of the disadvantages of the tokamak concept, since this implies a pulsed operation. Ongoing research also focuses on driving the plasma current non-inductively to extend the pulse duration or fully overcome the pulsed operation mode [11].

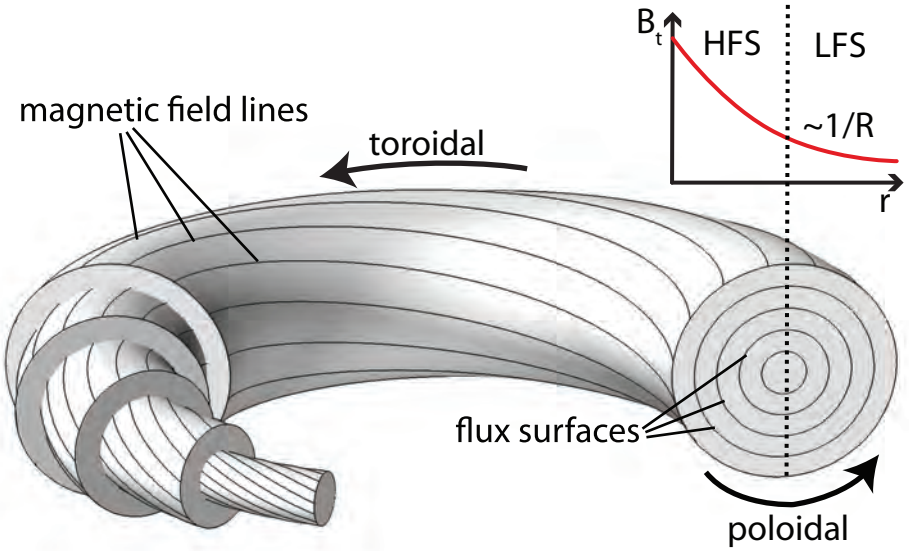

Figure 1.3: Nested magnetic flux surfaces in a tokamak configuration: The toroidal magnetic field (B_t) decreases from the inboard side of the torus towards the outboard one by $1/R$. This forms two regions on a flux surface, one with higher B_t (HFS) and one with lower B_t (LFS). Figure modified from [12].

1.2.2 Plasma equilibrium and flux coordinates

Because the magnetic geometry of a tokamak is toroidal, it is useful to apply a torus coordinate system for its description. Torus coordinates are spanned between the toroidal angle $\phi \in [0, 2\pi]$, poloidal angle $\theta \in [-\pi, \pi]$ and the radius $r > 0$. A quantity that describes the magnetic field lines that circulate around the torus is the safety factor (q):

$$q = \frac{2\pi}{\Delta\theta} = \frac{d\phi}{d\theta}. \tag{1.2}$$

It is a measure for the helicity of a magnetic field line or put simply the poloidal field line displacement $\Delta\theta$ per toroidal turn. If q is not a rational number $q \neq m/n$ ($n, m \in \mathbb{N}$) the magnetic field line circulates infinite times around the torus forming a surface of equal magnetic flux, a so-called flux surface. In a tokamak configuration these flux surfaces are intrinsically nested as shown for five of them in figure 1.3.

By applying Ampere's Law, integrating the toroidal magnetic field (B_t) around one toroidal turn the relation

$$\oint B_\mathrm{t} \mathrm{d}s = \mu_0 I \tag{1.3}$$

must hold at the inboard (R_in) and outboard (R_aus) side of the torus. Since the current I that flows trough the surfaces, which are expanded by these two paths, is constant:

$$2\pi R_\mathrm{in} B_\mathrm{t} = 2\pi R_\mathrm{aus} B_\mathrm{t} = \mu_0 I. \tag{1.4}$$

This follows that:

$$B_\mathrm{t}(R) \propto 1/R. \tag{1.5}$$

In consequence the helically twisted magnetic field line experiences a larger B_t at the inboard side of the torus than on the outboard side. For this reason these regions are also called high field side (HFS) and low field side (LFS) as indicated in figure 1.3. The gradient of the magnetic field is a drive for plasma instabilities at the LFS, while it stabilises the plasma at the HFS [13].

Another important feature of the tokamak configuration is that it is axis-symmetric in toroidal direction. For this reason a 2-D poloidal plane is representative for the 3-D magnetic equilibrium. In this context a magnetic equilibrium is the balance of the forces acting on the plasma particles from the thermal pressure (p) and the magnetic field. This is implemented through the magnetic part of the Lorentz force $\vec{j} \times \vec{B}$ and given from magnetohydrodynamics (MHD) [14]:

$$\vec{j} \times \vec{B} = \nabla p. \tag{1.6}$$

The relation implies that there is no parallel pressure gradient to $\vec{B}$. In consequence p must be constant along a magnetic field line, which causes constant p on a flux surface. Physical units that are constant on flux surfaces are called flux quantities. By introducing a coordinate system that represents the 2-D flux surface structure, flux quantities can be represented in 1-D profiles. In plasma edge physics usually two representations are applied. The normalised flux (Ψ_N)

$$\Psi_\mathrm{N} = \frac{\psi - \psi_\mathrm{axis}}{\psi_\mathrm{LCFS} - \psi_\mathrm{axis}}, \tag{1.7}$$

which is defined using the flux at the magnetic axis (ψ_axis), which represents the innermost flux surface that is basically an infinitesimally small tube, and the flux at the last closed flux surface (ψ_LCFS). The last closed flux surface (LCFS) represents the outermost flux surface of the plasma, which has no contact to the wall. Magnetic field lines that are radially further outside intersect wall elements. These 'open' field lines form the so-called scrape-off layer (SOL), where the plasma is 'scraped-off' by the wall elements, which are named limiters.

Another coordinate system that is applied to represent the flux surfaces is the normalised poloidal flux (ρ_{pol})

$$\rho_{\mathrm{pol}} = \sqrt{\Psi_{\mathrm{N}}}, \tag{1.8}$$

which is the square root of Ψ_{N}. According to the normalisation of Ψ_{N}, ρ_{pol} is 0 at the magnetic axis and 1 at the LCFS and larger than 1 in the SOL.

Another important quantity, the ratio of thermal to magnetic pressure (β)

$$\beta = \frac{p}{B^2/2\mu_0}, \tag{1.9}$$

describes the effectiveness of the plasma equilibrium. In nowadays tokamaks this value is roughly 2 %. Further, an ideal MHD limit determines the maximum achievable β [15], i.e. this parameter cannot be pushed to arbitrary numbers.

Besides its importance for plasma confinement, a reconstruction of the magnetic equilibrium is used to map measurements of plasma parameters, which originates from diagnostics that are at different radial, toroidal and poloidal locations around torus to flux coordinates. This enables combination or comparison of measurements originating from different plasma diagnostics (see chapter 3).

1.3 Divertor

Applying additional vertical magnetic fields e.g. with outer poloidal field coils (indicated grey in figure 1.2), the plasma shape in a poloidal cross section can be modified. By this a region of zero poloidal magnetic flux can be a achieved, which is called X-point. In this configuration the LCFS forms two legs that intersect with the wall in a dedicated region, the divertor. This is illustrated in figure 1.4a. Since the LCFS has closed as well as open magnetic field lines the term LCFS is imprecise. For this reason the flux surface between the confined region and the SOL in a diverted configuration is named separatrix.

The divertor region is usually equipped with tiles that can resist a large plasma heat load. According to the two legs of the separatrix two rings of tiles are assembled to intersect with the SOL plasma. These are called the inner and outer divertor targets according to their distance to the torus axis. Heat and particles that cross the separatrix e.g. at the magnetic midplane are guided towards the divertor targets along the open field lines in the SOL.

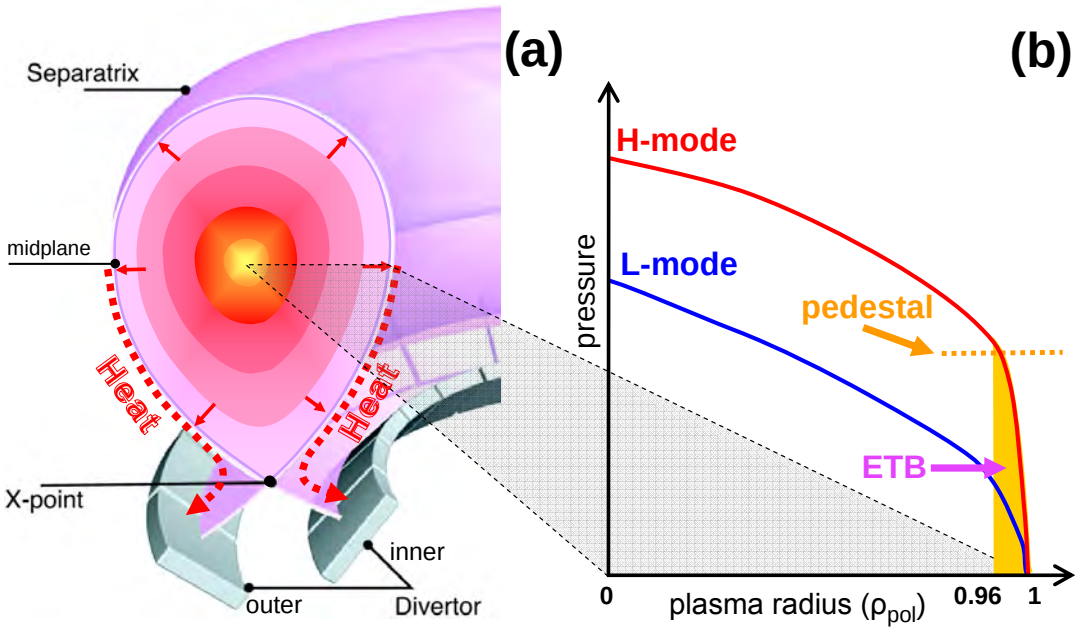

Figure 1.4: Divertor configuration and pressure profiles: (a) cutaway of the toroidal plasma with X-point and divertor target plates, (b) comparison of pressure profiles in L- and H-mode. In a diverted plasma the plasma is shaped in such a way that the LCFS self intersects forming X-point and separatrix. In H-mode an ETB leads to the formation of steep gradients in the plasma edge pressure profiles, which are called pedestal. Figure adapted from [16].

A diverted plasma configuration has several advantages:

- A spatial separation of the confined plasma and the location of the plasma-wall interaction. Wall material that is sputtered by the plasma is confined in the divertor region by geometric shielding and therefore, cannot contaminate the plasma.
- Neutrals can be pumped efficiently and by applying baffles can be compressed in the divertor region.
- The heat flux can be spread along the target according to the expansion of flux surfaces in the divertor region.
- It enables an easier access to the high confinement mode (see section 1.5).

Because of these and further advantages, the diverted plasma configuration will be used in ITER and is the most promising one for a tokamak-type fusion power plant.

technical data	
maximum toroidal magnetic field (B_t)	3.2 T
plasma current (I_p)	0.4 MA to 1.6 MA
plasma heating power (P_{heat})	up to 27 MW
plasma parameters	
major plasma radius (R_0)	1.65 m
minor plasma radius (a)	0.5 m
plasma volume	14 m^3
plasma mass	3 mg

Table 1.1: Design parameters of ASDEX Upgrade

1.4 ASDEX Upgrade

The Axially Symmetric Divertor Experiment Upgrade (ASDEX Upgrade) is a medium sized tokamak [17]. It was constructed between the late 80s and early 90s, is operated by the Max Planck Institute for Plasma Physics (IPP) and located in Garching near Munich, Germany. Besides the exploration of the diverted plasma configuration, the research nowadays focuses on the support of ITER and preparation of DEMO [18]. In addition to many scientific results that influenced the design of ITER and DEMO, ASDEX Upgrade is the worldwide leading experiment operating with an all-tungsten wall [19, 20].

Table 1.1 gives an overview of the design parameters. ASDEX Upgrade is approximately a factor of 2 smaller in minor plasma radius (a) (distance between magnetic axis and separatrix) and major plasma radius (R_0) (distance between the torus axis and the magnetic axis) than the Joint European Torus (JET) [21, 22], which is currently the world's largest tokamak experiment. With an external heating power (P_{heat}) of roughly 27 MW for a typical plasma volume of 14 m^3 it has a very high P_{heat} for its relatively small volume. Remarkably, the total mass of the plasma is just 3 mg (roughly $1.3 \cdot 10^{22}$ particles), which can be heated to temperatures so that an equivalent pressure of a truck tyre (approximately 5 bar) is reached.

1.5 High confinement mode

In the predecessor experiment of ASDEX Upgrade, ASDEX, an operational regime of improved plasma confinement was discovered in the early 1980s [23, 24]. In comparison to the low confinement mode (L-mode) operation, the energy confinement is

roughly a factor of two larger in high confinement mode (H-mode). The regime is accessed when a certain density and toroidal field dependent threshold in P_{heat}, the L-H power threshold ($P_{\mathrm{L-H}}$), is exceeded [25]. It has been found that the confinement improvement occurs in the plasma edge region due to an edge transport barrier (ETB). Its origin is a radially sheared $E \times B$ plasma flow, which is driven by the radial electric field (E_{r}) [26]. The sheared plasma flow reduces the turbulent transport due to decorrelation of the turbulent eddies [27]. Coming along with the ETB, the gradient of the plasma pressure profile steepens up at the plasma edge as illustrated in figure 1.4b. In ρ_{pol} coordinates the region of the ETB is approximately between 0.96 and 1.00 or in real space roughly 2 cm inside the separatrix.

The plasma temperature profiles in the core are found to be 'stiff' [28, 29], meaning that the achievable temperature gradient is limited or differently that the heat transport increases drastically, when a critical gradient is exceeded. Therefore, when the edge pressure gradient steepens up, also the core pressure is enlarged at unchanged gradient lengths. For this reason the region of the ETB is named pedestal because the core pressure is 'lifted up' according to the edge pressure increase. Larger pressure across the whole plasma volume results in an increased plasma performance, meaning more fusion reactions in a D-T plasma.

Because of the improved plasma performance, H-mode operation is highly favourable for a future fusion power plant. Therefore, it is also the foreseen plasma scenario for ITER.

1.6 Edge localised modes

The static picture of the pedestal and its gradients is a limited one. With exception to special operational regimes with improved confinement like quiescent H-mode (QH-mode) [30–32] or enhanced D_α (EDA) H-mode [33, 34], the steep pedestal pressure gradients are not temporally stable. Usually, they are limited by edge localised modes (ELMs) [35], which are quasi-periodic relaxations of the ETB and associated to a flattening of the pedestal gradients. Figure 1.5 illustrates this process. The ETB collapses, therefore, the gradients flatten and the pedestal is lowered.The lost energy and particles are expelled into the SOL and mainly hit the divertor targets.

According to their behaviour, e.g. ELM repetition frequency (f_{ELM}) dependency on P_{heat} or energy loss, several categories of ELMs were historically established [36]. The three main categories are:

Type-I Type-I ELMs usually occur in fully developed H-mode plasmas, when P_{heat} is far above $P_{\mathrm{L-H}}$. Typically 5 % to 10 % of the pedestal energy are lost by

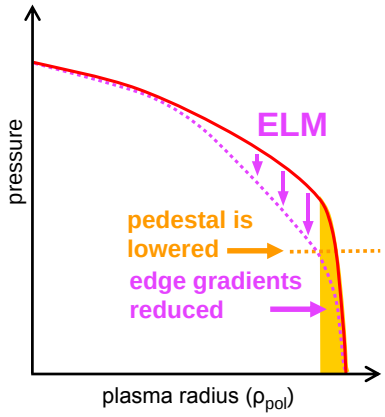

Figure 1.5: Illustration of an ELM crash: The ETB relaxes during the ELM leading to a collapse of the pedestal and flattening of the associated gradients. Figure adapted from [16].

a Type-I ELM crash. The energy loss increases towards larger fusion devices i.e. higher pedestals, leading to heat loads on the divertor tiles that exceed the material limits [37].

A feature that is used for the identification of type-I ELMs is that f_{ELM} increases with increasing P_{heat}. Typical f_{ELM} for type-I ELMs are ranging from approximately 10 Hz to 250 Hz.

Type-II These ELMs feature a high f_{ELM} (several hundreds of Hz) and a rather small energy loss. Usually, the plasma parameters leading to the occurrence of type-II ELMs are strongly shaped and highly collisional plasmas meaning large plasma density and low temperatures [38]. Therefore, this plasma regime is currently not scalable towards reactor relevant regimes.

Type-III These ELMs are rather small and occur immediately after the L-H transition with P_{heat} only marginally above $P_{\mathrm{L-H}}$. In contrast to type-I ELMs, f_{ELM} decreases with increasing P_{heat} [39]. Another feature of type-III ELMs is the onset and growth of an ELM precursor, which evolves into the ELM crash.

Owing to their size and occurrence under reactor relevant conditions type-I ELMs are of special interest. An impression of the impact of a type-I ELM crash on the plasma edge and SOL is given in figure 1.6 by fast camera images of visible light from a tangential view into the torus. Typically, a type-I ELM crash has a duration of 1 ms to 3 ms. The imaged light is a convolution of neutral and plasma density as well as temperature. The main light contribution originates from excited D atoms and intrinsic plasma impurities. For this reason, mainly the relatively cold plasma edge and SOL emit light since in the hot plasma core the atoms are fully ionised. In between the ELMs, the plasma is relatively quiet and the separatrix can be identified, figure 1.6a.

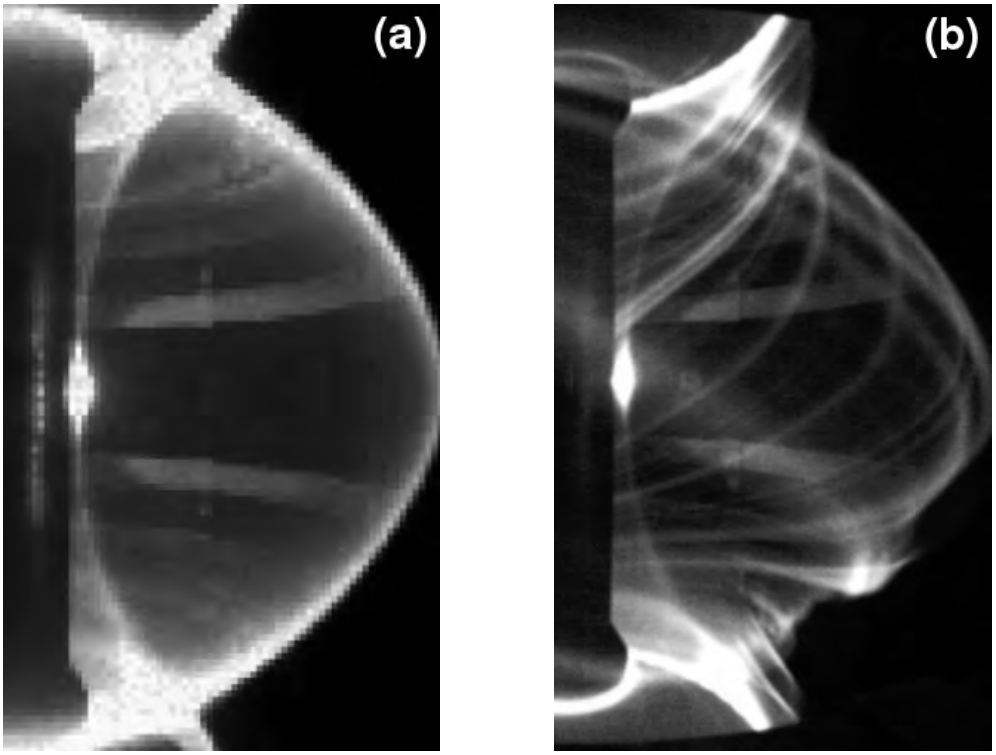

Figure 1.6: Fast camera images of visible light in the H-mode, measured at the Mega Ampere Spherical Tokamak (MAST): Tangential view into toroidal direction (a) in between ELMs and (b) during an ELM crash. While the edge plasma is relatively quiet in the inter-ELM period, filaments, which are helical, field aligned plasma perturbations that increase the emission, are expelled to the SOL and divertor. Figure adapted from [40].

During the ELM crash, when the pedestal collapses, a the plasma edge is much more turbulent. Filaments, which are field aligned plasma perturbations are expelled into the SOL, which cause enhanced light emission. These can be seen in figure 1.6b as bright bands, which are helically wound around torus.

Pulsed heat and particle loads due to type-I ELMs are an engineering challenge for plasma facing materials, especially in future devices such as ITER [41]. Therefore, fusion research emphasises on the mitigation, suppression and avoidance of large ELMs. Further, deeper insight in the underlying processes that determine the stability of the pedestal with respect to the occurrence of large ELM crashes is required to optimise plasma scenarios towards reactor applicability.

1.7 Objectives of this thesis

The aim of this thesis was to systematically investigate the evolution of the pedestal structure between type-I ELM crashes for a range of plasma parameters, which are known to influence the stability of the pedestal. By this approach, a variety of comparisons could be achieved and the pedestal structure as well as the dynamics were well characterised. These insights can support the improvement of pedestal models.

Investigating the inter-ELM pedestal structure evolution means to study the recovery of the pedestal electron density (n_e) and electron temperature (T_e) profiles after its collapse due to a type-I ELM crash. Throughout this thesis, whenever it is referred to an ELM, a type-I ELM is implied. This is to clarify that the results of this thesis apply to fully developed H-mode plasmas, i.e. the ETB is established and besides the ELMs no temporal dynamics of the plasma is expected.

The work of this thesis has been conducted in close collaboration between IPP and TU Wien, that is embedded in the European Consortium for the Development of Fusion Energy (EUROfusion). Within this framework, the experiments and plasma discharges that are presented in this thesis, were performed at the ASDEX Upgrade tokamak (section 1.4).

The structure of the presented thesis follows the main research goals and scientific tasks that were analysed. At the beginning, a deeper introduction into plasma edge physics and pedestal stability is given in chapter 2. Chapter 3 introduces the mainly utilised diagnostic principles and their specific set-ups at ASDEX Upgrade. By means of this unique set of plasma edge diagnostics [42] high quality pedestal profiles were provided. These data are the base for all scientific investigations, which are presented within this thesis.

The main scientific tasks of this thesis and the achieved results as well as their interpretation are summarised in the following chapters. These are structured as follows:

Inter-ELM pedestal recovery for different plasma collisionality (ν^*)
As it will be introduced in chapter 2, different microinstabilities are theoretically expected to appear in the pedestal region. Their occurrence is mainly coupled to several plasma parameters such as ν^* or p. Therefore, a variation of ν^*, without changing other plasma parameters was performed. This variation is used to investigate high frequency magnetic fluctuations in between ELMs. The results of these study have been published in [43] and, are reported in chapter 4.

Inter-ELM pedestal evolution in plasmas with different main ion species
An exchange of the main plasma isotope leads to a change of the particle and

energy confinement, i.e. lower mass hydrogenic species are confined worse. It is known that also f_{ELM} and ELM energy losses are affected by an isotope exchange. To shed new light on the mechanisms, that determine the pedestal structure, f_{ELM} and inter-ELM pedestal evolution, D, hydrogen (H) and ^{4}He plasmas are compared. The achieved results have been published in [44] and are summarised in chapter 5.

Connection of the inter-ELM divertor, SOL and pedestal evolution
Due to the expelled particles and heat, ELMs introduce changes on the divertor and SOL conditions. The impact of these dynamics on the inter-ELM pedestal recovery is investigated, emphasising on the n_{e} evolution. The related results are in preparation for publication [45] and are discussed in chapter 6.

Impact of plasma shape on pedestal stability, f_{ELM} and the inter-ELM evolution
It is known that the plasma edge stability is affected by the plasma shape e.g. triangularity (δ) [46]. A parameter scan of δ is performed and edge stability analysis was done for several cases. These results are summarised in chapter 7.

In chapter 8, a summary of the achieved results is given. Further, general conclusions, drawn from the combination of results from different scientific tasks, and a brief outlook into new questions for future work complete the thesis.

2 Introduction to plasma edge and pedestal physics

Since the discovery of the H-mode, the pedestal has been in focus of research to understand underlying mechanisms, leading to the formation of the ETB and its sustainment. Over the years an experimental as well as theoretical picture has been formed, up to now, however, it is still incomplete. Several key questions are currently under research, most of them addressing either trigger mechanisms of ELM crashes [47], the stabilisation of the pedestal afterwards and the remaining transport in the ETB [48]. Further, techniques for mitigation or suppression of large ELMs [49] are developed in order to be applied in ITER or DEMO.

This chapter introduces the current understanding of the pedestal and its dynamics in between ELM crashes. Section 2.1 focuses on the plasma edge stability, in section 2.2 the evolution between ELMs is emphasised.

2.1 Plasma edge stability

ELMs are large scale instabilities at the plasma edge. In a first step, it is important to understand the stability of the pedestal. As already introduced in section 1.2.2, the plasma equilibrium balances the forces acting on the particles (see equation (1.6)). Here, two important quantities enter, which are potential drives for instabilities: The thermal pressure (p) and the current flowing in the plasma ($\vec{j}$). An equilibrated state does not imply stable conditions, i.e. a perturbation to the state could either relax (stable conditions) or grow (unstable conditions) [13]. This also applies to the pedestal. The topology of the magnetic field, the steep thermal pressure gradient (∇p) in combination with large currents determine the pedestal stability. Only a small fraction of the current in the pedestal is induced by the ohmic transformer, its main contributors are Pfirsch-Schlüter (PS) currents, which are parallel to the magnetic field and cancel the charge separation of the diamagnetic drift, and the bootstrap current [50, 51]. The bootstrap current is a self-generated toroidally flowing current that is caused by the presence of ∇p in a toroidal magnetic configuration and particle collisions. For

this reason ∇p and $\vec{j}$ are coupled. The underlying mechanism that generates the bootstrap current is outlined in section 2.1.1.

2.1.1 Bootstrap current

For particles moving along field lines from LFS to HFS, a magnetic mirror is formed because of the radial ∇B. Their kinetic energy

$$E = \frac{1}{2} m (v_{\parallel} + v_{\perp})^2 \tag{2.1}$$

using the parallel ($v_{\parallel}$) and perpendicular ($v_{\perp}$) velocity component relative to the magnetic field, and their magnetic moment

$$\mu = \frac{1}{2} \frac{m v_{\perp}^2}{B} \tag{2.2}$$

are invariant along field lines. When the plasma particles move towards regions of higher B, $v_{\parallel}$ is reduced. If $v_{\parallel}$ becomes zero, the particle gets reflected. This is called trapped, since the particle cannot move freely parallel to the field lines. Owing to drifts in the plasma the particles are additionally pushed up- or downwards when moving relative to ∇B, leading to characteristic trajectories named banana orbits. A sketch of a trapped particle orbit is shown in figure 2.1. These orbits are named 'banana', since their poloidal projections are shaped like the eponymous fruit.

Considering two banana orbits, which intersect at one radial location, and a density gradient ∇n towards the plasma core, the inner banana orbit is traced by a larger amount of particles than the outer banana orbit. This leads to a net current in poloidal direction [52]. The momentum of the trapped particles is transferred to passing, non-trapped particles via collisional friction [53]. Passing particles have a large enough $v_{\parallel}$ to overcome ∇B. The resulting currents have opposite directions for electrons and ions owing to their charge. The bootstrap current is then the difference between these two currents. It has roughly the following parametric dependencies [54]:

$$j_{\mathrm{bs}} \propto \sqrt{\epsilon} \frac{\nabla p}{B_{\mathrm{pol}}}. \tag{2.3}$$

A more general expression of the bootstrap current has been derived taking into account plasma geometry and arbitrary plasma collision rates [55, 56].

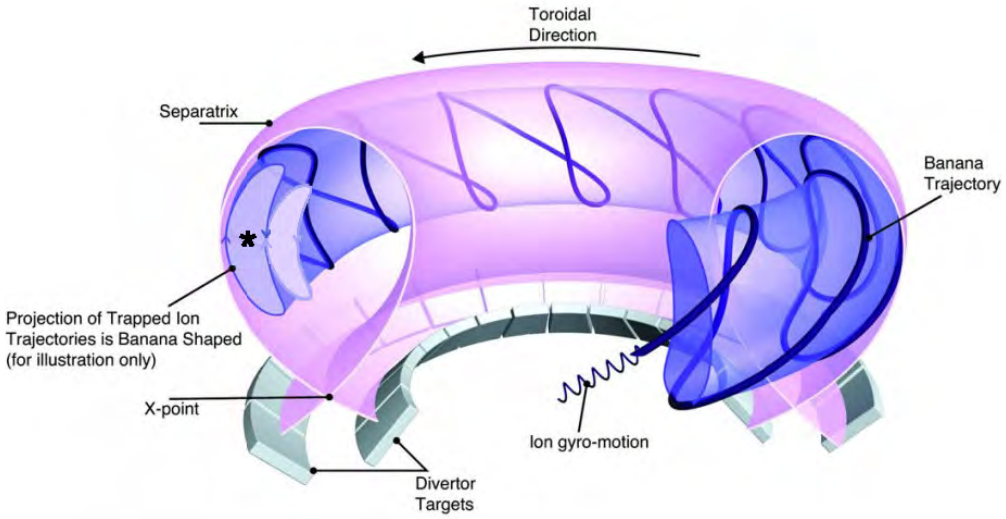

Figure 2.1: Banana orbit of a trapped particle in a tokamak: Additionally to the gyro-motion the trapped particle precesses in toroidal direction. In consequence of scattering processes between these trapped and passing particles a toroidal current, the bootstrap current, is produced. Figure taken from [12], which was originally modified from [10].

2.1.2 Plasma collisionality

The driven bootstrap current depends on the collision rate of the plasma particles because of the necessary momentum transfer from trapped to passing particles [57]. A dimensionless parameter, which is used to describe this quantity is the plasma collisionality (ν^*) for species j (e for electrons or i for ions):

$$\nu_{\mathrm{j}}^* = \frac{\nu_{\mathrm{j}}}{\epsilon\omega_{\mathrm{bj}}}. \tag{2.4}$$

It is the ratio of the particle collision frequency (ν_{j}) and the banana bounce frequency (ω_{bj}) weighted with the inverse aspect ratio $\epsilon = a/R_0$ and describes basically the number of collisions while passing a banana orbit. The particle collision frequency is given by

$$\nu_{\mathrm{j}} = \frac{Z\zeta_{\mathrm{j}} \ln\Lambda}{c_{\mathrm{j}}} \frac{n_{\mathrm{i}} e^4}{\varepsilon_0^2 m_{\mathrm{j}}^{1/2} T_{\mathrm{j}}^{3/2}} \tag{2.5}$$

using charge (Z), coulomb logarithm ($\ln\Lambda$), ion density n_i, elementary charge (e), vacuum permittivity (ε_0), species mass (m_j) and species temperature (T_j) [58]. The constants (c_j) are $c_\mathrm{i} = 12\pi^{3/2}$ and $\zeta_\mathrm{i} = 4$ for ions as well as $c_\mathrm{e} = 3\,(2\pi)^{3/2}$ and $\zeta_\mathrm{e} = 2$ for electrons. Further the banana bounce frequency is determined by

$$\omega_\mathrm{bj} = \frac{v_\perp}{qR_0}\left(\frac{r}{2R_0}\right)^{1/2} = \frac{T_\mathrm{j}^{1/2} r^{1/2}}{m_\mathrm{j}^{1/2} q R_0^{3/2}} \tag{2.6}$$

at a plasma radius (r) with major plasma radius (R_0), safety factor (q) and by approximating $v_\perp \approx v_\mathrm{T} = \sqrt{2T_\mathrm{j}/m_\mathrm{j}}$, which is the thermal velocity of the species.

This yields

$$\nu_\mathrm{j}^* = \frac{Z\zeta_\mathrm{j}\ln\Lambda}{c_\mathrm{j}\epsilon}\frac{R_0^{3/2} n_\mathrm{i} \mathrm{e}^4}{r^{1/2} T_\mathrm{j}^2 \varepsilon_0^2}, \tag{2.7}$$

which now can be evaluated either for the ions or electrons. Most important dependencies of ν^* are the proportionality to n_i and the inverse relation to T_j^2. This means that at constant p, ν^* decreases when the temperature increases.

2.1.3 Plasma shaping

As already seen in the introduction of the bootstrap current, where the inverse aspect ratio (ϵ) enters, geometrical conditions can impact plasma quantities, which then can change the stability. In the following, the most relevant ones are introduced.

A parameter, describing the ellipticity of the poloidal cross section is plasma elongation (κ):

$$\kappa = b/a. \tag{2.8}$$

It is defined as the ratio of vertical minor plasma radius (b) and horizontal minor plasma radius (a), which would be the main axis lengths of an ellipsis. Since real plasma shapes are not perfectly elliptical a more general definition of a and b is utilised:

$$a = \sqrt{\frac{\int_S (R - R_\mathrm{geo})^2 \mathrm{d}A}{\int_S \mathrm{d}A}}, \tag{2.9}$$

$$b = \sqrt{\frac{\int_S (z - z_\mathrm{geo})^2 \mathrm{d}A}{\int_S \mathrm{d}A}}. \tag{2.10}$$

By $\int_S \mathrm{d}A$ an integration within the separatrix is denoted. Further, the geometrical plasma axis radius (R_{geo}) is defined as

$$R_{\mathrm{geo}} = \frac{\int_S R \mathrm{d}A}{\int_S \mathrm{d}A} \tag{2.11}$$

and accordingly defined the geometrical plasma axis height (z_{geo})

$$z_{\mathrm{geo}} = \frac{\int_S z \mathrm{d}A}{\int_S \mathrm{d}A}. \tag{2.12}$$

In comparison to a circular plasma cross section, an elongated plasma has a roughly $(1+\kappa^2)/2$ larger poloidal circumference. For given I_{p}, B_{t}, a and R_0 this increases q by a similar factor [13]:

$$q_* = q_{\mathrm{circ}} \frac{1+\kappa^2}{2}. \tag{2.13}$$

Since enlarged q impact positively on the plasma stability, an elliptical shape $\kappa > 1$ stabilises the plasma.

Another quantity that positively impacts on the plasma stability is the triangularity (δ). To illustrate its determination, figure 2.2 shows a poloidal cross section of a diverted plasma, including the contributing parameters.

The upper (δ_{up}) and lower (δ_{low}) triangularity are calculated from the ratio of the radial distance ($r_{\mathrm{up,low}}$) between the uppermost/lowest point of the plasma ($R_{\mathrm{up,low}}$) and the mid radius (R_{mid}),

$$r_{\mathrm{up,low}} = R_{\mathrm{up,low}} - R_{mid}, \tag{2.14}$$

and the geometrical minor radius (a_{m}):

$$\delta_{\mathrm{up,low}} = \frac{r_{\mathrm{up,low}}}{a_{\mathrm{m}}}. \tag{2.15}$$

The average of δ_{up} and δ_{low} gives δ:

$$\delta = \frac{\delta_{\mathrm{up}} + \delta_{\mathrm{low}}}{2}. \tag{2.16}$$

It is a measure of the D-shape of a plasma. While a circular plasma has zero δ, a plasma with its top and bottom at R_{in} has $\delta = 1$. Also configurations with negative triangularity are possible with $R_{\mathrm{up,low}} > R_{\mathrm{mid}}$ [59]. Positive δ stabilises the plasma edge because the magnetic field lines are pushed towards the HFS. There ∇p and ∇B have opposite directions, which has a stabilising effect [13]. At the LFS ∇p

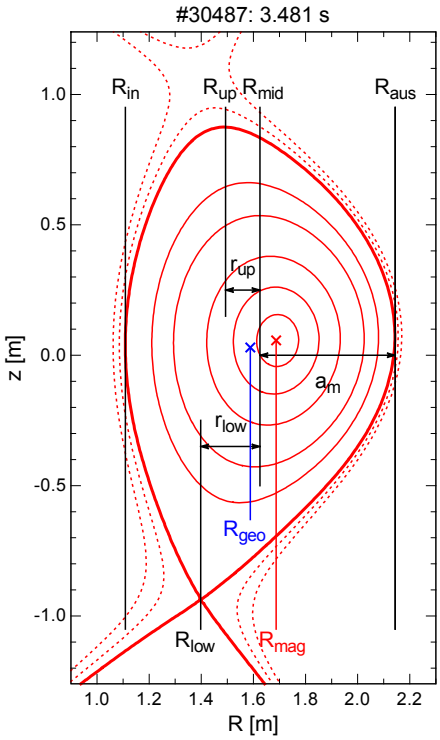

Figure 2.2: Definition of the triangularity (δ): the average of upper and lower triangularity $\delta_{\mathrm{up,low}}$, which are the ratios of the distance from mid radius to upper- and lowermost separatrix position radius $r_{\mathrm{up,low}}$ and geometric minor radius a_{m}. Further, the positions of the magnetic axis (R_{mag}) and the geometrical plasma axis (R_{geo}) as defined in equation (2.11) are indicated.

and ∇B point inwards, i.e. in the same direction, which is destabilising. This HFS-LFS difference will lead to characteristic instabilities, which are called ballooning modes.

2.1.4 Peeling-ballooning theory

As already discussed in section 2.1, the main drives for instabilities at the plasma edge, that can cause ELM crashes, are pressure gradient and current. From the ideal MHD equations the most common model to describe the plasma edge stability is derived [60], the so-called peeling-ballooning (PB) model. In MHD, instabilities are named 'modes' because their periodicity is used to characterise their structure, according to the mechanical analogue of eigenmodes from an oscillating string. In toroidal geometry the periodicity in toroidal direction is characterised by the toroidal mode number (n) and in poloidal direction by the poloidal mode number (m). The

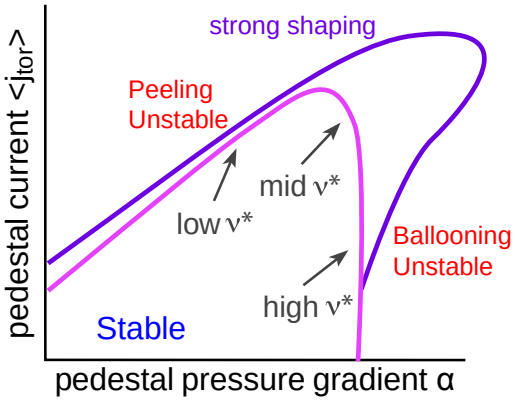

Figure 2.3: Illustration of the pedestal stability: normalised pressure gradient (α) and flux surface averaged toroidal current density $\langle j_{\mathrm{tor}} \rangle$ determine the stability boundary (magenta). Plasma shaping extends the region of stability towards larger α and $\langle j_{\mathrm{tor}} \rangle$ (purple). Figure modified from [62].

radial location of the mode is given by the flux surface that satisfies the condition

$$q = \frac{m}{n}, \tag{2.17}$$

which is called 'resonant' because the magnetic field line helicity is equal to the perturbation structure, i.e. in resonance. For example an $m/n = 3/2$ mode is localised at the $q = 1.5$ flux surface, has a toroidal periodicity of two and a poloidal periodicity of three.

The PB model is based on the coupling of pressure gradient driven ballooning modes and current driven peeling modes [61]. Figure 2.3 illustrates this by plotting the normalised pressure gradient (α) and average toroidal current density in the pedestal ($\langle j_{\mathrm{tor}} \rangle$). As a measure of the ∇p, α is defined as follows [63], using the plasma volume (V) at a given ψ:

$$\alpha = -2\mu_0 \frac{\partial V}{\partial \psi} \frac{1}{(2\pi)^2} \left(\frac{V}{2\pi^2 R_0} \right)^{1/2} \frac{\partial p}{\partial \psi}. \tag{2.18}$$

This expresses that:

$$\alpha \propto -\frac{2\mu_0 R_0 q^2}{B^2} \frac{dp}{dr}. \tag{2.19}$$

A region of stability is spanned between maximum normalised pressure gradient (α_{max}) and $\langle j_{\mathrm{tor}} \rangle$ that is limited by the PB or stability boundary. When exceeding this limit towards larger $\langle j_{\mathrm{tor}} \rangle$, it is likely that peeling modes exceed a critical growth rate, which dominantly happens at low ν^*. If the PB boundary is passed towards larger α_{max}, ballooning modes overcome critical growth. This is more likely at high ν^*. At intermediate ν^* the coupled PB modes get dominantly unstable, when the

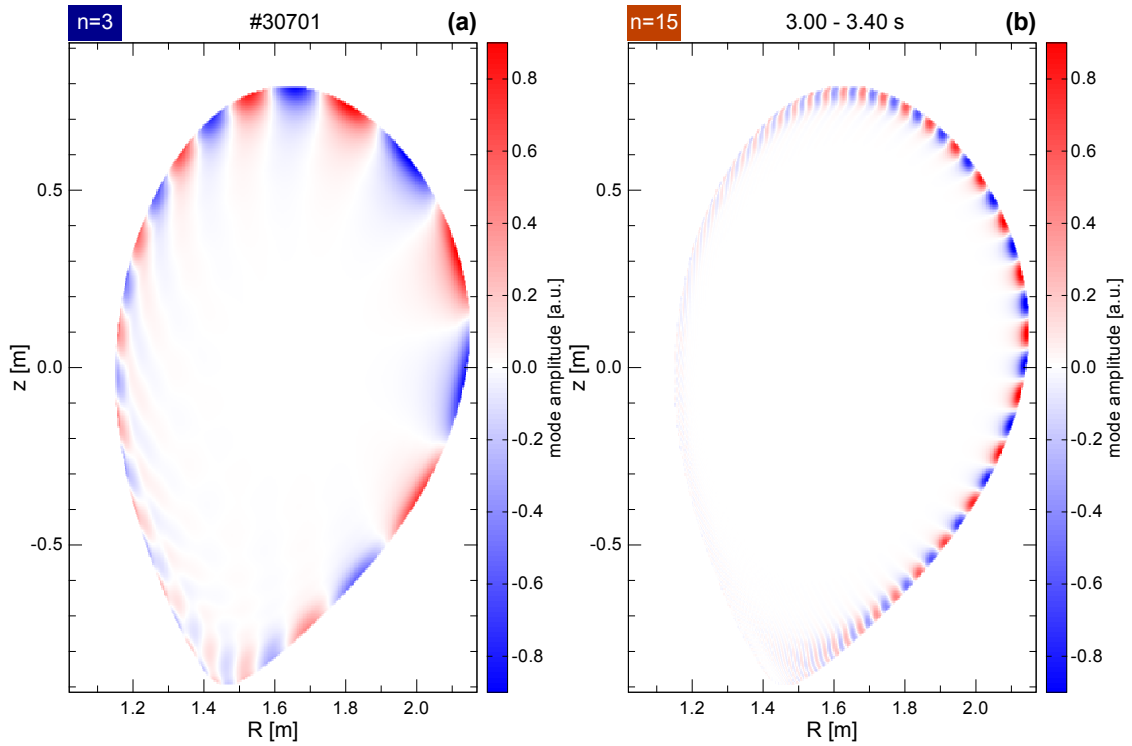

Figure 2.4: Poloidal mode structures: (a) of a low toroidal mode number (n) peeling mode and (b) a large n ballooning mode. Because of the dominant low n, peeling modes have a larger poloidal distance between amplitude minima and maxima. Further the amplitudes on HFS and LFS are comparable. The ballooning mode is dominant on the LFS due to the unfavourable magnetic topology.

stability boundary is exceeded. Stronger shaping of the plasma, i.e. mainly increasing δ, enlarges the stable region in j-α, and therefore, allows steeper pressure gradients and higher $\langle j_{\mathrm{tor}} \rangle$ at the plasma edge [62].

Because of the different drive mechanisms peeling and ballooning modes have characteristic mode numbers and features. The current driven peeling modes have low n and are poloidally large in size, i.e. the corresponding m is also rather low. The poloidal mode structure of an $n = 3$ peeling mode in real plasma geometry is presented in figure 2.4a. The mode structure is localised at the plasma edge and visible on the HFS. It seems that the outer part of the plasma is 'peeled' off, which is the reason for the mode's name.

In contrast to the peeling mode, the ballooning mode has relatively large n. An example of an $n = 15$ ballooning mode structure is shown in figure 2.4b. The mode sits dominantly on the LFS, which is caused by the HFS-LFS difference in the orientation

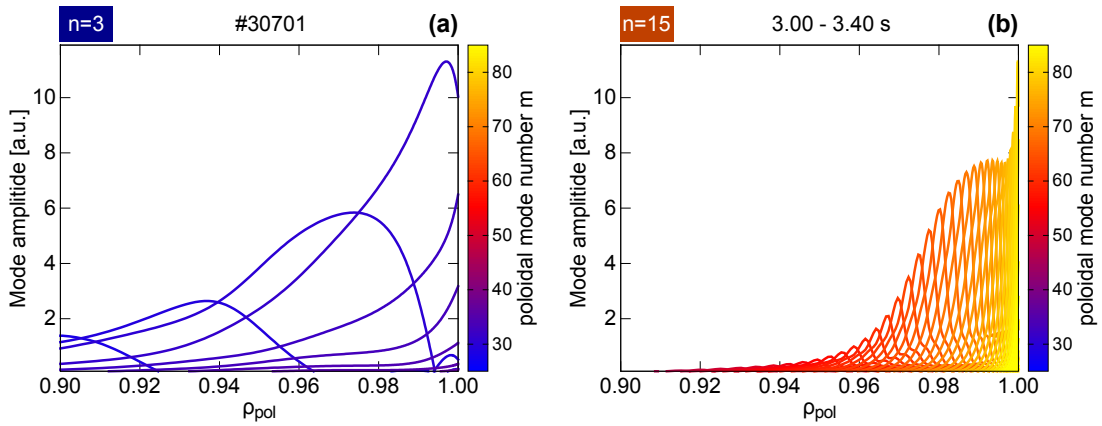

Figure 2.5: Radial spectrum of the mode amplitude and the poloidal mode numbers (m): (a) peeling and (b) ballooning mode. While the peeling mode is characterised by one radial large extended mode with distinct m, the ballooning mode is characterised by the superposition of several m.

of ∇p and ∇B. Further, the poloidal structure size is smaller. The associated m also have to be higher because peeling as well as ballooning modes are localised at the far plasma edge at similar q.

Another intrinsic difference between peeling and ballooning modes can be seen in a radial m spectrum as shown in figure 2.5. Peeling modes have one dominant m that extends radially inward over the full pedestal region, which is also reflected in their HFS-LFS symmetry (figure 2.5a). In contrast, the ballooning mode consists of several m, which cover the full pedestal region (figure 2.5b). The corresponding mode structure, which is ballooned on the LFS, is formed by the contributions of the different m. These couple such that they virtually cancel on the HFS and fully add up at the LFS midplane. The origin of the higher n of ballooning modes is that the different m contributions have to couple radially, which requires short distances. Since the variation of m implies a variety of resonant surfaces, these surfaces have to be close enough. For larger n the distance of the resonant surfaces decreases, enabling radial coupling and formation of a ballooning mode.

2.1.5 Linear MHD stability analysis

To determine the stability of the pedestal with respect to critical growth of PB modes, linear ideal MHD stability analysis can be performed. Since geometric and shaping effects have to be taken into account to accurately reproduce the experimental conditions, a reconstructed plasma equilibrium serves as input for the calculations. The ELM crash itself is a result of non-linear interaction [64, 65] and therefore, at least

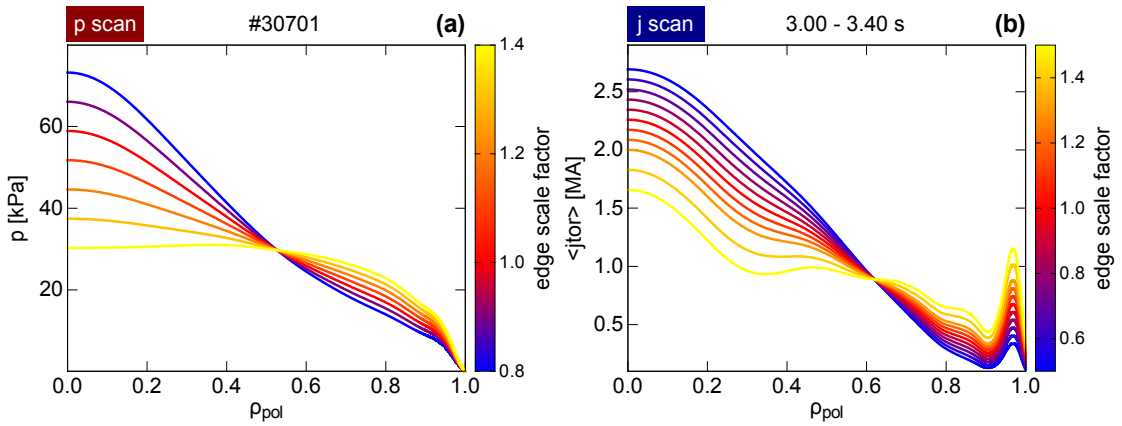

Figure 2.6: Illustration of an edge parameter scan: (a) pressure and (b) current scan. The pressure gradient at the edge is varied and the core profile is scaled contrariwise to keep W_{MHD} constant. A similar approach is used for the current scan, where $\langle j_{\mathrm{tor}} \rangle$ at the edge is scaled and I_{p} is kept constant.

requires non-linear MHD [66]. However, linear analysis is less computationally expensive and can be used to study the growth of PB modes in real plasma geometry [67, 68]. By scaling the input equilibrium to larger size, also analyses for the edge stability of ITER were performed [69].

For the linear stability analyses presented in this work, equilibria from the performed discharges served as input. These were reconstructed by two different equilibrium solvers that are usually used at ASDEX Upgrade, CLISTE [70, 71] and the recently established IDE solver [72]. Further, the edge pressure profile was constrained to the measured one, which significantly improves the reconstruction of the bootstrap current [73]. The equilibria of both solvers were compared and agreed within the experimental uncertainties. In the presented studies, whenever it is not explicitly specified the IDE equilibrium solver has been used for the reconstruction.

For the stability analysis the recently improved stability workflow at ASDEX Upgrade [74], called j-alpha work flow, has been applied. To remove the singularity in poloidal flux, the X-point from the input equilibrium is removed by cutting off flux surfaces outside 99.6 % of the poloidal flux inside the separatrix. The resulting data is fed to the fixed-boundary equilibrium solver HELENA [75], which determines the equilibrium of the experimentally measured operational point. In the next step, the resulting profiles of p and $\langle j_{\mathrm{tor}} \rangle$ are scaled at the edge, creating a grid in edge $\langle j_{\mathrm{tor}} \rangle$ and α_{max}. The scans of p and $\langle j_{\mathrm{tor}} \rangle$ are illustrated in figure 2.6. The red profiles of the operational point are scaled at the plasma edge as indicated by the different colours. This pressure variation

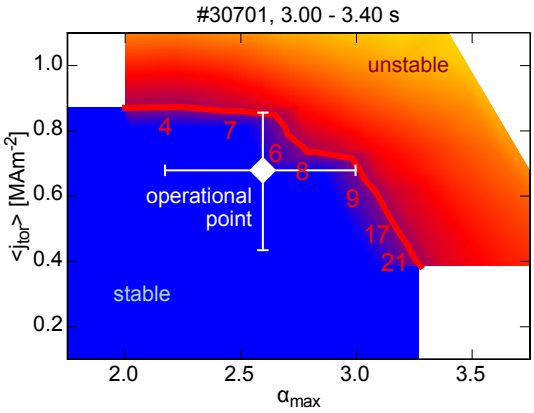

Figure 2.7: j-α diagram: operational point and stability boundary. The operational point represents the experimentally observed $\langle j_{\mathrm{tor}} \rangle$ and α_{max} with their uncertainties. The stability boundary is determined by combined pressure and current scans. The red numbers indicate the most unstable n along the stability boundary.

is performed such that the plasma stored energy (W_{MHD}),

$$W_{\mathrm{MHD}} = \frac{3}{2} \int p \mathrm{d}V, \tag{2.20}$$

is unchanged. Therefore, the core pressure is reduced, when the edge pressure is increased. A similar condition is applied for the variation of $\langle j_{\mathrm{tor}} \rangle$, here I_{p} remains unchanged.

In the following step, all resulting combinations of p and $\langle j_{\mathrm{tor}} \rangle$ profiles serve as input to HELENA and the corresponding equilibria are calculated. These are then analysed by an ideal MHD stability code. Within this work two codes, a fast version of MISHKA [76, 77] and ILSA [78], were used. Whenever it is not stated differently, MISHKA was utilised for the stability analysis. In the calculations, the stabilising effect of the diamagnetic drift were not taken into account.

With the linear MHD stability code the growth rates for a variety of n are calculated for each equilibrium that resulted from the j-α scan. The most unstable mode is determined from the resulting mode number spectra. If the growth rate of the most unstable mode number is larger than 4 % of the Alfven wave growth rate (γ_{Alfven}), critical growth and therefore, pedestal instability is assumed. The equilibria, which are closest to the operational points, and fulfil this condition give the stability or PB boundary as indicated in figure 2.7 (red line). All equilibria, which have smaller most unstable mode growth form the stable region in j-α space (blue area). In the presented case the operational point is located very close to the PB boundary, within

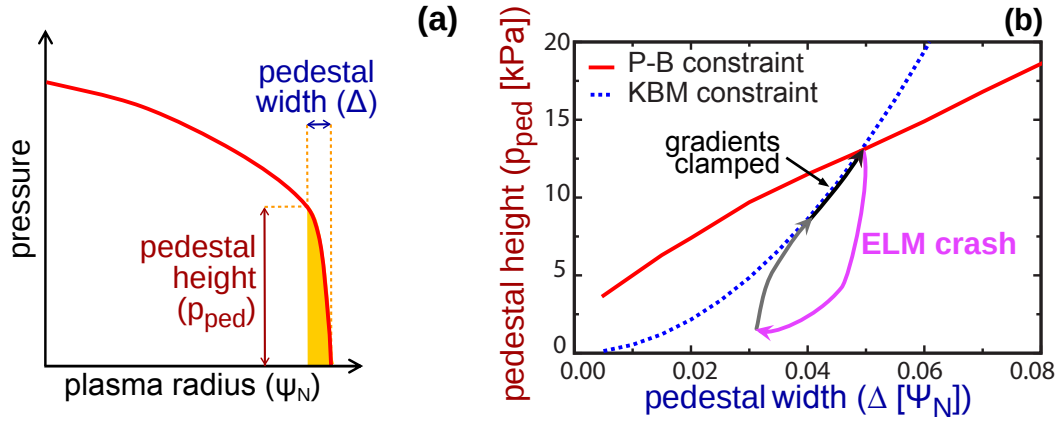

Figure 2.8: Illustration of a type-I ELM cycle: (a) sketch of pedestal height (p_{ped}) and pedestal width (Δ) as well as (b) evolution of pedestal height (p_{ped}) and pedestal width (Δ) throughout the ELM cycle according to the EPED model. After an initial recovery the pedestal evolves along the KBM constraint, which clamps the pressure gradient, towards the PB limit at which the ELM crash occurs. Figure modified from [62].

the uncertainties of the experimental equilibrium. Along the stability boundary the most unstable n are indicated in red. As expected, these are smaller at the peeling part (low α_{max}, large $\langle j_{\mathrm{tor}} \rangle$, n between 4 and 7) than at the ballooning part (large α_{max}, low $\langle j_{\mathrm{tor}} \rangle$, n between 17 and 21) of the stability boundary.

2.2 Inter-ELM pedestal evolution

Linear ideal MHD stability can determine the critical growth of modes that lead to an unstable pedestal. But the onset, i.e. the non-linear interaction of the modes that result in the ELM crash as well as the dynamics in between ELM crashes are not captured. Therefore, research also focuses on the periods in between ELM crashes, i.e. the inter-ELM dynamics, which give insights in the instabilities that are present in the pedestal and determine its evolution towards unstable conditions.

2.2.1 Theoretical description of the pedestal dynamics

One motivation to model the pedestal dynamics throughout the ELM cycle is to gain predictive capabilities for the pedestal height (p_{ped}) and pedestal width (Δ), which are illustrated in figure 2.8a. The p_{ped} is one crucial parameter for machine performance, because the edge pressure increase is directly transferred to the core

plasma. Therefore, scaling of p_{ped} towards ITER is desired. However, PB analysis does not give information about the maximum achievable p_{ped}.

To predict p_{ped} another constraint is required. Motivated from the experimental finding, that Δ scales with $\sqrt{\beta}$, the EPED model derives that KBM turbulence causes this dependency and leads to the relation, which links β and Δ [79]. Figure 2.8b illustrates the two constraints of p_{ped} and Δ used in the EPED model. Further, the evolution of both quantities during the ELM cycle is indicated. After the ELM crash the pedestal rapidly builds up in height. When the KBM constraint is reached, a 'soft' limit sets in that leads to clamping of ∇p. Now, p_{ped} and Δ are connected but increase further. The PB limit represents a 'hard' limit, which is related to the onset of the ELM crash.

2.2.2 Microturbulent instabilities in the pedestal

It is still under discussion, which type of instabilities cause the connection of p_{ped} and Δ in the second period of the ELM cycle. In the following section, findings from plasma edge turbulence simulations are summarized and the theoretical motivation for KBMs to cause the clamping of ∇p is discussed.

In the following, the most common microinstabilities are listed and their features e.g. poloidal propagation direction are characterised:

Kinetic ballooning mode (KBM)

KBMs are the kinetic analogues of ideal ballooning modes [80–82]. 'Kinetic' in this sense means that pressure fluctuations in parallel to the field lines, which are excluded in the ideal MHD equations, are allowed. Usually, gyrokinetic simulations are used to study KBMs. Besides the characteristic ballooned mode structure, KBMs show a stiff onset above a threshold of critical β, that is close to the onset for ideal MHD ballooning modes [83]. KBMs propagate poloidally in the direction of the ion flow, that is caused by the diamagnetic $\nabla p \times B$ drift. There is evidence from several experiments that KBMs are unstable in the steep gradient region of the pedestal, e.g. in MAST [84], JET [85] and ASDEX Upgrade [86].

Microtearing mode (MTM)

MTMs are the kinetic analogues to MHD tearing modes [87]. These are mainly driven by the electron temperature gradient (∇T_{e}), causing small scale magnetic islands and therefore, enhanced radial transport [88]. Their poloidal propagation is in electron-diamagnetic direction, i.e. opposite to the one of KBMs. In gyrokinetic studies, MTMs were found to exist at the pedestal top of MAST plasmas [89, 90], where also experimental measurements of fluctuation levels and scale sizes agree with the expectations for MTMs [91]. They were also identified

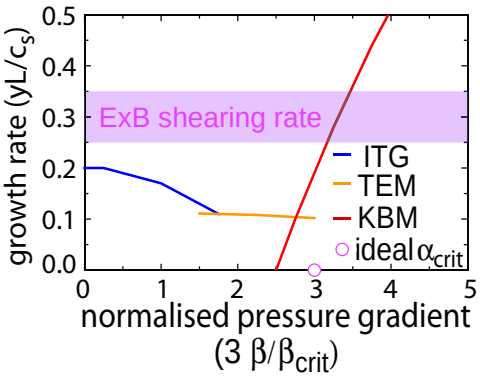

Figure 2.9: Illustration of turbulent regimes: While ion temperature gradient (ITG) turbulence and trapped electron modes (TEM) are dominant at low β but well below the $E \times B$ shearing rate, kinetic ballooning modes (KBMs) show large growth rates at experimentally observed β. Figure modified from [79].

in simulations of the pedestal region from JET [85, 92] and ASDEX Upgrade [93, 94]. At ASDEX Upgrade also experimental evidence of MTMs was found [95] as well as on the National Spherical Torus Experiment (NSTX), where measurements were in agreement with MTM turbulence [96]. Further, simulations of the NSTX pedestals revealed MTMs [97, 98].

Ion and electron temperature gradient mode (ITG, ETG)

These turbulent modes are usually present in the core plasma. Their drives are, according to their names, ion temperature gradient (∇T_i) [99] and ∇T_e [100]. Because of the difference in the gyro-radii ETG modes have much smaller scales than ITG. Further, they propagate in opposite poloidal directions; ETG in electron-diamagnetic and ITG in ion-diamagnetic direction. By an experimental variation of the plasma heating, i.e. dominant electron or ion heating, the corresponding temperature profiles can be varied and transitions between the ITG and the trapped electron modes (TEM) regime achieved [101].

Trapped electron modes (TEM)

Similar to ETGs, TEMs are driven by ∇T_e, however they have larger structure sizes, comparable to ITG and propagate in the electron-diamagnetic direction.

The motivation to relate KBMs to the clamping of ∇p is illustrated in figure 2.9. While ITG and TEM are dominant at lower β, than observed in the experiment, the growth rate of KBMs immediately increases when reaching the experimentally determined critical β. This is referred to as 'stiff' onset of KBM turbulence.

Up to now, the $E \times B$ flow of the background plasma has not been considered. But sheared flows rip apart or distort radial structures and therefore, suppress the development of turbulence, which is the case in the ETB. As indicated in figure 2.9 the $E \times B$ shearing can be transferred in a growth rate that must be exceeded. This simplified picture illustrates that turbulent instabilities below a certain critical growth are suppressed by the $E \times B$ flow shear. If this critical growth is reached, the instability develops and gets dominant. In this picture, solely KBMs exceed the critical growth.

2.2.3 Experimentally observed phases of the inter-ELM pedestal evolution

Previous studies on the inter-ELM profile evolution at ASDEX Upgrade revealed different recovery time scales for n_e and T_e [102]. Similar observations were made at the JAERI tokamak - 60 Upgarde (JT-60U) [103], DIII-D [104] and JET [105], however, at the latter one the sequence of n_e and T_e recovery was opposite to ASDEX Upgrade and JT-60U. At ASDEX Upgrade it was found that electron density gradient (∇n_e) and ∇T_e are clamped already of the order of ms before the ELM onset [102], which inspired the theoretical picture of the ELM cycle (see section 2.2.1).

In general, the major phases of the ELM cycle are similar in all experiments:

Pre-ELM phase

As the edge plasma reaches a stability limit, fluctuations in the magnetics, n_e and T_e can be found. Their characteristic frequencies reach from 5 kHz to 300 kHz and were observed at several experiments: Alto Campo Toro (Italian for high field torus) C-modification (Alcator C-Mod) [106, 107], ASDEX Upgrade [108], Experimental Advanced Superconducting Tokamak (EAST) [109, 110], DIII-D [111], HL-2A [112, 113] and JET [114, 115]. The origin of these fluctuation and their relation to the evolution of the pedestal structure, i.e. the clamping of ∇p, is not fully understood. Parts of the presented work emphasise on this phase (see chapters 4 and 5).

Collapse phase - the ELM crash

In this phase, non-linear interaction of modes leads to an eruptive-like event and the profiles of n_e and T_e collapse with a typical timescale of 1 ms. Particles and energy are released into the SOL, where they form filamentary structures as also visible in figure 1.6b.

Recovery Phase

After the collapse phase, the edge profiles of n_e and T_e are flattened. In the recovery phase the profiles start to steepen up to their original pre-ELM shape. In ASDEX Upgrade several phases of the pedestal structure build-up can be distinguished [102, 116]. These are shown in figure 2.10, which presents the temporal

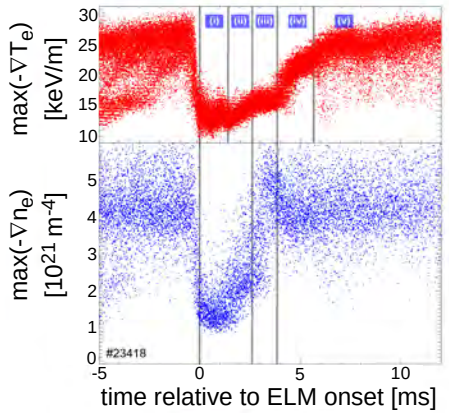

Figure 2.10: Inter-ELM pedestal recovery: Distinct recovery phases of maximum electron density gradient ($\max(-\nabla n_e)$) and maximum electron temperature gradient ($\max(-\nabla T_e)$) can be seen. While $\max(-\nabla n_e)$ recovers immediately after the ELM crash, the recovery $\max(-\nabla T_e)$ takes longer. The recovery is already completed 1 ms to 2 ms before the next ELM. Figure modified from [102].

evolution of the maximum electron temperature gradient ($\max(-\nabla T_e)$) (top) and of the maximum electron density gradient ($\max(-\nabla n_e)$) (bottom). The development of $\max(-\nabla T_e)$ (red) shows five distinguishable phases. First, the profile stays constant for approximately 1.5 ms (i), then there is a short recovery phase of 1 ms in which the ETB is re-established (ii). This is followed by a stagnation phase in which the gradient stays constant for 1.5 ms (iii), before a fast recovery of the original pre-ELM gradient takes place (iv). Here, the gradient steepens more than 50 % in 1.5 ms. Afterwards, $\max(-\nabla T_e)$ increases very slowly and saturates before the next ELM crash.

The evolution of $\max(-\nabla n_e)$ (blue) in the ELM-cycle happens on different timescales with less phases than $\max(-\nabla T_e)$. After the ELM crash $\max(-\nabla n_e)$ immediately starts to recover and the pre-ELM gradient is established within 3 ms. The data suggests a peaking of $\max(-\nabla n_e)$ but this is not clearly identifiable owing to scattering. Mentionable, this peaking ends at almost the same time as the development of $\max(-\nabla T_e)$ enters phase (iv). Afterwards $\max(-\nabla n_e)$ stays constant till the next ELM crash.

The saturation of $\max(-\nabla T_e)$ as well as $\max(-\nabla n_e)$ in the recovery phase means a clamping of ∇p. This phase is identical to the pre-ELM phase.

3 Utilised plasma diagnostics and data analysis

To investigate the evolution of the pedestal structure, SOL and divertor throughout the ELM cycle a variety of plasma diagnostics were utilised. The main quantities that were investigated within this work were electron density (n_e), electron temperature (T_e), ion temperature (T_i), D_α line radiation (D_α), thermoelectric SOL currents, neutral fluxes and radial magnetic field fluctuations ($\partial B_r/\partial t$).

The lithium beam (LIB) diagnostic (section 3.1) as well as reflectometry (section 3.2) measure the n_e profile. Additionally, deuterium cyanide laser interferometry (DCN) (section 3.3) gives line integrated measures of n_e. The Thomson scattering (TS) diagnostic (section 3.4) gives access to n_e and T_e at equal positions, which is very important to align the profiles of both quantities. At the divertor target plates, n_e and T_e are measured by Langmuir probes (LPs) (section 3.5). Further, the electron cyclotron emission (ECE) diagnostic (section 3.6) is used to measure the midplane T_e profile with high temporal resolution. The T_i profile is measured by the charge exchange recombination spectroscopy (CXRS) diagnostic (section 3.7).

A volume integrated spectroscopic detection of the D_α emission is installed in the inner and outer divertor region. The D_α emission intensity is a convolution of the divertor neutral density, the plasma density and the plasma temperature. The thermoelectric current in the SOL is measured by shunts that are attached to several tiles of the divertor [117]. Neutral fluxes are measured by pressure gauges [118]. To detect $\partial B_r/\partial t$ a set of toroidally distributed pick-up coils, so-called ballooning coils, are mounted close to the plasma [119].

The locations of the diagnostics are distributed around the torus and at different poloidal positions as presented in figure 3.1. To compare measurements from different diagnostics, the reconstructed plasma equilibrium is required. It allows mapping of the measurement positions on the flux surfaces. Therefore, e.g. n_e profiles of LIB and TS or T_e profiles of ECE and TS can be compared, when plotting them versus flux coordinates. At the plasma edge usually the normalised poloidal flux (ρ_{pol}) coordinate (equation (1.8)) is used, because it is defined in the confined region of the plasma as well as in the SOL.

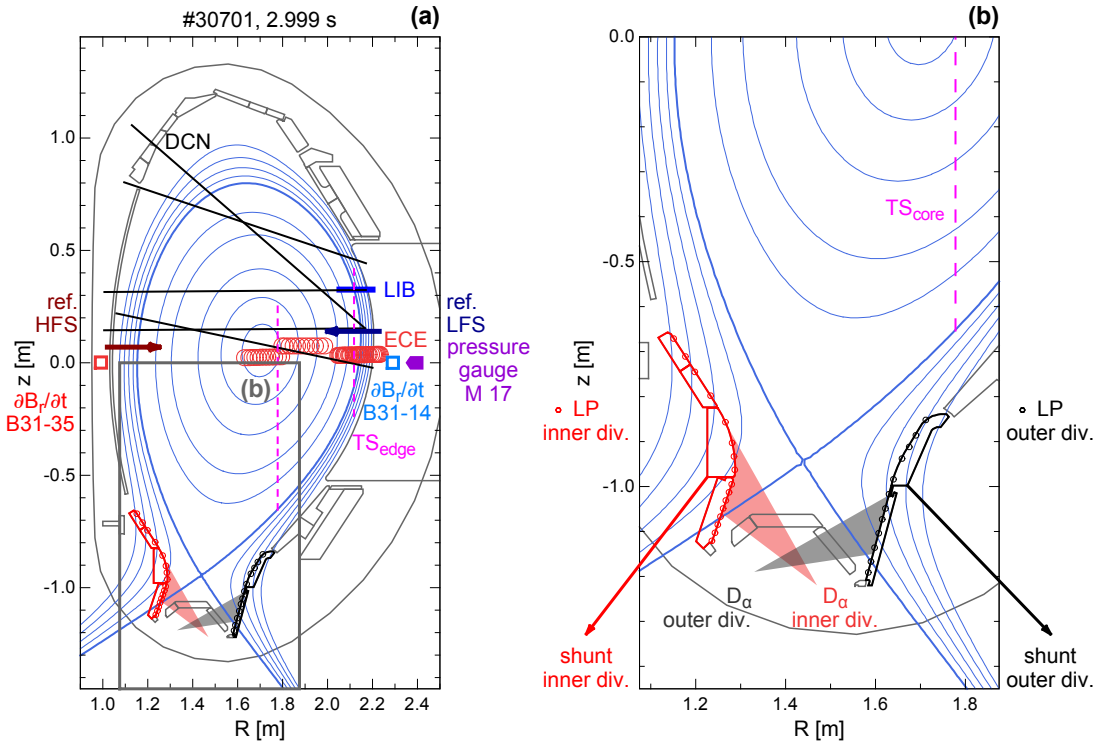

Figure 3.1: Poloidal locations of the main plasma diagnostics: (a) midplane and (b) divertor. The HFS and LFS SOL n_e profiles are measured by O-mode reflectometry (dark red, dark blue) and lithium beam (blue). Several chords of the DCN (black) provide line integrated measurements of n_e. The core and edge Thomson scattering (TS) systems (magenta) can measure n_e and T_e. The ECE diagnostic (red circles) gives profiles of T_e. Ballooning coils located at the HFS (red) and LFS (light blue) midplane are utilised to measure radial magnetic field fluctuations ($\partial B_r/\partial t$) and a pressure gauge that is oriented towards the plasma (violet) is used to measure the main chamber neutral fluxes. The inner (red) and outer (black) divertor regions are diagnosed by a set of triple Langmuir probes (LPs) (circles), optical volume integrated D_α line radiation (D_α) spectroscopy (light colours) and shunts that measure the thermoelectric SOL currents (coloured tiles).

3.1 Lithium beam

The principle of the LIB diagnostic is the spectroscopic measurement of the interaction between the plasma and a beam of lithium (Li) atoms [120]. Two kinds of spectroscopic measurements are usually be performed: CXRS and impact excitation spectroscopy (IXS) or also named beam emission spectroscopy (BES). While the diagnostic principle of CXRS (section 3.7) is used to measure T_i and plasma impurity densities [121, 122], BES is used to determine the n_e profile [123, 124] or to measure n_e fluctuations [125–129]. Because of their multiple applications, LIB diagnostics are installed at several experiments [130–133].

At ASDEX Upgrade the LIB is routinely used for plasma edge n_e profile measurements. By collisions of the Li atoms and mainly the electrons of the plasma, the Li atoms get excited or ionised. Further, de-excitation processes due to collisions are possible. After the natural lifetime, the excited state decays by emitting characteristic line radiation. For Li the Li(2p) state is the most populated one. It has a lifetime of approximately 27 ns and decays to the Li(2s) state by emitting the characteristic Li I ($2\mathrm{p} \rightarrow 2\mathrm{s}$) line radiation at 670.8 nm wavelength. This line emission is detected along the neutral beam by an optical observation system. The lines of sight (LOS) are equipped with interference filters, which just extract the spectral intensity of the Li I ($2\mathrm{p} \rightarrow 2\mathrm{s}$) line radiation, and photo-multipliers to detect the incoming light.

The current LIB diagnostic setup at ASDEX Upgrade [134] is illustrated in figure 3.2. In the LIB injector, Li ions are extracted from a β-eucryptite emitter, which is heated with roughly 200 W, a Li ion beam is formed, focused and accelerated to an energy of 45 keV. The beam is then neutralised in a heated sodium (Na) cell by charge exchange processes between the Na atoms and Li ions. The neutralised beam has a diameter of 10 mm to 15 mm. It is injected from the LFS into the plasma, approximately 30 cm above the midplane (see figure 3.1). Two optical observation systems for BES monitor the emission along the beam, in a region of approximately 20 cm from the wall towards the plasma.

Since the observation systems integrate the emission intensity along the LOS (also see figure 3.5), active contributions, originating from the LIB, and passive emission from the background have to be separated. For this purpose the LIB is modulated, i.e. switched on and off by a high voltage MOSFET switch [136]. During transient events such as ELM crashes, also the background radiation is modulated. To correctly subtract these contributions, either a fast modulation of the LIB has to be applied [136], or a synchronised background subtraction can be used as introduced in section 3.1.2.

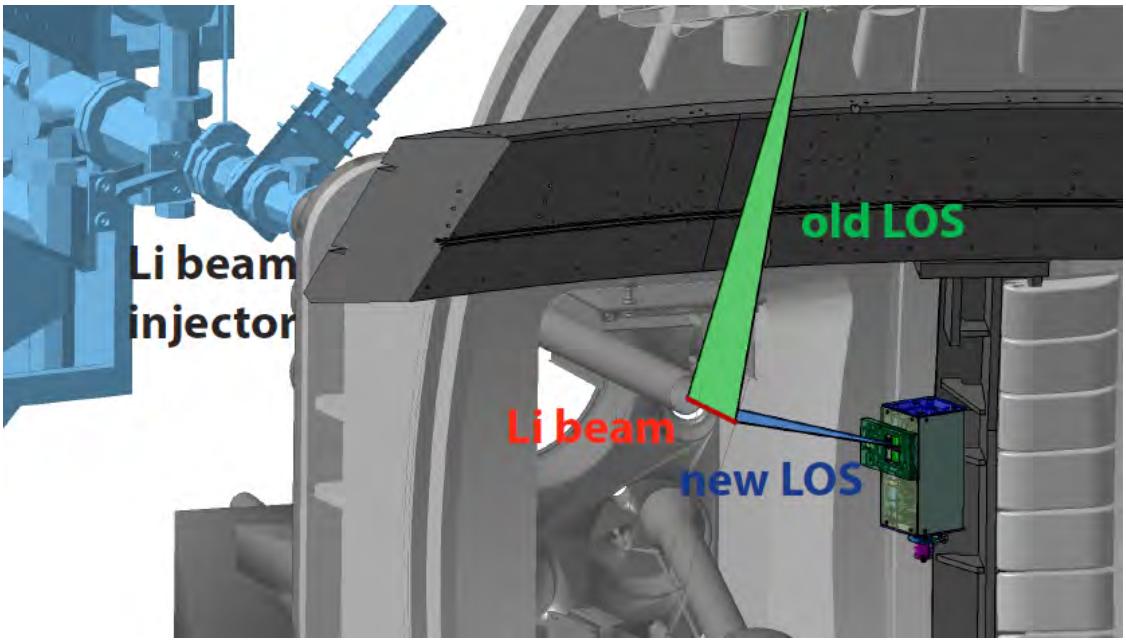

Figure 3.2: Setup of the lithium beam (LIB) diagnostic at ASDEX Upgrade: The Li injector forms the neutral Li beam, which is monitored by two optical observation systems (LOS) for BES. The new LOS (blue) are much shorter than the old (green) ones, giving larger count rates and better signal-to-noise ratio. Figure taken from [135].

3.1.1 Collisional radiative modelling

From the measured, background corrected line radiation profiles, the n_e profile can be evaluated by applying a collisional radiative model [123]:

$$\frac{dN_i(z)}{dz} = [n_e(z)a_{ij}(T_e(z)) + b_{ij}]N_j(z). \tag{3.1}$$

This system of coupled differential equations calculates the occupation numbers (N_i) of the energy levels of the Li atoms along the beam coordinate (z). The indices i and j represent the different energy levels Li(nl) starting from Li(2s) ($i, j = 1$), Li(2p) ($i, j = 2$) and so on. Excitation to energy levels with $n > 4$ are considered as ionisation. The rate coefficients (a_{ij}) for $i \neq j$ specify stimulated excitation and de-excitation processes from the energy level j to i. Ionisation or excitation to energy levels with $n > 4$ is described by a_{ii}. In an impurity free plasma a_{ij} depends on the electron temperature $T_e(z)$, and the resulting rate is proportional to the electron density $n_e(z)$.

Plasma impurities can be considered by the effective charge (Z_{eff}), which modifies a_{ij}. The atomic data, which underlays the rate coefficients, were calculated, measured and validated for several types of collisions [137–139]. The Einstein coefficients b_{ij} consider spontaneous, emissive de-excitation and are calculated from transition probabilities of excited Li atoms [140]. The boundary condition is that the beam enters the plasma at $z = 0$ with a fully occupied ground state:

$$N_{\mathrm{i}}(z = 0) = \delta_{1\mathrm{i}}. \tag{3.2}$$

The measured Li (2p $\rightarrow$ 2s) line radiation intensity along z ($I_{\mathrm{Li\ (2p\rightarrow 2s)}}(z)$) is assumed to be proportional to the occupation number of the Li(2p) state ($N_2(z)$):

$$N_2(z) = \alpha I_{\mathrm{Li\ (2p\rightarrow 2s)}}(z)\ ;\ \alpha = \mathrm{const.} \tag{3.3}$$

By integrating equation (3.1) stepwise from $z = 0$ the n_{e} profile ($n_{\mathrm{e}}(z)$) can be reconstructed [123]. A more advanced and robust method to reconstruct $n_{\mathrm{e}}(z)$ is a probabilistic data analysis approach, which models the $I_{\mathrm{Li\ (2p\rightarrow 2s)}}(z)$ profile [141]. It solves equation (3.1) for a given n_{e} profile, that is parametrised by cubic splines. Within Bayesian probability theory (BPT), that allows the inclusion of weak constraints on monotonicity of the density profiles, the input n_{e} profile is varied till the best agreement of the measured and the calculated line radiation profile is found. This approach is usually applied for the ASDEX Upgrade LIB n_{e} reconstruction. Similar approaches for the LIB evaluation are also applied at other experiments [142–144].

3.1.2 Background subtraction for ELM cycle resolved analysis

For an accurate n_{e} profile reconstruction the subtraction of the background radiation is crucial. Large, transient events such as ELM crashes, can lead to an enhanced background radiation as seen in figure 3.3a. Here, the Li line intensity of one channel is plotted. Whenever, an ELM crash occurs, leading to a burst of the divertor shunt current in figure 3.3b, the measured line intensity increases. This happens also when the LIB is switched off (unshaded areas in figure 3.3a), which means that also the average background radiation increases.

By determining the onset of the individual ELM crashes (dashed vertical lines in figures 3.3a and 3.3b) and synchronising the data in beam off phases relative to the ELM onset of several similar ELMs, the average background radiation during an ELM crash can be evaluated. The method of ELM synchronisation is described in more detail in section 3.9. The ELM synchronised data of beam on (active emission, red)

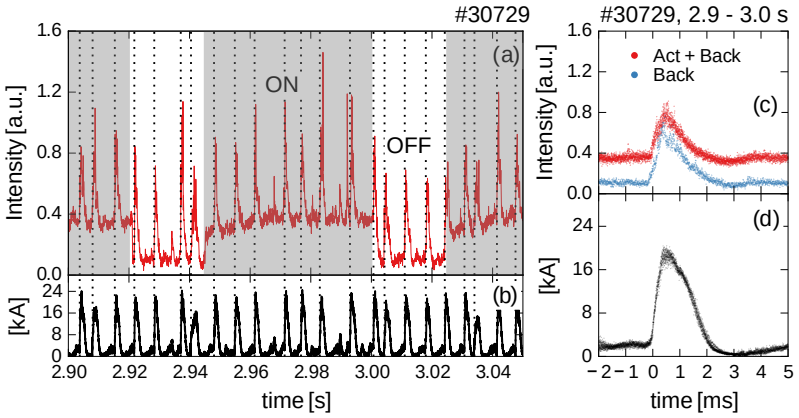

Figure 3.3: Background subtraction during the ELM crash: (a) Li intensity at one channel, (b) divertor shunt current, (c) synchronised time traces of the detected intensity with active (beam on, red) and background (beam off, blue) signal and (d) synchronised divertor shunt current. The grey shaded areas in (a) indicate the modulation of the LIB, which is performed to measure the background radiation. During the ELM crash, the background intensity increases, which has to be subtracted, when evaluating n_e profiles. Figure modified from [145].

and beam off (background emission, blue) phases are presented in figure 3.3c. Further, the ELM synchronised divertor shunt current is shown in figure 3.3d. Before reconstructing the n_e profile during the ELM crash, i.e. when divertor shunt current is high, the background radiation can be removed, enabling a more accurate n_e evaluation.

3.2 Microwave reflectometry

The diagnostic principle of microwave reflectometry diagnostics is to probe the plasma n_e by measuring the propagation time of an electromagnetic wave, which is reflected by the plasma [146]. One wave, which reflection is solely determined by n_e is the ordinary wave or mode, which is transverse and plane polarised. It is reflected at the so-called cut-off frequency, which is given by the plasma frequency (ω_p):

$$\omega_p = \sqrt{\frac{n_e e^2}{\varepsilon_0 m_e}}, \tag{3.4}$$

using elementary charge (e), vacuum permittivity (ε_0) and electron mass (m_e). When emitting, different wave frequencies, several density layers can be probed since $\omega_p \propto$

$\sqrt{n_e}$. From the time delay of incident and reflected wave, the distance between the cut-off density layer and the antenna can be calculated, which enables to display n_e profiles.

At ASDEX Upgrade two ordinary mode reflectometry diagnostics are installed [147]. These launch microwave beams at midplane from the HFS and LFS (see figure 3.1a). According to their probing frequencies usually the SOL and steep gradient region n_e profile is measured. With these two systems asymmetries in the HFS and LFS SOL n_e can be studied [148].

3.3 Deuterium cyanide laser interferometry

Interferometric diagnostics use the refraction of light, when passing through a plasma, which depends on n_e [149]. Therefore, the interferometric principle measures a line integrated n_e along a chord. The change of refractive index in a plasma in comparison to vacuum leads to a phase shift (φ) of the light:

$$\varphi = \lambda_0 r_e \int_0^L n_e(x) \mathrm{d}x. \tag{3.5}$$

Here, n_e is integrated along the beam path of length (L) within the plasma. The vacuum wavelength (λ_0) of the laser is given by

$$\lambda_0 = \frac{2\pi c}{\omega}, \tag{3.6}$$

with the frequency (ω) of the laser light source. Further, the classical electron radius (r_e)

$$r_e = \frac{e^2}{4\pi\varepsilon_0 m_e c^2}, \tag{3.7}$$

enters in equation (3.5).

Experimentally, φ is measured by a Mach–Zehnder interferometer, which has one beam path crossing the plasma and the other one as vacuum reference. Figure 3.4 illustrates the phase shift of an electromagnetic wave, that is caused when passing through a plasma. Deuterium cyanide lasers, operated at a wavelength of 195 µm, were chosen as light sources at ASDEX Upgrade. In total 5 chords of the DCN interferometer are installed (see figure 3.1a) [151]. These give mainly information on the core n_e and a n_e profile can be deconvolved from the line integrated measurements.

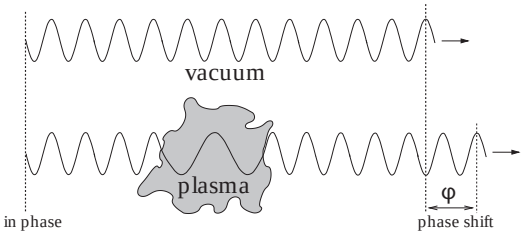

Figure 3.4: Interferometry principle: A light ray passing through a plasma gets phase shifted by φ with respect to a ray in vacuum. Figure adapted from [150].

3.4 Thomson Scattering

This widely used diagnostic is based on scattering of electromagnetic waves on charged particles [146]. The differential cross section for scattering processes is given by

$$\frac{d\sigma}{d\Omega} = \frac{q^4}{(4\pi\varepsilon_0 mc^2)^2} sin^2\Theta, \tag{3.8}$$

with particle charge (q) and particle mass (m). Owing to the $1/m^2$ dependence, mainly the electrons contribute to the scattering.

A TS diagnostic accesses the n_e and T_e profile at identical locations. Due to the thermal movement of the electrons, Doppler broadening of the scattered light is observed, which can be used to determine T_e. By integrating the intensity ($I(\omega)$) of the scattered light n_e can be evaluated.

At ASDEX Upgrade the TS diagnostic uses six neodymium-doped yttrium aluminium garnet (Nd:YAG) infrared lasers with a pulse energy of 1 J [152, 153]. These have a pulse duration of 15 ns and 20 Hz repetition frequency. There are two beam paths in vertical direction through the plasma (see figure 3.1). One probes the core plasma (core TS system) and the other one is localised at the plasma edge (edge TS system). Within the short pulse duration the plasma can be approximated as frozen, which enables the diagnostic to investigate fast, turbulence timescale events [154, 155]. But the low pulse repetition rate rather limits the resolution of full ELM cycles.

The advantage of the TS diagnostic is the intrinsic alignment of the n_e and T_e

profile. Therefore, the profiles form TS are used to relatively align the n_e profile from LIB diagnostic and the T_e profile from the ECE diagnostic (see section 3.6), which is e.g. especially important for the forward model of the ECE propagation [156].

3.5 Langmuir probes

Langmuir probes (LPs) are used to determine n_e, T_e, ion saturation current and floating potential of the plasma [146]. For this, plasma-matter interactions have to be accepted, i.e. this diagnostic principle is invasive and disturbs the plasma. However, in the divertor, where the plasma contacts the wall, LPs are well suited to characterise the plasma sheath.

In the inner and outer divertor targets of ASDEX Upgrade several LPs are embedded as shown in figure 3.1b. Some of them are operated in the so-called triple probe configuration, i.e. that three points along the current-voltage characteristic can be measured simultaneously by three probe tips, that are spatially close [157]. From these measurements n_e and T_e in the plasma sheath in front of the divertor can be determined.

3.6 Electron cyclotron emission

This diagnostic method is used to measure the T_e profile in the confined plasma region. Due to the gyro motion of the electrons, microwave radiation is emitted from the plasma with a frequency (f):

$$f = \frac{\omega}{2\pi} = l\frac{eB(R)}{2\pi m_e}, \tag{3.9}$$

with the harmonic number (l). Since $B \propto 1/R$ (see equation (1.5)) in a tokamak, f and its higher harmonics are radially dependent. Therefore, a radial localisation of the measurement is possible. When the plasma is optically thick, i.e when the radiated temperature is equal to T_e, and the energy distribution is close to thermal equilibrium the radiated intensity can be assumed as black body radiation (I_{BB}):

$$I_{BB}(\omega) = \frac{\omega^2}{8\pi^3 c^3} k_B T_e. \tag{3.10}$$

From this relation, T_e can be evaluated. But close to the plasma edge, the assumption of a black body radiator does not hold. The plasma becomes optically thin because

n_e is lower at the edge. To reconstruct the T_e profile at the plasma edge from ECE, an electron cyclotron forward model (ECFM) of the radiation transport trough the edge plasma needs to be applied [156].

The experimental realisation of the ECE diagnostic at ASDEX Upgrade is a heterodyne radiometer [158], which has 60 channels and is absolutely calibrated. Usually, the second harmonic of the ECE is measured. A recent upgrade included the exchange of the frequency mixer giving an improved signal-to-noise ratio and an increased radial resolution at the edge of 300 MHz per channel, which corresponds to 5 mm spatial width of one channel at B_t of 2.5 T [159].

3.7 Charge exchange recombination spectroscopy

The main diagnostic method to measure quantities of the plasma ions is charge exchange recombination spectroscopy (CXRS). It is based on the interaction of a neutral beam and intrinsic plasma impurities. Typically, this spectroscopic method is applied on a neutral beam injection (NBI) heating beam. Charge is transferred from the neutral D beam to ionized plasma impurities (A^{Z+}) [160]:

$$D^0 + A^{Z+} \rightarrow D^+ + A^{(Z-1)+^*}, \tag{3.11}$$

$$A^{(Z-1)+^*} \rightarrow A^{(Z-1)+} + h\nu. \tag{3.12}$$

These occupy excited states ($A^{(Z-1)+^*}$), which decay by emission of characteristic line radiation ($h\nu$). Usually, low Z impurities are used for CXRS, since they are fully ionised throughout the plasma, which allows a localised measurement along the neutral beam from the edge to the plasma core.

A measured spectrum of the He^{2+} ($4 \rightarrow 3$) transition is shown in figure 3.5 [145]. It consists of two contributions, the active one (blue), which results from CXRS processes from the neutral beam, and the passive one (red), which originates from residual neutrals along the LOS. From the active line spectrum, the impurity density (n_j), temperature (T_j) and rotation component in the direction of the LOS ($\vec{v}_j \cdot \vec{u}_{LOS}$) can be determined for the impurity species j. Assuming a thermal impurity temperature distribution, the line emission ($I_{CX}(\lambda)$) needs to be Gaussian shaped:

$$I_{CX}(\lambda) = I_0 \sqrt{\frac{m_j c^2}{2\pi k_B T_j \lambda_0^2}} \exp\left(-\frac{m_j c^2}{2 k_B T_j} \frac{(\lambda - \lambda_0)^2}{\lambda_0^2}\right). \tag{3.13}$$

The maximum spectral radiance (I_0), the impurity mass (m_j) and the un-shifted wavelength (λ_0) enter the spectral distribution. From the full width at half maximum (FWHM) of the distribution, T_j can be extracted. When the impurities are assumed

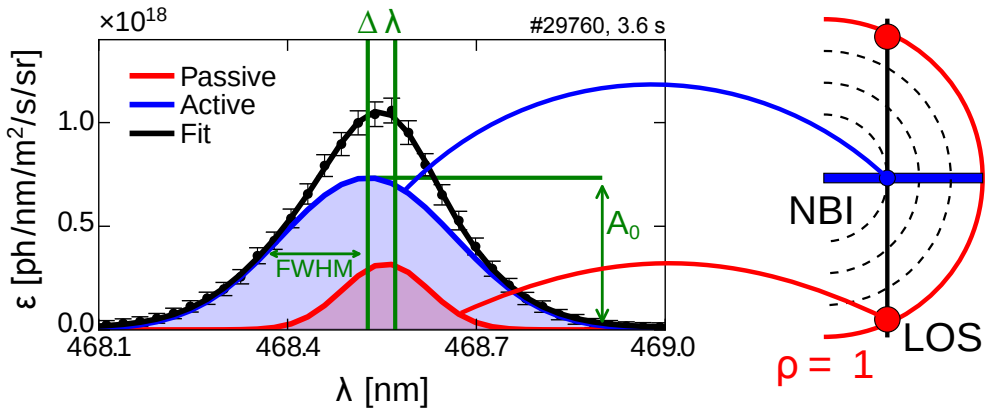

Figure 3.5: Principle of charge exchange recombination spectroscopy (CXRS): Active (blue) and passive (red) contributions are integrated along the LOS, which are reconstructed by fitting the measured spectrum. Figure modified from [145].

to be in thermal equilibrium with the main plasma ions, which is usually the case, T_i can be approximated by T_j.

From the Doppler shift ($\Delta\lambda$) of the active component, $\vec{v}_\mathrm{j}\cdot\vec{u}_\mathrm{LOS}$ is determined:

$$\frac{\Delta\lambda}{\lambda_0} = \frac{\vec{v}_\mathrm{j}\cdot\vec{u}_\mathrm{LOS}}{c}. \tag{3.14}$$

By using LOS in poloidal and toroidal direction, both rotation velocity components of the impurity ions can be accessed [161].

From the spectral radiance ($L_\mathrm{CX}(\lambda)$), n_j for the ionisation state (Z) can be evaluated:

$$L_\mathrm{CX}(\lambda) = \frac{h\nu}{4\pi}\sum_{k=1}^{n_b}\langle\sigma_n v\rangle_{k,\lambda}\int_\mathrm{LOS} n_{\mathrm{j,Z}}n_k\mathrm{d}l, \tag{3.15}$$

when the beam neutral density (n_b) for the beam energy components k is known, i.e. modelled correctly taking into account the beam geometry [162]. Further, the charge exchange rate coefficients for a specific velocity and a beam energy component ($\langle\sigma_n v\rangle_{k,\lambda}$) enter in L_CX.

At ASDEX Upgrade several CXRS diagnostic systems are installed [161, 163]. Recently, the edge CXRS system was upgraded with a new spectrometer [164], enabling a temporal resolution down to 70 µs (from originally 2.3 ms). This gives the possibility to study the inter-ELM evolution of T_i and E_r [165].

3.8 Integrated data analysis

Within the integrated data analysis (IDA) framework, measurements from several types of plasma diagnostics are combined to reconstruct continuous profiles of n_e and T_e from the plasma core to the SOL [166]. These are parametrised by cubic splines and combined within a BPT approach. All measurement locations are mapped via the reconstructed plasma equilibrium to ρ_{pol}, which enables the combination of the different diagnostics. For the n_e profile, usually LIB data from the plasma edge and DCN data for the core are used. Optionally, TS and reflectometry can also be included. The T_e profiles are routinely reconstructed from ECE and application of the ECFM, with optional input of TS. Owing to the limited repetition rate of the TS laser, these data are excluded from the analysis, because throughout this work the profiles are evaluated with a temporal resolution of 250 µs. However, the relative alignment of the reconstructed n_e and T_e profiles is cross checked with the TS profiles.

The combination of n_e and T_e profiles automatically reconstructs an electron pressure (p_e) profile, which served as input for the pressure constrained plasma equilibrium reconstruction. With the corresponding plasma equilibria the linear MHD stability analysis was performed (see section 2.1.5) as well as an improved IDA evaluation with more accurate mapping of the diagnostics locations.

3.9 ELM synchronisation

This basic data analysis method is applied throughout this work. Usually, single ELM cycles are poorly resolved due to the limited temporal resolution of profile reconstruction and features that are not generally characteristic. Superimposition of data from several, 'equal' ELM cycles increases the density of data points and conserves the general dynamic behaviour throughout the ELM cycle.

As illustrated in figure 3.6a, the onset of the individual ELM crashes in the analysed time interval is determined by the corresponding bursts in divertor shunt current measurement [167]. 'Equal' ELM cycles are characterised by similar f_{ELM}, length of the divertor shunt current burst and inter-ELM evolution of the divertor shunt current.

The time bases are collapsed relative to the corresponding ELM onset, i.e. each input data point is related to the previous and the next ELM crash. Then the resulting data points, which are twice as many as the input data, are superimposed and plotted relative to the onset of the next (negative sign) and previous (positive sign) ELM crash

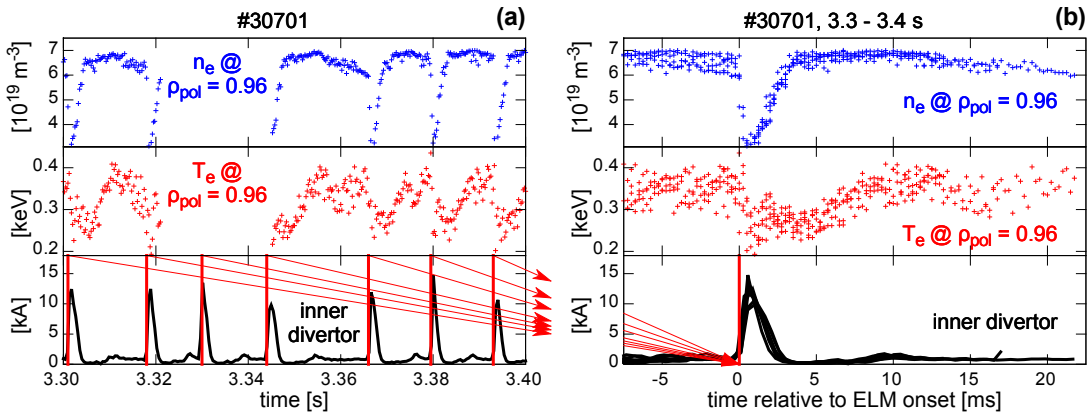

Figure 3.6: ELM synchronisation: (a) time traces of n_e, T_e at $\rho_{pol} = 0.96$ and the inner divertor shunt current and (b) ELM synchronised data of (a). The ELM onsets of the individual ELM crashes are determined by the bursts in the divertor shunt currents as indicated by vertical, red lines in (a). The time bases are collapsed relative to the individual ELM onsets and the corresponding data is superimposed as shown in (b), resulting in an ELM synchronised representation.

figure 3.6b. For this reason, no absolute value of time is now given on the abscissa but it is changed to the 'time relative to the ELM onset'.

In addition to the divertor shunt current measurements, n_e and T_e at a location close to the top of the pedestal ($\rho_{pol} = 0.96$) are plotted in figure 3.6. While the data scatters in the time traces in figure 3.6a and the overall trends of n_e and T_e are poorly visible, the ELM synchronised representation in figure 3.6b clearly reveals that the pedestal top n_e recovers faster than the pedestal top T_e after an ELM crash. This observation is in agreement with previous analyses of the inter-ELM profile evolution in ASDEX Upgrade [102].

The ELM synchronisation method of data analysis is also applied to raw data of the LIB diagnostic, i.e. to the Li line radiation profiles. By this means the background radiation is subtracted during the ELM crash for a more accurate reconstruction of the n_e profile (see section 3.1.2).

4 | Pedestal collisionality variation

Parts of the following chapter were already published in [43].

As discussed in sections 2.1.1 and 2.1.2, ν^* (see equation (2.7)) impacts on the bootstrap current and therefore, the stability of the plasma edge. Further, micro-instabilities such as MTMs (see section 2.2.2) show strong dependencies on ν^*. In order to disentangle the effect of ν^* and the pressure drive of instabilities, an experiment was performed, which aimed at a variation of ν^* without affecting p by simultaneously varying the n_e and T_e profile. This was achieved for two discharge intervals by adjusting P_{heat} and gas puff as described in section 4.1. Both discharge intervals show a similar sequence of pedestal recovery phases in between the ELM crashes. Further, high frequency magnetic fluctuations in radial direction are observed in the pre-ELM period. These can be interpreted as signature of instabilities, that are present in the pedestal and their onset is correlated to a clamping of the electron pressure gradient (∇p_e) (see section 4.2). The stability of both discharges during the period of clamped ∇p_e is consistent with PB theory.

Analysis of a larger data set reveals that the detected fluctuation frequency (in the lab frame) can be related to the $E \times B$ rotation at the plasma edge. Further, the fluctuations are also visible on the HFS and the underlying mode structure is found to be large scale with n of approximately -11 (see section 4.5). Possible interpretations of the observations are presented in section 4.6.

4.1 Investigated plasma scenario

In the following, the two discharges with similar p and a variation of ν^*, in which high frequency magnetic fluctuations prior to the ELM occur, are presented. Here, p is represented by ratio of electron to magnetic pressure (β_e). The β_e profile is calculated similar to β (equation (1.9)) by using only the profiles of the electrons:

$$\beta_e = \frac{n_e T_e}{B^2/2\mu_0} \tag{4.1}$$

using the local magnetic field (B) at the LFS midplane. The electron collisionality (ν_e^*) from equation (2.7), is modified by approximating the Coulomb logarithm leading to

$$\nu^*_{e,ped} = 0.0012 \frac{qR_0 Z_{eff} n_e[10^{19}\,\mathrm{m}^{-3}]}{\epsilon^{3/2}(T_e[\mathrm{keV}])^2}, \tag{4.2}$$

which is locally evaluated at the pedestal top ($\rho_{pol} = 0.96$). Here, Z_{eff} is set to 1 because there is no accurate measurement and the discharge conditions in both presented plasmas were similar.

The two discharges with different pedestal top electron collisionality ($\nu^*_{e,ped}$) were #30701 with high $\nu^*_{e,ped}$ of roughly 1.5, and #30721 with low $\nu^*_{e,ped}$ of approximately 0.6. Both have almost identical pedestal β_e as presented in section 4.1.1. The discharges were performed at I_p= 1.0 MA, B_t= −2.5 T (negative sign stands for opposite direction to I_p) and identical plasma shape. Time traces from the investigated, high ν^* discharge (#30701) are presented in figure 4.1. Here, two H-mode phases are induced by the application of external heating using NBI and electron cyclotron resonance heating (ECRH). When the H-mode is accessed, W_{MHD}, n_e at a central DCN chord ($n_{e,core}$) and at a plasma edge DCN chord ($n_{e,edge}$) as well as T_e at central location ($T_{e,core}$) and at the plasma edge ($T_{e,edge}$) immediately increase as seen at 0.7 s and 2.5 s. When neutral beam heating power (P_{NBI}) is roughly 4 MW and W_{MHD} in the region of 0.4 MJ, large type-I ELMs occur with f_{ELM} between 50 Hz and 100 Hz. For the detailed analysis of the inter-ELM profile evolution, time intervals with relatively constant f_{ELM} and similar ELM behaviour are chosen (grey shaded area, 3.3 s to 3.4 s).

The variation of $\nu^*_{e,ped}$, simultaneously keeping β_e constant, was achieved by a variation of P_{heat} and externally applied gas puff. In the high $\nu^*_{e,ped}$ case, P_{heat} (from NBI and ECRH) was 5.3 MW and the external deuterium puff was $11.3 \cdot 10^{21}\,\mathrm{e\,s^{-1}}$, whereas in the low $\nu^*_{e,ped}$ case P_{heat} was increased to 6.9 MW and the gas puff decreased to $2.1 \cdot 10^{21}\,\mathrm{e\,s^{-1}}$.

4.1.1 Pedestal profile analysis

The n_e and T_e profiles at the plasma edge are evaluated using the IDA approach as introduced in section 3.8. As mentioned in section 3.4, the application of the ECFM and successful fitting of the ECE 'shine-through' at the plasma edge, crucially depends on the alignment of the n_e and T_e profiles. Therefore, n_e and T_e are aligned relative to the TS measurements. Here, the T_e profile is slightly shifted (< 3 mm such that the separatrix T_e is 100 eV [42, 168]. The reliable evaluation of the T_e profiles as well as ∇T_e down to the separatrix, is essential because the onset of the high frequency

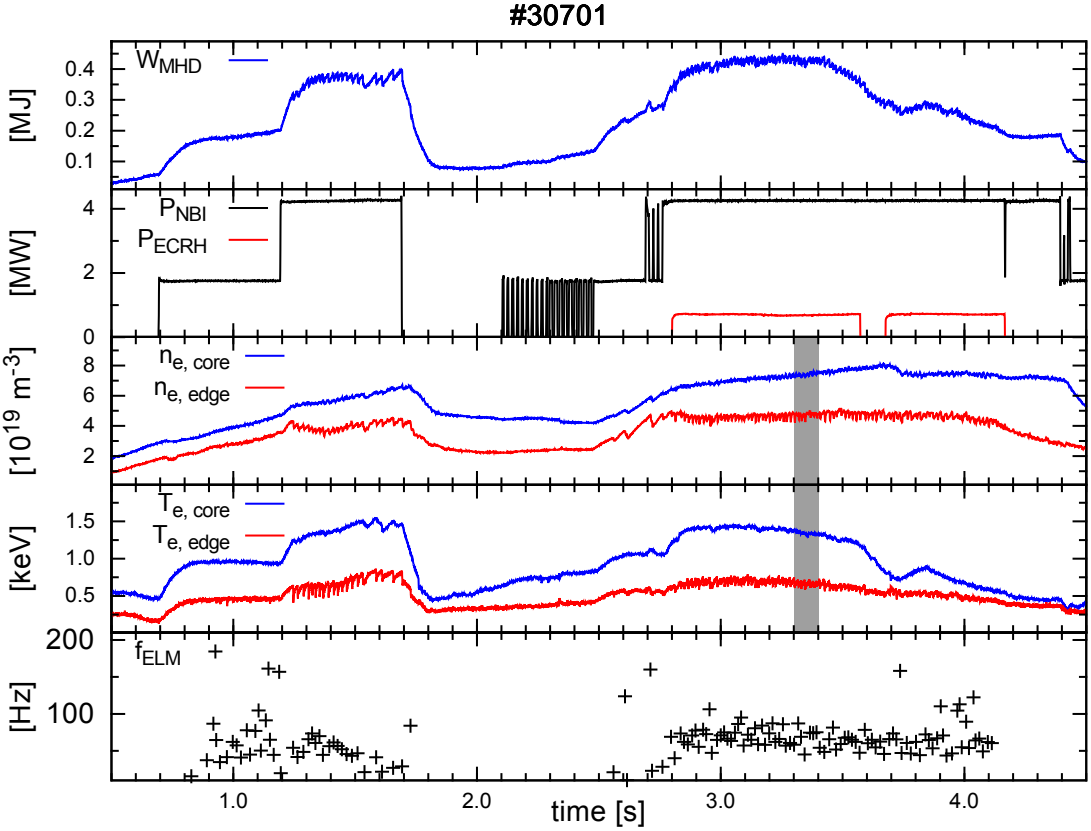

Figure 4.1: Time traces of the plasma stored energy (W_{MHD}), the heating power (P_{heat}) by neutral beam injection (P_{NBI}) and by microwave heating (P_{ECRH}), the line integrated electron density at a central chord ($n_{\mathrm{e,core}}$) and at a plasma edge chord ($n_{\mathrm{e,edge}}$), the electron temperature at central location ($T_{\mathrm{e,core}}$) and at the plasma edge ($T_{\mathrm{e,edge}}$), as well as the ELM repetition frequency (f_{ELM}) of discharge #30701. When external heating power is applied, the plasma enters the H-mode, which leads to a rise of n_{e}. In the fully developed H-mode, ELMs are occurring regularly. The ELM synchronisation and data analysis is done in phases with stable f_{ELM} (grey shaded area).

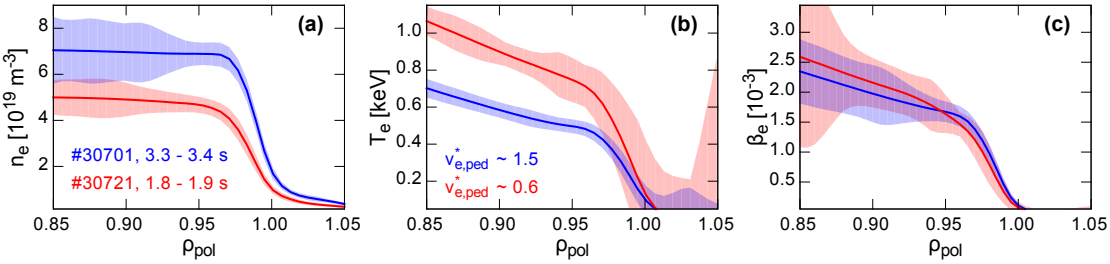

Figure 4.2: Pre-ELM (averaged between −2 ms and −1 ms relative to the ELM onset) profiles of (a) n_e, (b) T_e and (c) β_e. The shaded areas represent the uncertainties of the profile analysis (propagated from the IDA evaluation and the standard deviation of the ELM synchronised average). Both discharges have similar β_e profiles and vary in $\nu^*_{e,ped}$. Figure already published in [43].

magnetic fluctuations is correlated to the inter-ELM recovery of $\max(-\nabla T_e)$ at the edge.

The presented n_e and T_e profiles are evaluated with a temporal resolution of 250 µs. This is sufficient to resolve the full ELM cycle (average duration approximately 10 ms) and long enough to suppress scattering of the profiles due to measurement uncertainties. Figure 4.2 presents ELM synchronised profiles of n_e, T_e and β_e, which are averaged between −2 ms and −1 ms relative to the ELM onset, for the high $\nu^*_{e,ped}$ (#30701, blue) and low $\nu^*_{e,ped}$ (#30721, red) discharge.

These discharges are compared in the following: First, in terms of their inter-ELM pedestal evolution and then, the onset of high frequency magnetic fluctuations is characterised.

4.2 Pedestal profile evolution and onset of magnetic fluctuations

To detect $\partial B_r/\partial t$, several ballooning coils are installed in ASDEX Upgrade [119, 169]. A coil, which is located at the LFS midplane (B31-14), was used for the presented measurements (see section 4.5 and figures 3.1a and 4.7). Figure 4.3a presents a spectrogram of $\partial B_r/\partial t$ in the top plot. Additionally, time traces of n_e (blue), T_e (red), measured at the pedestal top ($\rho_{pol} = 0.96$), and inner divertor current (black) are shown. The grey shaded area marks a period when the Li-Beam was modulated to measure the background emission (details see section 3.1). Since there are no n_e profiles available in this time interval, the ECFM is not applicable and the T_e profiles are also not evaluated.

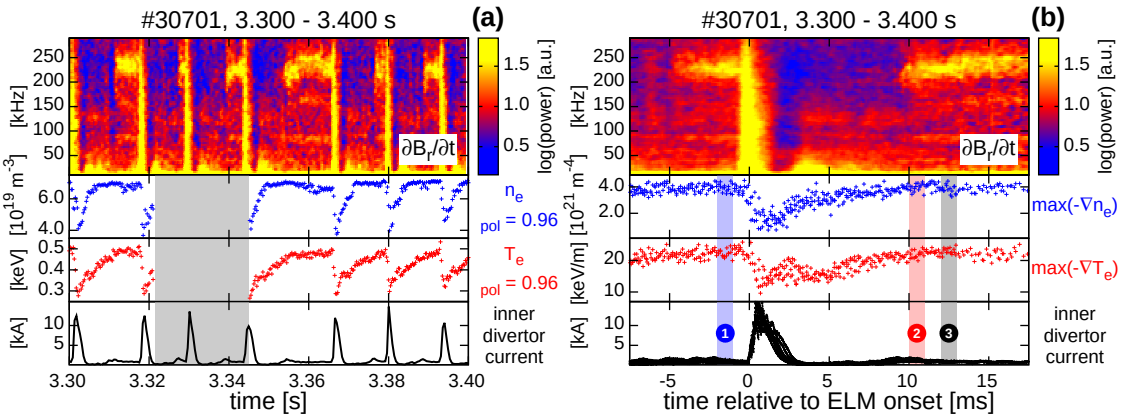

Figure 4.3: Pedestal evolution of the high $\nu^*_{\mathrm{e,ped}}$ case (#30701): (a) Spectrogram of $\partial B_\mathrm{r}/\partial t$ (top) and time traces of n_e (blue), T_e (red) at the pedestal top ($\rho_\mathrm{pol} = 0.96$) and inner divertor current (black). The grey shaded area indicates when the Li-beam was off to measure the background radiation. (b) ELM synchronised frequency histogram of $\partial B_\mathrm{r}/\partial t$ and ELM synchronised time traces of $\max(-\nabla n_\mathrm{e})$ (blue), $\max(-\nabla T_\mathrm{e})$ (red) and inner divertor current (black). After $\max(-\nabla T_\mathrm{e})$ is recovered (10 ms after the ELM onset) fluctuations with a frequency of approximately 240 kHz set in. The vertical bars and numbers indicate the phases in which the linear MHD stability analyses were performed (see section 4.3). Figure already published in [43].

A pulse in the divertor current (black) corresponds to an ELM crash. Although, the ELM frequency varies slightly, i.e. the duration of the inter-ELM period differs, the pedestal recovery is very similar after each ELM crash until the pre-ELM temperature gradient is established. This is directly related to the recovery of the pre-ELM pressure gradient. The evolution of the pedestal profile gradients is demonstrated in figure 4.3b, which presents an ELM synchronised frequency histogram of $\partial B_\mathrm{r}/\partial t$ together with $\max(-\nabla n_\mathrm{e})$ (blue), $\max(-\nabla T_\mathrm{e})$ (red) and inner divertor current (black). ELM synchronised plots superimpose the data with respect to the ELM onset (see section 3.9). For spectrograms the windows of the Fourier transform are superimposed relative to the ELM onset giving ELM synchronised frequency histograms.

The first inter-ELM recovery phase is from $\max(-\nabla n_\mathrm{e})$. In this period also the pedestal top n_e is re-established (approximately 5 ms relative to the ELM onset). This phase appears before the $\max(-\nabla T_\mathrm{e})$ recovery, which is the second phase of the inter-ELM pedestal recovery. These observations are in agreement with previous studies [102] (see section 2.2.3). After the recovery of $\max(-\nabla n_\mathrm{e})$, the onset of magnetic fluctuations in the region of up to 150 kHz can be seen (around 4 ms relative to the ELM onset). From their onset on, these fluctuations are then present throughout the

ELM cycle. They are associated to low n as shown in section 4.5. When $\max(-\nabla T_\mathrm{e})$ is recovered (approximately 10 ms relative to the ELM onset), magnetic fluctuations with rather high frequencies at roughly 240 kHz set in. These fluctuations continue until the next ELM crash, which occurs between 10 ms and 17 ms after the previous ELM. In figure 4.3b only data up to 1.5 ms before the following ELM crash are plotted. In this pre-ELM phase, from approximately 10 ms after the previous ELM, only marginal changes in $\max(-\nabla n_\mathrm{e})$ and $\max(-\nabla T_\mathrm{e})$ can be seen. The next ELM crash is connected to the disappearance of the magnetic fluctuations, which set in again after the recovery of $\max(-\nabla n_\mathrm{e})$ and $\max(-\nabla T_\mathrm{e})$. A similar behaviour can also be seen in figure 4.3a in the evolution of the pedestal top T_e (red points). The onset of the high frequency fluctuations is clearly correlated to the recovery of the T_e pedestal and, consequently, the p_e pedestal because the n_e pedestal is already recovered before. However, the duration of the period with high frequency fluctuations and clamped pedestal gradients differs in the presented case from ELM to ELM (figure 4.3a). This is an indication that the observed fluctuations are not ELM-precursors in a classical sense. From ELM-precursors one would expect continuous growth in amplitude, leading to the ELM crash. For this reason, a similar duration between precursor onset and ELM crash would be expected. The observed high frequency fluctuations do not show clear changes in their amplitude, which could be related to growth. A saturated mode, which sets in when a certain threshold (in terms of pedestal parameters) is exceeded, is a better explanation for the observed fluctuation signature. This mode is then either affected by the ELM crash, or the drive vanishes due to the flattening of the pedestal. Further, it has been observed that the high frequency fluctuations sometimes disappear before the ELM onset (< 0.5 ms) [119]. This could suggest a possible ELM trigger mechanism. Since the fluctuations clamp the pedestal gradient, their disappearance leads to a further increase of the gradient, which then leads to an unstable pedestal.

In the discharge with low $\nu^*_\mathrm{e,ped}$, the inter-ELM pedestal profile evolution shows similar behaviour (see figure 4.4, same plot setup as figure 4.3). The recovery of $\max(-\nabla n_\mathrm{e})$ and $\max(-\nabla T_\mathrm{e})$ has an identical sequence as in the high $\nu^*_\mathrm{e,ped}$ case (figure 4.3b), i.e. $\max(-\nabla n_\mathrm{e})$ is re-established before $\max(-\nabla T_\mathrm{e})$. In comparison to the high $\nu^*_\mathrm{e,ped}$ case, f_ELM is larger because P_heat is higher and for type-I ELMs, f_ELM increases with P_heat (see section 1.6).

After the recovery of $\max(-\nabla T_\mathrm{e})$ (6 ms relative to the ELM onset), magnetic fluctuations set in, which in this case are broadband with frequencies between 300 kHz and 400 kHz. The width of the frequency band is larger than in the high $\nu^*_\mathrm{e,ped}$ case and the fluctuations are not clearly seen before every ELM crash (figure 4.4a). Further, the fluctuation intensity also varies from ELM cycle to ELM cycle. It is important to note that the frequency of the fluctuations strongly differs from the one in the high $\nu^*_\mathrm{e,ped}$ case. However, the high frequency fluctuation onset is again correlated with the $\max(-\nabla T_\mathrm{e})$ recovery, and consequently with the re-establishment of the

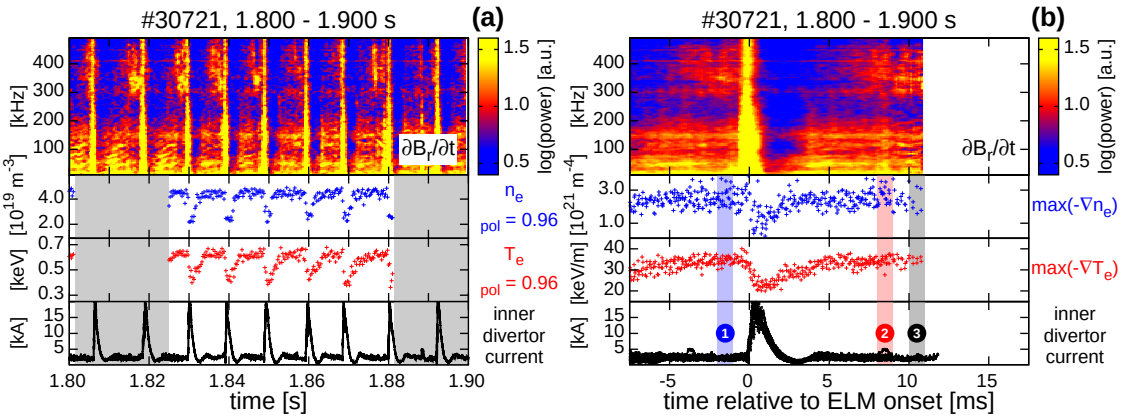

Figure 4.4: Pedestal evolution of the low $\nu^*_{\mathrm{e,ped}}$ case (#30721): (a) Spectrogram of $\partial B_\mathrm{r}/\partial t$ (top) and time traces of n_e (blue), T_e (red) at the pedestal top ($\rho_\mathrm{pol} = 0.96$) and inner divertor current (black). (b) ELM synchronised frequency histogram of $\partial B_\mathrm{r}/\partial t$ and ELM synchronised time traces of $\max(-\nabla n_\mathrm{e})$ (blue), $\max(-\nabla T_\mathrm{e})$ (red) and inner divertor current (black). Identical observations as in the high $\nu^*_{\mathrm{e,ped}}$ case can be made: The onset of high frequency magnetic fluctuations occurs after the recovery of the $\max(-\nabla T_\mathrm{e})$. Figure already published in [43].

maximum electron pressure gradient ($\max(-\nabla p_\mathrm{e})$). This points into the direction that the detected magnetic fluctuations (at low and high $\nu^*_{\mathrm{e,ped}}$) have a similar origin.

4.3 Stability analysis of the pre-ELM phase

To investigate possible drives for instabilities, which could cause the high frequency magnetic fluctuations, linear MHD stability analyses were performed for the high and low $\nu^*_{\mathrm{e,ped}}$ discharge. These are presented in figure 4.5. The applied stability chain, using a pressure constrained equilibrium reconstruction, the HELENA free boundary equilibrium solver and a fast version of MISHKA, is described in section 2.1.5. For every discharge three phases are analysed, in which the high frequency magnetic fluctuations are clearly present. The analysed intervals are (1) −2 ms to −1 ms relative to the ELM onset, (2) 10 ms to 11 ms relative to the ELM onset for #30701, 8 ms to 9 ms for #30721 and (3) 12 ms to 13 ms relative to the ELM onset for #30701, 10 ms to 11 ms for #30721. The vertical bars in figures 4.3b and 4.4b indicate the analysed intervals.

The operational points of both discharges are located close to the PB boundary in the analysed intervals, which is in line with the observation that the high frequency

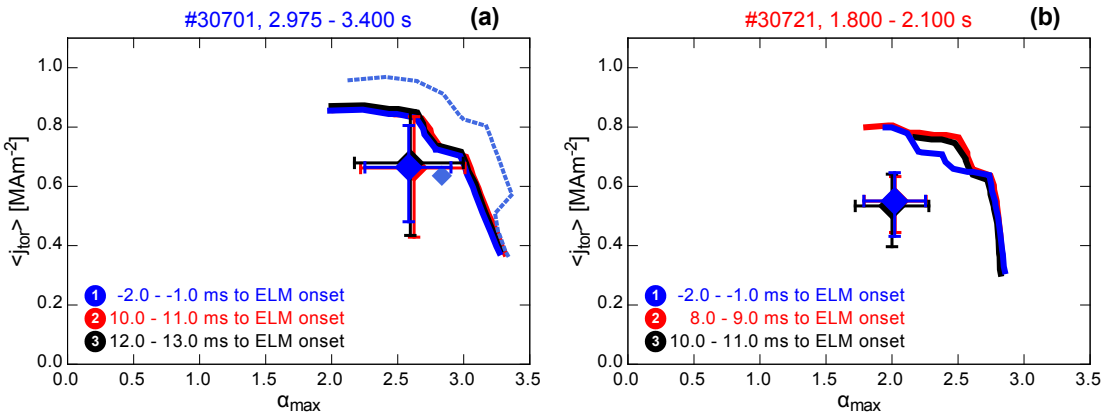

Figure 4.5: j-α diagrams for the period when high frequency fluctuations are present: (a) high $\nu^*_{\mathrm{e,ped}}$ case, for comparison the light blue, dashed boundary is calculated from a CLISTE equilibrium, and (b) low $\nu^*_{\mathrm{e,ped}}$ case. For the analysed time intervals, stability boundaries as well as operational points are similar.

fluctuations clamp the edge pressure gradient at a stable level. The uncertainties of the operational point are calculated from the statistical errors, i.e. the standard deviation, from the equilibrium reconstruction. There is no difference between the three analysed phases within the experimental uncertainties. Neither changes of the stability boundary can be seen nor movement of the operational point. This indicates that during the presence of the high frequency fluctuations the MHD behaviour of the pedestal does not change significantly.

4.4 Dependency of the detected fluctuation frequency

The high frequency inter-ELM magnetic fluctuations have been observed in several plasma discharges with a variation of frequencies. The pedestal profiles of these discharge intervals are analysed and correlated to the detected fluctuation frequency. To explain the measured frequencies, it was assumed that the instabilities causing these fluctuations are located in the pedestal region [106, 108]. This is reasonable, because the fluctuations are terminated by the ELM crash. In the pedestal region a strong background ($E \times B$) flow is observed [170], mainly caused by the E_r. The E_r profile at the plasma edge in H-mode, is well described by neoclassical theory [171]. At low toroidal rotation, the dominating term in E_r is $\nabla p_\mathrm{i}/\mathrm{Z}en_\mathrm{i}$ (using main ion pressure (p_i), ionisation state (Z) and main ion density (n_i)).

Since no measurements with the required temporal resolution were available for n_i and T_i, the quantities entering $\nabla p_\mathrm{i}/\mathrm{Z}en_\mathrm{i}$ are approximated by $\nabla n_\mathrm{i}/n_\mathrm{i} \approx \nabla n_\mathrm{e}/n_\mathrm{e}$ and

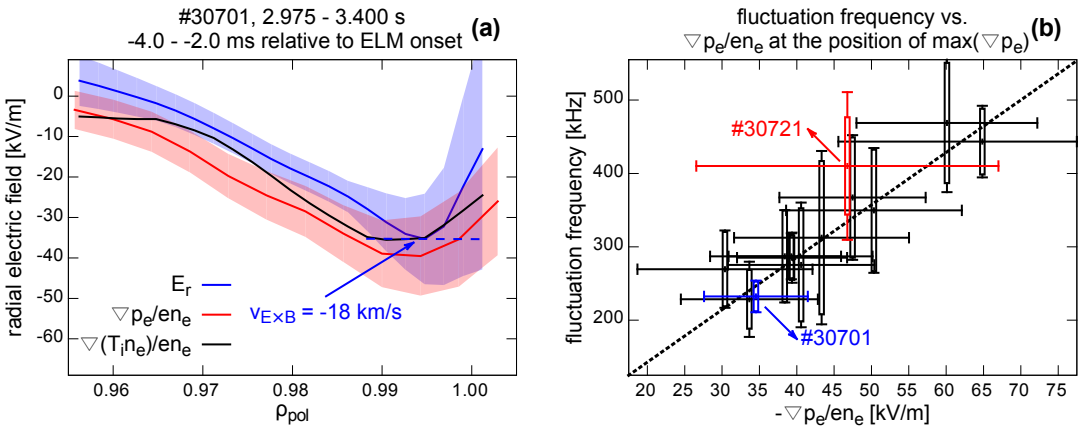

Figure 4.6: E_r, $\nabla p_\mathrm{e}/en_\mathrm{e}$ and fluctuation frequency: (a) Example profile of E_r (the blue dashed line indicates a $v_\mathrm{E\times B}$ of $-18\,\mathrm{km\,s^{-1}}$) and (b) $\partial B_\mathrm{r}/\partial t$ frequency over $-\nabla p_\mathrm{e}/en_\mathrm{e}$ ($\propto -E_\mathrm{r}$). The boxes along the frequency axis indicate the width of the fluctuation frequency band which can span up to 100 kHz. A linear dependence between the detected fluctuation frequency and the background flow velocity ($v_\mathrm{E\times B}$) can be seen (dashed line). Figure already published in [43].

$\max(\nabla T_\mathrm{i}) \approx \max(\nabla T_\mathrm{e})$. This should be valid in the plasma steep gradient region, when ν^* is sufficiently large. Furthermore, Z is 1 for hydrogenic plasma species. An example profile of E_r (red) of the high $\nu^*_\mathrm{e,ped}$ case, evaluated by CXRS [172], is compared to the estimations of $\nabla(T_\mathrm{i}n_\mathrm{e})/en_\mathrm{e}$ (black) and $\nabla p_\mathrm{e}/en_\mathrm{e}$ (blue) in figure 4.6a. The presented profiles agree within their uncertainties. Their minimum is around $-35\,\mathrm{kV/m}$, which corresponds to a $v_\mathrm{E\times B}$ of $-18\,\mathrm{km\,s^{-1}}$ (the negative sign indicates propagation into the electron diamagnetic direction). $\nabla(T_\mathrm{i}n_\mathrm{e})/en_\mathrm{e}$ and $\nabla p_\mathrm{e}/en_\mathrm{e}$ have similar shapes (within the error bars), which justifies the approximation of $\nabla p_\mathrm{i}/en_\mathrm{i}$ by $\nabla p_\mathrm{e}/en_\mathrm{e}$.

Figure 4.6b presents the fluctuation frequency (considering only frequency bands at a statistical distribution $> 200\,\mathrm{kHz}$) with respect to $-\nabla p_\mathrm{e}/en_\mathrm{e}$, taken at the position of the $\max(-\nabla p_\mathrm{e})$ (averaged between $-2.0\,\mathrm{ms}$ and $-0.5\,\mathrm{ms}$ relative to the ELM onset), for a set of 12 discharge intervals. The boxes on the frequency axis indicate the bandwidth of fluctuation, which are estimated by a FWHM criterion. The discharge intervals were chosen to span a wide range $-\nabla p_\mathrm{e}/en_\mathrm{e}$ and show the onset of high frequency magnetic fluctuations connected to the clamping of the pedestal pressure gradient in the pre-ELM phase, similar as observed for the high and low $\nu^*_\mathrm{e,ped}$ discharge (see section 4.2). The analysed discharge intervals have $\nu^*_\mathrm{e,ped}$ ranging from 0.55 to 1.80, determined by equation (4.2). It has been found for a similar range of ν^* at ASDEX Upgrade that the minimum of E_r agrees well with the approximation $\nabla p/en$ [173].

In figure 4.6b, a clear, linear correlation between fluctuation frequency and $-\nabla p_e/en_e$ can be seen. This suggests that the detected frequency (in the lab frame) is caused by a mode structure that rotates with the background $E\times B$ velocity at the edge.

It should be noted that the detected fluctuation frequency can change slightly for single ELMs (see figure 4.4a). Therefore, the analysis of single ELM cycles might give smaller bandwidths and separated blocks of the detected fluctuation frequencies. These could then be connected to slight changes of $\nabla p_e/en_e$. However, these analyses could not be performed, because of the limited time resolution and the uncertainties in the determination of the pedestal profiles.

4.5 Mode structure of the high frequency fluctuations

4.5.1 Detection of the fluctuations on the high field side

The poloidal structure of the observed inter-ELM magnetic fluctuations, can be characterised by ballooning coils with different locations. The mode structure can help to identify the underlying instability. In figure 4.7 the positions of two coils, located at the LFS (B31-14, red) and HFS (B31-35, blue) midplane, are indicated. Owing to the plasma position and shape, the HFS and LFS coil have different distances to the same flux surface and the magnetic axis (shown for $\rho_{\mathrm{pol}} = 0.99$). In cylindrical geometry with conducting wall the detected amplitude of a mode is lowered by $(r_m/(r_m + \Delta r))^{m+1}$ [13]. Here, the distance between the geometric axis and the mode location (r_m), the distance between the mode location and the coil location (Δr) and the poloidal mode number (m) are used. This effect has to be taken into account, when comparing fluctuation amplitudes from HFS and LFS, i.e. to gain insight if the mode structure is ballooned.

ELM synchronised frequency histograms of the LFS and HFS coil signals are presented in figure 4.8 (for the high $\nu^*_{e,\mathrm{ped}}$ case). Figure 4.8a shows the high frequency range for the spectrograms of the HFS (top) and LFS (bottom) coil. The inter-ELM fluctuation is clearly visible on the HFS too. It appears at similar time relative to the ELM onset as the fluctuations detected on the LFS. A strong fluctuation amplitude on the HFS would not be expected if the underlying instability has a ballooned mode structure e.g. KBMs. In figure 4.8b the integrated frequency histogram (from -2.5 to -0.5 ms relative to the ELM onset) is shown. A dominant mode is present in both spectrograms around 12 kHz, which is identified as $m/n = 1/1$ core mode. Taking this mode as reference and assuming that the 1/1 mode amplitude does not change from HFS to LFS, i.e. neglecting $m \pm 1$ sidebands and their relative phase, then the lower spectral intensity, detected on the HFS might be attributed to the $(r_m/(r_m + \Delta r))^{m+1}$ decay.

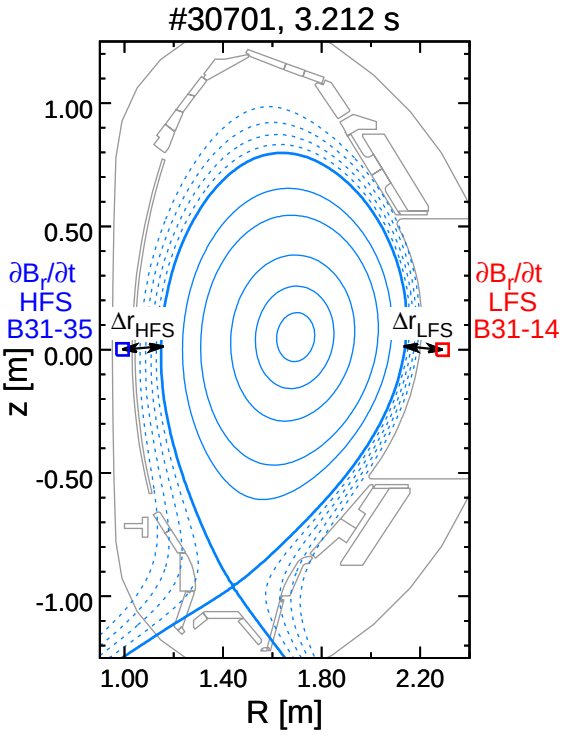

Figure 4.7: Ballooning coil positions: $\partial B_\mathrm{r}/\partial t$ is detected at the LFS as well as at the HFS midplane. The coils have different distances to the mode location (Δr). For $\rho_\mathrm{pol} = 0.99$ (steep gradient region) the LFS coil is approximately 8 mm closer to the flux surface than the HFS coil. Figure already published in [43].

In the cylindrical approximation the ratio of the detected LFS and HFS amplitudes for the 1/1 mode is given by

$$\left(\frac{r_\mathrm{m}/(r_\mathrm{m}+\Delta r_\mathrm{LFS})}{r_\mathrm{m}/(r_\mathrm{m}+\Delta r_\mathrm{HFS})}\right)^{1+1} = \left(\frac{r_\mathrm{m}+\Delta r_\mathrm{HFS}}{r_\mathrm{m}+\Delta r_\mathrm{LFS}}\right)^{1+1} \approx 1.38 \tag{4.3}$$

using $r_\mathrm{m} \approx 10.3\,\mathrm{cm}$, $\Delta r_\mathrm{HFS} \approx 60.0\,\mathrm{cm}$ and $\Delta r_\mathrm{LFS} \approx 49.6\,\mathrm{cm}$. This effect only explains parts of the weaker HFS signal for the 1/1 mode. Additionally, the HFS coil is located behind a tile of the inner heat shield, therefore, electromagnetic shielding might be another reason for the weaker detected signal. Further effects for the HFS-LFS discrepancy of the detected mode amplitude might be different gain factors in the data acquisition (DAQ), but both coils use identical DAQ systems, or the inaccurate assumption of constant mode amplitude.

The inter-ELM high frequency fluctuations are localised in the pedestal, therefore, the LFS to HFS ratio of the detectable amplitudes in cylindrical approximation

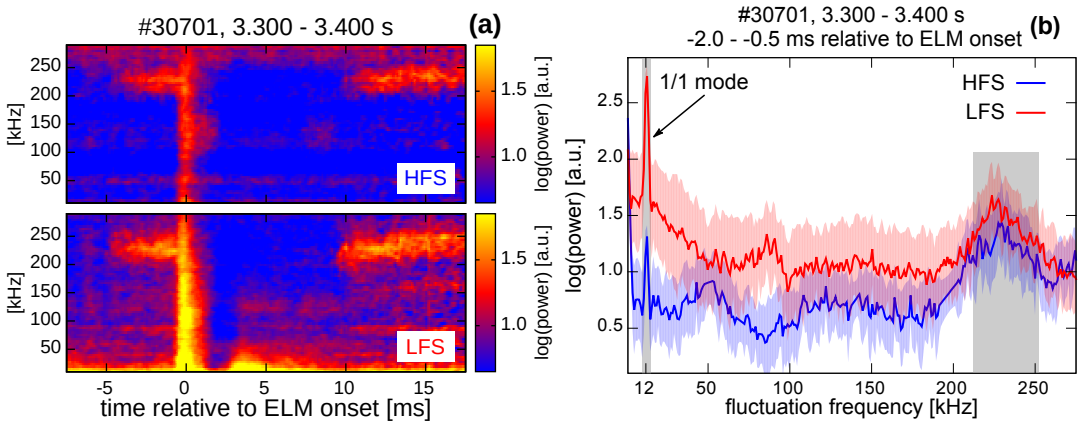

Figure 4.8: Comparison of the $\partial B_r/\partial t$ intensity at LFS and HFS: (a) Spectrogram of the HFS (top) and the LFS ballooning coil signals (bottom), (b) Integrated spectrum before the ELM onset. The high frequency fluctuations (240 kHz) are also detected at the HFS although the coil sensitivity might be lower (c.f. 1/1 mode). Figure already published in [43].

is

$$\left(\frac{r_m + \Delta r_{HFS}}{r_m + \Delta r_{LFS}}\right)^{55+1} \approx 2.01 \tag{4.4}$$

using $r_m \approx 48.9\,\text{cm}$, $\Delta r_{HFS} \approx 16.7\,\text{cm}$ and $\Delta r_{LFS} \approx 15.9\,\text{cm}$ and $m \approx 55$ (see section 4.5.2). This could be interpreted such that the fluctuation amplitude on the HFS might be even higher than detected, which is another indication that a ballooning type instability is not causing the high frequency fluctuations since a ballooned mode structure is expected to have zero amplitude on the HFS.

4.5.2 Toroidal mode structure of the fluctuations

The toroidal mode number (n) of the fluctuations can be determined from a set of ballooning coils, which are toroidally distributed at the LFS. The signal response of each coil is frequency dependent, therefore, phase shifts between the coils' signals are possible. This leads to inaccurate fits of the mode numbers. To reduce the systematic errors of the mode number fits, the transfer functions of the individual coils were measured and taken into account [169]. In figure 4.9 the ELM synchronised n histograms for the high $\nu^*_{e,ped}$ case (a) and the low $\nu^*_{e,ped}$ case (b) are presented. In this kind of plot, the n numbers are fitted in a period relative to the ELM onset for all ELMs in the analysed time interval. Then the resulting n are superimposed. There are different time intervals relative to the ELM onset for high $\nu^*_{e,ped}$ case ($-2.5\,\text{ms}$ to $-0.5\,\text{ms}$ relative to the ELM onset) and low $\nu^*_{e,ped}$ case ($-2.5\,\text{ms}$ to $-1.0\,\text{ms}$ relative to the

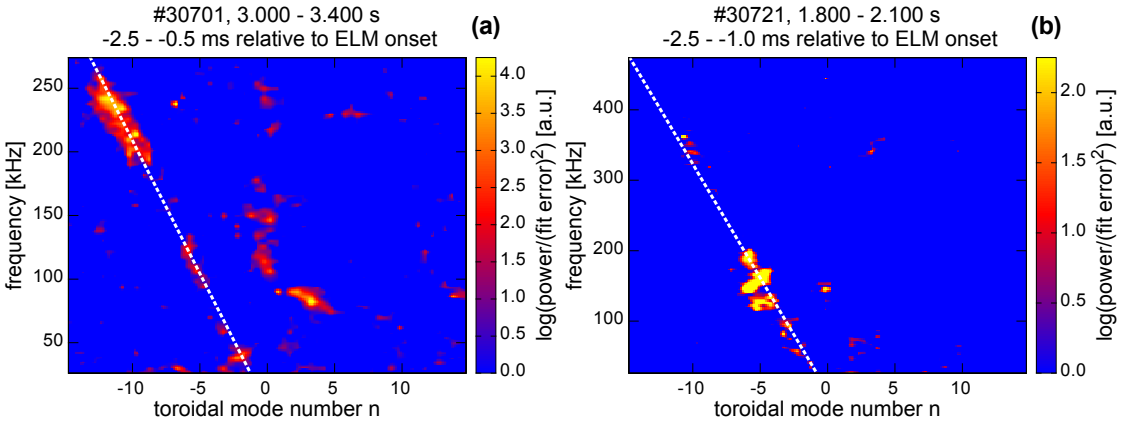

Figure 4.9: ELM synchronised toroidal mode number histograms: Determined from 5 toroidally distributed ballooning coils located at the LFS midplane, (a) for the high $\nu^*_{e,ped}$ and (b) low $\nu^*_{e,ped}$ case. Positive values of n correspond to co-current rotation of the mode, negative n to counter-current (electron diamagnetic) rotation. The dashed white line indicates constant frequency over n (f/n) ratio, meaning equal propagation velocity. The mode numbers of the high frequency fluctuations (at (a) 240 kHz and (b) 375 kHz are in both cases about -11. Figure already published in [43].

ELM onset) chosen because the high frequency fluctuations are dominantly present in different time periods relative to the ELM crash (compare figures 4.3b and 4.4b). In both $\nu^*_{e,ped}$ cases, clear mode numbers from $n= -2$ to $n= -8$ (negative sign for counter-current or electron diamagnetic rotation in the lab frame) are observed in the frequency range up to 180 kHz. These modes were previously found at JET and named washboard modes [174]. The onset of these washboard (150 kHz) modes is earlier in the ELM cycle and more related to the recovery of the density pedestal (see figures 4.3b and 4.4b). For the inter-ELM magnetic fluctuations with frequencies of 240 kHz (high $\nu^*_{e,ped}$) and 375 kHz (low $\nu^*_{e,ped}$) n is ranging between -10 and -12. Around $n = 0$ there are artefacts from timepoints with ill defined mode numbers appearing in the high and low $\nu^*_{e,ped}$ case. Comparing figures 4.9a and 4.9b, it can be seen that the observed magnetic fluctuations have a similar toroidal mode structure and different detected frequencies. This corresponds to the change of the background plasma rotation velocity, which is higher in the low $\nu^*_{e,ped}$ case.

The alignment in terms of frequency over n (dashed white lines in figures 4.9a and 4.9b) of the high frequency fluctuations and the low frequency washboard modes is observed. This is an indication that these modes have similar velocities relative to the lab frame, when projected into the toroidal plane. If the contributions of toroidal and poloidal rotation in the projection are similar, the low frequency washboard and the high frequency fluctuations are located at similar radial positions. Nevertheless, just after

the onset of the high frequency fluctuations a clamping of the pedestal $\max(-\nabla n_e)$ and $\max(-\nabla T_e)$, respectively $\max(-\nabla p_e)$, is seen.

Since the detected fluctuation frequencies are proportional to $\nabla p_e / e n_e$, i.e. the minimum of E_r in the pedestal, it is suggested that the modes are located in the steep gradient region. Using the evaluated background rotation velocity ($v_{E\times B}$) and the observed mode number, it is possible to estimate the detected fluctuation frequency in the lab frame and compare this to the experimentally measured frequency. Figure 4.6a indicates the minimum of the $v_{E\times B}$ velocity (blue dashed line), which is $-18.0 \pm 5.7\,\mathrm{km\,s^{-1}}$. At the position of the $v_{E\times B}$ minimum, q is ≈ 5, the toroidal plasma circumference (U_{tor}) is 13.4 m, and the poloidal circumference (U_{pol}) is 3.9 m resulting in an average field line pitch angle (α)

$$\tan(\alpha) = \frac{1}{q} \cdot \frac{U_{pol}}{U_{tor}} \approx 0.05814. \tag{4.5}$$

Taking into account the 'barberpole effect', the projection of $v_{E\times B}$ in the toroidal plane the total toroidal rotation measured in the lab frame ($v_{tor,lab}$) is given by

$$v_{tor,lab} = v_{E\times B}/\sin(\alpha) + v_{tor} \approx -299 \pm 88\,\mathrm{km\,s^{-1}}, \tag{4.6}$$

with the toroidal plasma velocity ($v_{tor} \approx 10\,\mathrm{km\,s^{-1}}$, measured by CXRS). The estimation of the detected fluctuation frequency in the lab frame (f_{lab}) is then

$$f_{lab} = \frac{v_{tor,lab} \cdot n}{U_{tor}} \approx 246 \pm 78\,\mathrm{kHz}, \tag{4.7}$$

using $n = -11$, which can be extracted from figure 4.9a for the magnetic fluctuation frequency of 240 kHz. This frequency agrees with the calculated f_{lab} within the experimental uncertainties, which additionally supports the hypothesis that the background plasma velocity dominates the mode propagation.

This behaviour is consistent with the linear dependence of the detected fluctuation frequency on $-\nabla p_e / e n_e$ found in section 4.2. From this dependency (dashed line in figure 4.6b) n can be estimated by assuming similar mode structures for all analysed discharge intervals. In figure 4.10 the detected fluctuation frequency is fitted in dependence of $v_{-\nabla p_e/en_e\times B}$ (taken at the position of $\max(-\nabla p_e)$). This results in an n of approximately -11, which is in good agreement with the magnetic measurements (see figure 4.9).

From [86], using the KBM and the MTM frequencies (ω) and scale sizes ($k_y \rho_s$), the phase velocity (ω/k_y) of KBMs and MTMs can be estimated for a similar plasma (see table 4.1). These are in the low $\mathrm{km\,s^{-1}}$ range for locations in the steep gradient region. These expected phase velocities and the propagation direction relative to the background $E \times B$ velocity cannot be extracted, because the measurement uncertainties of

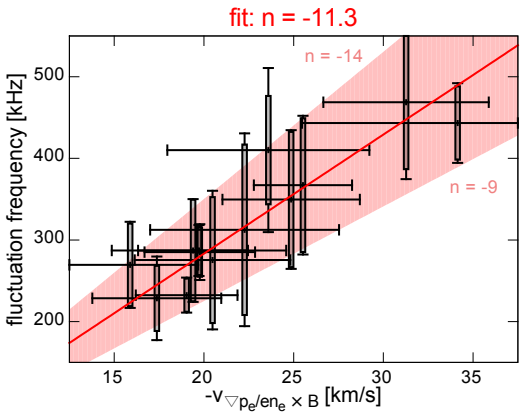

Figure 4.10: Neoclassically estimated background velocity and fitted n: Detected fluctuation frequency over $-v_{-\nabla p_e/en_e}$ ($\propto v_{\mathrm{E}\times\mathrm{B}}$). From the linear dependence between the detected fluctuation frequency and the background flow velocity a n number of approximately -11 can be determined (red line).

instability	ρ_{tor}	ρ_{pol}	c_{s} [km s^{-1}]	ρ_{s} [mm]	$k_{\mathrm{y}}\rho_{\mathrm{s}}$	ω $[c_{\mathrm{s}}/a]$	ω/k_{y} [km s^{-1}]
KBM	0.95	0.981	153	1.28	0.07	0.5	2.0
KBM	0.97	0.994	110	0.91	0.10	0.1	0.1
MTM	0.95	0.981	153	1.28	0.07	-2.5	-10.2
MTM	0.95	0.981	153	1.28	0.07	-3.5	-14.3
MTM	0.97	0.994	110	0.91	0.05	-2.0	-5.8
MTM	0.97	0.994	110	0.91	0.05	-3.0	-8.7

Table 4.1: Estimated phase velocities (ω/k_{y}) for MTM and KBM: Data taken from [86], (figures 7, 11), $a = 0.688\,\mathrm{m}$. This simulation was performed for plasma that is comparable to the high $\nu^*_{\mathrm{e,ped}}$ case that is presented in the paper. The estimated phase velocities (ω/k_{y}) are of the order of a few km s^{-1} in the region close to the E_{r} minimum ($\rho_{\mathrm{pol}} = 0.995$).

the background velocity are in a similar range or larger.

4.6 Theoretical interpretation of the high frequency fluctuations

For a variation of plasma edge ν^* it was found that the onset of high frequency fluctuations in the ELM cycle occurs at the same time as the re-establishment of the pressure gradient. During the presence of the high frequency magnetic fluctuations, the $\max(-\nabla p_{\mathrm{e}})$ is clamped, i.e. saturated. For this reason, the pre-ELM $\max(-\nabla p_{\mathrm{e}})$ is

already achieved of the order of milliseconds before the ELM crash. The corresponding mode structure propagates with the $E \times B$ background velocity at the edge, which indicates a location in the steep gradient region. Uncertainties in the measurements of the background velocity profile do not allow the determination of the propagation direction and phase velocities, if they are smaller than approximately $5\,\mathrm{km\,s^{-1}}$. For this reason, information on the structure propagation is not accessible to relate the observed structures to an underlying instability.

The strong signature of the fluctuations on the HFS can be interpreted as follows: In a turbulence picture, the current fluctuations leading to $\partial B_\mathrm{r}/\partial t$ are in parallel direction to the magnetic field, which implicitly requires non-adiabatic electron response. At the plasma edge this can become possible because the field line connection length increases (increasing q), the ion sound velocity (c_s) decreases and the density and temperature profiles have steep gradients [83, 175]. Consequently, the non-linear interaction between potential, pressure and current results in $\partial B_\mathrm{r}/\partial t$ on the HFS. These do not necessarily require a ballooned structure as an ideal linear MHD instability, which is solely driven by the pedestal gradient on the LFS. The observed toroidal mode structure and the enhanced transport, which is a consequence of the clamping of the gradients, might be only described by such non-linear interactions. Furthermore, the poloidal wave numbers ($k_\theta \rho_s$), calculated from the poloidal mode number, have similar scales ($0.1 < k_\theta \rho_s < 0.2$) at which KBMs and MTMs were found to be unstable in a similar discharge (see table 4.1).

Comparing the high frequency fluctuations to modes, which occur in ELM-free regimes as QH-mode [30] or EDA H-mode [33], the observations can be interpreted differently. The modes in ELM-free are localised at the very plasma edge, limiting the pressure gradient below the critical value. The magnetic signature of the EDA H-mode is broadband (between 0 kHz and 200 kHz) and for this reason, not comparable to the fluctuations investigated here. In QH-mode an edge harmonic oscillation (EHO) has been found, which usually has frequencies $< 50\,\mathrm{kHz}$. But at ASDEX Upgrade additionally a high frequency oscillation (HFO) is present simultaneously with the EHO. The HFO has frequencies in the range of 350 kHz to 500 kHz [31, 32], which are close to the highest detected fluctuation frequencies in this study (see figure 4.6b). Usually the QH-mode at ASDEX Upgrade is achieved at low pedestal top densities and ν^*. Therefore, the E_r wells in the pedestal are deep and the background $E \times B$ rotation is high. This is in line with a mode propagation with the background velocity. However, a low frequency fluctuation related to an EHO is not visible in the magnetic signals, when the inter-ELM high frequency fluctuations are present.

Linear MHD stability analysis has shown that DIII-D QH-mode plasmas are situated in the peeling region of the stability diagram close to the PB boundary. This suggested, that the EHO is caused by a saturated peeling mode [176]. For the high frequency magnetic fluctuations, the detected amplitude at the HFS is comparable

to the one measured on the LFS. This can be explained by peeling drive, which is HFS/LFS symmetric, however, current driven instabilities should show a dependency on ν^*.

5 | Isotope comparison

Parts of the following chapter were already published in [44].

ITER will start its operation with either H or more likely ^{4}He plasmas. This is required to commission the operationally relevant systems and plasma diagnostics in a non-nuclear environment, which enables easier access to components. Further, the plasma scenarios for D-T operation have to be developed [9]. But it is well known that plasma discharges with different main ion species show changes in their behaviour, e.g. $P_{\mathrm{L-H}}$, f_{ELM} and ELM size are affected by an isotope exchange (see section 5.1).

The impact of different main ion species on the pedestal was investigated by a matching experiment of the pedestal top n_{e} and T_{e} in D, H and ^{4}He plasmas (see section 5.2). Thereby, the pedestal structure, stability and inter-ELM evolution are characterised for these main ion species. First, the hydrogenic species plasmas (D,H) are compared and the PB stability of the pedestal is analysed (section 5.3). Then, section 5.4 presents a comparison to ^{4}He plasmas, resulting in the following, consistent picture (section 5.5): PB theory describes the pedestal stability for all investigated cases of main ion species and reproduces qualitative trends. No difference in the pedestal recovery phases, magnetic signature and corresponding structure of inter-ELM magnetic fluctuations could be identified. This suggests that there is no change of dominant processes, which determine the pedestal evolution, when the main plasma isotope is exchanged.

5.1 Impact of different main ion species on the plasma behaviour

To achieve the transition from L-mode to H-mode a certain power threshold, the L-H power threshold ($P_{\mathrm{L-H}}$), has to be exceeded [177]. This threshold differs when exchanging the main ion species of the plasma [178], which gives some uncertainty whether H-mode can be achieved in the non-nuclear phase of ITER with the available amount of P_{heat}. To investigate the access to the H-mode in plasmas with different

main ion species, studies on several experiments have been performed: ASDEX Upgrade [25, 179], DIII-D [180, 181], TCV [182] and JET [183, 184]. In summary, an inverse mass proportionality of $P_{\mathrm{L-H}} \propto A_{\mathrm{i}}^{-1}$ (atomic mass number (A_{i})) is reported for hydrogenic species meaning that $P_{\mathrm{L-H}}$ is approximately a factor of 2 higher in H than in D. Furthermore, $P_{\mathrm{L-H}}$ for ^{4}He plasmas is about similar to D in a metallic wall environment. More recent studies at ASDEX Upgrade revealed that the ion heat flux at the plasma edge plays an important role for the L-H transition [185]. It has been found that the edge ion heat flux at the L-H transition is about twice as high in H as in D plasmas at similar ∇T_{i}. E_{r} at the plasma edge is well described by neoclassical theory [171, 173]. The diamagnetic term ($\nabla p_{\mathrm{i}}/\mathrm{Z}en_{\mathrm{i}}$), using the main ion pressure (p_{i}), the ionisation state (Z), the elementary charge (e) and the main ion density (n_{i}), is the dominant contribution to the radial force balance. For this reason it is suggested that in D and H plasmas E_{r} at the L-H transition is similar.

Similar to the higher $P_{\mathrm{L-H}}$, which is caused by larger ion heat conductivity, better plasma confinement for heavier hydrogenic isotopes has been experimentally observed in L-mode [186] as well as H-mode [187, 188], also known as isotope effect. This behaviour is contrary to the expected confinement assuming gyro-Bohm diffusive transport because the gyro radius increases with mass at fixed temperature. Dimensionless scaling [189] of the H-mode plasma confinement requires a positive dependence on the ion mass [190]. The worse energy confinement in H plasmas was attributed to enlarged heat conductivity [191, 192]. Furthermore, the behaviour of ELMs, in terms of f_{ELM}, particle and energy losses, has been reported to change, when different main ion species are investigated [193] especially in ^{4}He plasmas [194, 195]. With respect to ITER's non-nuclear operation one important question is if the behaviour of H or ^{4}He plasmas can be extrapolated to scenarios for D-T operation.

In H-mode core and edge behaviour are coupled [196, 197] and especially ELMs lead to additional particle and energy losses. Therefore, all contributions to heat and particle transport as well as pedestal stability have to be analysed simultaneously. The presented investigations focus on a separation and ordering of core, edge and effects caused by ELMs in plasmas with different main ion species.

5.2 Motivation of the experiment and setup

The conducted experiments aimed at a quantitative comparison of pedestals in plasmas with different main ion species, respectively D, H and ^{4}He. For this reason it was intended to match the pedestal structure (fit n_{e}, T_{e} and T_{i} profiles) keeping a similar magnetic configuration (B_{t}, I_{p} and plasma shape). Figure 5.1 compares the plasma shapes of the performed D, H and ^{4}He plasma discharges. While the sepa-

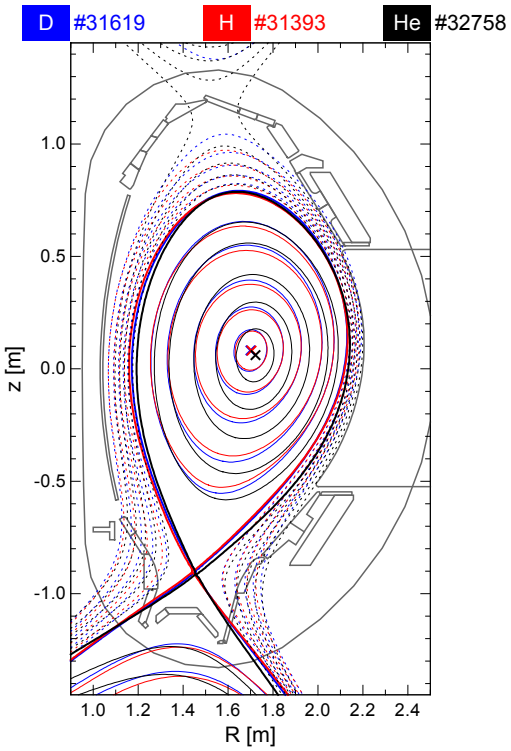

Figure 5.1: Comparison of the plasma cross section: For the D (blue), H (red) and ^{4}He (black) plasma discharge. The separatrix, strikepoint as well as flux surface locations of the D and H plasma agree well. The separatrix of the ^{4}He plasma (black) does not perfectly match these references on the LFS.

ratrix, strikepoint and flux surfaces locations are well matched for the D (blue) and H (red), the separatrix of the ^{4}He plasma (black) deviates on the LFS. This change of the separatrix location impacts the pedestal stability, i.e. the PB boundary is at reduced values of $\alpha_{\max}$ and $\langle j_{\mathrm{tor}} \rangle$ in comparison to the D and H discharge (compare figures 5.3 and 5.11).

The chosen plasma scenario was a lower single null (LSN) discharge with $I_{\mathrm{p}} = 1.0\,\mathrm{MA}$, $B_{\mathrm{t}} = -2.5\,\mathrm{T}$ (negative sign stands for opposite direction to I_{p}) at an average δ of 0.22. The varied control parameters were P_{heat} and the gas puff. This procedure enables a direct comparison of the edge stability between the different ion species. The ELM behaviour (frequency, losses and temporal evolution) with similar pre-ELM pedestal structure and the inter-ELM magnetic activity can be directly compared. Furthermore, from the necessary change of control parameters (necessary to achieve the match) possible changes in particle and/or energy transport due to the isotope exchange can be concluded.

The pedestal profiles were measured with high spatial and temporal resolution (see

chapter 3). The presented n_e and T_e profiles are analysed within the IDA framework (section 3.8) at a temporal resolution of 250 µs. The T_e profile is aligned such that 100 eV at the separatrix are achieved [168]. As discussed in section 4.1.1 relative alignment of the n_e and T_e profiles is cross checked with the TS diagnostic (section 3.4). In general only shifts smaller than 3 mm were applied.

The presented T_i profiles are measured by the edge CXRS system (see section 3.7) with a temporal resolution of 2.3 ms. The radial resolution is 3 mm at the edge and increases towards the pedestal top. Usually, T_i is measured on intrinsic light impurities such as boron or nitrogen. In ^{4}He plasmas T_i can be directly measured by CXRS processes on the main ions, resulting in large count rates. The recent upgrade of the spectrometer enabled a temporal resolution of 100 µs in the ^{4}He plasmas at the achieved signal levels. This gives the possibility to study the inter-ELM evolution of the pedestal T_i (see section 5.4). The presented T_i profiles are aligned relative to the T_e profile such that the $\max(-\nabla T_e)$ and maximum ion temperature gradient ($\max(-\nabla T_i)$) are located at a similar radial location. Also the radial shift of the T_i profile was below 3 mm.

5.3 Comparison of hydrogenic main ion species

The following section emphasises on the comparison of D and H plasmas, which aimed on a match of the pedestal n_e and T_e profiles.

5.3.1 Pedestal structure and stability

By a variation of two control parameters gas puff and P_{heat}, a match of T_e as well as good agreement of T_i pedestal profiles (pedestal top of T_i slightly higher in H) are achieved (see figure 5.2, blue: D, red: H). Only a match of the pedestal top n_e is possible due to a different ∇n_e (figure 5.2a). This pedestal top match required roughly a factor of 2 higher heating power (D: P_{heat} 3.9 MW, H: P_{heat} 7.5 MW) as well as a factor of almost 10 higher gas puff (D: $1.5 \cdot 10^{21}\,e\,s^{-1}$, H: $12.1 \cdot 10^{21}\,e\,s^{-1}$) in the H plasma. The heating systems were ECRH at central deposition location to avoid impurity accumulation (1.1 MW in both plasmas) and NBI operated with the particular ion species. The shallower ∇n_e in the H plasma is probably caused by the change of particle confinement, because a stronger ionization source due to the higher gas puff, further inside the plasma in H (at similar particle confinement), would lead to higher pedestal top n_e. It is very likely that the SOL transport behaviour is different in the compared plasmas since the SOL density is significantly higher in the H plasma. The formation of this 'SOL density shoulder' has been reported previously in D plasmas

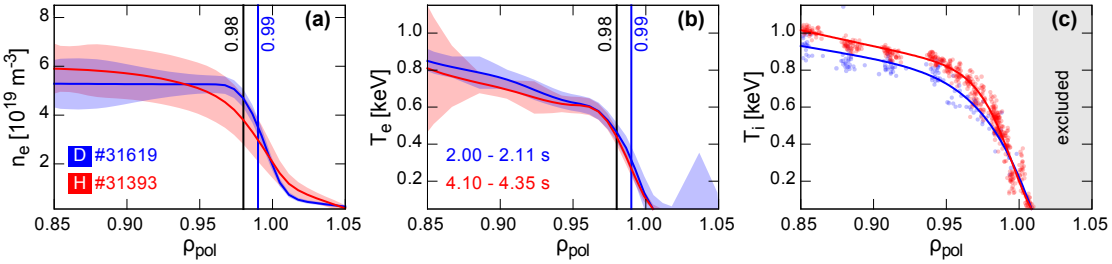

Figure 5.2: Pre-ELM (averaged between −2 ms to −1 ms relative to the ELM onset) profiles of (a) n_e, (b) T_e and (c) T_i for D (blue) and H (red). The coloured vertical bars indicate radial positions at which the inter-ELM temporal evolution of the corresponding quantities are tracked in figure 5.5. The gradient of the n_e profile in H is shallower than in D, leading to a wider pedestal and a reduction of the achievable pressure gradient (compare figure 5.3). Figure already published in [44].

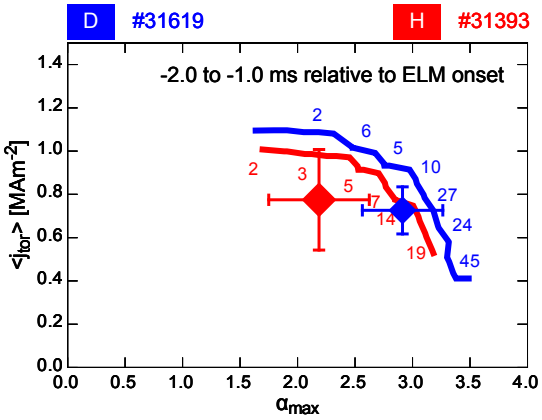

Figure 5.3: Comparison of the stability boundaries for the D (blue) and the H (red) plasma: average toroidal current density in the pedestal ($\langle j_{tor} \rangle$) and maximum normalised pressure gradient (α_{max}). Both operational points are located close to the PB part of the boundary. Figure already published in [44].

and is attributed to enlarged perpendicular transport by filaments (convection) owing to disconnection of filaments and wall [198, 199].

To compare the stability of both plasmas and investigate the impact of the shallower ∇n_e, linear MHD stability analysis were performed using the improved stability workflow (section 2.1.5). The resulting boundaries and corresponding operational points are presented in figure 5.3. Owing to the shallower ∇n_e in H, α_{max} is lower, leading to a reduced operational point in α_{max}. Within the experimental uncertainties both

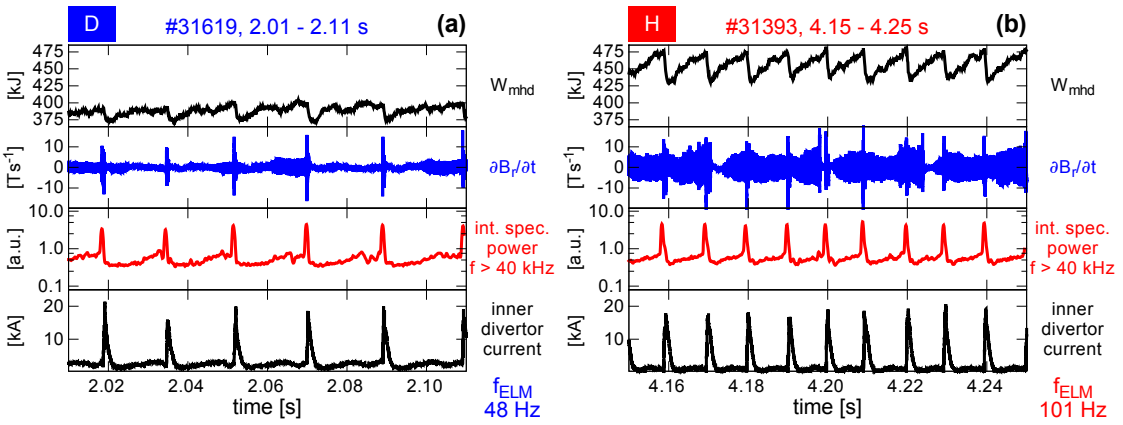

Figure 5.4: Time traces of 100 ms duration of the (a) D and (b) H plasma discharge: plasma stored energy (W_{MHD}, black, top plot), radial magnetic field fluctuations ($\partial B_{\mathrm{r}}/\partial t$, blue), the integrated spectral power of $\partial B_{\mathrm{r}}/\partial t$ for frequencies larger than 40 kHz (red) and divertor shunt current (black, bottom plot). In the H plasma, f_{ELM} is about twice as large as in the D plasma and the W_{MHD} losses due to ELMs are larger in H. Figure already published in [44].

plasmas are qualitatively consistent with PB theory.

5.3.2 ELM behaviour and losses

Moving from the static pre-ELM picture to a dynamic one, the evolution in between ELM crashes is compared using the time traces presented in figure 5.4 for D and H. W_{MHD}, $\partial B_{\mathrm{r}}/\partial t$ measured by a magnetic pickup coil that is located at the LFS midplane (B31-14), the integrated spectral power of $\partial B_{\mathrm{r}}/\partial t$ (for frequencies larger than 40 kHz) and divertor current, measured by shunts in divertor target plates (bursts indicate the ELM crashes), are plotted. By counting the number of ELMs (since the chosen time intervals have similar lengths), it is visible that f_{ELM} is about twice as large in the H plasma in comparison to the D plasma. A list of further ELM characterising quantities and their uncertainties can be found in table 5.1. In terms of average ELM energy losses (ΔW_{MHD}) the ELMs in H are almost twice as large as in D. But the W_{MHD} before the ELM crash is about 20 % higher in H due to slightly higher n_{e} and T_{i} from the pedestal inwards (compare figure 5.2). In principle the larger stored energy should be beneficial for the pedestal stability due to a bigger Shafranov shift. However, it can be seen in figure 5.3 that this effect is overruled by the shallower ∇n_{e} and only of secondary order in this comparison. Taking into account the differences in W_{MHD} and comparing the average, relative ELM energy losses, approximately 1.5 times higher losses are found in H in comparison to D. Combining f_{ELM} and ΔW_{MHD}, the power

species	shot	time [s]	f_{ELM} [Hz]	ΔW_{MHD} [kJ]	ΔW_{MHD} [%]
D	#31619	2.00−2.11	48 ± 17	20.1 ± 4.6	5.1 ± 1.2
H	#31393	4.10 - 4.35	101 ± 6	36.9 ± 5.2	7.9 ± 1.1
	P_{ELM} [MW]	P_{heat} [MW]	P_{net} [MW]	$P_{\mathrm{rad,sep}}$ [MW]	$\frac{P_{\mathrm{ELM}}}{P_{\mathrm{net}}-P_{\mathrm{rad,sep}}}$ [%]
D	0.97 ± 0.41	3.93	3.76	1.25 ± 0.15	38.6 ± 16.5
H	3.73 ± 0.97	7.51	7.28	0.72 ± 0.22	56.8 ± 8.9

Table 5.1: ELM energy and power losses for D and H: ELM repetition frequency (f_{ELM}), average ELM energy loss (ΔW_{MHD}), power loss by ELMs (P_{ELM}), heating power (P_{heat}), corrected heating power (P_{net}), radiated power inside the separatrix ($P_{\mathrm{rad,sep}}$) and relative power loss by ELMs ($P_{\mathrm{ELM}}/(P_{\mathrm{net}} - P_{\mathrm{rad,sep}})$). In both species about half of power crossing the separatrix is transported by ELMs. In absolute numbers an enhanced heat flux across the pedestal in H is required to balance the power.

losses caused by ELMs (P_{ELM}) in H are about 4 times higher than in D. Correcting for the radiated power inside the separatrix ($P_{\mathrm{rad,sep}}$), the relative power losses caused by ELMs ($P_{\mathrm{ELM}}/(P_{\mathrm{net}} - P_{\mathrm{rad,sep}})$) are calculated using the for beam losses and $\partial W_{\mathrm{MHD}}/\partial t$ corrected heating power (P_{net}). These are in the range of about 40 % to 50 % in both plasmas. To fulfil power balance the remaining power $P_{\mathrm{net}} - P_{\mathrm{rad,sep}} - P_{\mathrm{ELM}}$ has to be lost by heat transport. Therefore, a factor of 1.8 higher heat flux across the pedestal is required in H in comparison to D. Assuming conductive heat transport (inside the confined plasma region), the heat conductivity across the pedestal should also increase by a similar factor since the pedestal temperature profiles are similar in both plasmas, which is consistent with previous findings [191, 192].

An indicator for the presence of instabilities or modes in the plasma are fluctuations of the magnetic field. In the spectral analysis low frequencies in the range of a few tens of kHz are mostly associated to rotating modes in the core, whereas high frequencies are more connected to microinstabilities or fast poloidally rotating structures at the plasma edge. In between the ELM crashes, the detected $\partial B_{\mathrm{r}}/\partial t$ (figure 5.4, blue) is larger in amplitude for H than for D. This is mainly caused by a larger amplitude response of a core mode in the H plasma, which dominates the power in frequencies up to 40 kHz. The inter-ELM integrated spectral power for frequencies larger than 40 kHz (red) is at similar levels for both main ion species. Furthermore, the integrated spectral power shows a similar evolution. After the ELM crash, which appears as burst, a low level phase, correlated to the n_{e} pedestal recovery (see section 5.3.3), is observed. This phase is followed by an increase (during the T_{e} pedestal recovery), resulting in a saturated phase before the ELM onset, in which it has been found that the maximum pedestal gradients are clamped [43]. The toroidal structure of these

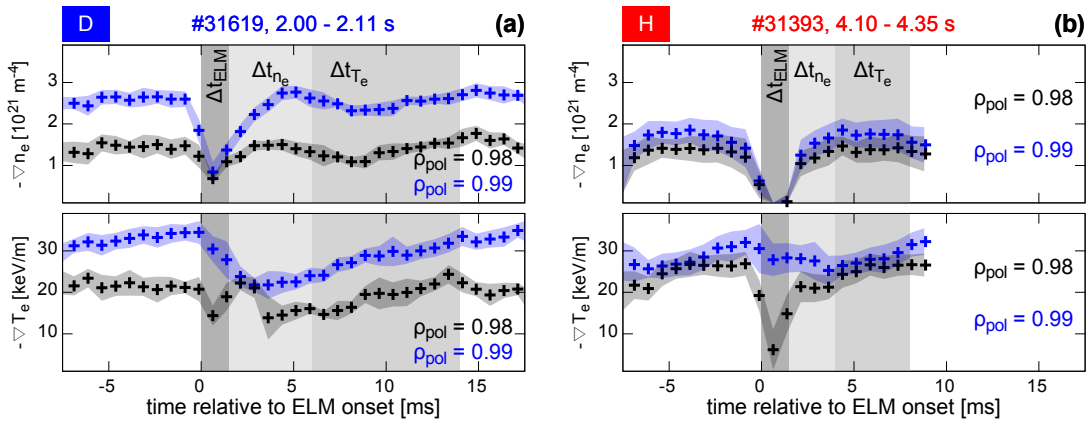

Figure 5.5: Pedestal gradient evolution throughout the ELM cycle: ∇n_e and ∇T_e at certain positions (ρ_pol ; compare figure 5.2) for the (a) D and (b) H plasma. The pedestal recovery phases have a similar sequence in both main ion species but different duration (Δt_{n_e}, Δt_{T_e}). Figure already published in [44].

fluctuations is analysed in more detail in section 5.3.4.

5.3.3 Inter-ELM pedestal evolution

Comparing the inter-ELM evolution of the n_e and T_e pedestal for the different ion species gives insight in the build-up of the pre-ELM pedestal structure. It has been found previously in D plasmas that the n_e pedestal recovers on a shorter timescale than the T_e pedestal [102]. A change of this behaviour in H would be a strong indication for different mechanisms acting on the pedestal. In figure 5.5 the ELM synchronised evolution of ∇n_e and ∇T_e for D and H at representative radial locations ($\rho_\mathrm{pol} = 0.98$ and 0.99), which are also indicated in figure 5.2, are presented. In both main ion species the pedestal shows qualitatively similar recovery phases, i.e. the n_e pedestal recovers faster than the T_e pedestal.

The first phase in the ELM-cycle is the ELM crash, which has a duration Δt_ELM of 1.5 ms for both plasmas, according to the duration of the bursts in the divertor shunt current. This phase is followed by the recovery of the n_e pedestal with duration Δt_{n_e}, which is longer in D. Two possible mechanisms could cause this difference in Δt_{n_e}: On the one hand the 10 times higher gas puff (larger particle source) as well as the faster velocity of recycled particles due to the lower mass in H or on the other hand an increased outward particle transport from the core to the pedestal top in H. The third phase is the recovery of the T_e pedestal, respectively ∇T_e. Here, the duration Δt_{T_e} is also longer in D, most probably caused by the lower heat flux

to the pedestal. During the last phase of the ELM cycle the pedestal gradients do not evolve and high frequency magnetic fluctuations set in (see section 5.3.4). This period lasts up to several milliseconds in D, whereas in H it is just present for 1 ms to 2 ms.

Qualitatively, a similar sequence of pedestal recovery phases is observed in D and H, giving no evidence in the direction that the dominant processes determining the pedestal recovery are changed by the isotope exchange. However, the different duration of the phases support quantitative changes in particle and heat transport.

5.3.4 Structure of pre-ELM magnetic fluctuations

Analysing the toroidal structure of magnetic fluctuations can give further insight in the underlying instabilities causing them. The comparison of the frequencies from the detected $\partial B_\mathrm{r}/\partial t$ enables the determination of propagation velocities of the structures.

The toroidal mode structures are reconstructed from measurements of a toroidal magnetic pickup coil array. Analysing relative phase shifts (and multiples of 2π added/subtracted) in between the coils signals, one can determine the toroidal structure of the detected fluctuation, represented by the toroidal mode number (n). It is important to consider that the pickup coils can have an intrinsic, frequency dependent phase response (due to inductances or shielding), especially at higher frequencies. For this reason, these intrinsic phases have to be taken into account to reliably determine n [169]. The method has been improved recently by statistically increasing the amount of data using ELM synchronization [119], which enables the analysis of n throughout the ELM cycle.

To compare the frequency resolved magnetic activity at the LFS midplane for the hydrogenic species, figure 5.6 presents ELM synchronised frequency histograms for D and H. At lower frequencies (< 40 kHz) the frequency histogram is dominated by a core mode in both presented cases. The post-ELM magnetic activity in the medium frequency range (40 kHz to 200 kHz) during the n_e pedestal recovery (Δt_{n_e}, compare figures 5.5a and 5.5b) is lower than in the other phases of the pedestal evolution. In D the fluctuations in this frequency range are more band-like than in H, where they are rather broadband. After the recovery of the T_e pedestal (Δt_{T_e}) high frequency fluctuations between 300 kHz and 400 kHz set in. The pre-ELM phases (between -2.1 ms and -0.1 ms relative to the ELM onset) are analysed in detail by the ELM synchronised toroidal mode number histograms (figures 5.6b and 5.6d). The sign of the mode numbers indicates their rotation direction. Positive n represent a co-current (toroidal) or ion-diamagnetic (poloidal) propagation direction, whereas negative n indicate a

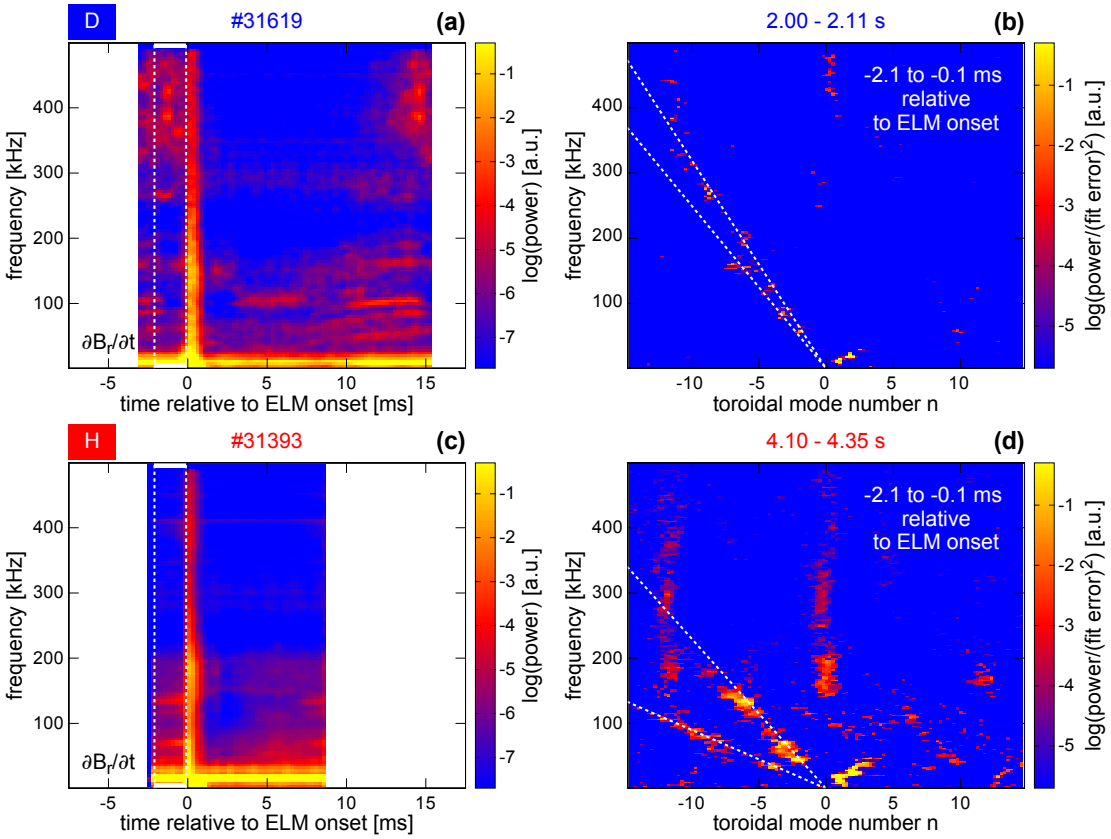

Figure 5.6: Comparison of the magnetic fluctuations: ELM synchronised (a,c) frequency and (b,d) toroidal mode number histograms (determined between $-2.1\,\mathrm{ms}$ and $-0.1\,\mathrm{ms}$ relative to the ELM onset) for (a,b) D and (c,d) H. The white dashed lines in (a,c) indicate the time interval of the mode number determination and in (b,d) the two mode branches with different propagation velocity. Similar inter-ELM activity and corresponding toroidal structure can be seen in D and H. The different detected frequencies for similar n correspond to different rotation velocities relative to the lab frame. Figure already published in [44].

species	shot	time [s]	P_{heat} [MW]	gas puff [$10^{21}\,\mathrm{e\,s^{-1}}$]	f_{ELM} [Hz]
D	#31547	3.50 - 3.95	6.8	4.2	88 ± 7
D	#31547	6.40 - 6.65	6.6	0.1	90 ± 10
H	#31393	4.10 - 4.35	7.1	12.0	101 ± 6
H	#31393	6.00 - 6.50	11.0	5.5	137 ± 7

Table 5.2: Varied control parameters in D and H: In D the gas puff was reduced to almost zero whereas in H a reduction by 50 % could be achieved when increasing P_{heat}.

counter-current (toroidal) or electron-diamagnetic (poloidal) propagation direction. At lower frequencies the core mode has a clear $n = 1$, 2 structure for both plasmas. The higher frequency range shows two mode branches with negative n for D and H as it has been previously found in a D discharge [119]. These are indicated by the white dashed lines, which inclination represent the rotation velocity relative to the lab frame. The different inclination means that the two branches rotate at different velocities. The shallower slopes of the branches in H in comparison to D indicate a lower rotation velocity. This can be explained by the different n_{e} profile in H, since the $E \times B$ flow at the edge is proportional to $\nabla p_{\mathrm{i}}/\mathrm{Z}en_{\mathrm{i}}$. Assuming $\nabla n_{\mathrm{i}}/n_{\mathrm{i}} \approx \nabla n_{\mathrm{e}}/n_{\mathrm{e}}$, the shallower ∇n_{e} in H leads to a lower background $E \times B$ velocity.

It can be seen that the branches have similar structure in both main ion species. At medium frequencies n is in the region of -3 to -8. Consistent with the more broadband ELM synchronised frequency histograms in H, the measured n have less distinct peaks in the mode number range than in D. The high frequency fluctuations are related to n in the region of -11 in both main ion species.

The comparison of the pre-ELM structure of $\partial B_{\mathrm{r}}/\partial t$ reveals similar n for both main ion species, which also supports that similar instabilities are present in these plasmas. The detected rotation velocities differ, since the background flow velocity is affected by the shallower ∇n_{e} in H.

5.3.5 Control parameter variation

To support the matching experiments, a variation of the two utilised control parameters (P_{heat} and gas puff) were performed to investigate their impact on the pedestal structure. In D at constant P_{heat} the gas puff was reduced to almost zero, whereas in H the gas puff could be reduced when increasing P_{heat}. Detailed numbers on these variations can be found in table 5.2. Comparing the ELM behaviour in D, two ELM

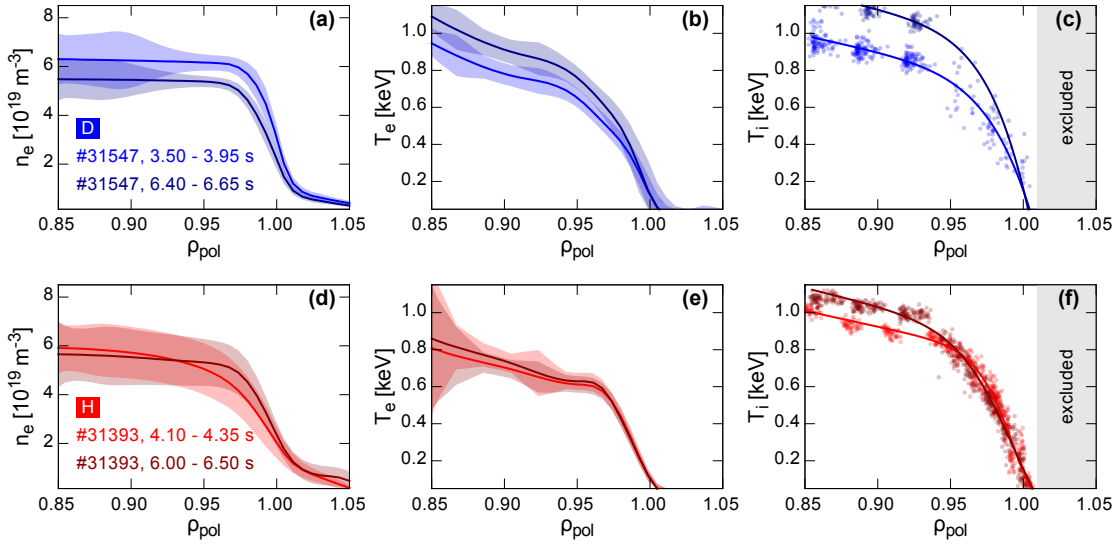

Figure 5.7: Effect of a control parameter variation on the pedestal profiles in (a-c) D (high gas puff: blue, low gas puff: dark blue) and (d-f) H (high gas puff: red, low gas puff: dark red): (a,d) n_e, (b,e) T_e and (c,f) T_i. The gas puff reduction in D (dark blue) leads to an inward shift of the n_e profile, giving better pedestal stability, therefore, higher T_e and T_i pedestals. In H the increased P_{heat} in the period of gas puff reduction (dark red) leads to a higher Shafranov shift and increased pedestal stability, as indicated by the steeper ∇n_e.

repetition frequency bands [102] are found in the period of higher gas puff. In table 5.2 the f_{ELM} of the frequency band, which is the dominant in terms of number of ELMs, is given. The dominating f_{ELM} does not change by the reduction of gas puff, but the second ELM repetition frequency band with higher frequency disappears. In the compared H cases, there is one ELM repetition frequency band identified. Here, f_{ELM} increases in the period with reduced gas puff and increased P_{heat}. This is related to the higher P_{heat}, which provides a higher heat flux to the pedestal, provoking a faster recovery of the T_e pedestal (shorter Δt_{T_e}) and therefore, a higher f_{ELM}.

The pre-ELM pedestal structure is compared in figure 5.7 for D (high gas puff: blue, low gas puff: dark blue) and H (high gas puff: red, low gas puff: dark red). In D the reduction of the gas puff leads to a radial inward shift of the n_e profile (dark blue) with respect to the T_e profile. It has previously been shown that such a shift increases the pedestal stability [200], which is also valid, however, less pronounced, in the presented case. The T_e and T_i pedestal increase, because of a positive feedback loop due to the higher W_{MHD} and Shafranov shift.

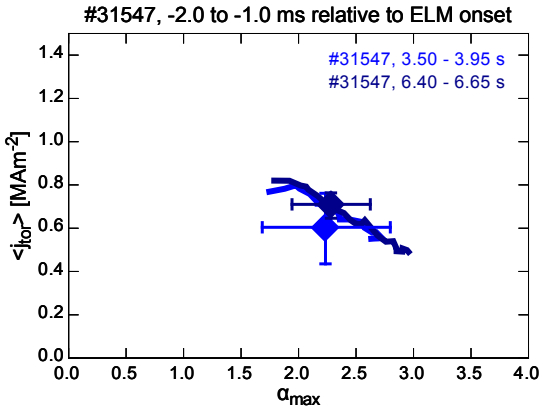

Figure 5.8: Comparison of the stability boundaries for the gas puff variation in D: Normal (blue) and reduced (dark blue) gas puff. When the gas puff is reduced and the n_e profile shifts radially inwards, the operational point is located at slightly higher α_{max} and $\langle j_{tor} \rangle$ at unchanged PB boundary.

A j-α diagram for the two D discharge intervals are presented in figure 5.8. The corresponding PB analyses were performed using the ILSA ideal MHD stability code, which gives the possibility to analyse the radial mode spectrum and exclude core instabilities from the analyses. When the n_e profile is shifted inwards, the operational point moves to slightly higher α_{max} and $\langle j_{tor} \rangle$. However, the increased pedestal top temperatures are compensated by a lower n_e at the pedestal top, only leading to slightly higher pedestal top pressure. The PB boundary is unaffected by the n_e profile shift.

In H the variation of the gas puff (figures 5.7d to 5.7f) does not show such clear results since it was on the one hand not possible to achieve a similar variation of the gas puff as in D and on the other hand necessary to increase P_{heat}. When decreasing the gas puff and increasing P_{heat} the n_e profile (dark red) steepens. This can be explained by the higher W_{MHD} that leads to a higher Shafranov shift, which increases the pedestal stability. Therefore, also a slightly larger T_i at the pedestal top can be sustained. However, the pedestal improvement by this effect is smaller than the effect of the n_e profile shift observed in D.

Putting the observations of the control parameter variation together, the explanations from the pedestal matching experiments are further supported. The pedestal stability in D and H is determined by similar mechanisms: Relative inward shifts of the n_e profile with respect to the T_e profile are beneficial for the stability. An increased W_{MHD} stabilises the pedestal by a larger Shafranov shift in both main ion species. The different response to a gas puff reduction (P_{heat} increase in H), points into the direction of a worse particle confinement in H in comparison to D.

In H the n_e pedestal was stabilised by higher amount of P_{heat}, which was applied by NBI. Therefore, the core fuelling was also expected to increase, which is, in combination with the higher gas puff required in H, a strong evidence for worse particle confinement in H in comparison to D.

5.4 Helium plasmas

For further comparison to another main ion species, ^{4}He plasmas were performed. Again a match of the pedestal n_e and T_e profiles to the D and H references (see section 5.3.1) was envisaged. However, due to the two electrons provided by a ^{4}He atom to the plasma, the n_i will be lower in comparison to hydrogenic species at similar n_e.

In ^{4}He several operational boundaries at ASDEX Upgrade have to be taken into account. For the density control only a small pumping rate by the turbomolecular pumps is available since cryopumps do not freeze ^{4}He. By applying argon frosting [201], in which an argon frost layer is condensed on the cryopump to enable the binding of ^{4}He atoms, this issue can be overcome. Operating the NBI injectors with ^{4}He causes a significant reduction of available heating power owing to a limitation of the extractable beam current. Furthermore, the pumping of the NBI neutralisers is crucial, since at ASDEX Upgrade titanium sublimation pumps are used, which inefficiently pump ^{4}He. Using ^{4}He NBI gives huge neutral influx from the NBI neutralisers, a reduced available P_{heat} and no CXRS measurements for T_i. For this reason it was decided to operate the NBI with H for these experiments.

The achievement of plasma scenarios with large and low frequent ELMs turned out to be rather challenging since density control is quite difficult. Finally, the most suitable scenarios were operated with a small discharge pre-fill of ^{4}He and with almost no additional gas puff. The overall plasma behaviour of these discharges was rather stable with no indication of impurity accumulation, which usually causes problems in hydrogenic plasmas, operated without gas puff and wall conditioning by boronization.

Time traces of a ^{4}He discharge (with argon frosted cryopump) are presented in figure 5.9. In the discharge ramp-up phase one H NBI source is used to stabilise the H-mode. Then the NBI is switched off to keep the level of H in the ^{4}He plasma as low as possible. During this ECRH only phase at low n_e (for ^{4}He plasmas), which is well controlled by the argon frosting, the ELMs disappear. Two short H NBI blips at roughly 2.3 s and 2.8 s were performed for CXRS T_i measurements. When the P_{NBI} is ramped-up, W_{MHD} and n_e increase and the ELMs return. The short switching off

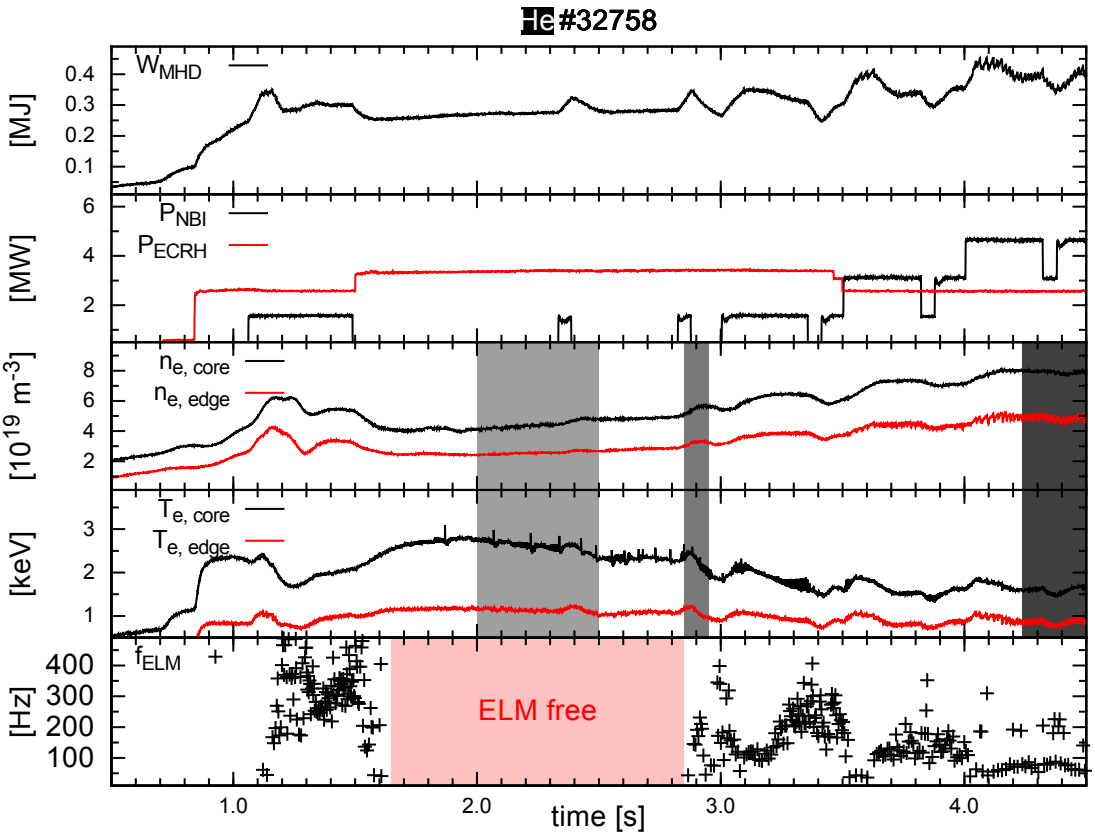

Figure 5.9: Time traces of a matching discharge in ^{4}He: (a) W_{MHD}, (b) H neutral beam heating power (P_{NBI}, black) and electron cyclotron resonance heating power (P_{ECRH}, red), (c) line integrated n_{e} in the core and at the edge, (d) T_{e} in the core (black) and at the edge (red) and (e) f_{ELM}. At roughly 2.3 s and 2.8 s neutral beam injection (NBI) blips were performed for T_{i} measurements by CXRS, whereas at 3.3 s, 3.8 s and 4.2 s the beam source for CXRS was switched off to measure the passive emission. The grey shaded boxes indicate the time intervals in which the pedestal profiles are analysed (see figure 5.10). After the discharge ramp-up using H NBI, an ECRH only phase was performed to keep the plasma as pure as possible. During this period an ELM-free phase occurred. At the end of the discharge the heating power was increased and the ELMs reappeared.

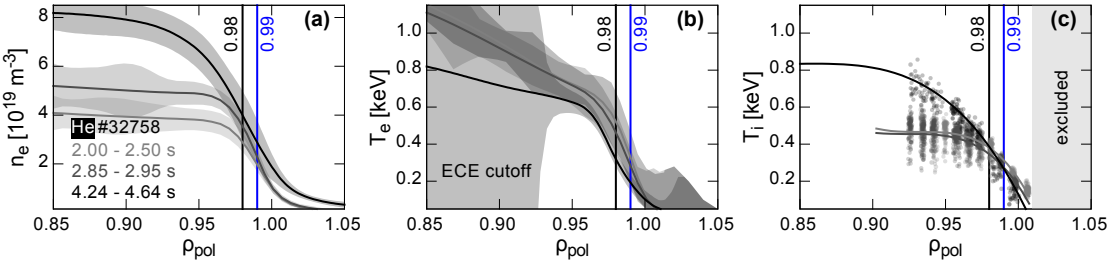

Figure 5.10: Pedestal profiles in ^{4}He: (a) n_e, (b) T_e, (c) T_i. Between the ELM-free phase (grey) and the phase immediately after the ELMs return (black, averaged between -2 ms to -1 ms relative to the ELM onset) n_e increased, whereas T_e and T_i do not change. Consequently, p is increased, which moves the operational point closer to the PB boundary.

of the NBI source, at which CXRS measurements were made, was performed to measure the passive emission of the background ^{4}He radiation. By ELM synchronization the background can be determined throughout the ELM cycle and correspondingly subtracted from the active signal, similar as presented for the LIB diagnostic in section 3.1.2. This method enables the reliable evaluation of the inter-ELM T_i evolution of the main plasma species, as presented in section 5.4.2.

5.4.1 Pedestal structure

The ELM-free phase has its origin in the pedestal structure as it will be shown by linear stability analysis. In figure 5.10 the pedestal profiles of the ELM-free phase (grey) and the phase short after the re-occurrence of the ELMs (black) are compared. The n_e pedestal is higher in the phase with ELMs, while T_e is similar in both phases, meaning that the larger n_e increases the pedestal pressure, moving the operational point to the PB boundary. This is shown by stability analysis (figure 5.11), performed in a similar manner as described in section 5.3.1. Three phases of the discharge are analysed as indicated in figure 5.9: One period during the ELM-free phase, in which no stability boundary is identified since the pedestal is deeply PB stable, and two in which n_e and later P_{heat} are increased. When α_{max} increases due to the larger n_e, a peeling ballooning boundary is found, that moves further towards the operational point, when P_{heat} is increased. This qualitatively explains the experimental observations.

In the phase when the first n_e increase takes place (2.85 s and 2.95 s), the n_e and T_e pedestal profiles are similar to the ones achieved in the D plasma. Comparing the ELMs with the ones in D plasmas, a much larger f_{ELM} as well as lower ΔW_{MHD} losses are found. Since W_{MHD} in ^{4}He is about 20 % lower than in D owing to the lower n_i, the

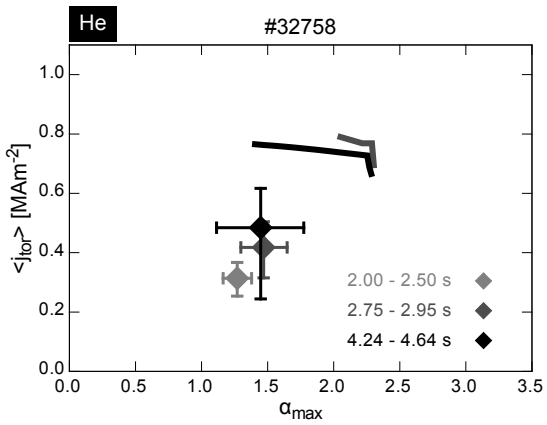

Figure 5.11: Comparison of the stability boundaries in ^{4}He: ELM-free ECRH only phase (grey), small ELMs (dark grey) and large ELMs at higher n_e (black). In the ELM-free phase no stability boundary could be determined, meaning that the pedestal is PB stable. When increasing the pedestal pressure by increasing the density the operational point evolves to larger α_{max} and a close PB boundary is found, which is in line with the re-occurrence of ELMs.

species	shot	time [s]	f_{ELM} [Hz]	ΔW_{MHD} [kJ]	ΔW_{MHD} [%]
^{4}He	#32758	2.85 - 2.95	148 ± 61	11.3 ± 2.6	3.5 ± 0.8
^{4}He	#32758	4.24 - 4.64	73 ± 15	36.0 ± 4.2	9.1 ± 0.5

Table 5.3: ELM energy losses (ΔW_{MHD}) for the analysed intervals of the ^{4}He discharge.

relative ΔW_{MHD} is in a similar range. The detailed values are listed in table 5.3. The main heating method was ECRH for reasons of plasma purity. This is different to the heating scheme of the D and H discharges, where mainly NBI was used. For this reason quantitative comparisons of the power losses are rather uncertain and estimations of the energy and particle transport are not possible.

5.4.2 Inter-ELM pedestal evolution

When f_{ELM} gets lower, the inter-ELM pedestal evolution can be investigated. In comparison to the D and H discharges higher n_e pedestals are present in this period but W_{MHD}, f_{ELM} and relative ΔW_{MHD} are comparable to the D discharge (table 5.3). In figure 5.12 the evolution of ∇n_e, ∇T_e and ∇T_i at radial positions close to the separatrix (ρ_{pol} 0.98, 0.99) are shown. Similar recovery phases as in the hydrogenic plasmas are

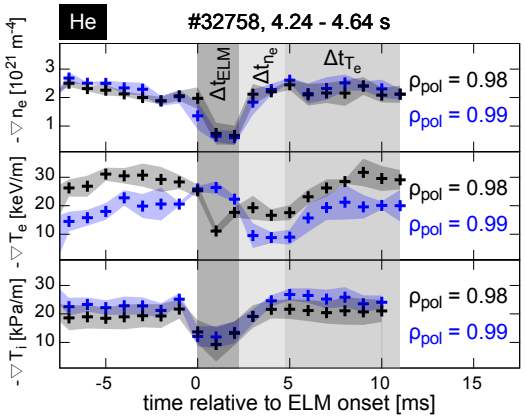

Figure 5.12: Temporal evolution of the pedestal gradients in ^{4}He: ∇n_e, ∇T_e and ∇T_i at two positions in the pedestal ($\rho_\mathrm{pol} = 0.98, 0.99$). The recovery of ∇n_e and ∇T_i take place on similar timescales (Δt_{n_e}), whereas ∇T_e is established later in the ELM cycle (Δt_{T_e}). Figure already published in [44].

identified. Again n_e, respectively ∇n_e recovers faster than ∇T_e. Remarkably, ∇T_i does not follow the evolution of ∇T_e but is re-established after Δt_{n_e}, which is the recovery timescale of n_e. Such a behaviour was also suggested by the comparison of the neoclassically estimated current in the pedestal (using T_i equal to T_e) and the current in the pedestal reconstructed from magnetic measurements [202], because the neoclassical current evolved more slowly than the reconstructed one. More recently, the recovery behaviour of T_i has also been investigated in D plasmas, where impurities were puffed for fast T_i measurements [165]. It has also been found that the T_i pedestal recovers on a similar timescale as the n_e pedestal.

5.4.3 Structure of pre-ELM magnetic fluctuations

As it can be seen in the ELM synchronised frequency histograms there is much less medium and high frequency magnetic activity (100 kHz to 400 kHz, figure 5.13a) than in the investigated cases of D and H. Also the frequency of an acting core mode is lower in ^{4}He. Both are indications that the rotation velocities are lower in this case. The low core rotation can be explained by the lower NBI momentum input than e.g. in H (less NBI sources), whereas a lower poloidal edge rotation can be explained by a change in the $\nabla p_\mathrm{i}/Zen_\mathrm{i}$ term.

During Δt_{n_e} a phase with very low magnetic activity is present, similar to the one observed in the hydrogenic plasmas. Later on in the ELM cycle well defined frequency bands develop, which last till the onset of the next ELM.

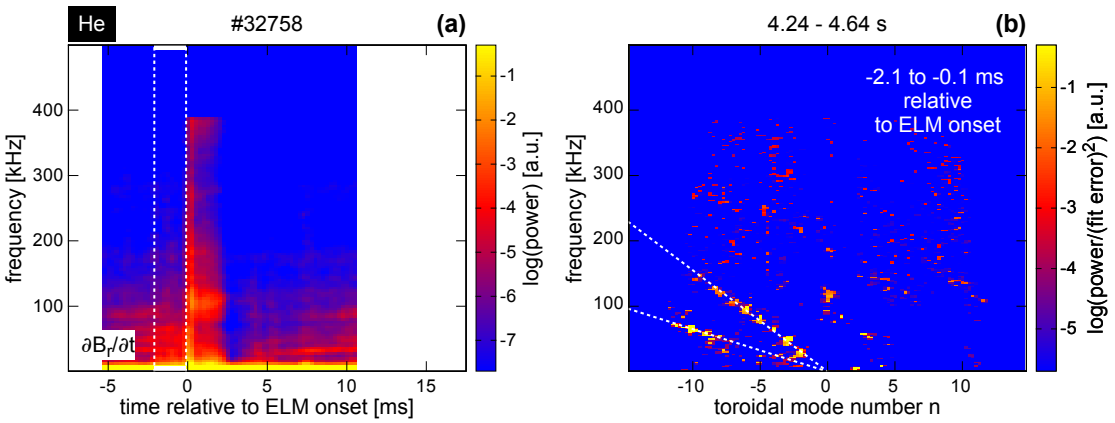

Figure 5.13: Comparison of the magnetic fluctuations: ELM synchronised (a) frequency and (b) toroidal mode number histograms (determined between $-2.1\,\mathrm{ms}$ and $-0.1\,\mathrm{ms}$ relative to the ELM onset) for ^{4}He. The white dashed lines in (a) indicate the time interval of the mode number determination and in (b) the two mode branches with different propagation velocity. In comparison to D and H similar magnetic activity and n are found at lower detected frequencies owing to the lower propagation velocity relative to the lab frame. Figure already published in [44].

Analysing the pre-ELM (determined between $-2.1\,\mathrm{ms}$ and $-0.1\,\mathrm{ms}$ relative to the ELM onset) toroidal structure (figure 5.13b), two mode branches are found, similar to the one in D and H. The contributing mode numbers are well defined and in the range of n -2 to -11. As indicated by the white dashed lines the propagation velocities relative to the lab frame are lower than in the hydrogenic plasmas. This is in line with a lower rotation of the plasma owing to the previously discussed arguments. In summary, clear evidence is found that the same kind of instabilities as in hydrogenic plasmas are also present and dominant in the pedestal of ^{4}He plasmas with ELMs.

5.5 Summary and interpretation of the observations

Pedestal matching experiments between D, H and ^{4}He plasmas were performed to compare the pedestal structure, stability and inter-ELM evolution. The overall behaviour of these discharges was different in the sense that different energy as well as particle confinement is observed. E.g. in H due to lower particle confinement a shallower ∇n_e is found and a factor of approximately 2 higher heat flux across the pedestal is estimated in comparison to D. In ^{4}He due to the higher plasma dilution (lower n_i)

the W_{MHD} is roughly 20 % lower than for the D reference with similar pedestal n_{e} and T_{e} profiles.

All investigated pedestals are found to be consistent with linear PB stability analysis. The occurrence of an ELM-free phase in ^{4}He can also be explained by PB theory. The analyses of the inter-ELM n_{e} and T_{e} profile evolutions showed similar sequences in the pedestal recovery for D, H and ^{4}He. After the ELM crash the n_{e} pedestal recovers first, then the T_{e} pedestal recovers. In ^{4}He detailed studies on the inter-ELM recovery of the T_{i} pedestal were made. These show that T_{i} recovers on the same timescale as n_{e}, as suggested previously [202] and also observed in D plasmas with impurity seeding [165]. The magnetic activity throughout the ELM cycle is comparable in all investigated main ions species. After the ELM, which causes large magnetic fluctuations a phase with very low activity is found. Its duration corresponds to the recovery of the n_{e} pedestal. Later on the magnetic fluctuations set in and continue till the next ELM crash. These have similar n in the range of -3 to -8 in all presented cases. When the pedestals of n_{e} and T_{e} are recovered, fluctuations with n in the region of -11 set in, which are connected to the clamping of $\max(-\nabla p_{\mathrm{e}})$. Furthermore, two mode branches with different propagation velocities relative to the lab frame can be identified. Comparing the different main ion species, differences in the $E \times B$ flow due to changes in the edge profiles can explain the different propagation velocity relative to the lab frame.

In conclusion, the experimental observations suggest that independently of main ion species, the pedestal stability can be sufficiently described by PB theory. Furthermore, the inter-ELM pedestal recovery behaviour and the identified magnetic structures point into the direction that the dominant mechanisms in the pedestal are acting independently of the main ion species.

6 | Divertor, SOL and pedestal evolution

Parts of the following chapter are in preparation for publication in [45].

Since ELMs cause a quasi-periodical collapse of ETB and pedestal, they lead to an enhanced particle and heat transport across the separatrix into the SOL. By conduction along the magnetic field lines most of the expelled plasma is guided towards the divertor and depending on the divertor state either dumped on the target plates (attached) or dissipated in a neutral gas cushion above the target plate (detached) [203]. In a future fusion power plant (DEMO) a stable detached divertor operation is required [204]. For this reason the impact of transient particle and heat fluxes on the divertor condition is crucial.

At the onset of divertor detachment a region of high plasma density is formed at the entrance of the inner divertor that can extend up to the HFS midplane. This is also named the high field side high density region (HFSHD) [205] and originates from drift-caused neutral particle accumulation in front of the inner target that is ionised by the SOL plasma [206]. Since the density of the HFSHD is typically an order of magnitude larger than the density at the separatrix, it also affects the pedestal density profile and therefore, the pedestal stability with respect to ELM crashes [207]. Further, the divertor conditions and the HFSHD evolve throughout the ELM cycle, which can also impact the dynamics of the inter-ELM pedestal evolution.

Previous work at ASDEX Upgrade has identified the evolution of the outer divertor into a high recycling regime after an ELM crash [208, 209], that is connected to large plasma densities in front of the target and high D_α emission. Similar observations have been made at JET and it is suggested that the enhanced D_α emission is related to outgassing of D, which was implanted by the ELM crash [210]. However, this strong change of recycling cannot be reproduced by diffusion-trapping modelling of hydrogen in tungsten under pulsed, ELM-like plasma loads [211]. On DIII-D two dimensional modelling of the ELM cycle reproduced a phase after the ELM crash with relatively dense and cold divertor plasma but without increased D_α emission [212].

In the following, the evolution of the divertor, SOL and pedestal for a typical ELM cycle is characterised and connected. The recovery of the pedestal n_e profile is corre-

lated with the magnetic activity in the pedestal and the particle transport across the pedestal is simply estimated by applying the continuity equation. Section 6.1 introduces the investigated plasma scenario and the large set of plasma edge and divertor diagnostics used in this study. In section 6.2 the dynamics throughout the ELM cycle at the inner and outer divertor target as well as the HFS and LFS midplane are compared. The measured pedestal n_e profiles are used to estimate the particle flux across the pedestal in section 6.3. This rough approximation suggests that the particle flux across the edge is strongly reduced during the recovery of ∇n_e and increases afterwards (section 6.3.2).

6.1 Investigated plasma scenario and utilised diagnostics

For the purpose of this study a plasma discharge with relatively low ELM frequency of approximately 70 Hz is used so that the phases of the pedestal recovery are sufficiently long and well discriminable. The discharge was performed with a standard magnetic configuration of plasma current I_p=1.0 MA and toroidal magnetic field B_t=−2.5 T (negative sign stands for opposite direction to I_p) in LSN. During the analysed discharge phase a P_{heat} of 5.3 MW by neutral beam injection and electron cyclotron resonance heating was applied. Further a moderate neutral gas puff of $11.3 \cdot 10^{21}\,\mathrm{e\,s^{-1}}$ was injected from valves that are located in the lower divertor.

Chapter 3 and figure 3.1 give an overview of the plasma diagnostics, which are utilised within this study. The lower divertor of ASDEX Upgrade (figure 3.1b) is equipped with a set of triple Langmuir probes (LPs) [157], which are used to measure n_e and T_e at the divertor target (see section 3.5). A volume integrated spectroscopic detection of the D_α emission for the inner and outer divertor is installed. The D_α emission intensity is a convolution of the divertor neutral density, the plasma density and the plasma temperature. Further shunts are attached to several tiles of the inner and outer divertor that measure the thermoelectric current in the SOL [117].

The midplane profiles of n_e at the HFS and LFS are measured by two O-mode reflectometers (see section 3.2). Slightly above the LFS midplane a lithium beam (LIB) diagnostic is installed, which measures the n_e profile up to the pedestal top (see section 3.1). This enables on the one hand a comparison of the LFS SOL n_e profile by two independent measurements and on the other hand a connection of the pedestal and SOL n_e. Main chamber neutral fluxes are measured by a pressure gauge (M 17), that is located at the LFS midplane and oriented towards the plasma [118]. To detect the magnetic signature a set of toroidally distributed ballooning coils are mounted at the LFS midplane [119].

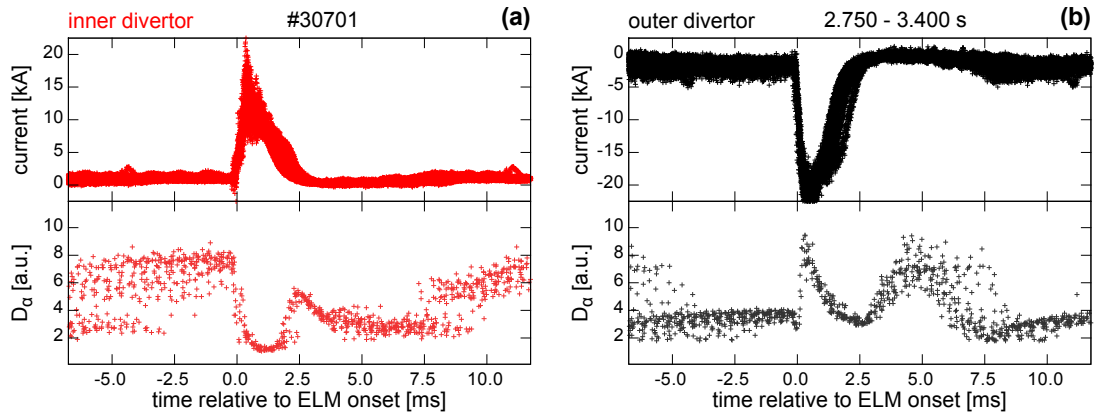

Figure 6.1: ELM synchronised evolution of the SOL current and D_α emission at the (a) inner and (b) outer divertor target: The SOL current flows from the outer to the inner target. The D_α emission at the outer target increases approximately 2.5 ms after ELM onset a second time, which is not connected to another ELM crash but to high neutral recycling.

6.2 Inter-ELM evolution of the SOL

The following section characterises the divertor plasma throughout the ELM cycle as well as the dynamics of SOL n_e at inner and outer midplane, which are clearly connected with the divertor evolution.

6.2.1 Divertor conditions in the ELM cycle

Figure 6.1 presents ELM synchronised time traces of the SOL current measurements and the D_α emission at the inner and outer divertor target. The SOL current consists of PS current contributions, ohmically driven currents and thermoelectric currents, that originate from temperature differences of the inner and outer divertor plasma [117]. In a standard ASDEX Upgrade magnetic field configuration, like the investigated plasma was performed in, the current flows through the plasma SOL from the outer to the inner target. For this reason the measurements in the inner and outer targets have opposite signs. The ELM crash appears as large burst in the SOL current and has a duration of approximately 2 ms. Then a period of reduced SOL current is observed from 2 ms to 7 ms relative to the ELM onset especially at the outer target. During this phase the D_α emission at the outer target has a second peak that is of similar magnitude as the observed emission at the ELM crash. This is characteristic for a regime of high recycling [208]. For times larger than 7 ms after the ELM onset the D_α emission lowers to its pre-ELM values, indicating an attached divertor plasma

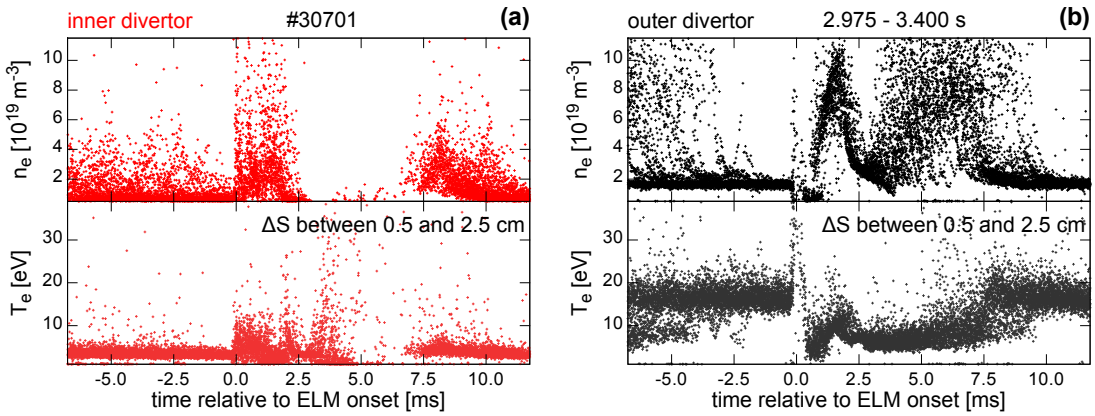

Figure 6.2: n_e and T_e at the (a) inner and (b) outer divertor target: ELM synchronised evolution and spatially superimposed triple LP measurements between 0.5 cm and 2.5 cm outside the strike line (ΔS). While the inner divertor is partially detached in the inter-ELM period, the plasma at the outer target is relatively hot and T_e decreases in the period of high recycling, while n_e increases.

as it will be discussed later. At the inner divertor target the D_α evolves differently than at the outer divertor. The large pre-ELM D_α emission indicates that neutral radiation is already present in front of the target and the inner divertor is at least partially detached. During the ELM crash the D_α emission is reduced, which can be interpreted as re-attachment of the inner divertor target since a larger amount of hot particles flows to the divertor. After the ELM crash the D_α emission increases (2.0 ms to 2.5 ms relative to the ELM onset) indicating a post-ELM detachment of the inner target. Then D_α decreases slightly during the high recycling period of the outer divertor. In this phase the inner target fully-detaches and the D_α radiation front moves upwards towards the midplane and therefore, out of the lines of sight of the D_α detector. Approximately 7.5 ms relative to the ELM onset the D_α emission jumps to pre-ELM values indicating, that the radiation front moves quickly towards the target again. A more detailed view on the state of the inner and outer divertor targets throughout the ELM cycle is given by divertor LP measurements of n_e and T_e. These are presented in Figure 6.2 as ELM synchronised plots. The data is superimposed for locations between 0.5 cm and 2.5 cm outside of the strike line position (ΔS) in the SOL. Before the ELM onset the inner divertor is partially detached since T_e is below 5 eV. During the ELM crash T_e and n_e are increasing, indicating re-attachment of the inner divertor. After the ELM (between 2.5 ms and 7.0 ms relative to the ELM onset) n_e at the target fully vanishes, which is an indication for full detachment. At the outer divertor target the plasma is attached in the pre-ELM phase and T_e is roughly 15 eV to 20 eV. When the ELM crash starts (between 0.0 ms and 0.5 ms relative to the ELM onset) a pulse of hot plasma ('electron heat pulse'; T_e larger than 30 eV)

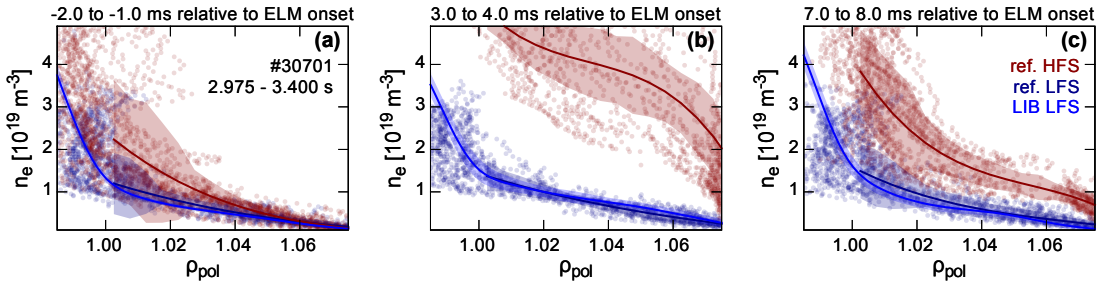

Figure 6.3: Comparison of the HFS and LFS n_e profiles from reflectometry (ref.) and lithium beam (LIB): (a) pre-ELM (averaged between −2.0 ms and −1.0 ms relative to ELM onset), (b) post-ELM (averaged between 3.0 ms and 4.0 ms relative to ELM onset) and (c) far post-ELM (superimposed between 7.0 ms and 8.0 ms relative to ELM onset) profiles. The LFS n_e profiles of reflectometry and LIB agree very well. When the HFS-LFS asymmetry is largest, the HFSHD extends up to the midplane and radially outwards to the wall of the inner heat shield.

is observed, that is followed by a phase of larger n_e (0.5 ms to 2.0 ms relative to the ELM onset). After the ELM crash, the plasma T_e at the outer divertor target is approximately 5 eV to 10 eV during the period of high recycling. It is accompanied by relatively high plasma n_e at the outer target, which reaches a similar magnitude as the n_e peak caused by the ELM crash.

6.2.2 SOL electron density evolution at the midplane

To connect the divertor conditions with the midplane, SOL n_e profiles at the HFS and LFS are compared. These are measured by reflectometry and at the LFS additionally by the LIB. ELM synchronised profiles are presented for three different time intervals relative to the ELM onset in figures 6.3a to 6.3c. The superimposed reflectometry profiles, which were measured in the corresponding time interval relative to the ELM onset, are fitted by a spline curve. The LFS reflectometry profiles are shown in dark blue, whereas the HFS profiles are shown in dark red. For comparison the LIB n_e profiles, which are also averaged in the corresponding time interval relative to the ELM onset, are shown in blue. Both independent LFS diagnostics measure similar SOL n_e profiles in all time intervals relative to the ELM onset. In the pre-ELM phase the HFS and LFS profiles are similar and below $2.0 \cdot 10^{19}\,\mathrm{m}^{-3}$. A large asymmetry is found in the post-ELM phase in figure 6.3b, when the inner divertor target is fully detached and the HFSHD is present, which in this case reaches up to the midplane causing the strong difference of the HFS and LFS SOL n_e profiles. This asymmetry decreases, when the HFSHD is reduced as seen in figure 6.3c.

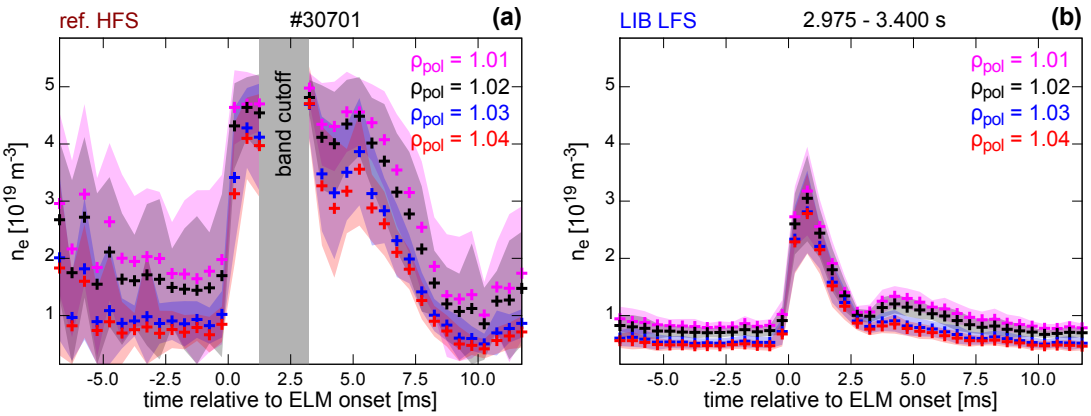

Figure 6.4: Comparison of the inter-ELM (a) HFS and (b) LFS SOL n_e evolution: n_e at four different radial positions (ρ_{pol}) from near (1.01) to far (1.04) SOL. After the ELM crash a strong asymmetry between LFS and HFS SOL n_e is observed, which timescale corresponds to the appearance of the HFSHD that probably extends up to the LFS, where the SOL density shoulder appears.

The dynamics of the SOL n_e profiles for HFS and LFS are presented in figure 6.4. On four radial positions from near to far SOL, n_e is tracked. After the ELM crash the HFS n_e at the tracked positions is larger than the cut-off n_e for the reflectometer. The decay of the HFSHD has a similar timescale as the measurements in the divertor would suggest. During the presence of the high recycling regime in the outer divertor also an increased n_e in the LFS SOL is observed. This was previously named the SOL n_e shoulder and its formation is suggested to be associated to a change of the SOL transport regime [199].

6.3 Inter-ELM pedestal evolution

The inter-ELM evolution of the SOL and divertor plasma is closely related to the inter-ELM evolution of the pedestal, since SOL and divertor represent in some sense the boundary of the pedestal. It was previously discussed that the inter-ELM pedestal evolution of n_e and T_e profiles at ASDEX Upgrade has different timescales (chapters 4 and 5). First, the $\max(-\nabla n_e)$ is established, then the $\max(-\nabla T_e)$ builds up. Already several milliseconds before the ELM onset, the pedestal gradients are clamped. This period is accompanied by the onset of high frequency magnetic fluctuations, which have n in the region of -11 [43, 119]. In the following the recovery of the n_e pedestal will be connected to the magnetic activity and the neutral fluxes at the LFS midplane.

6.3.1 Pedestal recovery and LFS magnetic activity

The recovery of the n_e pedestal usually takes of the order of less than 2 ms. This short timescale indicates that lost particles due to the ELM are immediately replaced after the ELM crash. A larger neutral particle source caused by neutralisation of the plasma, which is expelled by the ELM crash, the appearance of the HFSHD or a change of the particle transport in the pedestal are possible reasons to explain the short recovery timescale of the n_e pedestal. Figure 6.5 presents ELM synchronised frequency histograms of $\partial B_r/\partial t$ at the LFS midplane, LFS midplane neutral fluxes measured by the manometer M 17 (see figure 3.1a), which were temporally shifted by -1.5 ms, n_e and ∇n_e at four radial positions. The temporal shift of the neutral fluxes was applied to align the increase of the fluxes due to the ELM crash with the actual ELM onset. Because of the finite volume and the small aperture of the manometer, an intrinsic response delay of roughly -1.5 ms is estimated, in which the gas streams into the manometer and fills its volume.

The radial magnetic field fluctuations ($\partial B_r/\partial t$) at the LFS midplane (figure 6.5a) shows low activity between 1.5 ms and 3.0 ms relative to the ELM onset for all frequencies. During this period the n_e pedestal and, respectively, ∇n_e in the steep gradient region recover (figure 6.5d). Remarkably, the steepening of the gradient is not solely attributed to a rise of the n_e pedestal but also related to a n_e decrease in the confined region close to the separatrix (figure 6.5c), i.e. at $\rho_{pol} = 0.99$. This is an indication for a reduced particle flux across the pedestal region. The neutral fluxes at the LFS midplane (figure 6.5b) stay high while the n_e pedestal recovers. It is unknown, whether in addition to the time delay, also a temporal smearing of the measured neutral fluxes occurs, which would lead to a longer detected period of higher neutral fluxes. However, if present a similar timescale as the one of the delay could be assumed, which would be in the region of 1 ms. An indication that the fast n_e pedestal recovery is not directly linked to the evolution of the source is that between 3.0 ms and 5.0 ms relative to the ELM onset, the neutral flux slowly decays. In this period neither ∇n_e nor the pedestal top n_e evolution are affected by this decrease of the source. For this reason the n_e pedestal recovery is not directly related to the evolution of the source, especially the prompt saturation of the $\max(-\nabla n_e)$ at 3.0 ms relative to the ELM onset. This will be studied in detail in section 6.3.2. Temporally correlated to the stagnation of the n_e pedestal recovery is the onset of medium frequency fluctuations in the range of 30 kHz to 150 kHz approximately 3 ms relative to the ELM onset. These fluctuations could cause an additional particle flux across the pedestal, leading to the saturation of $\max(-\nabla n_e)$ and causing the high recycling phase in the outer divertor. Roughly 7.5 ms after the ELM onset the $\max(-\nabla T_e)$ is clamped and high frequency fluctuations set in. The period between 3.0 ms and 7.5 ms is also the timescale of the high recycling in the outer divertor and the HFSHD is present. These two effects are not temporally correlated to the establishment of ∇n_e and the fast recovery of the

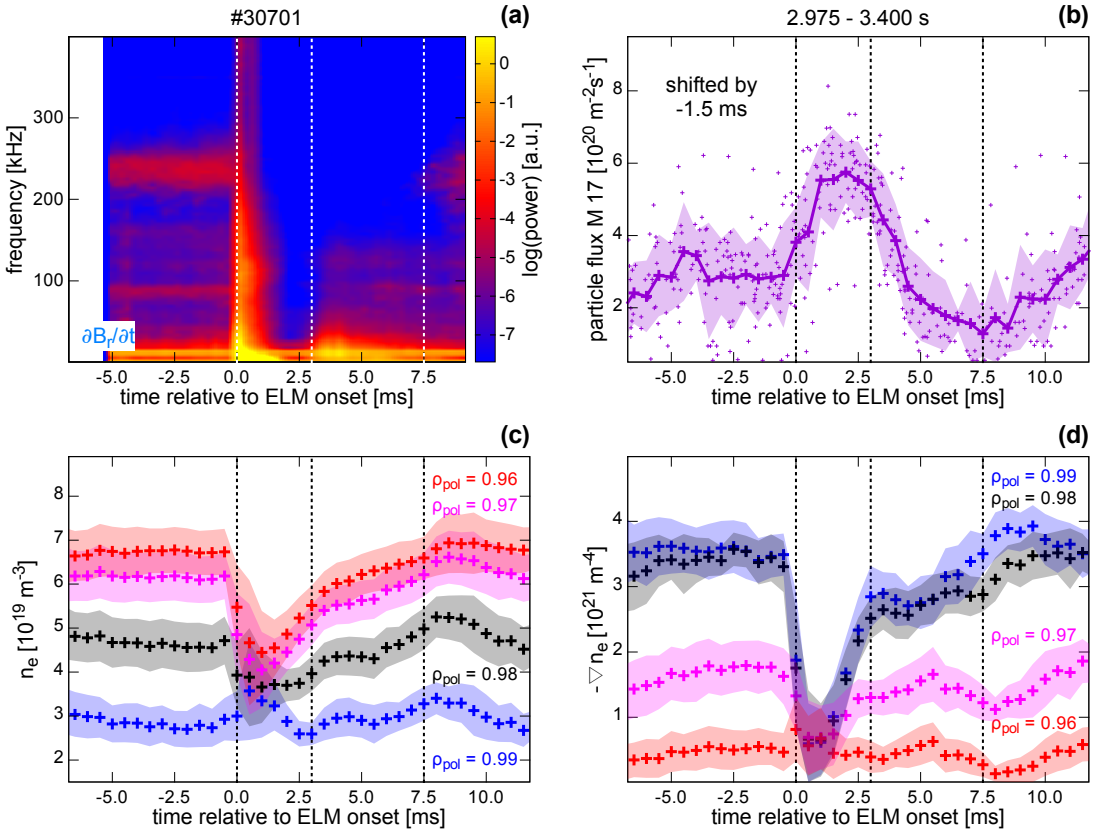

Figure 6.5: Correlating the ELM synchronised n_e pedestal recovery with the magnetic activity and the main chamber neutral fluxes: (a) ELM synchronised frequency histogram of $\partial B_r/\partial t$ measured at the LFS midplane, (b) LFS midplane neutral fluxes (shifted by -1.5 ms), (c) n_e and (d) ∇n_e at four radial positions (ρ_{pol}) in the confined plasma from the pedestal top (0.96) to the steep gradient region (0.99). During the recovery of ∇n_e in the steep gradient region (between 1.5 ms and 3.0 ms) a phase of low magnetic activity is found. During this period also the particle flux at the LFS main chamber is enhanced, well before the D_α emission and n_e increase in the outer divertor and the appearance of the high recycling regime.

n_e pedestal, which already takes place before. The experimental data suggest that a reduced particle flux is connected to the fast recovery of the n_e pedestal or vice versa an increased particle flux across the pedestal causes the stagnation of the n_e recovery as well as the second D_α peak in the divertor.

6.3.2 Estimation of the particle flux across the pedestal

A simple estimation of the particle flux (Γ) across the pedestal can be done by applying the continuity equation:

$$\frac{\partial n_e}{\partial t} = \frac{\partial \Gamma}{\partial V} + \alpha S_i. \tag{6.1}$$

The particle flux into the volume ($\partial\Gamma/\partial V$) and ionisation source (S_i) including the proportionality factor (α) determine the temporal evolution of electron density recovery rate ($\partial n_e/\partial t$). The n_e evolution at certain positions from figure 6.5c can be used to determine $\partial n_e/\partial t$. Figure 6.6a presents $\partial n_e/\partial t$ at four radial positions in the pedestal region. S_i profiles are determined by the 1.5-D neutral transport code KN1D [213]. Of course a spatial 1-D treatment of the neutral distribution is a very simplistic picture in a toroidal plasma. But the LFS main chamber has been found to be the main region for neutral fuelling [206], especially when the HFSHD is present. The neutral flux at the LFS midplane as shown in figure 6.5b was used as condition at the wall and the n_e profiles of the LIB diagnostic, which are measured at the LFS served as input. Since there are no midplane SOL T_e measurements with the required temporal resolution available, the SOL T_e was parametrised by an exponential decay with a characteristic decay length according to the H-mode scaling for ASDEX Upgrade [214]. With this procedure a possible variation of the SOL T_e throughout the ELM cycle is not considered. Further, the SOL T_i is assumed to be equal to T_e, which is reasonable in the sense that the cross sections of ion-neutral collisions do not have strong dependencies on T_i in the relevant temperature range.

The evolution of the S_i profiles is presented in figure 6.6b. They are mainly determined by the evolution of the midplane neutral fluxes, which strongly increase after the ELM crash between 2.5 ms and 6.0 ms relative to the ELM onset. When the SOL n_e is higher, e.g. during and immediately after the ELM, only few neutrals can penetrate into the confined plasma region, leading to a reduction of S_i.

To adapt the S_i profiles from the 1-D simulation to experimental conditions, a single profile of α is utilised for the whole ELM cycle. In the pre-ELM phase between -4 ms and -1 ms relative to the ELM onset α can be determined since $\partial n_e/\partial t$ is close to zero and the pedestal gradients are clamped. Therefore, Γ can be chosen in such a way that the diffusion coefficient (D) is in agreement with the ones that are observed

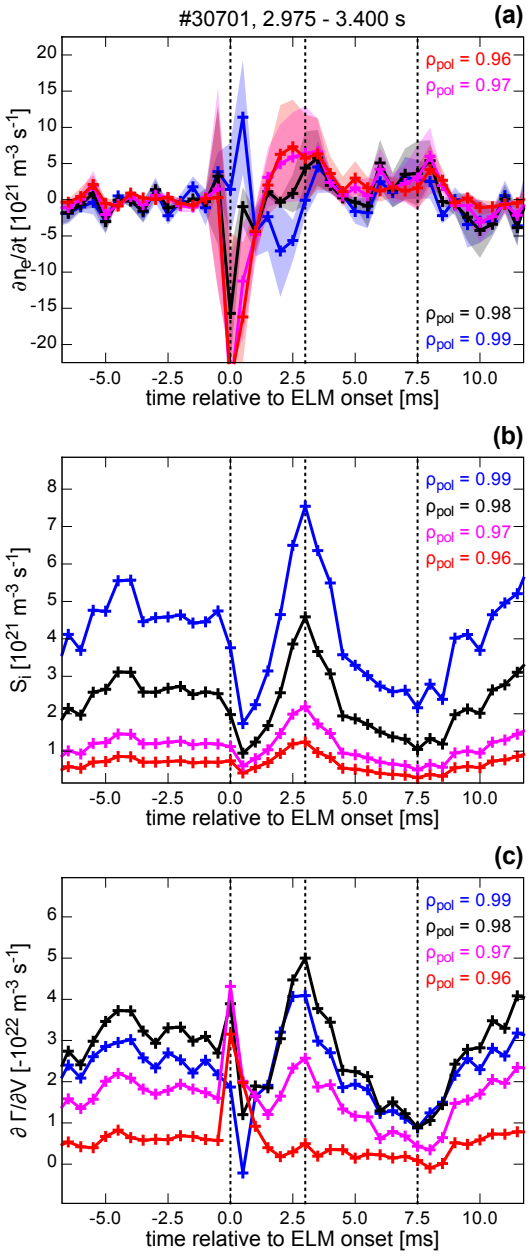

Figure 6.6: Estimation of the particle flux across the pedestal: (a) electron density recovery rate ($\partial n_e/\partial t$), (b) ionisation source (S_i) and (c) estimated particle flux into the volume ($\partial\Gamma/\partial V$) at four radial positions (ρ_{pol}) in the pedestal (pedestal top (0.96) to the steep gradient region (0.99). After the ELM, owing to the increasing S_i also the outward particle flux across the edge increases. This takes place in a similar phase, when the magnetic fluctuations at the LFS midplane set in.

in H-mode [118]:

$$\Gamma = -\frac{\partial V}{\partial \rho_{\mathrm{pol}}} \langle (\nabla \rho_{\mathrm{pol}})^2 \rangle D \frac{\partial n_{\mathrm{e}}}{\partial \rho_{\mathrm{pol}}}. \tag{6.2}$$

The assumption of solely diffusive transport in the steep gradient region is rather rough and based on previous results of modelling the L-H transition [215]. Here, a small pinch velocity could not be excluded, but the transport at the edge was dominantly diffusive. Nevertheless, within this work the assumption of diffusive transport is solely used to determine α. A radial dependent D profile ranging from $0.10\,\mathrm{m^2\,s^{-1}}$ at the separatrix to $0.25\,\mathrm{m^2\,s^{-1}}$ at the pedestal top, assumed between $-4\,\mathrm{ms}$ and $-1\,\mathrm{ms}$ relative to the ELM onset, gives a continuous profile of α.

The temporal evolution of $\partial\Gamma/\partial V$, shown in figure 6.6c, is determined from the continuity equation (equation (6.1)) at every timestep. The ELM onset leads to an outward burst of plasma particles. After the ELM crash the particle flux across the pedestal is strongly reduced. During this period $\partial n_{\mathrm{e}}/\partial t$ is largest for the pedestal top and no magnetic activity is present in figure 6.5a. When S_{i} increases after the ELM crash, then also $\partial\Gamma/\partial V$ goes up since $\partial n_{\mathrm{e}}/\partial t$ is already reduced. This is another indication that the fast recovery of the n_{e} pedestal is more related to a reduced particle flux in the gradient region than to an increased particle source. When S_{i} decreases roughly $5.0\,\mathrm{ms}$ relative to the ELM onset, $\partial\Gamma/\partial V$ is also reduced, indicating the strong coupling between these quantities. Since the magnetic activity in the medium frequency range is only slightly reduced in this period, the reduction of $\partial\Gamma/\partial V$ cannot be related to a change of turbulent transport in the pedestal.

When attributing Γ to D then the behaviour of the n_{e} pedestal recovery becomes more visible. Figure 6.7 shows the evolution of D in the ELM cycle. During the ELM crash ∇n_{e} is flattened, therefore D increases especially at positions far inside the separatrix. The reduced Γ after the ELM crash is reflected in a lower D at the pedestal top. When the S_{i} is large, between $2.5\,\mathrm{ms}$ and $5.0\,\mathrm{ms}$ relative to the ELM onset a larger D is required since ∇n_{e} does not change. After the recovery of the T_{e} pedestal and the onset of the high frequency fluctuations, D increases again.

6.4 Discussion

The inter-ELM dynamics in the divertor, SOL and in the pedestal and their corresponding timescales can be summarised in a consistent picture. The phases of the n_{e} pedestal recovery can be well related to the magnetic activity in the pedestal and to the conditions in the divertor and SOL. The ELM crash expels heat and particles to the SOL, causing a re-attachment of the inner divertor target. During the recovery of ∇n_{e} the magnetic activity in the pedestal is reduced significantly. Further, the

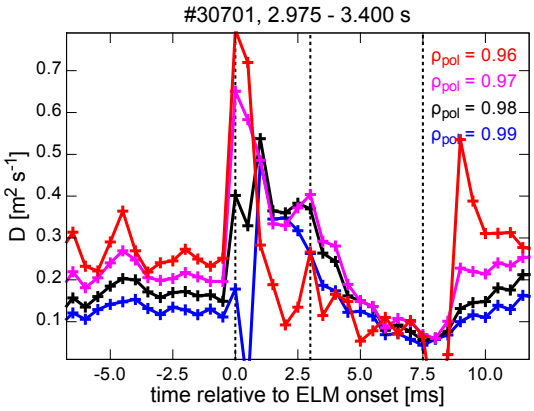

Figure 6.7: Estimated particle diffusion coefficient (D): Determined at four radial positions (ρ_{pol}) from pedestal top (0.96) to the steep gradient region (0.99). After the ELM crash D drops strongly during the phase of the n_{e} pedestal recovery and simultaneously increases with Γ.

corresponding timescale of the ∇n_{e} recovery is only reproduced by the change in the magnetic activity. When ∇n_{e} is recovered, approximately 3 ms relative to the ELM onset, medium frequency fluctuations between 30 kHz and 150 kHz set in. Further, the LFS SOL n_{e} increases, which is accompanied by high recycling in the outer divertor and full detachment of the inner divertor target and the HFSHD appears. In the following, $\partial n_{\mathrm{e}}/\partial t$ decreases and $\max(-\nabla n_{\mathrm{e}})$ evolves much more slowly than directly after the ELM crash. Because S_{i} is high in this period, Γ through the edge is also large to balance it. When S_{i} decreases, also Γ does so. High frequency magnetic fluctuations (around 240 kHz) set in approximately 7.5 ms relative to the ELM onset. In this phase the pedestal ∇n_{e} as well as the ∇T_{e} are clamped, the latter suggests an additional heat flux towards the SOL. The recycling in the outer divertor is reduced because no additional neutrals are provided for ionisation, leading to a hotter SOL plasma, which is related to the T_{e} increase at the outer target. Further, the HFSHD is reduced and the inner divertor moves to a partially detached state. In summary, the dynamics in the divertor and SOL are well connected with and likely caused by the evolution of the pedestal, because changes in the heat and particle fluxes across the pedestal introduce transient changes to the SOL plasma.

7 | Shaping and ELM frequency bands

In section 2.1.3, it was already discussed that higher δ and κ are beneficial for the plasma edge stability, enabling steeper profile gradients and higher pedestal pressure. The positive impact of δ on the pedestal height has also been experimentally confirmed in several tokamak experiments [216–218]. It has been found that higher δ is connected to an increase of the n_e [219, 220], which increases the edge pressure. This dependency could be biased by changes of the strikepoint positions in the active divertor, which were necessary to vary δ, because they can impact on the neutral pumping efficiency and divertor conditions. For this reason, the presented experiments aimed for a variation of δ without changing the strike- and X-point position in the active divertor.

Additionally to the changes in the pedestal structure, a variation of δ impacts on the ELM behaviour, mainly f_{ELM} [39]. In general, Type-I ELM behaviour, respectively f_{ELM} and ELM duration, can be influenced by several discharge conditions, e.g. impurity seeding [200, 221, 222] or neutral influx like external gas puff [167, 223]. At ASDEX Upgrade two separated f_{ELM} bands have been observed [102, 224]. Similar observations have been also made on the Korea Superconducting Tokamak Advanced Research (KSTAR) experiment [225], here, referred to as secondary ELM peaks, and at Tokamak à configuration variable (TCV) [226].

In the following, an experiment is introduced that was performed to compare H-mode plasma discharges with a variation of δ, P_{heat} and gas puff (section 7.1). In section 7.2 the general discharge behaviour is described, emphasising on the impact of δ on f_{ELM}, pedestal and W_{MHD}. The stabilising effect of δ on the pedestal is presented in section 7.3 and the inter-ELM evolution for selected cases of δ are shown. In the conducted discharges several phases with two distinct f_{ELM} bands occurred. These are analysed in section 7.4 giving insight that the 'fast' ELM cycle (higher f_{ELM} band) is ended by an ELM crash, which occurs at an inward shifted n_e profile with shallower ∇n_e. In section 7.5 the main results are recapped, showing that enlarged δ increases the pedestal top n_e and the pedestal stability towards higher ∇p_e. At higher δ, f_{ELM} decreases because the inter-ELM recovery phases are prolonged, especially the pre-ELM phase with clamped pedestal gradients [43].

7.1 Conducted experiment

To perform a δ scan without changing the divertor conditions in the active divertor, a LSN plasma scenario was chosen and only δ_{up} was intended to be varied. The achievable range of δ is limited by operational boundaries on maximum coil currents at ASDEX Upgrade. Further, increasing δ increases the n_{e} pedestal, which can lead to n_{e} above the ECE cut-off and therefore, limiting the diagnostic capabilities. For these reasons, a plasma scenario with reduced I_{p} in contrast to the ASDEX Upgrade standard configuration was chosen. The main parameters were I_{p}= 0.8 MA and B_{t}= −2.5 T (negative sign stands for opposite direction to I_{p}). This gives an enlarged q at the edge in comparison to the I_{p} 1.0 MA standard configuration, lowers the required poloidal coil currents for shaping by roughly 20 % and extends the achievable discharge length because of less flux consumption of the transformer coil.

7.1.1 Shape comparison and varied parameters

Usually, a variation in δ by solely changing the shaping coil currents also impacts on κ, which influences the stability. For this reason it was emphasised to adjust the shaping accordingly that only small variations of κ occur. Further, changes of P_{heat} and correspondingly W_{MHD} impact on the Shafranov shift and therefore, modify the plasma shape. To avoid this, the shaping coil currents were adjusted, such that δ or κ remained unchanged, when steps in P_{heat} were performed.

The general experimental procedure was to establish a plasma scenario at fixed δ and then vary P_{heat} and neutral gas puff. In the following, δ was varied from discharge to discharge. By this procedure the achieved range of δ was between 0.20 and 0.45

Figure 7.1 presents a comparison of the plasma shapes for low (dark blue), medium (dark red) and high (orange) δ. In figure 7.1a it can be seen that at higher δ the SOL flux surfaces open up towards the upper divertor. A more detailed view on the separatrix and strikeline positions is presented in figure 7.1b. At low and medium delta a nice match of X-point and strikepoint locations were achieved, while the location of the plasma top was moved inwards resulting in an increased δ. For the high δ scenario a small change in the strikeline positions of the order of 3 cm had to be accepted. Since the targets in this region are usually well conditioned no impact on the divertor conditions or neutral recycling is expected by this change.

The accessed parameter range of P_{heat} and neutral gas puff is presented in figure 7.2. In principle two levels of P_{heat} were applied: A lower level between 6.5 MW and 7.5 MW (blue shaded area) and a higher level in the range from 11.5 MW to 13.0 MW (red

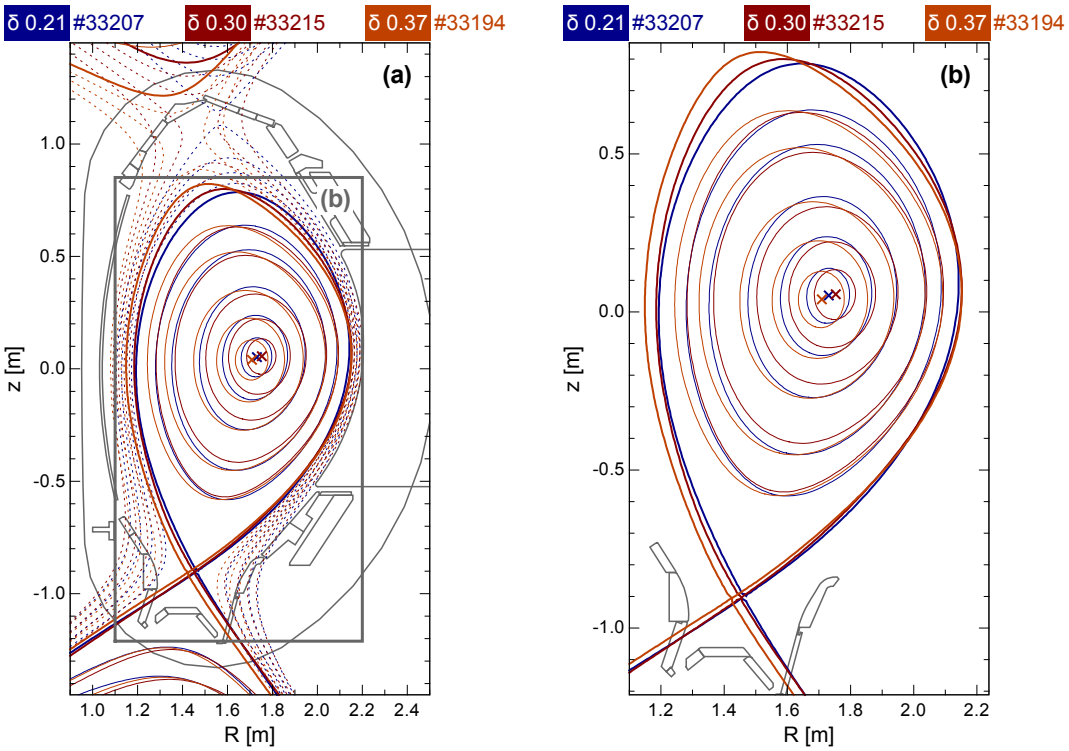

Figure 7.1: Comparison of the plasma shapes with varied δ_{up}: (a) Overview including SOL flux surfaces and (b) zoom-in to the separatrix location. At low (0.21, dark blue) and medium (0.30, dark red) δ the strike- and X-point locations are the same, whereas at high (0.37, orange) δ the strikelines have slightly different locations (shift at the outer target in the region of 3 cm) and δ_{low} is higher.

shaded area). The gas puff was varied between $0 \cdot 10^{21}\,\mathrm{e\,s^{-1}}$ and $10 \cdot 10^{21}\,\mathrm{e\,s^{-1}}$ in such a way that usually towards the end of the discharge it was turned off completely. A variation of κ in the region of $\pm 5\,\%$ was tolerated.

7.1.2 Performed data analysis

This study is mainly focused on the investigation of the pedestal structure for the electrons and inter-ELM dynamics. Therefore, the n_e and T_e profiles are evaluated using the IDA approach, which was introduced in section 3.8. The relative alignment of the n_e and T_e profiles was determined by cross comparison to the corresponding profiles of the TS diagnostic (see section 3.4). The quality of the raw data allows a profile evaluation with a temporal resolution of 250 µs.

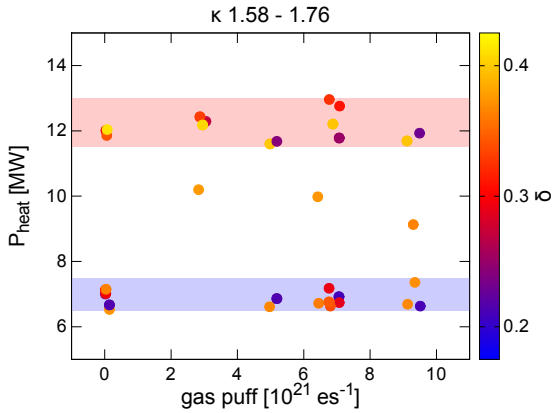

Figure 7.2: Varied control parameters: At mainly two levels of P_{heat} (6.5 MW to 7.5 MW, blue shaded area and 11.5 MW to 13.0 MW, red shaded area) a scan of the gas puff was performed for the different δ. A variation of κ in the region of $\pm 5\,\%$ was tolerated.

To reconstruct the plasma equilibria and corresponding quantities like, e.g. δ and κ, the IDE solver [72] was routinely applied, which implements a constraint on the pedestal pressure profile according to the one evaluated by IDA at the corresponding timepoint. The equilibria are reconstructed at a temporal resolution of 1 ms and also serve as input for the PB stability analyses, which are presented in sections 7.3.1 and 7.4.3.

7.2 General behaviour

In the following, the overall discharge behaviour at different δ with respect to the pedestal and ELM behaviour is discussed. As shown in figure 7.3, f_{ELM} decreases at higher δ, which is in agreement with previous observations [39]. In this figure only discharge intervals with a single f_{ELM} band are considered. In comparison to the lower level P_{heat} (points) f_{ELM} increases at the higher level of P_{heat} (triangles), which is characteristic for type-I ELMs (section 1.6). For both levels of P_{heat} the anti-correlation of f_{ELM} and δ is found. Scattering of the data could be related to the applied gas puff, which also impacts on f_{ELM}, however, no clear ordering in terms of gas puff can be seen (compare colour scale). In this comparison it is evident, that the impact of δ is much stronger than the one of the gas puff in the investigated parameter range.

Another general trend of previous studies is that n_{e} increases with δ [219]. This is also reproduced in the conducted experiment as shown in figure 7.4a. Here, the pre-ELM

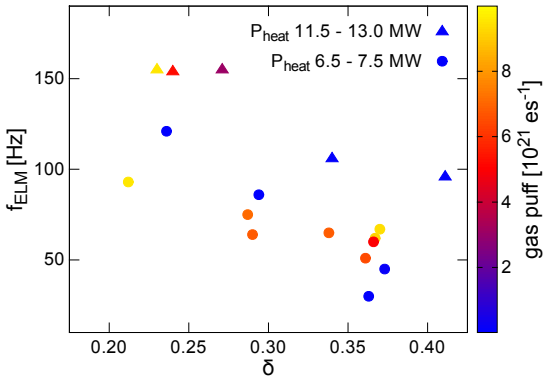

Figure 7.3: Dependency of f_{ELM} on δ: Only discharge intervals with a single f_{ELM} are considered. For high (triangles) and low (circles) P_{heat}, f_{ELM} decreases with δ. Additional scattering in the data might be due to the varying gas puff.

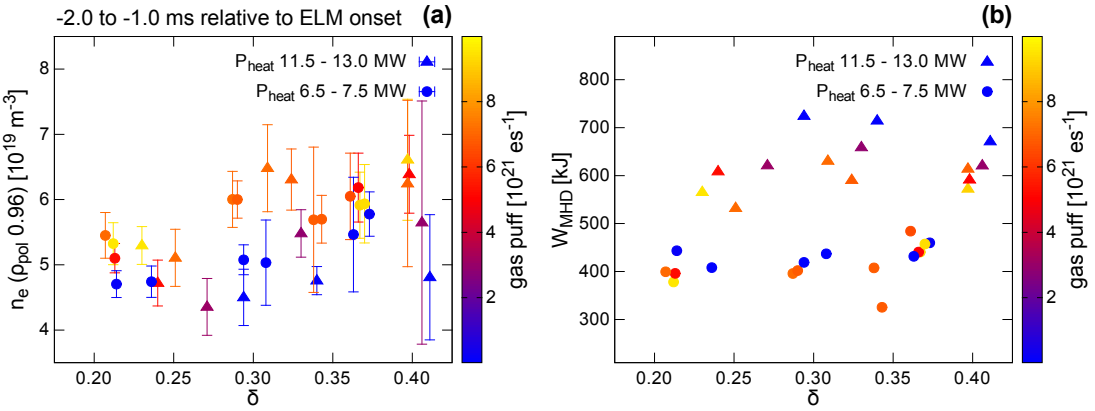

Figure 7.4: Impact of δ on: (a) the pedestal top n_{e} ($\rho_{\mathrm{pol}} = 0.96$) and (b) W_{MHD}. The pre-ELM pedestal top n_{e} increases with δ. As expected a separation of W_{MHD} for the different P_{heat} is found. At high P_{heat} a clear degradation of W_{MHD} can bee seen with increased gas puff (colour scale).

pedestal top n_e, averaged between $-2.0\,\mathrm{ms}$ and $-1.0\,\mathrm{ms}$ relative to the ELM onset and measured at $\rho_{pol} = 0.96$, is plotted in dependency of δ. At medium and high gas puff (orange and yellow markers) the trend is obvious, whereas at low gas puff (blue and purple markers) lower pedestal top n_e are measured at very large δ. This could be related to a reduction of the available amount of neutrals, which are required to 'fill-up' the n_e pedestal. No clear dependence of the pedestal top n_e on the two different P_{heat} (compare points and triangles) can be identified.

Comparing the pre-ELM W_{MHD} in dependency of δ (figure 7.4b) no trend can be observed. This indicates that at high δ, where the n_e is larger the core T_e profiles are reduced. However, within the presented study no deeper emphasis was taken on the core profiles as well as MHD behaviour. The most dominant impact on the W_{MHD} is given by P_{heat}, when comparing points and triangles. By applying approximately two times the P_{heat}, W_{MHD} is increased by roughly 50 % in the covered δ range.

At the higher level of P_{heat} a separation for the different applied gas puffs can be seen (colour scale). While at low gas puff (blue) the highest values of W_{MHD} are measured for all δ, the confinement is reduced at higher gas puff (red). This is in agreement with results from JET and ASDEX Upgrade, where a confinement degradation with high gas puff was observed [207, 227].

7.3 Impact of triangularity on the pedestal

As already discussed in section 7.2 the pedestal top n_e increases at higher δ. In the following the relation between pedestal structure and δ is analysed and compared to PB stability analysis.

7.3.1 Pedestal structure and stability

To investigate the impact of δ on the pedestal structure and stability, three different discharge intervals, performed at the lower level of P_{heat}, are investigated. These have a similar κ and also the applied gas puff is in the range of $5 \cdot 10^{21}\,\mathrm{e\,s^{-1}}$ to $7 \cdot 10^{21}\,\mathrm{e\,s^{-1}}$. The corresponding pre-ELM profiles of n_e, T_e and p_e are compared in figure 7.5. The three different discharge intervals correspond to the low (0.21, dark blue), medium (0.29, dark red) and high (0.37, orange) δ. The vertical lines correspond to different radial locations at which layers of n_e and T_e are tracked throughout the ELM cycle in figure 7.7.

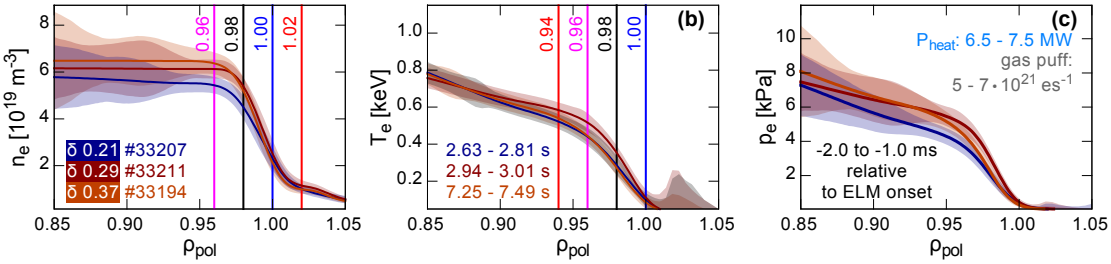

Figure 7.5: Comparison of the pre-ELM pedestal structure at low (0.21, dark blue), medium (0.29, dark red) and high (0.37, orange) δ: (a) n_e, (b) T_e and (c) p_e profile. At similar gas puff and P_{heat} the n_e pedestal systematically increases with δ, while T_e shows no clear trend. In combination, a higher and steeper p_e pedestal is found at higher δ.

When increasing δ the pedestal top n_e increases (see figure 7.5a) and so does ∇n_e too, meaning that the pedestal width is not strongly affected. The T_e profiles (figure 7.5b) of the low and high δ case overlay, however, the medium δ case has a higher pedestal top T_e and a steeper ∇T_e. The origin of this inconsistent T_e variation remains unknown, since no clear deviation in comparison to both other cases was identified. Probably changes in the core transport could be the cause. The combined p_e profiles (figure 7.5c) reflect the variation of n_e and T_e. In general, at higher δ a higher p_e pedestal and steeper ∇p_e is observed.

As theoretically predicted, the steeper gradients are achievable owing to the stabilising effect of higher δ (see section 2.1). The j-α diagram for the low and high δ case are presented in figure 7.6. Similar to the illustration in figure 2.3, at higher δ the PB boundary is extended towards larger $\langle j_{tor} \rangle$ and α_{max}. This allows the operational point to shift towards larger α_{max} as also shown in figure 7.5c. For this reason, the investigated pre-ELM pedestals are in agreement with PB theory. At high δ the distance between operational point and PB boundary increases in comparison to the low δ case, however, this is not a robust observation and usually within the uncertainties in the location of the PB boundary.

7.3.2 Inter-ELM evolution

The comparison of the inter-ELM pedestal development for the different δ can give insight on the changes in f_{ELM} and the temporal approach of the stability limit. Figure 7.7 presents the dynamics of the pedestal n_e and T_e profiles throughout the ELM cycle at low (figures 7.7a and 7.7b), medium (figures 7.7c and 7.7d) and high (figures 7.7e and 7.7f) δ. The n_e profiles are tracked on four radial locations from the SOL ($\rho_{pol} = 1.02$) towards the pedestal top ($\rho_{pol} = 0.96$) and the T_e profiles are

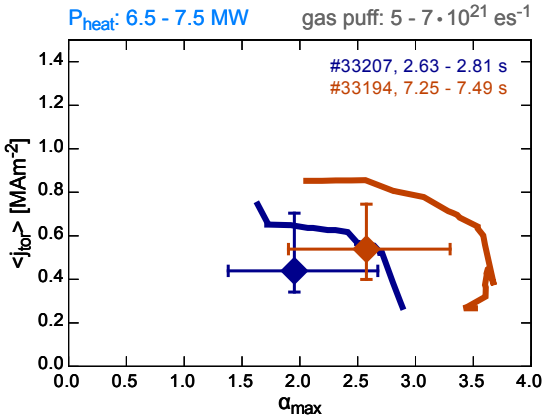

Figure 7.6: PB stability diagram for low (dark blue) and high (orange) δ: As illustrated in figure 2.3 the stability boundary at high δ is pushed towards higher $\alpha_{\max}$ and $\langle j_{\text{tor}} \rangle$. The steeper p_{e} gradient at high δ moves the operational point towards larger $\alpha_{\max}$.

tracked in the confined plasma region from $\rho_{\text{pol}} = 1.00$ to $\rho_{\text{pol}} = 0.94$ (see vertical lines in figure 7.5).

A similar sequence of pedestal recovery phases as in the collisionality variation (chapter 4) and isotope comparison (chapter 5) studies is observed at all δ. After the ELM crash with duration Δt_{ELM}, the n_{e} pedestal recovers first ($\Delta t_{n_{\text{e}}}$), followed by the recovery of the T_{e} pedestal ($\Delta t_{T_{\text{e}}}$) and the pre-ELM phase in which $\max(-\nabla p_{\text{e}})$ is clamped (see chapter 4).

When comparing the different δ cases, the W_{MHD} losses per ELM increase at higher δ. Further, $\Delta t_{n_{\text{e}}}$ as well as $\Delta t_{T_{\text{e}}}$ also increase at higher δ. This can be either related to lower recovery rates of the n_{e} and T_{e} pedestal or related to the higher ELM loss and therefore, drop in n_{e} and T_{e}. For the n_{e} pedestal the recovery times are too short to perform a quantitative comparison of $\partial n_{\text{e}}/\partial t$ for the different δ cases. At high δ, T_{e} at the positions $\rho_{\text{pol}} = 0.96$ and $\rho_{\text{pol}} = 0.94$ is lower in the beginning of $\Delta t_{T_{\text{e}}}$ than at low δ. This would be related to a higher ELM loss, causing the longer pedestal recovery time.

Most prominently, the duration the pre-ELM phase with clamped pedestal gradient is almost doubled from low to high δ. This is the largest contribution to the observed lower f_{ELM} at higher δ and an indicator that at high δ especially this period is more stable and therefore, prolonged.

In summary, the higher pedestal top n_{e} is established immediately after the ELM crash in the n_{e} pedestal recovery phase. All phases in the ELM cycle are longer at higher δ, especially, the pre-ELM phase. For the n_{e} and T_{e} pedestal this prolongation is very likely caused by higher ELM losses, whereas in the pre-ELM phase this might be

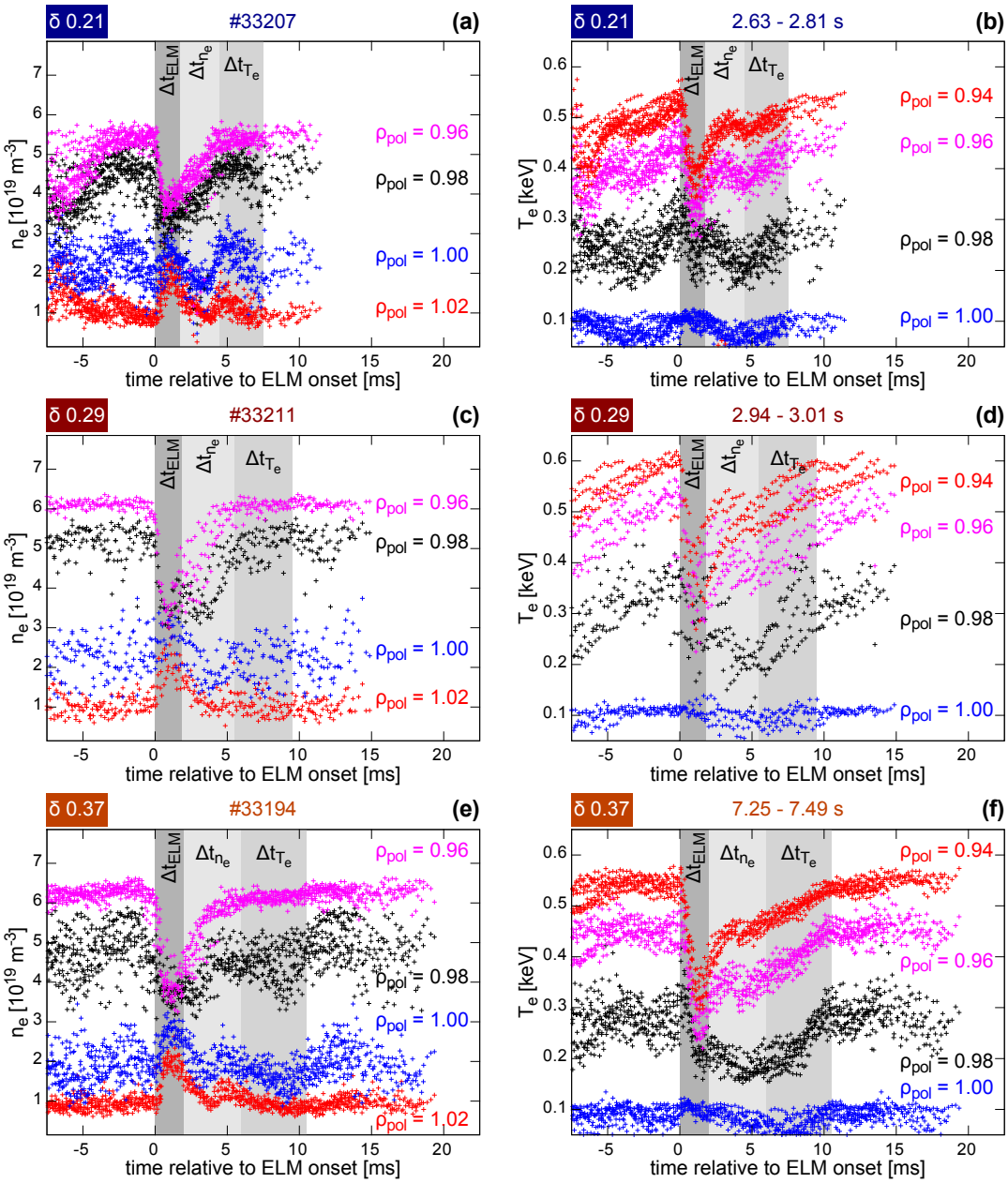

Figure 7.7: Inter-ELM pedestal evolution: (a,c,e) n_e and (b,d,f) T_e at certain radial positions across the pedestal (ρ_{pol}) for (a,b) low, (c,d) medium and (e,f) high δ. For all cases the n_e pedestal is re-established before the T_e pedestal and the sequence of recovery phases is similar. All recovery phases (Δt_{n_e} and Δt_{T_e}) increase their duration with increasing δ, which corresponds to a decrease of f_{ELM}.

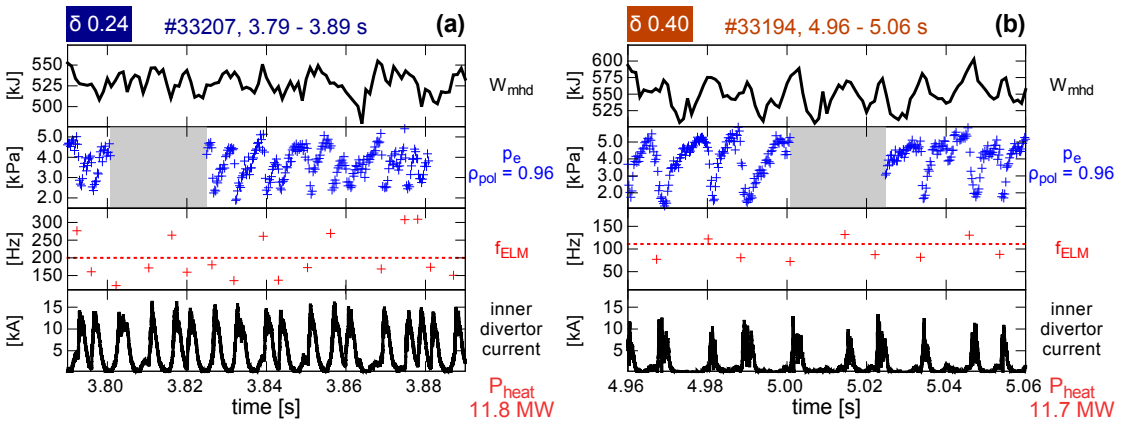

Figure 7.8: Discharge intervals with two f_{ELM} bands: Time traces of W_{MHD}, pedestal top p_{e}, f_{ELM} and inner divertor current at (a) low and (b) high δ. The threshold in f_{ELM} discriminating between 'fast' and 'slow' ELM cycle is indicated by the red dashed line. Both types of ELM cycles appear irregularly.

linked either to enhanced particle and heat fluxes across the pedestal or the stabilising effect of δ allowing higher global W_{MHD}.

7.4 ELM frequency bands

At all investigated δ, discharge phases with two f_{ELM} bands were observed. Their appearance cannot be related to certain parameter combinations of P_{heat} and gas puff. It is rather set individually for each δ. At high δ, it is more likely that the two f_{ELM} bands appear at the higher level of P_{heat}.

7.4.1 Observation of 'slow' and 'fast' ELM cycles

The two f_{ELM} bands are associated to ELM cycles of different duration. Therefore, according to the observation, it is discriminated between 'fast' and 'slow' ELM cycles, which are related to the high and low f_{ELM} band. Exemplary time traces of discharge intervals with two f_{ELM} bands are presented in figure 7.8a at low δ and in figure 7.8b at high δ. Here, W_{MHD}, pedestal top p_{e} (tracked at $\rho_{\mathrm{pol}} = 0.96$), f_{ELM} and inner divertor current are shown. The burst in the divertor current is associated to the ELM crash, f_{ELM} is determined by the inversion of the time period from an ELM crash until the following one. In both discharge intervals a similar P_{heat} is applied. In agreement with the data presented in figure 7.3, both f_{ELM} bands have a higher

frequency at low δ. The frequencies, which discriminate the f_{ELM} bands, are indicated by the vertical, red dashed lines.

In both presented cases, 'slow' and 'fast' ELM cycles appear irregularly, i.e. there is now systematic relation between them. At low δ it can be seen that the 'fast' ELM cycle ends at reduced pedestal top p_{e} in comparison to the slow ELM cycle. The detailed pre-ELM pedestal structure of both kinds of ELM cycles is analysed in section 7.4.3. In the following, the pedestal dynamics of the 'fast' and 'slow' ELM cycles are investigated at low and high δ.

7.4.2 Pedestal development of 'slow' and 'fast' ELM cycles

In the low δ case the higher f_{ELM} has a frequency of roughly 250 Hz to 300 Hz. In combination with Δt_{ELM} of approximately 2 ms, this gives the pedestal only a short time to recover in a 'fast' ELM cycle. In figure 7.9 the ELM synchronised evolutions of the n_{e} and T_{e} pedestal are presented for 'fast' (figures 7.9a and 7.9b) and 'slow' (figures 7.9c and 7.9d) ELM cycles. The n_{e} and T_{e} profiles are tracked at equal locations as in figure 7.7. In comparison to the 'slow' ELM cycle, the 'fast' ELM cycle immediately ends after a short recovery phase of approximately 1.5 ms. The 'slow' ELM cycle is longer. Because of the scattering in the data, it is still too short to distinguish between n_{e} and T_{e} pedestal recovery phases.

At higher δ, the limitation in temporal resolution of the inter-ELM phases relaxes since f_{ELM} is lower. Figure 7.10 the pedestal development of the high δ case is shown in a similar setup as figure 7.9. Here, the pedestal recovery phases are well resolved and indicated by grey shaded areas. The 'fast' ELM cycle ends during the T_{e} pedestal recovery phase and therefore, also the pre-ELM phase is missing. In both types of ELM cycles the n_{e} and T_{e} pedestal recovery behaves similar up to the point when the following ELM crash appears. This suggests that during the inter-ELM pedestal development, one or possibly more pedestal configurations could become unstable, leading to an ELM crash. To investigate the pedestal stability at the end of both ELM cycles, the pedestal structure is analysed.

7.4.3 Pre-ELM pedestal conditions and stability

Figure 7.11 compares the pedestal n_{e}, T_{e} as well as resulting p_{e} profiles for 'fast' (blue) and 'slow' (red) ELM cycle. These are averaged in the time interval between -0.75 ms and -0.25 ms relative to the onset of the following ELM crash, i.e. at the end of the corresponding ELM cycle. For both cases of δ, the T_{e} profiles (figures 7.11b and 7.11e) are similar for 'fast' and 'slow' ELM cycle. The largest difference is observed in the n_{e} profiles (figures 7.11a and 7.11d). While n_{e} for $\rho_{\mathrm{pol}} < 0.96$ is similar for both

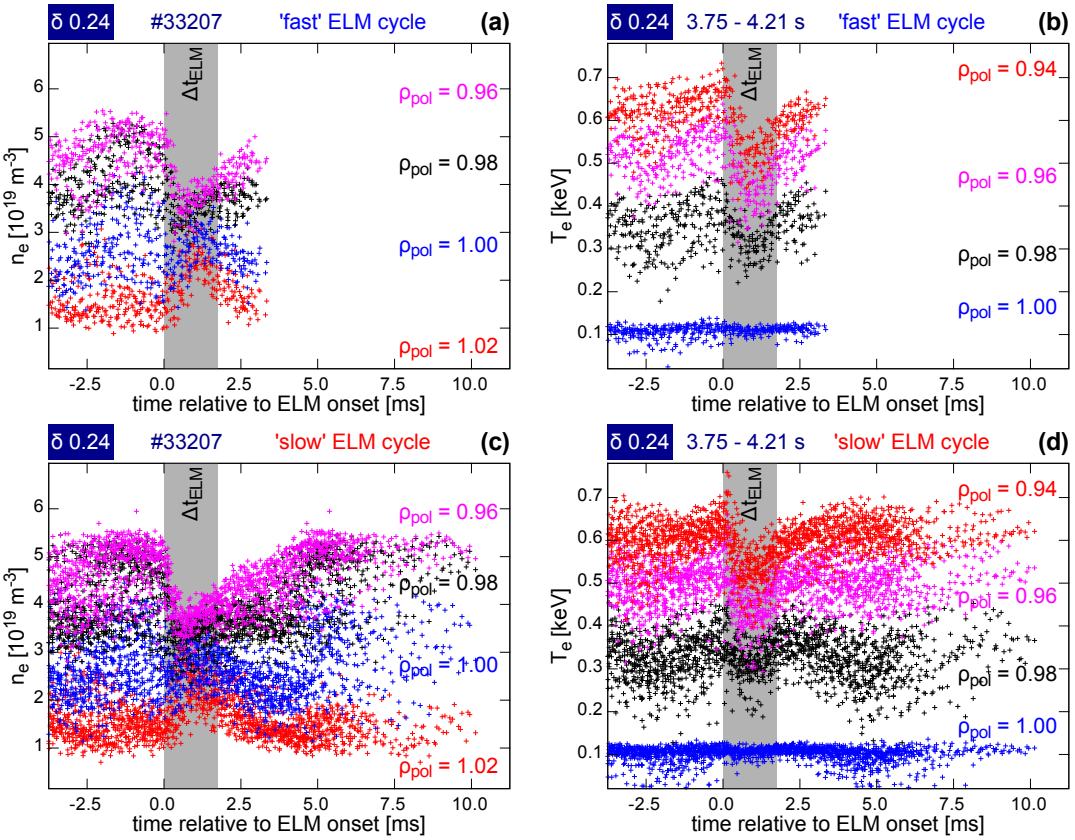

Figure 7.9: Pedestal evolution at low δ for the two f_{ELM} bands: (a,c) n_{e} and (b,d) T_{e} at several radial positions (ρ_{pol}) for the (a,b) 'fast' and (c,d) 'slow' ELM cycles. Roughly 1.5 ms after the end of the ELM crash (Δt_{ELM}) the 'fast' ELM cycle is ended by another ELM crash.

types of ELM cycles, the pre-ELM n_{e} profile of the 'fast' ELM cycle is located further inwards and also ∇n_{e} is shallower. In the p_{e} profiles this is reflected by a reduced ∇p_{e}.

The different edge profiles in combination with changes in W_{MHD} can impact on the PB stability. Therefore, stability analyses were performed with the corresponding equilibria at the end of the 'fast' and 'slow' ELM cycles. In figure 7.12 the corresponding j-α diagrams are presented. At both investigated δ, the operational points at the end of the 'fast' ELM cycles (blue) are located at lower α_{max} as a result of the inward located n_{e} profile. The PB stability boundaries are shifted similar to the operational points at low δ. Further, the operational points are very close to the PB boundary for both types of ELM cycles, which indicates that it is very likely for the pedestal to become unstable. At high δ the PB boundary of the 'slow' ELM cycle (red) moves to higher $\langle j_{\mathrm{tor}} \rangle$ and α_{max} as the corresponding operational point.

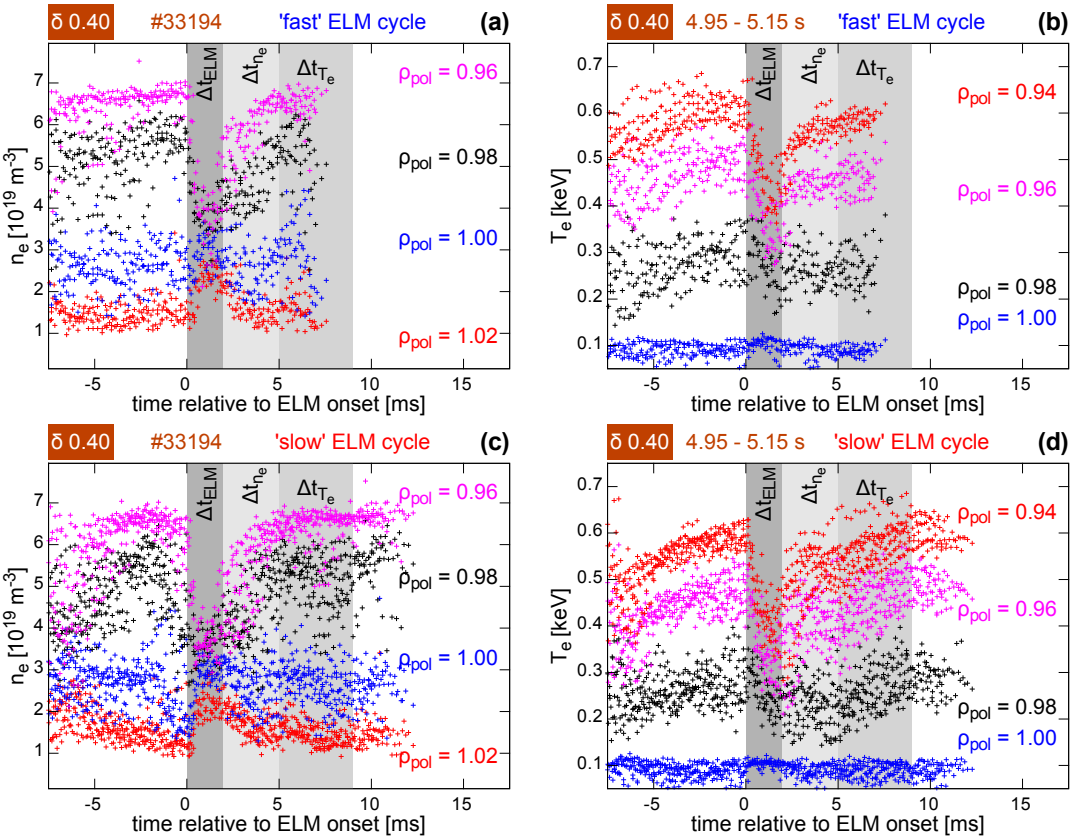

Figure 7.10: Pedestal evolution at high δ for the two f_{ELM} bands: (a,c) n_{e} and (b,d) T_{e} at several radial positions (ρ_{pol}) for the (a,b) 'fast' and (c,d) 'slow' ELM cycles. In comparison to the low δ case, the pedestal top n_{e} is re-established in the 'fast' ELM cycle but the 'slow' ELM cycle has an prolonged T_{e} evolution.

Nevertheless, it is very likely that the pedestal gets PB unstable at the end of the 'fast' ELM cycles, since the 'slow' ELM cycles represents the maximum achievable pedestal.

All in all, the pre-ELM pedestals at the end of the 'fast' and 'slow' ELM cycles agree with PB stability. This can be interpreted such that the pedestal in between ELMs evolves through configurations which become more likely unstable. Therefore, the occurrence of two f_{ELM} bands is linked to the inter-ELM pedestal stability.

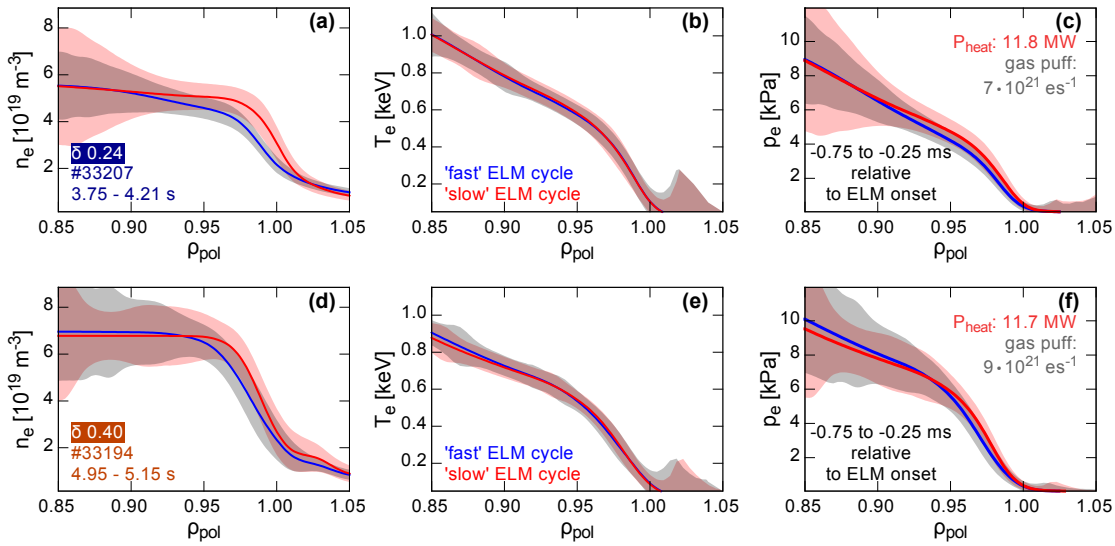

Figure 7.11: Pre-ELM pedestal profiles at the end of the different ELM cycles: (a,d) n_e, (b,e) T_e and (c,f) p_e for the (a,b,c) low and (d,e,f) high δ cases. At the end of the 'fast' ELM cycle the n_e profile is located further inwards for both δ, resulting in a reduced ∇p_e.

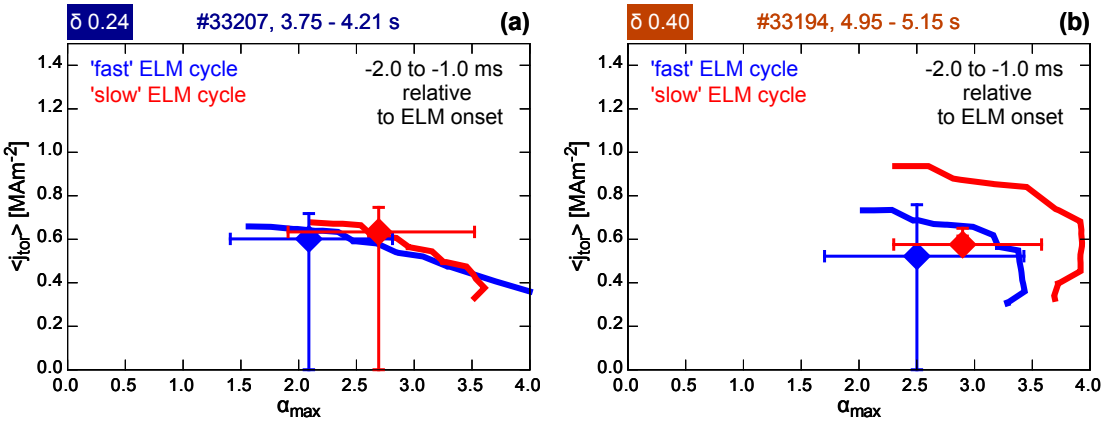

Figure 7.12: Pre-ELM stability at the end of the 'fast' and 'slow' ELM cycle: (a) at low and (b) high δ. The operational points are located at higher α_{max} at the end of the 'slow' ELM cycle for both δ. The PB boundary is shifted correspondingly at low δ, while at high δ, the distance between operational point and PB boundary increases.

7.5 Summary of the main observations

The presented results are consistent with previous studies on the impact of δ on the pedestal structure. Higher δ enhances the pedestal top n_e although W_{MHD} is not strongly affected, which might be due to changes in the core transport. Further, f_{ELM} decreases with increasing δ.

The pre-ELM pedestal structure agrees with PB theory and at higher δ the PB stability boundary is moved towards larger $\langle j_{tor} \rangle$ and α_{max} allowing the higher pedestal top p_e. The inter-ELM evolution shows a similar sequence of pedestal recovery phases for all δ. The enhanced pedestal top n_e at higher δ is already established during the recovery phase of the n_e pedestal. The lower f_{ELM} at high δ is caused by prolongation of the pedestal recovery phases. For the T_e pedestal recovery phase, this is related to the higher ELM loss. The extended pre-ELM phase at high δ could be either caused by an increased particle and heat flux across the edge or by the beneficial effect of δ on the edge stability.

The occurrence of two f_{ELM} bands is connected to the inter-ELM pedestal stability. Both types of ELM cycles pass through a similar pedestal development. At the end of a 'fast' ELM cycle the n_e profile is located radially inwards relative to the n_e profile at the end of a 'slow' ELM cycle, leading to a reduced ∇p_e. When analysing the PB stability of the pedestals at the end of both types of ELM cycles, the PB boundary is in similar distance to the operational point, indicating that both pedestals can become PB unstable.

8 | Summary and Conclusions

The main results of this thesis were presented in the chapters 4 to 7. In the following a summary of them is given (section 8.1) and general conclusions are drawn (section 8.2). Further a brief outlook is given on topics for future work and questions resulting from the presented work (section 8.3).

8.1 Summary

In chapter 4, a variation of the pedestal ν^* was investigated and the inter-ELM pedestal evolution was compared. A similar sequence of pedestal recovery phases is observed. Further, the re-establishment of the pedestal $\max(-\nabla p_e)$ occurs already of the order of ms before the ELM onset. This pre-ELM saturation of $\max(-\nabla p_e)$ is accompanied by the onset of high frequency magnetic fluctuations. Their detected fluctuation frequency is linearly correlated to the neoclassical estimation of the $E \times B$ background flow velocity at the plasma edge. This indicates that the underlying mode structures are localised at the plasma edge and that the instability has a low phase velocity relative to the background flow. Because of the uncertainties of the background flow velocity, it is not possible to extract phase velocities and relate the underlying instability to known microturbulent instabilities, which have characteristic propagation directions.

The high frequency fluctuations are also seen on the HFS of the torus, which is not expected for a ballooned mode structure. The toroidal mode structure of the high frequency fluctuations has n in the range from -11. These mode numbers were independently estimated by analysis of magnetic measurements and by fitting the linear relation between detected fluctuation frequency and approximated background velocity.

In chapter 5, the pedestal structure, stability and inter-ELM evolution was investigated for D, H and ^{4}He plasmas. Comparing the hydrogenic species plasmas roughly a factor of 2 higher P_{heat} was required in H as well as a factor of 10 higher gas puff to match the pedestal top n_e and T_e. In the ^{4}He discharges a match of the pedestal top n_e with the hydrogenic references led to an ELM-free phase, because of the larger

Z_{eff} in ^{4}He (at similar p_{e}) p is reduced since n_{i} is lower. The disappearance of ELMs is also reproduced in stability analyses of different discharge periods, where the operational point is found in the deeply stable j-α space when ELMs are absent. The comparison of the D and H pedestals reveals shallower ∇n_{e} in H, which affects the pedestal stability and pushes the operational point to a reduced α_{max}. Furthermore, the inter-ELM heat flux across the pedestal is estimated to be 2 times larger in H in comparison to D.

Nevertheless, the inter-ELM pedestal evolves in a similar sequence of recovery phases for all investigated main ion species, which is also consistent with the results of chapter 4 and the associated magnetic activity to the recovery phases is similar. At ASDEX Upgrade, first, the n_{e} pedestal, respectively ∇n_{e}, is re-established after the ELM crash. This fast recovery phase is associated with low magnetic fluctuation intensity in the whole spectral range. After the n_{e} pedestal recovery the T_{e} pedestal and $\max(-\nabla T_{\mathrm{e}})$ recovers, in this period, low frequency fluctuations in the region from 50 kHz to 150 kHz are present. When the pre-ELM $\max(-\nabla p_{\mathrm{e}})$ is achieved, high frequency fluctuations set in, which are then associated to a clamping of $\max(-\nabla p_{\mathrm{e}})$, which is sustained up to the next ELM-crash. In the ^{4}He plasma, the evolution of ∇T_{i} has been found to be connected to the recovery timescale of ∇n_{e}, i.e. that ∇T_{i} recovers faster than ∇T_{e}.

For all investigated main ions species a similar toroidal mode structure of the pre-ELM magnetic fluctuations is observed, which has a significant n contribution between -10 and -12 in the high frequency component. This is in line with the observed mode structures in chapter 4. Further, two mode number branches were observed in the investigated cases, which indicate different propagation velocities relative to the lab frame and therefore, different radial locations of the underlying mode structures.

In chapter 6, the mechanisms that lead to the fast recovery of the n_{e} pedestal were investigated by a multiple diagnostic approach, which characterised the inter-ELM evolution of the pedestal, of the LFS and of the HFS SOL as well as in the divertor region. The n_{e} in these areas can impact on the n_{e} pedestal evolution. It is found that during the ELM cycle the HFSHD appears and extends up to the HFS midplane. Further, the ELM crash induced particle loss from the confined plasma leads to an enhanced neutral flux at the main chamber wall. However, the timescales of both effects do not fit the recovery time of the pedestal ∇n_{e}, which is faster. This timescale is only reflected in the magnetic activity, which shows a significantly reduced intensity during this period, indicating a lower fluctuation level.

A rough estimation of the particle flux across the pedestal, shows a well correlated evolution with the ionisation source, which also increases when the magnetic activity sets

in after the recovery of ∇n_e. When ∇T_e is established and the high frequency fluctuations set in, additional particle flux trough the edge is observed, which is related to the stagnation of the n_e recovery rates at the pedestal top.

In chapter 7 the impact of the plasma shape on the edge stability and inter-ELM pedestal evolution was investigated. For a variation of δ the pre-ELM pedestal structure as well as the inter-ELM profile development was analysed. At high δ the pedestal top n_e is enhanced and f_{ELM} reduced in comparison to plasmas with lower δ. The higher pedestal top n_e is already established during the recovery phase of the n_e pedestal, which takes place directly after the ELM crash. In general, a similar sequence of pedestal recovery phases is observed at all investigated δ, which agree with the ones observed in chapters 4 and 5. The reduction of f_{ELM} at high δ is due to longer pedestal recovery phases.

Two f_{ELM} bands appeared in several discharge intervals. Their occurrence is related to the pedestal stability during the inter-ELM evolution. The f_{ELM} bands are associated to 'fast' and 'slow' ELM cycles, which both have a similar pedestal development, till the onset of the following ELM crash. The n_e profile is located radially inwards at the end of the 'fast' ELM cycle. At the end of both types of ELM cycles, the pedestal stability is similar. Therefore, it is likely that at the end of the 'fast' and 'slow' ELM cycle the pedestal becomes PB unstable.

8.2 Conclusions

From the results which were presented in this thesis the following general conclusions on the pedestal and its recovery behaviour can be drawn:

Pedestal evolution

The sequence of pedestal recovery phases is robust, i.e. observed in all investigated cases and independent of the varied parameters like e.g. main ion species, gas puff, P_{heat} or plasma shape. This points into the direction that mechanisms and underlying drives that determine the pedestal recovery are dominant in the same sequence.

Pre-ELM phase

When a saturation of the $\max(-\nabla p_e)$ in the pre-ELM phase is observed, it is correlated to the onset of high frequency fluctuations. The toroidal mode structure of n between -10 and -12 points in the direction of a global, large scale instability that is independent of ν^* (in the investigated range) and main ion species.

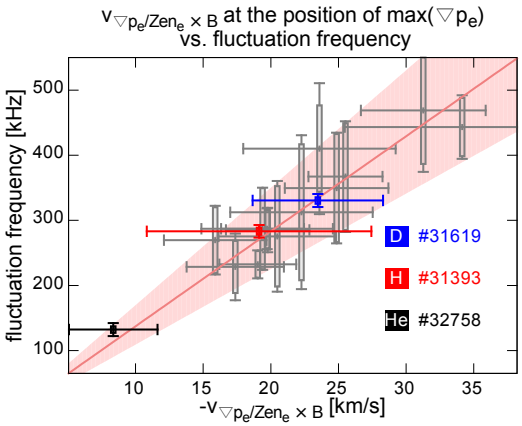

Figure 8.1: Estimated background velocity ($v_{-\nabla p_e/Zen_e}$) and detected fluctuation frequency: Data combined from figures 4.10, 5.6b, 5.6d and 5.13b. For the n equal -11 contribution of the high frequency fluctuations the detected fluctuation frequency is linearly proportional to $v_{-\nabla p_e/Zen_e}$ independently of main ion species.

Propagation of the $\max(-\nabla p_e)$ clamping instability

The detected magnetic fluctuation frequency originates from the mode structure of the underlying instability and its propagation relative to the lab frame, where the pickup coil sits. For the high frequency fluctuations it has been shown that the detected fluctuation frequency is linearly proportional to the estimated plasma background velocity ($v_{-\nabla p_e/Zen_e}$). This holds for different main ion species of the plasma. Figure 8.1 combines the data, presented in figure 4.10 and the detected fluctuation frequencies for the $n= -11$ component of the isotope comparison, that are presented in figures 5.6b, 5.6d and 5.13b. The $E \times B$ rotation is reduced in ^{4}He plasmas because of the higher Z.

Evolution of the magnetic flucutations int the ELM cycle

The magnetic activity in between ELM crashes is correlated to the phases of the pedestal recovery. During the n_e pedestal recovery phase, the overall spectral intensity is lowest, while during the T_e pedestal recovery phase medium frequency magnetic activity is observed. The associated mode structure is in the range from -3 to -8. In the pre-ELM phase, additionally the fluctuations in the high frequency range set in. This behaviour of the magnetic activity is observed generally and therefore, supports that similar mechanisms dominate the pedestal recovery, independently of the varied parameters.

Recovery of the n_e pedestal

It is a robust observation at ASDEX Upgrade that the n_e pedestal is re-established quickly after the ELM crash. The timescale of the n_e recovery is almost independent of the applied neutral gas puff. For this reason, the recycled particles

stemming from the ELM crash, fuelling from the core plasma or a transport reduction are explanations for the fast recovery of the n_e pedestal. The reduced magnetic activity during the n_e pedestal recovery phase suggests a change of the dominating instabilities in the pedestal, however, owing to the larger neutral source a higher particle flux across the pedestal is found.

Impact of δ

In a large set of discharge intervals a higher n_e pedestal as well as improved stability was observed at higher δ. When investigating the inter-ELM pedestal development, it is found the the enhanced n_e at high δ is already established directly after the ELM crash in the n_e pedestal recovery phase. The reduction of f_{ELM} at high δ is related on the one hand to the larger ELM losses and on the other hand to a prolonged pre-ELM phase with clamped pressure gradient.

f_{ELM} bands

Two distinct f_{ELM} bands are observed in a variety of plasma discharges. Their appearance is related to the pedestal stability during the inter-ELM evolution. It is found that the pedestals at the end of the 'fast' and 'slow' ELM cycles are likely to become PB unstable. This underlines that PB modes set the stability limit of the pedestal.

8.3 Outlook

Research is an ongoing process, therefore, the end of this thesis does not imply completeness. The presented results, summarised in section 8.1, give a characterisation and interpretation of the inter-ELM pedestal development at ASDEX Upgrade over a wide range of varied parameters. Nevertheless, throughout the conducted work new questions arose and the importance of questions that have not been sufficiently addressed so far was highlighted. For this reason several topics have to be accessed in future work:

Mode localisation and coupling

The exact localisation of the mode, which causes the high frequency magnetic fluctuations and clamp the pressure gradient, could give deeper insight in the underlying instability. Here, on the one hand resonant flux surfaces can become important or probably areas with reduced magnetic shear. Further, investigations on the coupling of the different n contributions in the mode number branches or of the two mode number branches, can shed light on the saturation of the fluctuations [119]. Furthermore, mode coupling is also a candidate for the ELM trigger mechanism.

Pedestal optimisation

Another, more applied approach, which could take advantage of the observed pedestal gradient clamping would be to optimise, respectively, control, the pedestal such that the pre-ELM phase is extended without ending up in an ELM crash. This points towards the realisation and optimisation of an ELM-free plasma scenario with improved performance, below the PB pedestal stability limit.

Neutral dynamics

When investigating the fast recovery of the n_e pedestal, the impact of the neutrals and their dynamic changes in between ELM crashes turned out to be the key parameter. Here, more accurate modelling of the source profile, i.e. with 3-D neutral codes like B2-EIRENE [228] could give better information. Further, possible diagnostic principles, to resolve neutral density profiles in a tokamak environment should be evaluated and realised, to experimentally study the neutral dynamics.

Transport analysis

With the measurements of all sources, sinks as well as profiles for electrons and ions, coupled heat and particle transport analysis in the inter-ELM periods could be performed. The utilisation of more advanced transport solvers like ASTRA [229] allows the comparison of the experimentally observed to theoretically predicted transport coefficients [48, 230].

In conclusion, the end of this thesis underlines the necessity to tackle the remaining challenges on the path to establish nuclear fusion as a reliable and sustainable source for electricity production.

Acronyms

$\boldsymbol{\alpha}$ normalised pressure gradient

$\boldsymbol{\alpha_{max}}$ maximum normalised pressure gradient

$\boldsymbol{a}$ minor plasma radius

Alcator C-Mod Alto Campo Toro (Italian for high field torus) C-modification; Shut down, Previously operated by the Massachusetts Institute of Technology, United States

ASDEX Upgrade Axially Symmetric Divertor Experiment Upgrade; Operated by the Max Planck Institute for Plasma Physics, Germany

BES beam emission spectroscopy

β ratio of thermal to magnetic pressure

β_e ratio of electron to magnetic pressure

BPT Bayesian probability theory

$\boldsymbol{B_t}$ toroidal magnetic field

$\boldsymbol{\partial B_r / \partial t}$ radial magnetic field fluctuations

$\boldsymbol{c_s}$ ion sound velocity

CXRS charge exchange recombination spectroscopy

D deuterium

D-T deuterium-tritium

$\boldsymbol{D_\alpha}$ D_α line radiation

DAQ data acquisition

DCN deuterium cyanide laser interferometry

$\boldsymbol{\delta}$ triangularity

$\boldsymbol{\Delta}$ pedestal width

DEMO DEMOnstration power station

DIII-D Tokamak; Operated by General Atomics, United States

$\boldsymbol{D}$ diffusion coefficient

$\mathbf{e}$ elementary charge

EAST Experimental Advanced Superconducting Tokamak; Operated by the Hefei Institutes of Physical Science, China

$\boldsymbol{\epsilon}$ inverse aspect ratio

ECE electron cyclotron emission

ECFM electron cyclotron forward model

ECRH electron cyclotron resonance heating

EDA enhanced D_α

EHO edge harmonic oscillation

ELM edge localised mode

EUROfusion European Consortium for the Development of Fusion Energy

$\boldsymbol{E_r}$ radial electric field

ETB edge transport barrier

ETG electron temperature gradient

$\boldsymbol{f_{ELM}}$ ELM repetition frequency

FWHM full width at half maximum

$\boldsymbol{\Gamma}$ particle flux

$\boldsymbol{\partial\Gamma/\partial V}$ particle flux into the volume

H hydrogen

H-mode high confinement mode

$^{\mathbf{3}}$**He** helium-3

$^{\mathbf{4}}$**He** helium

HFS high field side

HFSHD high field side high density region

HFO high frequency oscillation

HL-2A Tokamak constructed from major ASDEX components; Operated by the Southwestern Institute of Physics, China

IDA integrated data analysis

I_{p} plasma current

IPP Max Planck Institute for Plasma Physics

ITER the Latin word for 'the way'; Tokamak that is currently constructed in Cadarache, France

ITG ion temperature gradient

IXS impact excitation spectroscopy

$\langle j_{\mathrm{tor}} \rangle$ average toroidal current density in the pedestal

JET Joint European Torus; Operated by the Culham Centre for Fusion Energy, United Kingdom

JT-60U JAERI tokamak - 60 Upgarde; Shut down, Previously operated by the Japan Atomic Energy Research Institute, Japan

κ plasma elongation

KBM kinetic ballooning mode

KSTAR Korea Superconducting Tokamak Advanced Research; Operated by National Fusion Research Institute, South Korea

L-mode low confinement mode

LCFS last closed flux surface

Li lithium

LIB lithium beam

LFS low field side

LOS lines of sight

LP Langmuir probe

LSN lower single null

m poloidal mode number

MAST Mega Ampere Spherical Tokamak; Operated by the Culham Centre for Fusion Energy, UK

MHD magnetohydrodynamic

MTM microtearing mode

n toroidal mode number

n_e electron density

$\partial n_e / \partial t$ electron density recovery rate

∇n_e electron density gradient

$\max(-\nabla n_e)$ maximum electron density gradient

n_i main ion density

ν^* plasma collisionality

$\nu^*_{e,ped}$ pedestal top electron collisionality

Na sodium

NBI neutral beam injection

NSTX National Spherical Torus Experiment; Upgraded to NSTX-U, Operated by the Princeton Plasma Physics Laboratory, United States

PB peeling-ballooning

P_{ECRH} electron cyclotron resonance heating power

P_{heat} heating power

p thermal pressure

∇p thermal pressure gradient

p_e electron pressure

∇p_e electron pressure gradient

$\max(-\nabla p_e)$ maximum electron pressure gradient

p_i main ion pressure

p_{ped} pedestal height

P_{L-H} L-H power threshold

P_{NBI} neutral beam heating power

PS Pfirsch-Schlüter

q safety factor

QH-mode quiescent H-mode

$\boldsymbol{q}$ safety factor

$\boldsymbol{R_0}$ major plasma radius

$\boldsymbol{S_i}$ ionisation source

SOL scrape-off layer

T tritium

TCV Tokamak à configuration variable; Operated by the École polytechnique fédérale de Lausanne, Suisse

$\boldsymbol{T_e}$ electron temperature

$\boldsymbol{\nabla T_e}$ electron temperature gradient

$\boldsymbol{\max(-\nabla T_e)}$ maximum electron temperature gradient

$\boldsymbol{T_i}$ main ion temperature

TEM trapped electron modes

$\boldsymbol{T_i}$ ion temperature

$\boldsymbol{\nabla T_i}$ ion temperature gradient

$\boldsymbol{\max(-\nabla T_i)}$ maximum ion temperature gradient

TS Thomson scattering

$\boldsymbol{W_{MHD}}$ plasma stored energy

W7-X Wendelstein 7-X; Operated by the Max Planck Institute for Plasma Physics, Germany

$\boldsymbol{Z_{eff}}$ effective charge

Acknowledgement

Da steh ich nun, ich armer Tor!
Und bin so klug als wie zuvor;
Heiße Magister, heiße Doktor

- Johann Wolfgang von Goethe,
Faust: Der Tragödie Erster Teil

Es ist vielleicht ein wenig weit hergeholt die Danksagung mit einem Faust Zitat einzuleiten, allerdings beschreibt es sehr gut eine Erkenntnis, die ich im Laufe der letzten Jahre des Öfteren hatte. Die Arbeit und das Verfassen einer Dissertation fordern viel Durchhaltevermögen und von Zeit zu Zeit die Einsicht, dass Dinge doch nicht so sind wie man geglaubt hatte bzw. dass man schon verstanden Geglaubtes doch noch nicht vollständig begriffen hat.
Am Ende ist es die Unterstützung vieler, die einem die Zuversicht gibt mit seinen Problemen nicht alleine zu sein und die hilft den Fokus, die Dissertation erfolgreich abzuschließen, nicht aus den Augen zu verlieren.
Als eine wichtige Grundlage meiner wissenschaftlichen Arbeit sehe ich die ausreichende Finanzierung für mein Dissertationsvorhaben. Deshalb möchte ich mich bei der Friedrich Schiedel Stiftung für Energietechnik und im Speziellen bei Ulrike Schiedel für das großzügige Stipendium bedanken, das es mir ermöglichte frei von finanziellen Sorgen zu forschen. Außerdem geht mein Dank an die europäischen Steuerzahlenden, die durch ihre Beiträge an EURATOM, einen Teil meiner zahlreichen Forschungsaufenthalte finanziert haben.
Neben der finanziellen Sicherheit ist es genau so wichtig eine gute Themenstellung als Ausgangslage für eine Dissertation bzw. im Laufe der Arbeit immer eine Ansprechstelle und Quelle für Lösungsansätze zu haben. Hierzu ist eine gute Betreuung notwendig und ich durfte mich in der glücklichen Lage schätzen, gleich eine Betreuerin und einen Betreuer, wie ich finde beide von der besten Sorte, an meiner Seite zu wissen. Deswegen ergeht mein besonderer Dank an meine „Doktormutter“ Elisabeth Wolfrum und meinen „Doktorvater“ Friedrich Aumayr. Liebe Lisl, du hattest immer für mich Zeit, wenn ich von Tag zu Tag „kurz stören“ kam, und auch stets guten Input sowie Feedback parat. Außerdem hast du sämtliche meiner Verschriftlichungen sehr gewissenhaft korrigiert und meine immer wiederkehrenden Tipp- bzw. Schreibfehler ausgebessert. Durch dein Zutun und deine kontinuierliche Unterstützung, hast du diese Dissertation wesentlich mitgestaltet. Lieber Fritz, als ich vor viereinhalb Jahren in deine Gruppe

(mittlerweile Forschungsbereich) kam, hätte ich mir nie erwartet, dass ich eines Tages an der TU Wien promovieren werde. Ich durfte mit dir eine spannende Zeit der Veränderung erleben, in der du die Verantwortung des Institutsvorstandes übernommen hast. Du hast mir große Freiräume gegeben, die ich manchmal ausgereizt habe, und hast so manche Kindereien toleriert bzw. selbst mitgemacht, was für gute Stimmung sowie ein angenehmes Arbeitsklima gesorgt hat.
Natürlich haben an einem angenehmen Arbeitsklima auch die vielen, netten Kolleginnen und Kollegen großen Anteil. Hier ergeht ein großer Dank an die Mitglieder des Forschungsbereichs „Atom- und Plasmaphysik“ an der TU Wien, das „ASDEX Upgrade Team“ (auch unter dem Namen „A-Team“ bekannt) am IPP Garching, die Mitglieder des Doktoratskollegs „HEPP“ und das „EUROfusion MST1 Team“ als europäisches Netzwerk der Fusionsforschung. Die vielen Gespräche, die wissenschaftlicher wie auch privater Natur waren, sowie das viele Feedback, haben mich in der Zeit meiner Dissertation sehr geprägt, mich weitergebildet und bereichert.
An dieser Stelle möchte ich einigen für mich besonderen Menschen danken sowie gemeinsam Erlebtes festhalten.
Dem „Li-BES Team“, bestehend aus Karola Bald, Gregor Birkenmeier, Rainer Fischer und den beiden jüngeren Mitgliedern Georg Harrer und Nils Leuthold, möchte ich einen großen Dank für die gute Zusammenarbeit beim Betrieb der Li-Strahl Diagnostik aussprechen. Gregor, du warst nicht nur mein erster Ansprechpartner, was Sorgen und Organisatorisches bezüglich der Diagnostik betrifft, sondern hast mir auch fachlich sehr viel beigebracht. Unser Urlaub in Kalifornien wird mir stets in guter Erinnerung bleiben. Georg, du kennst mich als einer der wenigen bei meiner Arbeit in Wien sowie in Garching. Als Essenslieferant hast du mich während der intensiven Zeit des Verfassens der Dissertation mit dem Lebensnotwendigen versorgt. Auf diesem Wege dir auch alles Gute für deine Dissertation.
Des Weiteren möchte ich mich bei meinen Kolleginnen und Kollegen im Doktoranden-Büro in Garching, Marco Cavedon, Alexander Lebschy, Anna Medvedeva, Ulrike Plank und Dmitrii Prisiazhniuk bedanken. Ihr habt meine Aufenthalte in Garching zu Erlebnissen gemacht und mich des Öfteren mit einem neu gestalteten Schreibtisch überrascht, wenn ich länger nicht anwesend war. Alex, du hast als Doktorandensprecher dich stets um uns alle bemüht und warst ein guter Zimmerkollege auf so mancher Dienstreise bzw. hast mir dein Zimmer zur Verfügung gestellt um meinen Jetlag auszuschlafen. Wir haben gemeinsam den Donnerstagsbesuch des „Spinnradls“ während der Programmseminare auf Schloss Ringberg etabliert und du hast bereits am Premierenabend für ein Highlight gesorgt, das zum Glück ohne große Konsequenzen blieb, aber deinen Ruf als Ausparkstratege geprägt hat. Marco, du hast uns „La Dolce Vita“ vermittelt und das Büro mit „recyceltem Dolce“ vom Foodsharing versorgt. Um Kaffee zu den ganzen Leckereien verfügbar zu machen, habe ich die in Wien ausgediente Kaffeemaschine im Rahmen der „österreichischen Entwicklungszusammenarbeit“ nach Garching überführt und repariert. Das hat auch meinen Vorgänger Matthias Willensdorfer sehr erfreut, der mittlerweile am IPP „wissenschaftlich unter der Haube ist“.

Matthias, du hast, wenn du auf eine Kaffeepause vorbei gekommen bist, mit deinem Humor für österreichischen Charme gesorgt. Leider muss ich dich auch darauf hinweisen, dass du noch etliche Kaffees in unser Kaffeekonsum-Erfassungsprogramm „gmkh“ nachtragen musst, da du es ja nicht immer so genau genommen hast. Eine Freude war es mir auch, wenn David Rittich auf eine Partie Darts ins eigens dafür ausgestattete Doktoranden-Büro vorbei kam. David, uns hat sowieso die Freude am Sport verbunden, denn es war auch toll dich im Volleyballtraining zu treffen.
Ein spezieller Dank ergeht auch an all meine Co-Autorinnen und Co-Autoren von Publikationen sowie Zuarbeiterinnen und Zuarbeitern: Matthias Bernert, Alexander Bock, Andreas Burckhart, Mike Dunne, Sina Fietz, Benedikt Geiger, Michael Griener, Athina Kappatou, Peter Manz, Rachael McDermott, Felician Mink, Steffen Potzel, Philip Schneider, Branka Vanovac und Eleonora Viezzer. Einerseits wären die wissenschaftlichen Resultate dieser Dissertation nicht ohne sie erzielbar gewesen, da die Arbeit an einem Großexperiment immer nur im Team gelingt, andererseits darf ich auf viele gemeinsame Erlebnisse bei Konferenzen und Tagungen zurückblicken. Als besondere Highlights sind hier sicher die Trachtenoutfits beim bayrischen Abend im Zuge der Programmseminare auf Schloss Ringberg sowie die Aufenthalte in Lissabon, Leuven und San José zu nennen. Persönlich hat mich Portugal für die Jahre meiner Dissertation sehr geprägt, habe ich doch dort beschlossen auf Alkohol über einen längeren Zeitraum vollständig zu verzichten.
In den letzten Jahren habe ich natürlich auch einige Zeit in Wien verbracht. Hier habe ich viel mit den Mitgliedern des Forschungsbereichs „Atom- und Plasmaphysik“, der AG Aumayr, erlebt. Im Speziellen möchte ich Bernhard Berger, Katharina Dobeš, Elisabeth Gruber, Janine Schwestka, Valerie Smejkal, Reinhard Stadlmayr und Paul Szabo sowie den Studenten, die ich im Rahmen meiner Dissertation betreuen durfte, Johannes Gnilsen, Johannes Gugler und Sebastian Keerl, danken. Elisabeth, du hast mich von allen am längsten aushalten müssen, sei es als unruhiger Bürokollege oder als Möchtegernpsychologe. Unsere gemeinsame Zeit schätze ich sehr, denn wir hatten auch extrem viel Spaß beim Scherzen oder uns kreative Ideen für diverse Feiern, wie z.B. den 55. Geburtstag von Fritz, auszudenken. Unterm Strich war es eine emotionale Achterbahnfahrt, aber alles andere ist ohnehin zu langweilig für dich. Kathi, du warst die gute Seele der Arbeitsgruppe und hattest stets den Überblick über alle Aktivitäten. Auch deshalb hatte dein Büro den Beinamen Sekretariat bekommen. An „jenem“ legendären Abend hast du uns auch gezeigt, dass du eine der Härtesten, was Work-Life-Balance angeht, bist. Vali, mit dir war die vierköpfige Mädelsrunde komplett. Respektive war ich froh, dass ich bei euch dreien mitmachen durfte. Du hast die Gruppe mit deiner offenen und unternehmungslustigen Art sehr bereichert: Jahre, Wahn und Sinn. Gemeinsam galt es so einige Büroparties zu feiern. Janine, du warst die letzte meiner Bürokolleginnen bevor dein Aufstieg in den 5. Stock weiterging. So manches Mal hast du mich in „die Welt der Jungen“ mitgenommen, was mir viel Spaß bereitet und mich kurzfristig um ein paar Jahre jünger gemacht hat. Schmu, du hast es geschafft mich im Sommer zum Bootcamp mitzuschleifen, was eine

willkommene Abwechslung zur Arbeit war. Paul, als besonnener Ruhepol bist du ein wichtiger Teil im Gefüge der Gruppe, deine gut bedachten Kommentare sind in unseren Diskussionen immer ein geschätzter Beitrag. Bernhard, was soll ich über dich alles hier niederschreiben? Wir kennen uns mittlerweile seit beinahe 10 Jahren und haben große Teile unseres Studiums miteinander absolviert. Seit du vor etwas mehr als drei Jahren in die AG Aumayr gekommen bist, haben wir uns den Arbeitstag mit so manchem Spaß lustig gemacht. Du hast mich während meiner Aufenthalte in Garching immer auf dem neuesten Stand aus Wien gehalten. Uns verbindet eine Freundschaft, die über die Arbeit hinaus geht. Gerne erinnere ich mich an unsere gemeinsamen Urlaubserlebnisse, deinen Polterabend, deine Hochzeit und die Geburt deines Sohnes Ferdinand. Gemeinsam haben wir einige Projekte vorangetrieben und umgesetzt, wie zum Beispiel einen Film für die Institutsweihnachtsfeier 2015, der vielen sehr gut in Erinnerung geblieben ist.
Natürlich gab es auch im privaten Bereich mehrere Personen, denen ich für die willkommene Abwechslung zum Arbeitsalltag danken möchte: Ingeborg Berger, Christina und Roland Bliem sowie Anna Galler, Thomas Hausmaninger und Martin Kainz. Inge, du bist in deiner Art einfach einzigartig und bringst viel Gelassenheit mit. Christina, wir hatten viel Spaß als ich mich zum Kasnudelkochen in deine Küche eingeladen habe, außerdem erinnere ich mich gerne an meinen Besuch in Boston zurück. Roland, dir verdanke ich sicher zum Teil auch, dass ich mein Studium absolviert habe. Du warst immer ein guter Anhalt, wenn es um Lernziele bzw. Prüfungsvorbereitung ging. Privat haben wir auch viel gemeinsam unternommen und es gibt so manche nette Anekdote, wie z.B. über deine Ambitionen die Murtalbahn zu verlängern (dein Polterabend) oder das unerwartete Antreffen beim Frühstück im Hotel nach deiner Hochzeit. Anna, deine Geschichten sind immer hörenswert und deine Wohnung hat uns einen denkwürdigen Abend beschert. Eigentlich wollten wir bei deinem Nachbarn einen Flaschenöffner ausborgen, haben aber einen verstörenden Anblick bekommen. Thomas, auch wenn es dich für die Zeit deiner Dissertation nach Schweden verschlagen hat, so ist es immer eine besondere Freude, dich im Rahmen von Wienbesuchen oder Hochzeiten zu treffen und mit dir die aktuellen Lebenslagen auszutauschen. Martin, als ehemaliges Mitglied der AG Aumayr bist du uns zum Glück länger erhalten geblieben. Deine Besuche und die Gespräche mit dir, sei es über Handball, Wissenschaft oder deine Freundin, erfreuen mich immer. Auch die Nachtschichten am Institut waren bei deiner Anwesenheit um eine Facette reicher, wenngleich du meist der Erste warst, der eingeschlafen ist.
Abschließend möchte ich noch meiner Familie danke sagen. Sie hat mich durch mein Leben hindurch unterstützt und mir den Rückhalt gegeben, der mir das Erreichen meiner Ziele möglich machte. Meine Eltern, Ingrid und Martin Laggner, sind der Grund meines Daseins. Ihr habt mir meine Ausbildung und mein Studium ermöglicht, wofür ich euch immer dankbar sein werde. Mutti, du hast mich wohl behütet und im wahrsten Sinne des Wortes groß gezogen, mir aber auch die notwendige Selbstständigkeit beigebracht. Vati, du hast dafür gesorgt, dass es allen in der Familie gut ging. In guter

Erinnerung sind mir auch unsere vielen Familienausflüge, für deren Planung meist du zuständig warst. Gemeinsam habt ihr meinen Geschwistern und mir ein solides Fundament für unser weiteres Leben gegeben und einen Umfeld geschaffen, das ich stolz meine Heimat nennen darf.
Meine Geschwister, Peter, Thomas und Franziska Laggner waren die Begleiter meiner Kindheit. Mittlerweile haben wir alle das Elternhaus verlassen, umso schöner ist es, sich dort von Zeit zu Zeit wieder zu treffen. Peter, du hast deine wilden Jahre mit mir in Wien verbracht. Mittlerweile hat es dich nach Graz gezogen, wo ich dich im Laufe der letzten Jahre gerne besucht habe. Thomas, du bist sicher der Motivierteste von uns vieren, was das Studium betrifft. Nicht umsonst hast du deinen Diplomingenieur unter der Mindeststudiendauer abgeschlossen. Auf diesem Wege wünsche ich auch dir alles Gute und viel Durchhaltevermögen für deine Dissertation. Franziska, mit dir durfte ich, wenngleich auch nur kurze Zeit, in Wien gemeinsam wohnen. Mittlerweile hast du dich umorientiert, bist in Kärnten zurück und hast dort deinen Weg für ein glückliches Leben gefunden.
Zu allerletzt ergeht mein Dank an Caroline Moosmüller, meine bezaubernde Freundin. Caroline, du bist jener Mensch, der mir in den letzten Jahren am nächsten gestanden ist. Ich denke, es war sicher nicht immer einfach, da wir einige räumliche Distanz zwischen uns hatten. Aber wir haben uns den Herausforderungen gestellt und sind an ihnen gewachsen. Wenn wir uns meistens unter der Woche nicht gesehen haben, waren unsere gemeinsamen Wochenenden (in Feldkirchen, Garching, Graz, Wien oder sonst wo) gut zum Abschalten vom Alltagsstress und eine wertvolle Zeit. Nachdem ich deiner Meinung nach in Danksagungen viel zu viel preisgebe, verzichte ich darauf unsere Erlebnisse hier niederzuschreiben, behalte sie aber dafür in umso besserer Erinnerung. Ich freue mich schon auf viele weitere Erfahrungen auf unserem gemeinsamen Weg, der uns in Zukunft wohl über den Atlantik führen wird.

Von nichts kommt nichts.

- frei nach Lukrez,
römischer Dichter und Philosoph

Bibliography

[1] International Energy Agency, 'World Energy Outlook 2014', Technical report, OECD Publishing (2014)

[2] Houghton J., 'Global warming', *Reports on Progress in Physics*, **68**, 1343 (2005), URL http://dx.doi.org/10.1088/0034-4885/68/6/R02

[3] Miley G.H., Towner H. and Ivich N., 'FUSION CROSS SECTIONS AND REACTIVITIES', (1974), URL http://dx.doi.org/10.2172/4014032

[4] Bosch H.S. and Hale G.M., 'Improved Formulas for Fusion Cross-Sections and Thermal Reactivities', *Nuclear Fusion*, **32**, 611 (1992), URL http://dx.doi.org/10.1088/0029-5515/32/4/I07

[5] Lawson J.D., 'Some Criteria for a Power Producing Thermonuclear Reactor', *Proceedings of the Physical Society of London Section B*, **70**, 6 (1957), URL http://dx.doi.org/10.1088/0370-1301/70/1/303

[6] Keefe D., 'Inertial Confinement Fusion', *Annual Review of Nuclear and Particle Science*, **32**, 391 (1982), URL http://dx.doi.org/10.1146/annurev.ns.32.120182.002135

[7] Ongena J., Koch R., Wolf R. and Zohm H., 'Magnetic-confinement fusion', *Nature Physics*, **12**, 398 (2016), URL http://dx.doi.org/10.1038/nphys3745

[8] Sunn Pedersen T., Otte M., Lazerson S., Helander P., Bozhenkov S., Biedermann C., Klinger T., Wolf R.C., Bosch H.S. and the Wendelstein 7-X Team, 'Confirmation of the topology of the Wendelstein 7-X magnetic field to better than 1:100,000', *Nature Communications*, **7**, 13493 (2016), URL http://dx.doi.org/10.1038/ncomms13493

[9] Aymar R., Barabaschi P., Shimomura Y. and ITER Team, 'The ITER design', *Plasma Physics and Controlled Fusion*, **44**, 519 (2002), URL http://dx.doi.org/10.1088/0741-3335/44/5/304

[10] 'EUROfusion - European Consortium for the Development of Fusion Energy', (2017), URL http://www.euro-fusion.org/

[11] Westerhof E., 'Non-Inductive Current Drive', *Fusion Science and Technology*, **57**, 222 (2010)

[12] Bock A., 'Generation and Analysis of Plasmas with Centrally Reduced Helicity in Full-Tungsten ASDEX Upgrade', PhD thesis, Ludwig-Maximilians-Universität München (2016)

[13] Zohm H., *Magnetohydrodynamic Stability of Tokamaks*, WILEY-VCH, Weinheim (2014), URL http://www.wiley-vch.de/de?option=com_eshop&view=product&isbn=9783527412327&title=Magnetohydrodynamic%20Stability%20of%20Tokamaks

[14] Chen F., *Introduction to Plasma Physics and Controlled Fusion*, Springer International Publishing, Cham (2016), URL http://link.springer.com/book/10.1007%2F978-3-319-22309-4

[15] Troyon F., Gruber R., Saurenmann H., Semenzato S. and Succi S., 'MHD-Limits to Plasma-Confinement', *Plasma Physics and Controlled Fusion*, **26**, 209 (1984), URL http://dx.doi.org/10.1088/0741-3335/26/1a/319

[16] Connor J.W., Kirk A. and Wilson H.R., 'Edge Localised Modes (ELMs): Experiments and theory', *Turbulent Transport in Fusion Plasma*, **1013**, 174 (2008), URL http://dx.doi.org/10.1063/1.2939030

[17] Vernickel H., Blaumoser M., Ennen K., Gruber J., Gruber O., Jandl O., Kaufmann M., Kollotzek H., Koppendorfer W., Kotzlowski H., Lackner E., Lackner K., Neuhauser J., Noterdaeme J.M., Pillsticker M., Pohlchen R., Preis H., Rauh K.G., Rohr H., Schneider H., Schneider W., Seidel U., Sombach B., Streibl B., Venus G., Wesner F. and Wieczorek A., 'ASDEX Upgrade - a Poloidal Divertor Tokamak Adapted to Reactor Requirements', *Journal of Nuclear Materials*, **128**, 71 (1984), URL http://dx.doi.org/10.1016/0022-3115(84)90330-1

[18] Zohm H., the ASDEX Upgrade Team and the EUROfusion MST1 Team, 'Recent ASDEX Upgrade research in support of ITER and DEMO', *Nuclear Fusion*, **55**, 104010 (2015), URL http://dx.doi.org/Artn10401010.1088/0029-5515/55/10/104010

[19] Neu R., Dux R., Geier A., Kallenbach A., Pugno R., Rohde V., Bolshukhin D., Fuchs J.C., Gehre O., Gruber O., Hobirk J., Kaufmann M., Krieger K., Laux M., Maggi C., Murmann H., Neuhauser J., Ryter F., Sips A.C.C., Stabler A., Stober J., Suttrop W., Zohm H. and the ASDEX Upgrade Team, 'Impurity behaviour in the ASDEX Upgrade divertor tokamak with large area tungsten walls', *Plasma Physics and Controlled Fusion*, **44**, 811 (2002), URL http://dx.doi.org/10.1088/0741-3335/44/6/313

[20] Neu R., Kallenbach A., Balden M., Bobkov V., Coenen J.W., Drube R., Dux R., Greuner H., Herrmann A., Hobirk J., Hohnle H., Krieger K., Kocan M., Lang P., Lunt T., Maier H., Mayer M., Muller H.W., Potzel S., Pütterich T., Rapp J., Rohde V., Ryter F., Schneider P.A., Schweinzer J., Sertoli M., Stober J., Suttrop W., Sugiyama K., van Rooij G., Wischmeier M. and the ASDEX Upgrade Team, 'Overview on plasma operation with a full tungsten wall in ASDEX Upgrade', *Journal of Nuclear Materials*, **438**, S34 (2013), URL `http://dx.doi.org/10.1016/j.jnucmat.2013.01.006`

[21] Commission of the European Communities, 'The JET Project', Technical report, Commission of the European Communities (1976)

[22] Rebut P.H., Bickerton R.J. and Keen B.E., 'The Joint European Torus: installation, first results and prospects', *Nuclear Fusion*, **25**, 1011 (1985), URL `http://dx.doi.org/10.1088/0029-5515/25/9/003`

[23] Wagner F., Fussmann G., Grave T., Keilhacker M., Kornherr M., Lackner K., Mccormick K., Muller E.R., Stabler A., Becker G., Bernhardi K., Ditte U., Eberhagen A., Gehre O., Gernhardt J., Vongierke G., Glock E., Gruber O., Haas G., Hesse M., Janeschitz G., Karger F., Kissel S., Kluber O., Lisitano G., Mayer H.M., Meisel D., Mertens V., Murmann H., Poschenrieder W., Rapp H., Rohr H., Ryter F., Schneider F., Siller G., Smeulders P., Soldner F., Speth E., Steuer K.H., Szymanski Z. and Vollmer O., 'Development of an Edge Transport Barrier at the H-Mode Transition of ASDEX', *Physical Review Letters*, **53**, 1453 (1984), URL `http://dx.doi.org/10.1103/PhysRevLett.53.1453`

[24] Wagner F., 'A quarter-century of H-mode studies', *Plasma Physics and Controlled Fusion*, **49**, B1 (2007), URL `http://dx.doi.org/10.1088/0741-3335/49/12b/S01`

[25] Ryter F., Pütterich T., Reich M., Scarabosio A., Wolfrum E., Fischer R., Adamov M.G., Hicks N., Kurzan B., Maggi C., Neu R., Rohde V., Tardini G. and the ASDEX Upgrade Team, 'H-mode threshold and confinement in helium and deuterium in ASDEX Upgrade', *Nuclear Fusion*, **49**, 062003 (2009), URL `http://dx.doi.org/10.1088/0029-5515/49/6/062003`

[26] Connor J.W. and Wilson H.R., 'A review of theories of the L-H transition', *Plasma Physics and Controlled Fusion*, **42**, R1 (2000), URL `http://dx.doi.org/10.1088/0741-3335/42/1/201`

[27] Biglari H., Diamond P.H. and Terry P.W., 'Influence of Sheared Poloidal Rotation on Edge Turbulence', *Physics of Fluids B-Plasma Physics*, **2**, 1 (1990), URL `http://dx.doi.org/10.1063/1.859529`

[28] Ryter F., Angioni C., Beurskens M., Cirant S., Hoang G.T., Hogeweij G.M.D., Imbeaux F., Jacchia A., Mantica P., Suttrop W. and Tardini G., 'Experimental studies of electron transport', *Plasma Physics and Controlled Fusion*, **43**, A323 (2001), URL http://dx.doi.org/10.1088/0741-3335/43/12a/325

[29] Ryter F., Camenen Y., DeBoo J.C., Imbeaux F., Mantica P., Regnoli G., Sozzi C., Stroth U., ASDEX Upgrade Contributors, DIII-D Contributors, FTU Contributors, JET-EFDA Contributors, the TCV Team and the Tore Supra Team, 'Electron heat transport studies', *Plasma Physics and Controlled Fusion*, **48**, B453 (2006), URL http://dx.doi.org/10.1088/0741-3335/48/12b/S43

[30] Burrell K.H., Austin M.E., Brennan D.P., DeBoo J.C., Doyle E.J., Fenzi C., Fuchs C., Gohil P., Greenfield C.M., Groebner R.J., Lao L.L., Luce T.C., Makowski M.A., McKee G.R., Moyer R.A., Petty C.C., Porkolab M., Rettig C.L., Rhodes T.L., Rost J.C., Stallard B.W., Strait E.J., Synakowski E.J., Wade M.R., Watkins J.G. and West W.P., 'Quiescent double barrier high-confinement mode plasmas in the DIII-D tokamak', *Physics of Plasmas*, **8**, 2153 (2001), URL http://dx.doi.org/10.1063/1.1355981

[31] Suttrop W., Maraschek M., Conway G.D., Fahrbach H.U., Haas G., Horton L.D., Kurki-Suonio T., Lasnier C.J., Leonard A.W., Maggi C.F., Meister H., Muck A., Neu R., Nunes I., Pütterich T., Reich M., Sips A.C.C. and the ASDEX Upgrade Team, 'ELM-free stationary H-mode plasmas in the ASDEX upgrade tokamak', *Plasma Physics and Controlled Fusion*, **45**, 1399 (2003), URL http://dx.doi.org/10.1088/0741-3335/45/8/302

[32] Suttrop W., Hynönen V., Kurki-Suonio T., Lang P.T., Maraschek M., Neu R., Stäbler A., Conway G.D., Hacquin S., Kempenaars M., Lomas P.J., Nave M.F.F., Pitts R.A., Zastrow K.D., the ASDEX Upgrade Team and Contributors to the JET-EFDA workprogramme, 'Studies of the 'Quiescent H-mode' regime in ASDEX Upgrade and JET', *Nuclear Fusion*, **45**, 721 (2005), URL http://dx.doi.org/10.1088/0029-5515/45/7/021

[33] Greenwald M., Boivin R., Bonoli P., Budny R., Fiore C., Goetz J., Granetz R., Hubbard A., Hutchinson I., Irby J., LaBombard B., Lin Y., Lipschultz B., Marmar E., Mazurenko A., Mossessian D., T. Sunn Pedersen, Pitcher C.S., Porkolab M., Rice J., Rowan W., Snipes J., Schilling G., Takase Y., Terry J., Wolfe S., Weaver J., Welch B. and Wukitch S., 'Characterization of enhanced Dα high-confinement modes in Alcator C-Mod', *Physics of Plasmas*, **6**, 1943 (1999), URL http://dx.doi.org/10.1063/1.873451

[34] Maingi R., 'Enhanced confinement scenarios without large edge localized modes in tokamaks: control, performance, and extrapolability issues for ITER', *Nuclear Fusion*, **54**, 114016 (2014), URL http://dx.doi.org/10.1088/0029-5515/54/11/114016

[35] Zohm H., 'Edge localized modes (ELMs)', *Plasma Physics and Controlled Fusion*, **38**, 105 (1996), URL http://dx.doi.org/10.1088/0741-3335/38/2/001

[36] Connor J.W., 'Edge-localized modes - physics and theory', *Plasma Physics and Controlled Fusion*, **40**, 531 (1998), URL http://dx.doi.org/10.1088/0741-3335/40/5/002

[37] Loarte A., Becoulet M., Saibene G., Sartori R., Campbell D.J., Eich T., Herrmann A., Laux M., Suttrop W., Alper B., Lomas P.J., Matthews G., Jachmich S., Ongena J., Innocente P. and EFDA-JET Workprogramme Collaborators, 'Characteristics and scaling of energy and particle losses during Type I ELMs in JET H-modes', *Plasma Physics and Controlled Fusion*, **44**, 1815 (2002), URL http://dx.doi.org/10.1088/0741-3335/44/9/303

[38] Wolfrum E., Bernert M., Boom J.E., Burckhart A., Classen I.G.J., Conway G.D., Eich T., Fischer R., Gude A., Herrmann A., Luhmann N.C., Maraschek M., McDermott R., Park H.K., Pütterich T., Vicente J., Wieland B., Willensdorfer M. and the ASDEX Upgrade Team, 'Characterization of edge profiles and fluctuations in discharges with type-II and nitrogen-mitigated edge localized modes in ASDEX Upgrade', *Plasma Physics and Controlled Fusion*, **53**, 085026 (2011), URL http://dx.doi.org/10.1088/0741-3335/53/8/085026

[39] Suttrop W., 'The physics of large and small edge localized modes', *Plasma Physics and Controlled Fusion*, **42**, A1 (2000), URL http://dx.doi.org/10.1088/0741-3335/42/5a/301

[40] Kirk A., Ayed N.B., Counsell G., Dudson B., Eich T., Herrmann A., Koch B., Martin R., Meakins A., Saarelma S., Scannell R., Tallents S., Walsh M., Wilson H.R. and the MAST Team, 'Filament structures at the plasma edge on MAST', *Plasma Physics and Controlled Fusion*, **48**, B433 (2006), URL http://dx.doi.org/10.1088/0741-3335/48/12b/S41

[41] Federici G., Loarte A. and Strohmayer G., 'Assessment of erosion of the ITER divertor targets during type I ELMs', *Plasma Physics and Controlled Fusion*, **45**, 1523 (2003), URL http://dx.doi.org/10.1088/0741-3335/45/9/301

[42] Wolfrum E., Viezzer E., Burckhart A., Dunne M.G., Schneider P.A., Willensdorfer M., Fable E., Fischer R., Hatch D., Jenko F., Kurzan B., Manz P., Rathgeber S.K. and the ASDEX Upgrade Team, 'Overview of recent pedestal studies at ASDEX Upgrade', *Nuclear Fusion*, **55**, 053017 (2015), URL http://dx.doi.org/10.1088/0029-5515/55/5/053017

[43] Laggner F.M., Wolfrum E., Cavedon M., Mink F., Viezzer E., Dunne M.G., Manz P., Doerk H., Birkenmeier G., Fischer R., Fietz S., Maraschek M., Willensdorfer M., Aumayr F., the EUROfusion MST1 Team and the ASDEX Upgrade

Team, 'High frequency magnetic fluctuations correlated with the inter-ELM pedestal evolution in ASDEX Upgrade', *Plasma Physics and Controlled Fusion*, **58**, 065005 (2016), URL http://dx.doi.org/10.1088/0741-3335/58/6/065005

[44] Laggner F.M., Wolfrum E., Cavedon M., Mink F., Bernert M., Dunne M.G., Schneider P.A., Kappatou A., Birkenmeier G., Fischer R., Willensdorfer M., Aumayr F., the EUROfusion MST1 Team and the ASDEX Upgrade Team, 'Pedestal structure and inter-ELM evolution for different main ion species in ASDEX Upgrade', *Physics of Plasmas*, **24**, 056105 (2017), URL http://dx.doi.org/10.1063/1.4977461

[45] Laggner F.M., the EUROfusion MST1 Team and the ASDEX Upgrade Team, 'Divertor scrape off layer and pedestal dynamics in the ELM cycle on ASDEX Upgrade', *in preparation* (2017)

[46] Stober J., Gruber O., Kallenbach A., Mertens V., Ryter F., Stabler A., Suttrop W., Treutterer W. and the ASDEX Upgrade Team, 'Effects of triangularity on confinement, density limit and profile stiffness of H-modes on ASDEX upgrade', *Plasma Physics and Controlled Fusion*, **42**, A211 (2000), URL http://dx.doi.org/10.1088/0741-3335/42/5a/324

[47] Kirk A., Dunai D., Dunne M., Huijsmans G., Pamela S., Becoulet M., Harrison J.R., Hillesheim J., Roach C. and Saarelma S., 'Recent progress in understanding the processes underlying the triggering of and energy loss associated with type I ELMs', *Nuclear Fusion*, **54**, 114012 (2014), URL http://dx.doi.org/10.1088/0029-5515/54/11/114012

[48] Viezzer E., Cavedon M., Fable E., Snicker A., Angioni C., Dux R., Fietz S., Laggner F.M., McDermott R.M., Pütterich T., Odstrcil T., Ryter F., Wolfrum E., the the ASDEX Upgrade Team and the the EUROfusion MST1 Team, 'Ion heat and toroidal momentum transport studies in the H-mode transport barrier of ASDEX Upgrade', *submitted to Nuclear Fusion* (2017)

[49] Leonard A.W., 'Edge-localized-modes in tokamaks', *Physics of Plasmas*, **21**, 090501 (2014), URL http://dx.doi.org/10.1063/1.4894742

[50] Bickerton R.J., Connor J.W. and Taylor J.B., 'Diffusion Driven Plasma Currents and Bootstrap Tokamak', *Nature Physical Science*, **229**, 110 (1971), URL http://dx.doi.org/10.1038/physci229110a0

[51] Coronado M. and Wobig H., 'On the definition of Pfirsch–Schlüter and bootstrap currents in toroidal systems', *Physics of Fluids B: Plasma Physics*, **4**, 1294 (1992), URL http://dx.doi.org/10.1063/1.860085

[52] Freidberg J.P., *Plasma Physics and Fusion Energy*, Cambridge University Press, New York (2007)

[53] Peeters A.G., 'The bootstrap current and its consequences', *Plasma Physics and Controlled Fusion*, **42**, B231 (2000), URL http://dx.doi.org/10.1088/0741-3335/42/12b/318

[54] Miyamoto K., *Plasma Physics and Controlled Nuclear Fusion*, volume 38 of *Atomic, Optical, and Plasma Physics*, Springer (2005), URL http://link.springer.com/book/10.1007/3-540-28097-9

[55] Sauter O., Angioni C. and Lin-Liu Y.R., 'Neoclassical conductivity and bootstrap current formulas for general axisymmetric equilibria and arbitrary collisionality regime', *Physics of Plasmas*, **6**, 2834 (1999), URL http://dx.doi.org/10.1063/1.873240

[56] Sauter O., Angioni C. and Lin-Liu Y.R., 'Erratum: "Neoclassical conductivity and bootstrap current formulas for general axisymmetric equilibria and arbitrary collisionality regime" [Phys. Plasmas 6, 2834 (1999)]', *Physics of Plasmas*, **9**, 5140 (2002), URL http://dx.doi.org/10.1063/1.1517052

[57] Kessel C.E., 'Bootstrap Current in a Tokamak', *Nuclear Fusion*, **34**, 1221 (1994), URL http://dx.doi.org/10.1088/0029-5515/34/9/I04

[58] Wesson J., *Tokamaks*, Oxford University Press, Oxford, 3 edition (2004)

[59] Camenen Y., Pochelon A., Behn R., Bottino A., Bortolon A., Coda S., Karpushov A., Sauter O. and Zhuang G., 'Impact of plasma triangularity and collisionality on electron heat transport in TCV L-mode plasmas', *Nuclear Fusion*, **47**, 510 (2007), URL http://dx.doi.org/10.1088/0029-5515/47/7/002

[60] Wilson H.R., Cowley S.C., Kirk A. and Snyder P.B., 'Magneto-hydrodynamic stability of the H-mode transport barrier as a model for edge localized modes: an overview', *Plasma Physics and Controlled Fusion*, **48**, A71 (2006), URL http://dx.doi.org/10.1088/0741-3335/48/5a/S06

[61] Snyder P.B., Wilson H.R., Ferron J.R., Lao L.L., Leonard A.W., Osborne T.H., Turnbull A.D., Mossessian D., Murakami M. and Xu X.Q., 'Edge localized modes and the pedestal: A model based on coupled peeling-ballooning modes', *Physics of Plasmas*, **9**, 2037 (2002), URL http://dx.doi.org/10.1063/1.1449463

[62] Snyder P.B., Groebner R.J., Leonard A.W., Osborne T.H. and Wilson H.R., 'Development and validation of a predictive model for the pedestal height', *Physics of Plasmas*, **16**, 056118 (2009), URL http://dx.doi.org/10.1063/1.3122146

[63] Miller R.L., Chu M.S., Greene J.M., Lin-Liu Y.R. and Waltz R.E., 'Noncircular, finite aspect ratio, local equilibrium model', *Physics of Plasmas*, **5**, 973 (1998), URL http://dx.doi.org/10.1063/1.872666

[64] Wilson H.R. and Cowley S.C., 'Theory for explosive ideal magnetohydrodynamic instabilities in plasmas', *Physical Review Letters*, **92**, 175006 (2004), URL http://dx.doi.org/10.1103/PhysRevLett.92.175006

[65] Huysmans G.T.A., Pamela S., van der Plas E. and Ramet P., 'Non-linear MHD simulations of edge localized modes (ELMs)', *Plasma Physics and Controlled Fusion*, **51**, 124012 (2009), URL http://dx.doi.org/Artn12401210.1088/0741-3335/51/12/124012

[66] Huysmans G.T.A. and Czarny O., 'MHD stability in X-point geometry: simulation of ELMs', *Nuclear Fusion*, **47**, 659 (2007), URL http://dx.doi.org/10.1088/0029-5515/47/7/016

[67] Huysmans G.T.A., 'ELMs: MHD instabilities at the transport barrier', *Plasma Physics and Controlled Fusion*, **47**, B165 (2005), URL http://dx.doi.org/10.1088/0741-3335/47/12b/S13

[68] Huysmans G.T.A., 'External kink (peeling) modes in x-point geometry', *Plasma Physics and Controlled Fusion*, **47**, 2107 (2005), URL http://dx.doi.org/10.1088/0741-3335/47/12/003

[69] Maget P., Artaud J.F., Bécoulet M., Casper T., Faustin J., Garcia J., Huijsmans G.T.A., Loarte A. and Saibene G., 'MHD stability of the pedestal in ITER scenarios', *Nuclear Fusion*, **53**, 093011 (2013), URL http://dx.doi.org/10.1088/0029-5515/53/9/093011

[70] Carthy P.J.M., 'Analytical solutions to the Grad–Shafranov equation for tokamak equilibrium with dissimilar source functions', *Physics of Plasmas*, **6**, 3554 (1999), URL http://dx.doi.org/10.1063/1.873630

[71] Carthy P.J.M., 'Identification of edge-localized moments of the current density profile in a tokamak equilibrium from external magnetic measurements', *Plasma Physics and Controlled Fusion*, **54**, 015010 (2012), URL http://dx.doi.org/10.1088/0741-3335/54/1/015010

[72] Fischer R., Bock A., Dunne M., Fuchs J.C., Giannone L., Lackner K., McCarthy P.J., Poli E., Preuss R., Rampp M., Schubert M., Stober J., Suttrop W., Tardini G., Weiland M. and the ASDEX Upgrade Team, 'Coupling of the Flux Diffusion Equation with the Equilibrium Reconstruction at ASDEX Upgrade', *Fusion Science and Technology*, **69**, 526 (2016), URL http://dx.doi.org/10.13182/fst15-185

[73] Dunne M.G., 'Inter-ELM evolution of the edge current density profile on the ASDEX Upgrade tokamak', PhD thesis, University College Cork (2013)

[74] Dunne M.G., Frassinetti L., Beurskens M.N.A., Cavedon M., Fietz S., Fischer R., Giannone L., Huijsmans G.T.A., Kurzan B., Laggner F.M., McCarthy P.J., McDermott R.M., Tardini G., Viezzer E., Willensdorfer M., Wolfrum E., the EUROfusion MST1 Team and the ASDEX Upgrade Team, 'Global performance enhancements via pedestal optimisation on ASDEX Upgrade', *Plasma Physics and Controlled Fusion*, **59**, 025010 (2017), URL `http://dx.doi.org/10.1088/1361-6587/59/2/025010`

[75] Huysmans G.T.A., Goedbloed J., Kerner W. and Tenner A., 'Helena code', in *CP90 Europhysics Conf. on Computational Physics*, 371, World Scientific Publ. Co.

[76] Mikhailovskii A.B., Huysmans G.T.A., Kerner W.O.K. and Sharapov S.E., 'Optimization of computational MHD normal-mode analysis for tokamaks', Technical Report JET-P-96-25 (1997)

[77] Huysmans G.T.A., Sharapov S.E., Mikhailovskii A.B. and Kerner W., 'Modeling of diamagnetic stabilization of ideal magnetohydrodynamic instabilities associated with the transport barrier', *Physics of Plasmas*, **8**, 4292 (2001), URL `http://dx.doi.org/10.1063/1.1398573`

[78] Falchetto G.L., Coster D., Coelho R., Scott B.D., Figini L., Kalupin D., Nardon E., Nowak S., Alves L.L., Artaud J.F., Basiuk V., Bizarro J.P.S., Boulbe C., Dinklage A., Farina D., Faugeras B., Ferreira J., Figueiredo A., Huynh P., Imbeaux F., Ivanova-Stanik I., Jonsson T., Klingshirn H.J., Konz C., Kus A., Marushchenko N.B., Pereverzev G., Owsiak M., Poli E., Peysson Y., Reimer R., Signoret J., Sauter O., Stankiewicz R., Strand P., Voitsekhovitch I., Westerhof E., Zok T. and Zwingmann W., 'The European Integrated Tokamak Modelling (ITM) effort: achievements and first physics results', *Nuclear Fusion*, **54**, 043018 (2014), URL `http://dx.doi.org/10.1088/0029-5515/54/4/043018`

[79] Snyder P.B., Groebner R.J., Hughes J.W., Osborne T.H., Beurskens M., Leonard A.W., Wilson H.R. and Xu X.Q., 'A first-principles predictive model of the pedestal height and width: development, testing and ITER optimization with the EPED model', *Nuclear Fusion*, **51**, 103016 (2011), URL `http://dx.doi.org/10.1088/0029-5515/51/10/103016`

[80] Frieman E.A., Rewoldt G., Tang W.M. and Glasser A.H., 'General-Theory of Kinetic Ballooning Modes', *Physics of Fluids*, **23**, 1750 (1980), URL `http://dx.doi.org/10.1063/1.863201`

[81] Tang W.M., Connor J.W. and Hastie R.J., 'Kinetic-Ballooning-Mode Theory in General Geometry', *Nuclear Fusion*, **20**, 1439 (1980), URL http://dx.doi.org/10.1088/0029-5515/20/11/011

[82] Tang W.M., Rewoldt G., Cheng C.Z. and Chance M.S., 'Kinetic-Analysis of Mhd Ballooning Modes in Tokamaks', *Nuclear Fusion*, **25**, 151 (1985), URL http://dx.doi.org/10.1088/0029-5515/25/2/003

[83] Scott B.D., 'Computation of electromagnetic turbulence and anomalous transport mechanisms in tokamak plasmas', *Plasma Physics and Controlled Fusion*, **45**, A385 (2003), URL http://dx.doi.org/10.1088/0741-3335/45/12a/025

[84] Dickinson D., Roach C.M., Saarelma S., Scannell R., Kirk A. and Wilson H.R., 'Kinetic Instabilities that Limit beta in the Edge of a Tokamak Plasma: A Picture of an H-Mode Pedestal', *Physical Review Letters*, **108**, 135002 (2012), URL http://dx.doi.org/10.1103/PhysRevLett.108.135002

[85] Saarelma S., Beurskens M.N.A., Dickinson D., Frassinetti L., Leyland M.J., Roach C.M. and EFDA-JET Contributors, 'MHD and gyro-kinetic stability of JET pedestals', *Nuclear Fusion*, **53** (2013), URL http://dx.doi.org/10.1088/0029-5515/53/12/123012

[86] Hatch D.R., Told D., Jenko F., Doerk H., Dunne M.G., Wolfrum E., Viezzer E., Pueschel M.J. and the ASDEX Upgrade Team, 'Gyrokinetic study of ASDEX Upgrade inter-ELM pedestal profile evolution', *Nuclear Fusion*, **55**, 063028 (2015), URL http://dx.doi.org/10.1088/0029-5515/55/6/063028

[87] Doerk H., Jenko F., Pueschel M.J. and Hatch D.R., 'Gyrokinetic microtearing turbulence', *Physical Review Letters*, **106**, 155003 (2011), URL http://dx.doi.org/10.1103/PhysRevLett.106.155003

[88] Hatch D.R., Pueschel M.J., Jenko F., Nevins W.M., Terry P.W. and Doerk H., 'Origin of magnetic stochasticity and transport in plasma microturbulence', *Physical Review Letters*, **108**, 235002 (2012), URL http://dx.doi.org/10.1103/PhysRevLett.108.235002

[89] Dickinson D., Saarelma S., Scannell R., Kirk A., Roach C.M. and Wilson H.R., 'Towards the construction of a model to describe the inter-ELM evolution of the pedestal on MAST', *Plasma Physics and Controlled Fusion*, **53**, 115010 (2011), URL http://dx.doi.org/10.1088/0741-3335/53/11/115010

[90] Dickinson D., Roach C.M., Saarelma S., Scannell R., Kirk A. and Wilson H.R., 'Microtearing modes at the top of the pedestal', *Plasma Physics and Controlled Fusion*, **55**, 074006 (2013), URL http://dx.doi.org/10.1088/0741-3335/55/7/074006

[91] Hillesheim J.C., Dickinson D., Roach C.M., Saarelma S., Scannell R., Kirk A., Crocker N.A., Peebles W.A. and Meyer H., 'Intermediate-k density and magnetic field fluctuations during inter-ELM pedestal evolution in MAST', *Plasma Physics and Controlled Fusion*, **58**, 014020 (2015), URL `http://dx.doi.org/10.1088/0741-3335/58/1/014020`

[92] Hatch D.R., Kotschenreuther M., Mahajan S., Valanju P., Jenko F., Told D., Görler T. and Saarelma S., 'Microtearing turbulence limiting the JET-ILW pedestal', *Nuclear Fusion*, **56**, 104003 (2016), URL `http://dx.doi.org/10.1088/0029-5515/56/10/104003`

[93] Told D., Jenko F., Xanthopoulos P., Horton L.D., Wolfrum E. and the ASDEX Upgrade Team, 'Gyrokinetic microinstabilities in ASDEX Upgrade edge plasmas', *Physics of Plasmas*, **15**, 102306 (2008), URL `http://dx.doi.org/10.1063/1.3000132`

[94] Doerk H., Jenko F., Gorler T., Told D., Pueschel M.J. and Hatch D.R., 'Gyrokinetic prediction of microtearing turbulence in standard tokamaks', *Physics of Plasmas*, **19**, 055907 (2012), URL `http://dx.doi.org/10.1063/1.3694663`

[95] Manz P., Boom J.E., Wolfrum E., Birkenmeier G., Classen I.G.J., Luhmann N.C., Stroth U. and the ASDEX Upgrade Team, 'Velocimetry analysis of type-I edge localized mode precursors in ASDEX Upgrade', *Plasma Physics and Controlled Fusion*, **56**, 035010 (2014), URL `http://dx.doi.org/10.1088/0741-3335/56/3/035010`

[96] Diallo A., Kramer G.J., Smith D.R., Maingi R., Bell R.E., Guttenfelder W., LeBlanc B.P., Podesta M., McKee G.J. and Fonck R., 'Observation of ion scale fluctuations in the pedestal region during the edge-localized-mode cycle on the National Spherical Torus Experiment', *Physics of Plasmas*, **20**, 012505 (2013), URL `http://dx.doi.org/10.1063/1.4773402`

[97] Guttenfelder W., Candy J., Kaye S.M., Nevins W.M., Wang E., Zhang J., Bell R.E., Crocker N.A., Hammett G.W., LeBlanc B.P., Mikkelsen D.R., Ren Y. and Yuh H., 'Simulation of microtearing turbulence in national spherical torus experiment', *Physics of Plasmas*, **19**, 056119 (2012), URL `http://dx.doi.org/10.1063/1.3694104`

[98] Coury M., Guttenfelder W., Mikkelsen D.R., Canik J.M., Canal G.P., Diallo A., Kaye S., Kramer G.J., Maingi R. and NSTX-U Team, 'Linear gyrokinetic simulations of microinstabilities within the pedestal region of H-mode NSTX discharges in a highly shaped geometry', *Physics of Plasmas*, **23**, 062520 (2016), URL `http://dx.doi.org/10.1063/1.4954911`

[99] Kendl A., Scott B.D. and Ribeiro T.T., 'Nonlinear gyrofluid computation of edge localized ideal ballooning modes', *Physics of Plasmas*, **17**, 072302 (2010), URL http://dx.doi.org/10.1063/1.3449807

[100] Jenko F., Dorland W. and Hammett G.W., 'Critical gradient formula for toroidal electron temperature gradient modes', *Physics of Plasmas*, **8**, 4096 (2001), URL http://dx.doi.org/10.1063/1.1391261

[101] Happel T., Navarro A.B., Conway G.D., Angioni C., Bernert M., Dunne M., Fable E., Geiger B., Gorler T., Jenko F., McDermott R.M., Ryter F., Stroth U. and the ASDEX Upgrade Team, 'Core turbulence behavior moving from ion-temperature-gradient regime towards trapped-electron-mode regime in the ASDEX Upgrade tokamak and comparison with gyrokinetic simulation', *Physics of Plasmas*, **22**, 032503 (2015), URL http://dx.doi.org/10.1063/1.4914153

[102] Burckhart A., Wolfrum E., Fischer R., Lackner K., Zohm H. and the ASDEX Upgrade Team, 'Inter-ELM behaviour of the electron density and temperature pedestal in ASDEX Upgrade', *Plasma Physics and Controlled Fusion*, **52**, 105010 (2010), URL http://dx.doi.org/10.1088/0741-3335/52/10/105010

[103] Kojima A., Oyama N., Sakamoto Y., Kamada Y., Urano H., Kamiya K., Fujita T., Kubo H., Aiba N. and the JT-60 Team, 'Fast dynamics of type I and grassy ELMs in JT-60U', *Nuclear Fusion*, **49**, 115008 (2009), URL http://dx.doi.org/10.1088/0029-5515/49/11/115008

[104] Groebner R.J., Osborne T.H., Leonard A.W. and Fenstermacher M.E., 'Temporal evolution of H-mode pedestal in DIII-D', *Nuclear Fusion*, **49**, 045013 (2009), URL http://dx.doi.org/10.1088/0029-5515/49/4/045013

[105] Devynck P., Fedorczak N., Meyer O. and JET Contributors, 'Scaling of the frequencies of the type one edge localized modes and their effect on the tungsten source in JET ITER-like wall', *Plasma Physics and Controlled Fusion*, **58**, 125014 (2016), URL http://dx.doi.org/10.1088/0741-3335/58/12/125014

[106] Diallo A., Hughes J.W., Greenwald M., Labombard B., Davis E., Baek S.G., Theiler C., Snyder P., Canik J., Walk J., Golfinopoulos T., Terry J., Churchill M., Hubbard A., Porkolab M., Delgado-Aparicio L., Reinke M.L., White A. and the Alcator C-Mod Team, 'Observation of edge instability limiting the pedestal growth in tokamak plasmas', *Physical Review Letters*, **112**, 115001 (2014), URL http://dx.doi.org/10.1103/PhysRevLett.112.115001

[107] Diallo A., Hughes J.W., Baek S.G., LaBombard B., Terry J., Cziegler I., Hubbard A., Davis E., Walk J., Delgado-Aparicio L., Reinke M.L., Theiler C., Churchill R.M., Edlund E.M., Canik J., Snyder P., Greenwald M., White A. and the Alcator C-Mod Team, 'Quasi-coherent fluctuations limiting the pedestal

growth on Alcator C-Mod: experiment and modelling', *Nuclear Fusion*, **55**, 053003 (2015), URL http://dx.doi.org/10.1088/0029-5515/55/5/053003

[108] Bolzonella T., Zohm H., Maraschek M., Martines E., Saarelma S., Gunter S. and the ASDEX Upgrade Team, 'High frequency MHD activity related to type I ELMs in ASDEX upgrade', *Plasma Physics and Controlled Fusion*, **46**, A143 (2004), URL http://dx.doi.org/10.1088/0741-3335/46/5a/015

[109] Gao X., Zhang T., Han X., Zhang S.B., Wang Y.M., Liu Z.X., Yang Y., Liu S.C., Shi N., Ling B.L., Li J.G. and the EAST Team, 'Observation of Pedestal Plasma Turbulence on EAST Tokamak', *Plasma Science and Technology*, **15**, 732 (2013), URL http://dx.doi.org/10.1088/1009-0630/15/8/03

[110] Gao X., Zhang T., Han X., Zhang S.B., Kong D.F., Qu H., Wang Y.M., Wen F., Liu Z.X. and Huang C.B., 'Experimental study of pedestal turbulence on EAST tokamak', *Nuclear Fusion*, **55**, 083015 (2015), URL http://dx.doi.org/10.1088/0029-5515/55/8/083015

[111] Diallo A., Groebner R.J., Rhodes T.L., Battaglia D.J., Smith D.R., Osborne T.H., Canik J.M., Guttenfelder W. and Snyder P.B., 'Correlations between quasi-coherent fluctuations and the pedestal evolution during the inter-edge localized modes phase on DIII-D', *Physics of Plasmas*, **22**, 056111 (2015), URL http://dx.doi.org/10.1063/1.4921148

[112] Zhong W.L., Zou X.L., Shi Z.B., Duan X.R., Xu Y., Xu M., Chen W., Jiang M., Yang Z.C., Zhang B.Y., Shi P.W., Liu Z.T., Song X.M., Cheng J., Ji X.Q., Zhou Y., Yu D.L., Li J.X., Dong J.Q., Ding X.T., Liu Y., Yan L.W., Yang Q.W. and Liu Y., 'Excitation of edge plasma instabilities and their role in pedestal saturation in the HL-2A tokamak', *Plasma Physics and Controlled Fusion*, **58**, 065001 (2016), URL http://dx.doi.org/10.1088/0741-3335/58/6/065001

[113] Zhong W.L., Zou X.L., Gao J.M., Shi Z.B., Feng B.B., Cui Z.Y., Xu M., Shen Y., Dong J.Q., Ding X.T., Duan X.R., Liu Y. and the HL-2A Team, 'Impact of fuelling and impurity on pedestal dynamics and instabilities in the HL-2A tokamak', *Plasma Physics and Controlled Fusion*, **59**, 014030 (2017), URL http://dx.doi.org/10.1088/0741-3335/59/1/014030

[114] Perez C.P., Koslowski H.R., Hender T.C., Smeulders P., Loarte A., Lomas P.J., Saibene G., Sartori R., Becoulet M., Eich T., Hastie R.J., Huysmans G.T.A., Jachmich S., Rogister A., Schuller F.C. and JET-EFDA Contributors, 'Washboard modes as ELM-related events in JET', *Plasma Physics and Controlled Fusion*, **46**, 61 (2004), URL http://dx.doi.org/10.1088/0741-3335/46/1/005

[115] Perez C.P., Koslowski H.R., Huysmans G.T.A., Hender T.C., Smeulders P., Alper B., de la Luna E., Hastie R.J., Meneses L., Nave M.F.F., Parail V., Zerbini

M. and JET-EFDA Contributors, 'Type-I ELM precursor modes in JET', *Nuclear Fusion*, **44**, 609 (2004), URL http://dx.doi.org/10.1088/0029-5515/44/5/005

[116] Wolfrum E., Burckhart A., Fischer R., Hicks N., Konz C., Kurzan B., Langer B., Pütterich T., Zohm H. and the ASDEX Upgrade Team, 'Investigation of inter-ELM pedestal profiles in ASDEX Upgrade', *Plasma Physics and Controlled Fusion*, **51**, 124057 (2009), URL http://dx.doi.org/10.1088/0741-3335/51/12/124057

[117] Kallenbach A., Carlson A., Pautasso G., Peeters A., Seidel U., Zehrfeld H.P. and the ASDEX Upgrade Team, 'Electric currents in the scrape-off layer in ASDEX Upgrade', *Journal of Nuclear Materials*, **290**, 639 (2001), URL http://dx.doi.org/10.1016/S0022-3115(00)00445-1

[118] Chankin A.V., Coster D.P., Dux R., Fuchs C., Haas G., Herrmann A., Horton L.D., Kallenbach A., Kaufmann M., Konz C., Lackner K., Maggi C., Muller H.W., Neuhauser J., Pugno R., Reich M. and Schneider W., 'SOLPS modelling of ASDEX upgrade H-mode plasma', *Plasma Physics and Controlled Fusion*, **48**, 839 (2006), URL http://dx.doi.org/10.1088/0741-3335/48/6/010

[119] Mink F., Wolfrum E., Maraschek M., Zohm H., Horváth L., Laggner F.M., Manz P., Viezzer E. and Stroth U., 'Toroidal mode number determination of ELM associated phenomena on ASDEX Upgrade', *Plasma Physics and Controlled Fusion*, **58**, 125013 (2016), URL http://dx.doi.org/10.1088/0741-3335/58/12/125013

[120] Aumayr F. and Winter H., 'Plasmadiagnostik mit Lithiumatomstrahl-aktivierter Umladungsspektroskopie', *Annalen der Physik*, **497**, 228 (1985), URL http://dx.doi.org/10.1002/andp.19854970304

[121] Schorn R.P., Hintz E., Rusbuldt D., Aumayr F., Schneider M., Unterreiter E. and Winter H., 'Absolute Concentrations of Light Impurity Ions in Tokamak Discharges Measured with Lithium-Beam-Activated Charge-Exchange Spectroscopy', *Applied Physics B-Photophysics and Laser Chemistry*, **52**, 71 (1991), URL http://dx.doi.org/10.1007/Bf00357658

[122] Reich M., Wolfrum E., Schweinzer J., Ehmler H., Horton L.D., Neubauser J. and the ASDEX Upgrade Team, 'Lithium beam charge exchange diagnostic for edge ion temperature measurements at the ASDEX upgrade tokamak', *Plasma Physics and Controlled Fusion*, **46**, 797 (2004), URL http://dx.doi.org/10.1088/0741-3335/46/5/005

[123] Schweinzer J., Wolfrum E., Aumayr F., Pockl M., Winter H., Schorn R.P., Hintz E. and Unterreiter A., 'Reconstruction of Plasma Edge Density Profiles from Li

I (2s-2p) Emission Profiles', *Plasma Physics and Controlled Fusion*, **34**, 1173 (1992), URL http://dx.doi.org/10.1088/0741-3335/34/7/001

[124] Wolfrum E., Aumayr F., Wutte D., Winter H.P., Hintz E., Rusbuldt D. and Schorn R.P., 'Fast Lithium-Beam Spectroscopy of Tokamak Edge Plasmas', *Review of Scientific Instruments*, **64**, 2285 (1993), URL http://dx.doi.org/10.1063/1.1144460

[125] Thomas D.M., Hyatt A.W. and Thomas M.P., 'Edge Density Fluctuation Diagnostic for DIII-D Using Lithium Beams', *Review of Scientific Instruments*, **61**, 3040 (1990), URL http://dx.doi.org/10.1063/1.1141720

[126] Huber A., Samm U., Schweer B. and Mertens P., 'Results from a double Li-beam technique for measurement of both radial and poloidal components of electron density fluctuations using two thermal beams', *Plasma Physics and Controlled Fusion*, **47**, 409 (2005), URL http://dx.doi.org/10.1088/0741-3335/47/3/002

[127] Zoletnik S., Fiedler S., Kocsis G., McCormick G.K., Schweinzer J. and Winter H.P., 'Determination of electron density fluctuation correlation functions via beam emission spectroscopy', *Plasma Physics and Controlled Fusion*, **40**, 1399 (1998), URL http://dx.doi.org/10.1088/0741-3335/40/7/013

[128] Zoletnik S., Petravich G., Bencze A., Berta M., Fiedler S., McCormick K. and Schweinzer J., 'Two-dimensional density and density fluctuation diagnostic for the edge plasma in fusion devices', *Review of Scientific Instruments*, **76**, 073504 (2005), URL http://dx.doi.org/10.1063/1.1947757

[129] Kobayashi T., Birkenmeier G., Wolfrum E., Laggner F.M., Willensdorfer M., Stroth U., Inagaki S., Itoh S.I. and Itoh K., 'Method for estimating the propagation direction of a coherent plasma structure using a one-dimensional diagnostic array', *Review of Scientific Instruments*, **85**, 083507 (2014), URL http://dx.doi.org/10.1063/1.4893482

[130] Fiedler S., Brandenburg R., Baldzuhn J., McCormick K., Aumayr F., Schweinzer J., Winter H.P., the W7-AS and the ASDEX Upgrade Team, 'Edge plasma diagnostics on W7-AS and ASDEX-Upgrade using fast Li beams', *Journal of Nuclear Materials*, **266-269**, 1279 (1999), URL http://dx.doi.org/10.1016/s0022-3115(98)00862-9

[131] Kojima A., Kamiya K., Fujita T., Kubo H., Iguchi H., Oyama N., Suzuki T. and Kamada Y., 'Development of a Lithium Beam Probe and Measurement of Density Pedestal in JT-60U', *Plasma and Fusion Research*, **5**, 015 (2010), URL http://dx.doi.org/10.1585/pfr.5.015

[132] Brix M., Dodt D., Dunai D., Lupelli I., Marsen S., Melson T.F., Meszaros B., Morgan P., Petravich G., Refy D.I., Silva C., Stamp M., Szabolics T., Zastrow K.D., Zoletnik S. and JET-EFDA Contributors, 'Recent improvements of the JET lithium beam diagnostic', *Review of Scientific Instruments*, **83**, 10D533 (2012), URL http://dx.doi.org/10.1063/1.4739411

[133] Stoschus H., Thomas D.M., Hudson B., Watkins M., Finkenthal D.F., Moyer R.A. and Osborne T.H., 'Status and characterization of the lithium beam diagnostic on DIII-D', *Review of Scientific Instruments*, **84**, 083503 (2013), URL http://dx.doi.org/10.1063/1.4816824

[134] Willensdorfer M., Birkenmeier G., Fischer R., Laggner F.M., Wolfrum E., Veres G., Aumayr F., Carralero D., Guimarais L., Kurzan B. and the ASDEX Upgrade Team, 'Characterization of the Li-BES at ASDEX Upgrade', *Plasma Physics and Controlled Fusion*, **56**, 025008 (2014), URL http://dx.doi.org/10.1088/0741-3335/56/2/025008

[135] Willensdorfer M., 'Temporal behavior of the plasma edge density throughout the L-H transition in ASDEX Upgrade', PhD thesis, Technische Universität Wien (2013)

[136] Willensdorfer M., Wolfrum E., Fischer R., Schweinzer J., Sertoli M., Sieglin B., Veres G., Aumayr F. and the ASDEX Upgrade Team, 'Improved chopping of a lithium beam for plasma edge diagnostic at ASDEX Upgrade', *Review of Scientific Instruments*, **83**, 023501 (2012), URL http://dx.doi.org/10.1063/1.3682003

[137] Brandenburg R., Schweinzer J., Aumayr F. and Winter H.P., 'Li(2p <- 2s) excitation by impact of slow ions', *Journal of Physics B: Atomic, Molecular and Optical Physics*, **31**, 2585 (1998), URL http://dx.doi.org/10.1088/0953-4075/31/11/019

[138] Brandenburg R., Schweinzer J., Fiedler S., Aumayr F. and Winter H.P., 'Modelling of fast neutral Li beams for fusion edge plasma diagnostics', *Plasma Physics and Controlled Fusion*, **41**, 471 (1999), URL http://dx.doi.org/10.1088/0741-3335/41/4/002

[139] Schweinzer J., Brandenburg R., Bray I., Hoekstra R., Aumayr F., Janev R.K. and Winter H.P., 'Database for inelastic collisions of lithium atoms with electrons, protons, and multiply charged ions', *Atomic Data and Nuclear Data Tables*, **72**, 239 (1999), URL http://dx.doi.org/10.1006/adnd.1999.0815

[140] Wiese W.L., Smith M.W. and Miles B.M., *Atomic Transition Probabilities*, NSRDS- NBS 22. U.S.A. National Bureau of Standards, Washington DC (1969)

[141] Fischer R., Wolfrum E., Schweinzer J. and the ASDEX Upgrade Team, 'Probabilistic lithium beam data analysis', *Plasma Physics and Controlled Fusion*, **50**, 085009 (2008), URL http://dx.doi.org/10.1088/0741-3335/50/8/085009

[142] Kwak S., Svensson J., Brix M., Ghim Y.C. and JET Contributors, 'Bayesian modelling of the emission spectrum of the Joint European Torus Lithium Beam Emission Spectroscopy system', *Review of Scientific Instruments*, **87**, 023501 (2016), URL http://dx.doi.org/10.1063/1.4940925

[143] Kwak S., Svensson J., Brix M. and Ghim Y.C., 'Bayesian electron density inference from JET lithium beam emission spectra using Gaussian processes', *Nuclear Fusion*, **57**, 036017 (2017), URL http://dx.doi.org/10.1088/1741-4326/aa5072

[144] Guszejnov D., Pokol G.I., Pusztai I., Refy D., Zoletnik S., Lampert M. and Nam Y.U., 'Three-dimensional modeling of beam emission spectroscopy measurements in fusion plasmas', *Review of Scientific Instruments*, **83**, 113501 (2012), URL http://dx.doi.org/10.1063/1.4764564

[145] Cavedon M., 'The role of the radial electric field in the development of the edge transport barrier in the ASDEX Upgrade tokamak', PhD thesis, Technische Universität München (2016)

[146] Hutchinson I.H., *Principles of Plasma Diagnostics*, Cambridge University Press, New York, 2 edition (2005)

[147] Silva A., Manso M.E., Cupido L., Albrecht M., Serra F., Varela P., Santos J., Vergamota S., Eusebio F., Fernandes J., Grossmann T., Kallenbach A., Kurzan B., Loureiro C., Meneses L., Nunes I., Silva F. and Suttrop W., 'Ultrafast broadband frequency modulation of a continuous wave reflectometry system to measure density profiles on ASDEX Upgrade', *Review of Scientific Instruments*, **67**, 4138 (1996), URL http://dx.doi.org/10.1063/1.1147517

[148] Guimarais L., Potzel S., Silva C., Bernert M., Carralero D., Conway G.D., Gil L., Manso M.E., Nikolaeva V., Reimold F., Santos J., Silva A., Vicente J., Wolfrum E., the the ASDEX Upgrade Team and the EUROfusion MST1 Team, 'Poloidal asymmetries in the edge density profiles on ASDEX-Upgrade', *In preparation for Nuclear Fusion* (2017)

[149] Stroth U., *Plasmaphysik* (2011), URL http://link.springer.com/book/10.1007/978-3-8348-8326-1

[150] Mlynek A., 'Real-time control of the plasma density profile on ASDEX Upgrade', PhD thesis, Ludwig–Maximilians–Universität München (2010)

[151] Mlynek A., Reich M., Giannone L., Treutterer W., Behler K., Blank H., Buhler A., Cole R., Eixenberger H., Fischer R., Lohs A., Luddecke K., Merkel R., Neu G., Ryter F., Zasche D. and the ASDEX Upgrade Team, 'Real-time feedback control of the plasma density profile on ASDEX Upgrade', *Nuclear Fusion*, **51**, 043002 (2011), URL http://dx.doi.org/10.1088/0029-5515/51/4/043002

[152] Kurzan B., Murmann H., Salzmann H. and the ASDEX Upgrade Team, 'Improvements in the evaluation of Thomson scattering data on ASDEX upgrade', *Review of Scientific Instruments*, **72**, 1111 (2001), URL http://dx.doi.org/10.1063/1.1321747

[153] Kurzan B., Jakobi M., Murmann H. and the ASDEX Upgrade Team, 'Signal processing of Thomson scattering data in a noisy environment in ASDEX Upgrade', *Plasma Physics and Controlled Fusion*, **46**, 299 (2004), URL http://dx.doi.org/10.1088/0741-3335/46/1/019

[154] Kurzan B., Murmann H.D., Neuhauser J. and the ASDEX Upgrade Team, 'Fine structure of type-I edge-localized modes in the steep gradient region', *Physical Review Letters*, **95**, 145001 (2005), URL http://dx.doi.org/10.1103/PhysRevLett.95.145001

[155] Kurzan B., Fuchs C., Scarabosio A., Scott B.D. and the ASDEX Upgrade Team, 'Scale lengths of inter-ELM fluctuations in the pedestal of ASDEX Upgrade', *Plasma Physics and Controlled Fusion*, **51**, 065009 (2009), URL http://dx.doi.org/10.1088/0741-3335/51/6/065009

[156] Rathgeber S.K., Barrera L., Eich T., Fischer R., Nold B., Suttrop W., Willensdorfer M., Wolfrum E. and the ASDEX Upgrade Team, 'Estimation of edge electron temperature profiles via forward modelling of the electron cyclotron radiation transport at ASDEX Upgrade', *Plasma Physics and Controlled Fusion*, **55**, 025004 (2013), URL http://dx.doi.org/10.1088/0741-3335/55/2/025004

[157] Weinlich M., 'Elektrostatische Sonden in starken Magnetfeldern', PhD thesis, Technische Universität München (1995)

[158] Suttrop W., Peeters A.G., the ASDEX Upgrade Team and the NBI group, 'Practical limitations to plasma edge electron temperature measurements by radiometry of electron cyclotron emission', Technical report (1996)

[159] Willensdorfer M., Denk S.S., Strumberger E., Suttrop W., Vanovac B., Brida D., Cavedon M., Classen I., Dunne M., Fietz S., Fischer R., Kirk A., Laggner F.M., Liu Y.Q., Odstrčil T., Ryan D.A., Viezzer E., Zohm H. and Luhmann I.C., 'Plasma response measurements of external magnetic perturbations using electron cyclotron emission and comparisons to 3D ideal MHD equilibrium', *Plasma Physics and Controlled Fusion*, **58**, 114004 (2016), URL http://dx.doi.org/10.1088/0741-3335/58/11/114004

[160] Isler R.C., 'A Review of Charge-Exchange Spectroscopy and Applications to Fusion Plasmas', *Physica Scripta*, **35**, 650 (1987), URL http://dx.doi.org/10.1088/0031-8949/35/5/007

[161] Viezzer E., Pütterich T., Dux R., McDermott R.M. and the ASDEX Upgrade Team, 'High-resolution charge exchange measurements at ASDEX Upgrade', *Review of Scientific Instruments*, **83**, 103501 (2012), URL http://dx.doi.org/10.1063/1.4755810

[162] Geiger B., 'Fast-ion transport studies using FIDA spectroscopy at the ASDEX Upgrade tokamak', PhD thesis, Ludwig-Maximilians-Universität München (2012)

[163] Pütterich T., Wolfrum E., Dux R., Maggi C.F. and the ASDEX Upgrade Team, 'Evidence for Strong Inversed Shear of Toroidal Rotation at the Edge-Transport Barrier in the ASDEX Upgrade', *Physical Review Letters*, **102**, 025001 (2009), URL http://dx.doi.org/10.1103/PhysRevLett.102.025001

[164] Cavedon M., Pütterich T., Viezzer E., Dux R.M., Geiger B., McDermott R., Meyer H., Stroth U. and the the ASDEX Upgrade Team, 'A fast acquisition rate system for charge exchange measurements at the plasma edge at the ASDEX Upgrade tokamak', *Submitted to Review of Scientific Instruments* (2017)

[165] Cavedon M., Pütterich T., Viezzer E., Laggner F.M., Burckhart A., Dunne M.G., Fischer R., Lebschy A., Mink F., Stroth U., Willensdorfer M., Wolfrum E. and the ASDEX Upgrade Team, 'Pedestal and E_r profile evolution during an edge localized mode cycle at ASDEX Upgrade', *Submitted to Plasma Physics and Controlled Fusion* (2017)

[166] Fischer R., Fuchs C.J., Kurzan B., Suttrop W., Wolfrum E. and the ASDEX Upgrade Team, 'Integrated Data Analysis of Profile Diagnostics at ASDEX Upgrade', *Fusion Science and Technology*, **58**, 675 (2010), URL http://dx.doi.org/10.13182/FST10-110

[167] Urano H., Suttrop W., Horton L.D., Herrmann A., Fuchs J.C. and the ASDEX Upgrade Team, 'Energy and particle losses during type-I ELMy H-mode in ASDEX Upgrade', *Plasma Physics and Controlled Fusion*, **45**, 1571 (2003), URL http://dx.doi.org/10.1088/0741-3335/45/9/303

[168] Neuhauser J., Coster D., Fahrbach H.U., Fuchs J.C., Haas G., Herrmann A., Horton L., Jakobi M., Kallenbach A., Laux M., Kim J.W., Kurzan B., Muller H.W., Murmann H., Neu R., Rohde V., Sandmann W., Suttrop W., Wolfrum E. and the ASDEX Upgrade Team, 'Transport into and across the scrape-off layer in the ASDEX Upgrade divertor tokamak', *Plasma Physics and Controlled Fusion*, **44**, 855 (2002), URL http://dx.doi.org/10.1088/0741-3335/44/6/316

[169] Horváth L., Poloskei P.Z., Papp G., Maraschek M., Schuhbeck K.H., Pokol G.I., the EUROfusion MST1 Team and the ASDEX Upgrade Team, 'Reducing systematic errors in time-frequency resolved mode number analysis', *Plasma Physics and Controlled Fusion*, **57**, 125005 (2015), URL http://dx.doi.org/10.1088/0741-3335/57/12/125005

[170] Ida K. and Hidekuma S., 'Edge electric-field profiles of H-mode plasmas in the JFT-2M tokamak', *Physical Review Letters*, **65**, 1364 (1990), URL http://dx.doi.org/10.1103/PhysRevLett.65.1364

[171] Viezzer E., Pütterich T., Angioni C., Bergmann A., Dux R., Fable E., McDermott R.M., Stroth U., Wolfrum E. and the ASDEX Upgrade Team, 'Evidence for the neoclassical nature of the radial electric field in the edge transport barrier of ASDEX Upgrade', *Nuclear Fusion*, **54**, 012003 (2014), URL http://dx.doi.org/10.1088/0029-5515/54/1/012003

[172] Viezzer E., Pütterich T., Conway G.D., Dux R., Happel T., Fuchs J.C., McDermott R.M., Ryter F., Sieglin B., Suttrop W., Willensdorfer M., Wolfrum E. and the ASDEX Upgrade Team, 'High-accuracy characterization of the edge radial electric field at ASDEX Upgrade', *Nuclear Fusion*, **53**, 053005 (2013), URL http://dx.doi.org/10.1088/0029-5515/53/5/053005

[173] Viezzer E., Pütterich T., McDermott R.M., Conway G.D., Cavedon M., Dunne M.G., Dux R. and Wolfrum E., 'Parameter dependence of the radial electric field in the edge pedestal of hydrogen, deuterium and helium plasmas', *Plasma Physics and Controlled Fusion*, **56**, 075018 (2014), URL http://dx.doi.org/10.1088/0741-3335/56/7/075018

[174] Perez von Thun C.P., Maraschek M., da Graça S., Buttery R.J., Herrmann A., Stober J., Conway G., Eich T., Fuchs J.C., Horton L.D., Igochine V., Kallenbach A., Loarte A., Müller H.W., Nunes I., Saibene G., Sartori R., Sips A.C.C., Suttrop W. and Wolfrum E., 'Identifying the MHD signature and power deposition characteristics associated with type-II ELMs in ASDEX Upgrade', *Plasma Physics and Controlled Fusion*, **50**, 065018 (2008), URL http://dx.doi.org/10.1088/0741-3335/50/6/065018

[175] Scott B.D., 'The nonlinear drift wave instability and its role in tokamak edge turbulence', *New Journal of Physics*, **4**, 52 (2002), URL http://dx.doi.org/10.1088/1367-2630/4/1/352

[176] Snyder P.B., Burrell K.H., Wilson H.R., Chu M.S., Fenstermacher M.E., Leonard A.W., Moyer R.A., Osborne T.H., Umansky M., West W.P. and Xu X.Q., 'Stability and dynamics of the edge pedestal in the low collisionality regime: physics mechanisms for steady-state ELM-free operation', *Nuclear*

Fusion, **47**, 961 (2007), URL http://dx.doi.org/10.1088/0029-5515/47/8/030

[177] Boucher D. and Mukhovatov V., 'Impact of H-mode power threshold on ITER performance and operation', *Plasma Physics and Controlled Fusion*, **38**, 1225 (1996), URL http://dx.doi.org/10.1088/0741-3335/38/8/013

[178] Martin Y.R., Takizuka T. and the ITPA CDBM H-mode Threshold Database Working Group, 'Power requirement for accessing the H-mode in ITER', *11th Iaea Technical Meeting on H-Mode Physics and Transport Barriers*, **123**, 012033 (2008), URL http://dx.doi.org/10.1088/1742-6596/123/1/012033

[179] Ryter F., Rathgeber S.K., Orte L.B., Bernert M., Conway G.D., Fischer R., Happel T., Kurzan B., McDermott R.M., Scarabosio A., Suttrop W., Viezzer E., Willensdorfer M., Wolfrum E. and the ASDEX Upgrade Team, 'Survey of the H-mode power threshold and transition physics studies in ASDEX Upgrade', *Nuclear Fusion*, **53**, 113003 (2013), URL http://dx.doi.org/10.1088/0029-5515/53/11/113003

[180] Gohil P., Jernigan T.C., Scoville J.T. and Strait E.J., 'The H-mode power threshold in hydrogen plasmas in DIII-D', *Nuclear Fusion*, **49**, 115004 (2009), URL http://dx.doi.org/10.1088/0029-5515/49/11/115004

[181] Gohil P., Jernigan T.C., Osborne T.H., Scoville J.T. and Strait E.J., 'The torque dependence of the H-mode power threshold in hydrogen, deuterium and helium plasmas in DIII-D', *Nuclear Fusion*, **50**, 064011 (2010), URL http://dx.doi.org/10.1088/0029-5515/50/6/064011

[182] Behn R., Labit B., Duval B.P., Karpushov A., Martin Y., Porte L. and the TCV Team, 'Threshold power for the transition into H-mode for H, D, and He plasmas in TCV', *Plasma Physics and Controlled Fusion*, **57**, 025007 (2015), URL http://dx.doi.org/10.1088/0741-3335/57/2/025007

[183] Righi E., Bartlett D., Conway G., Cordey J.G., Eriksson L.G., Gormezano C., de Haas J.C.M., Horton L., Jacquinot J., Lowry C., Saibene G., Sartori R., Stamp M., Start D.F.H. and Thomsen K., 'Global and local conditions for the L-H and H-L transitions on JET', *Plasma Physics and Controlled Fusion*, **40**, 721 (1998), URL http://dx.doi.org/10.1088/0741-3335/40/5/031

[184] Righi E., Bartlett D.V., Christiansen J.P., Conway G.D., Cordey J.G., Eriksson L.G., De Esch H.P.L., Fishpool G.M., Gowers C.W., de Haas J.C.M., Harbour P.J., Hawkes N.C., Jacquinot J., Jones T.T.C., Kerner W., King Q.A., Lowry C.G., Monk R.D., Nielsen P., Rimini F.G., Saibene G., Sartori R., Schunke B., Sips A.C.C., Smith R.J., Stamp M.F., Start D.F.H., Thomsen K., Tubbing B.J.D. and Zornig N., 'Isotope scaling of the H mode power threshold

on JET', *Nuclear Fusion*, **39**, 309 (1999), URL http://dx.doi.org/10.1088/0029-5515/39/3/302

[185] Ryter F., Cavedon M., Happel T., McDermott R.M., Viezzer E., Conway G.D., Fischer R., Kurzan B., Pütterich T., Tardini G., Willensdorfer M. and the ASDEX Upgrade Team, 'L-H transition physics in hydrogen and deuterium: key role of the edge radial electric field and ion heat flux', *Plasma Physics and Controlled Fusion*, **58**, 014007 (2016), URL http://dx.doi.org/10.1088/0741-3335/58/1/014007

[186] Tibone F., Balet B., Bures M., Cordey J.G., Jones T.T.C., Lomas P.J., Lawson K., Morsi H.W., Nielsen P., Start D.F.H., Tanga A., Taroni A., Thomsen K. and Ward D.J., 'Dependence of L-Mode Confinement on Plasma Ion Species in JET', *Nuclear Fusion*, **33**, 1319 (1993), URL http://dx.doi.org/10.1088/0029-5515/33/9/I07

[187] Bessenrodt-Weberpals M., Wagner F., Gehre O., Giannone L., Hofmann J.V., Kallenbach A., McCormick K., Mertens V., Murmann H.D., Ryter F., Scott B.D., Siller G., Soldner F.X., Stabler A., Steuer K.H., Stroth U., Tsois N., Verbeek H. and Zohm H., 'The isotope effect in ASDEX', *Nuclear Fusion*, **33**, 1205 (1993), URL http://dx.doi.org/10.1088/0029-5515/33/8/i09

[188] Wagner F. and Stroth U., 'Transport in toroidal devices-the experimentalist's view', *Plasma Physics and Controlled Fusion*, **35**, 1321 (1993), URL http://dx.doi.org/10.1088/0741-3335/35/10/002

[189] Luce T.C., Petty C.C. and Cordey J.G., 'Application of dimensionless parameter scaling techniques to the design and interpretation of magnetic fusion experiments', *Plasma Physics and Controlled Fusion*, **50**, 043001 (2008), URL http://dx.doi.org/10.1088/0741-3335/50/4/043001

[190] McDonald D.C., 'The dimensionless scaling of ELMy H-mode confinement', *Comptes Rendus Physique*, **7**, 584 (2006), URL http://dx.doi.org/10.1016/j.crhy.2006.06.003

[191] Urano H., Takizuka T., Kikuchi M., Nakano T., Hayashi N., Oyama N. and Kamada Y., 'Small Ion-Temperature-Gradient Scale Length and Reduced Heat Diffusivity at Large Hydrogen Isotope Mass in Conventional H-Mode Plasmas', *Physical Review Letters*, **109** (2012), URL http://dx.doi.org/10.1103/PhysRevLett.109.125001

[192] Urano H., Takizuka T., Fujita T., Kamada Y., Nakano T., Oyama N. and the JT-60 Team, 'Energy confinement of hydrogen and deuterium H-mode plasmas in JT-60U', *Nuclear Fusion*, **52**, 114021 (2012), URL http://dx.doi.org/10.1088/0029-5515/52/11/114021

[193] Bhatnagar V.P., Lingertat J., Barnsley R., Breger P., Christiansen J.P., Clement S., Cordey J.G., Davies S.J., Ehrenberg J.K., Eriksson L.G., Fishpool G.M., Harbour P.J., Horton L.D., Jacquinot J., Jackel H.J., Lawson K., Lowry C.G., Maggi C.F., Matthews G.F., Monk R.D., O'Brien D.P., Parail V.V., Righi E., Saibene G., Sartori R., Schunke B., Sips A.C.C., Stamp M.F., Start D.F.H. and Thomsen K., 'Edge localized modes and edge pedestal in NBI and ICRF heated H, D and T plasmas in JET', *Nuclear Fusion*, **39**, 353 (1999), URL `http://dx.doi.org/10.1088/0029-5515/39/3/305`

[194] Scarabosio A., Fuchs C., Herrmann A., Wolfrum E. and the ASDEX Upgrade Team, 'ELM characteristics and divertor heat loads in ASDEX Upgrade helium discharges', *Journal of Nuclear Materials*, **415**, S877 (2011), URL `http://dx.doi.org/10.1016/j.jnucmat.2010.10.062`

[195] McDonald D.C., Cordey J.G., Righi E., Ryter F., Saibene G., Sartori R., Alper B., Becoulet M., Brzozowski J., Coffey I., de Baar M., de Vries P., Erents K., Fundamenski W., Giroud C., Jenkins I., Loarte A., Lomas P.J., Maddison G.P., Mailloux J., Murari A., Ongena J., Rapp J., Pitts R.A., Stamp M., Strachan J., Suttrop W. and JET-EFDA Contributers, 'ELMy H-modes in JET helium-4 plasmas', *Plasma Physics and Controlled Fusion*, **46**, 519 (2004), URL `http://dx.doi.org/10.1088/0741-3335/46/3/007`

[196] Urano H., Takizuka T., Aiba N., Kikuchi M., Nakano T., Fujita T., Oyama N., Kamada Y., Hayashi N. and the JT-60 Team, 'Hydrogen isotope effects on ITG scale length, pedestal and confinement in JT-60 H-mode plasmas', *Nuclear Fusion*, **53**, 083003 (2013), URL `http://dx.doi.org/10.1088/0029-5515/53/8/083003`

[197] Urano H., 'Pedestal structure in H-mode plasmas', *Nuclear Fusion*, **54**, 116001 (2014), URL `http://dx.doi.org/10.1088/0029-5515/54/11/116001`

[198] Carralero D., Manz P., Aho-Mantila L., Birkenmeier G., Brix M., Groth M., Muller H.W., Stroth U., Vianello N., Wolfrum E., the ASDEX Upgrade Team, JET Contributors and the EUROfusion MST1 Team, 'Experimental Validation of a Filament Transport Model in Turbulent Magnetized Plasmas', *Physical Review Letters*, **115**, 215002 (2015), URL `http://dx.doi.org/10.1103/PhysRevLett.115.215002`

[199] Carralero D., Madsen J., Artene S.A., Bernert M., Birkenmeier G., Eich T., Fuchert G., Laggner F.M., Naulin V., Manz P., Vianello N. and Wolfrum E., 'A study on the density shoulder formation in the SOL of H-mode plasmas', *Nuclear Materials and Energy* (2016), URL `http://dx.doi.org/10.1016/j.nme.2016.11.016`

[200] Dunne M.G., Potzel S., Reimold F., Wischmeier M., Wolfrum E., Frassinetti L., Beurskens M., Bilkova P., Cavedon M., Fischer R., Kurzan B., Laggner F.M., McDermott R.M., Tardini G., Trier E., Viezzer E. and Willensdorfer M., 'The role of the density profile in the ASDEX-Upgrade pedestal structure', *Plasma Physics and Controlled Fusion*, **59**, 014017 (2017), URL http://dx.doi.org/10.1088/0741-3335/59/1/014017

[201] Wade M.R., Hillis D.L., Hogan J.T., Mahdavi M.A., Maingi R., West W.P., Brooks N.H., Burrell K.H., Groebner R.J., Jackson G.L., Klepper C.C., Laughon G., Menon M.M. and Mioduszewski P.K., 'Helium Exhaust Studies in H-Mode Discharges in the DIII-D Tokamak Using an Argon-Frosted Divertor Cryopump', *Physical Review Letters*, **74**, 2702 (1995), URL http://dx.doi.org/10.1103/PhysRevLett.74.2702

[202] Dunne M.G., McCarthy P.J., Wolfrum E., Fischer R., Giannone L., Burckhart A. and the ASDEX Upgrade Team, 'Measurement of neoclassically predicted edge current density at ASDEX Upgrade', *Nuclear Fusion*, **52**, 123014 (2012), URL http://dx.doi.org/10.1088/0029-5515/52/12/123014

[203] Neuhauser J., Alexander M., Becker G., Bosch H.S., Buchl K., Coster D., Dux R., Field A., Fiedler S., Fuchs C., Gehre O., Gruber O., Haas G., Herrmann A., Hirsch S., Kallenbach A., Kaufmann M., Lackner K., Lieder G., Mast K.F., Mertens V., Murmann H., Napiontek B., Neu R., Ryter F., Salzmann H., Schneider R., Schweinzer J., Sokoll M., Steuer K.H., Stober J., Suttrop W., Weinlich M., Wenzel U., Zehrfeld H.P., Zohm H., Albrecht M., Asmussen K., Behler K., Behringer K., Bessenrodt-Weberpals M., Brambilla M., Carlson A., Chodura R., Cupido L., DeBlank H.J., Hempel S.D.P., Deschka S., Dorn C., Drube R., Engelhardt W., Fahrbach H.U., Feist H.U., Fieg G., Fussmann G., Garcia-Rosales C., Gernhardt J., Herrmann W., Ignacz P., Juttner B., Junker W., Kass T., Koppendorfer W., Kollotzek H., Krieger K., Kurzan B., Lang P., Lang R., Laux M., Manso M.E., Maraschek M., McCarthy P., Meisel D., Merkel R., Naujoks D., Neu G., Niethammer M., Noterdaeme J.M., Pautasso G., Pitcher C.S., Poschenrieder W., Raupp G., Rohr H., Roth J., Sandmann W., Schilling H.B., Schittenhelm M., Schneider H., Schneider W., Schonmann K., Schramm G., Seidel U., Serra F., Silva A., Speth E., Stabler A., Streibl B., Treutterer W., Troppmann M., Ulrich M. *et al.*, 'The compatibility of high confinement times and complete divertor detachment in ASDEX-Upgrade', *Plasma Physics and Controlled Fusion*, **37**, A37 (1995), URL http://dx.doi.org/10.1088/0741-3335/37/11a/003

[204] Wenninger R.P., Bernert M., Eich T., Fable E., Federici G., Kallenbach A., Loarte A., Lowry C., McDonald D., Neu R., Pütterich T., Schneider P., Sieglin B., Strohmayer G., Reimold F. and Wischmeier M., 'DEMO divertor limitations

during and in between ELMs', *Nuclear Fusion*, **54**, 114003 (2014), URL http://dx.doi.org/10.1088/0029-5515/54/11/114003

[205] Potzel S., Wischmeier M., Bernert M., Dux R., Reimold F., Scarabosio A., Brezinsek S., Clever M., Huber A., Meigs A., Stamp M., the ASDEX Upgrade Team and JET-EFDA Contributors, 'Formation of the high density front in the inner far SOL at ASDEX Upgrade and JET', *Journal of Nuclear Materials*, **463**, 541 (2015), URL http://dx.doi.org/10.1016/j.jnucmat.2014.12.008

[206] Reimold F., Wischmeier M., Potzel S., Guimarais L., Reiter D., Bernert M. and Dunne M.G., 'The high-field side high density region in SOLPS-modeling of nitrogen-seeded H-modes in ASDEX Upgrade', *submitted to Nuclear Materials and Energy* (2017)

[207] Dunne M.G., 'Impact of impurity seeding and divertor conditions on transitions, pedestal structure and ELMs', *Nuclear Fusion*, **57**, 025002 (2017), URL http://dx.doi.org/10.1088/0029-5515/57/2/025002

[208] Wischmeier M., Kallenbach A., Chankin A.V., Coster D.P., Eich T., Herrmann A. and Muller H.W., 'High recycling outer divertor regimes after type-I ELMs at high density in ASDEX Upgrade', *Journal of Nuclear Materials*, **363**, 448 (2007), URL http://dx.doi.org/10.1016/j.jnucmat.2007.01.041

[209] Kallenbach A., Dux R., Eich T., Fischer R., Giannone L., Harhausen J., Herrmann A., Muller H.W., Pautasso G., Wischmeier M. and the ASDEX Upgrade Team, 'Divertor power and particle fluxes between and during type-I ELMs in the ASDEX Upgrade', *Nuclear Fusion*, **48**, 085008 (2008), URL http://dx.doi.org/10.1088/0029-5515/48/8/085008

[210] Brezinsek S., Wiesen S., Harting D., Guillemaut C., Webster A.J., Heinola K., Meigs A.G., Rack M., Gao Y., Sergienko G., Philipps V., Stamp M.F., Jachmich S. and JET Contributors, 'Characterisation of the deuterium recycling at the W divertor target plates in JET during steady-state plasma conditions and ELMs', *Physica Scripta*, **T167**, 014076 (2016), URL http://dx.doi.org/10.1088/0031-8949/t167/1/014076

[211] Schmid K., 'Diffusion-trapping modelling of hydrogen recycling in tungsten under ELM-like heat loads', *Physica Scripta*, **T167**, 014025 (2016), URL http://dx.doi.org/10.1088/0031-8949/t167/1/014025

[212] Pigarov A.Y., Krasheninnikov S.I., Rognlien T.D., Hollmann E.M., Lasnier C.J. and Unterberg E., 'Multi-fluid transport code modeling of time-dependent recycling in ELMy H-mode', *Physics of Plasmas*, **21**, 062514 (2014), URL http://dx.doi.org/10.1063/1.4885346

[213] LaBombard B., 'KN1D: A 1-D Space, 2-D Velocity, Kinetic Transport Algorithm For Atomic and Molecular Hydrogen in an Ionizing Plasma', Technical Report PSFC/RR-01-3, Plasma Science and Fusion Center, Massachusetts Institute of Technology (2001)

[214] Sun H.J., Wolfrum E., Eich T., Kurzan B., Potzel S. and Stroth U., 'Study of near scrape-off layer (SOL) temperature and density gradient lengths with Thomson scattering', *Plasma Physics and Controlled Fusion*, **57**, 125011 (2015), URL http://dx.doi.org/10.1088/0741-3335/57/12/125011

[215] Willensdorfer M., Fable E., Wolfrum E., Aho-Mantila L., Aumayr F., Fischer R., Reimold F. and Ryter F., 'Particle transport analysis of the density build-up after the L–H transition in ASDEX Upgrade', *Nuclear Fusion*, **53**, 093020 (2013), URL http://dx.doi.org/10.1088/0029-5515/53/9/093020

[216] Saibene G., Horton L.D., Sartori R., Balet B., Clement S., Conway G.D., Cordey J.G., De Esch H.P.L., Ingesson L.C., Lingertat J., Monk R.D., Parail V.V., Smith R.J., Taroni A., Thomsen K. and von Hellermann M.G., 'The influence of isotope mass, edge magnetic shear and input power on high density ELMy H modes in JET', *Nuclear Fusion*, **39**, 1133 (1999), URL http://dx.doi.org/Doi10.1088/0029-5515/39/9/307

[217] Suttrop W., Gruber O., Kurzan B., Murmann H.D., Neuhauser J., Schweinzer J., Stober J., Treutterer W. and the ASDEX Upgrade Team, 'Effect of plasma shape variation on ELMs and H-mode pedestal properties in ASDEX Upgrade', *Plasma Physics and Controlled Fusion*, **42**, A97 (2000), URL http://dx.doi.org/10.1088/0741-3335/42/5a/308

[218] Osborne T.H., Ferron J.R., Groebner R.J., Lao L.L., Leonard A.W., Mahdavi M.A., Maingi R., Miller R.L., Turnbull A.D., Wade M. and Watkins J., 'The effect of plasma shape on H-mode pedestal characteristics on DIII-D', *Plasma Physics and Controlled Fusion*, **42**, A175 (2000), URL http://dx.doi.org/10.1088/0741-3335/42/5a/319

[219] Kallenbach A., Beurskens M.N.A., Korotkov A., Lomas P., Suttrop W., Charlet M., McDonald D.C., Milani F., Rapp J., Stamp M., EFDA-JET Workprogramme Contributors and the ASDEX Upgrade Team, 'Scaling of the pedestal density in type-I ELMy H-mode discharges and the impact of upper and lower triangularity in JET and ASDEX upgrade', *Nuclear Fusion*, **42**, 1184 (2002), URL http://dx.doi.org/10.1088/0029-5515/42/10/302

[220] Saibene G., Sartori R., Loarte A., Campbell D.J., Lomas P.J., Parail V., Zastrow K.D., Andrew Y., Sharapov S., Korotkov A., Becoulet M., Huysmans G.T.A., Koslowski H.R., Budny R., Conway G.D., Stober J., Suttrop W., Kallenbach A., von Hellermann M. and Beurskens M., 'Improved performance

of ELMy H-modes at high density by plasma shaping in JET', *Plasma Physics and Controlled Fusion*, **44**, 1769 (2002), URL http://dx.doi.org/10.1088/0741-3335/44/9/301

[221] Beurskens M.N.A., Arnoux G., Brezinsek A.S., Challis C.D., de Vries P.C., Giroud C., Huber A., Jachmich S., McCormick K., Pitts R.A., Rimini F.G., Alfier A., de la Luna E., Fundamenski W., Gerasimov S., Giovannozzi E., Joffrin E., Kempenaars M., Litaudon X., Loarer T., Lomas P., Mailloux J., Pasqualotto R., Pericoli-Ridolfini V., Pugno R., Rachlew E., Saarelma S., Solano E., Walsh M., Zabeo L., Zastrow K.D. and JET-EFDA Contributors, 'Pedestal and ELM response to impurity seeding in JET advanced scenario plasmas', *Nuclear Fusion*, **48**, 095004 (2008), URL http://dx.doi.org/10.1088/0029-5515/48/9/095004

[222] Frassinetti L., Dunne M.G., Beurskens M., Wolfrum E., Bogomolov A., Carralero D., Cavedon M., Fischer R., Laggner F.M., McDermott R.M., Meyer H., Tardini G. and Viezzer E., 'ELM behavior in ASDEX Upgrade with and without nitrogen seeding', *Nuclear Fusion*, **57**, 022004 (2017), URL http://dx.doi.org/10.1088/0029-5515/57/2/022004

[223] Leyland M.J., Beurskens M.N.A., Frassinetti L., Osborne T., Snyder P.B., Giroud C., Jachmich S., Maddison G., Lomas P., von Thun C.P., Saarelma S., Saibene G., Gibson K.J. and JET-EFDA Collaborators, 'Pedestal study across a deuterium fuelling scan for high delta ELMy H-mode plasmas on JET with the carbon wall', *Nuclear Fusion*, **53** (2013), URL http://dx.doi.org/10.1088/0029-5515/53/8/083028

[224] Burckhart A., Dunne M., Wolfrum E., Fischer R., McDermott R., Viezzer E. and Willensdorfer M., 'ELM behaviour and linear MHD stability of edge ECRH heated ASDEX Upgrade plasmas', *Nuclear Fusion*, **56**, 056011 (2016), URL http://dx.doi.org/10.1088/0029-5515/56/5/056011

[225] Ahn J.W., Kim H.S., Park Y.S., Terzolo L., Ko W.H., Park J.K., England A.C., Yoon S.W., Jeon Y.M., Sabbagh S.A., Bae Y.S., Bak J.G., Hahn S.H., Hillis D.L., Kim J., Kim W.C., Kwak J.G., Lee K.D., Na Y.S., Nam Y.U., Oh Y.K. and Park S.I., 'Confinement and ELM characteristics of H-mode plasmas in KSTAR', *Nuclear Fusion*, **52**, 114001 (2012), URL http://dx.doi.org/10.1088/0029-5515/52/11/114001

[226] Degeling A.W., Martin Y.R., Bak P.E., Lister J.B. and Llobet V., 'Dynamics of edge localized modes in the TCV tokamak', *Plasma Physics and Controlled Fusion*, **43**, 1671 (2001), URL http://dx.doi.org/10.1088/0741-3335/43/12/304

[227] Maggi C.F., Saarelma S., Casson F.J., Challis C., de la Luna E., Frassinetti L., Giroud C., Joffrin E., Simpson J., Beurskens M., Chapman I., Hobirk J., Leyland M., Lomas P., Lowry C., Nunes I., Rimini F., Sips A.C.C. and Urano H., 'Pedestal confinement and stability in JET-ILW ELMy H-modes', *Nuclear Fusion*, **55**, 113031 (2015), URL `http://dx.doi.org/10.1088/0029-5515/55/11/113031`

[228] Maddison G. and Reiter D., 'Recycling source terms for edge plasma fluid models and impact on convergence behaviour of the BRAAMS "B2"code', Technical report, Forschungszentrum Jülich (1994)

[229] Pereverzev G.V. and Yushmanov P.N., 'ASTRA Automated System for TRansport Analysis', IPP report IPP 5/98, Max-Planck-Institut für Plasmaphysik (2002)

[230] Viezzer E., Fable E., Cavedon M., Angioni C., Dux R., Laggner F.M., Bernert M., Burckhart A., McDermott R.M., Pütterich T., Ryter F., Willensdorfer M. and Wolfrum E., 'Investigation of inter-ELM ion heat transport in the H-mode pedestal of ASDEX Upgrade plasmas', *Nuclear Fusion*, **57**, 022020 (2017), URL `http://dx.doi.org/10.1088/0029-5515/57/2/022020`

Florian Martin Laggner

✉ *laggner@iap.tuwien.ac.at*
✉ *florian.laggner@ipp.mpg.de*

Personal Data

born August 3rd, 1988 in St. Veit an der Glan

citizenship Austrian

Education

From 12/2013 **PhD studies in "Technical Sciences"**, *Institute of Applied Physics (IAP) at the TU Wien in cooperation with the Max Planck Institute for Plasma Physics (IPP)*, Vienna, Austria & Garching, Germany.
PhD thesis: "Inter-ELM pedestal structure development in ASDEX Upgrade"; Supervisor at IAP: Prof. Friedrich Aumayr, Supervisor at IPP: Dr. Elisabeth Wolfrum

05/2011–12/2013 **Master studies in "Technical Physics"**, *TU Wien*, Vienna, Austria.
Master thesis: "Electron Density Perturbations at the Plasma Edge of the ASDEX Upgrade Tokamak"; Supervisor at IAP: Prof. Friedrich Aumayr, Supervisor at IPP: Dr. Elisabeth Wolfrum

10/2007–05/2011 **Bachelor studies in "Technical Physics"**, *TU Wien*, Vienna, Austria.
Bachelor thesis: "Investigations on the Temperature Control System of the Vibrating Sample Magnetometer MagLab VSM"; Supervisor: Prof. Franz Sauerzopf

09/1998–07/2006 **High school**, *Bundesrealgymnasium Feldkirchen*, Feldkirchen in Kärnten, Austria.
Matura exam

09/1994–07/1998 **Elementary school**, *St. Martin*, Feldkirchen in Kärnten, Austria.

Languages

German, *Mother Tongue.*

English, *Fluent.*

French, *Classes for 4 years at high school.*

Work experience

From 12/2013 **Project-Assistant**, *Institute of Applied Physics, TU Wien*, Vienna, Austria.
This position has been mainly funded by receiving a research scholarship. www.iap.tuwien.ac.at

02/2012–01/2014 **Freelance collaborator**, *Physikmobil*, Vienna, Austria.
"Physikmobil" does science communication in public spaces as parks or swimming baths. Easy physics experiments are performed with everyday material. www.physikmobil.at

07/2009–07/2012 **Handball player**, *Fivers WAT Margareten*, Vienna, Austria.
Fivers WAT Margareten is a professional handball team, playing in the Premier Austrian Handball League. www.fivers.at

04/2007–09/2007 **Employee**, *Laggner glass Ltd*, Feldkirchen in Kärnten, Austria.
Laggner glass Ltd. is a family owned company which is specialized in glass constructions. www.laggnerglas.at

07/2006 **Laboratory internship**, *Institute of Molecular Immunology at the Medical University of Vienna*, Vienna, Austria.
In the framework of the GEN-AU Summer School I had the possibility to do genomic research and worked with cell cultures investigating binding protein that takes an important role in immune defence. www.muw.ac.at/hai

07/2005–08/2005 **Internship**, *Schraml Glastechnik Ltd.*, Großraming, Austria.
Schraml Glastechnik Ltd. is a company that builds and trades machines for glass working. In this company I worked at the customer support service, travelling to different countries in Central Europe. www.schraml.at

Further Activities, scholarships and sporting successes

01/2014–04/2017 **Graduate school membership**, *International Helmholtz Graduate School for Plasma Physics*.
www.ipp.mpg.de/hepp

11/2016 **Conference participation scholarship**, *International Office of TU Wien*.
www.ai.tuwien.ac.at

03/2014–03/2016 **Research scholarship**, *Friedrich Schiedel Foundation for Energy Technology*.
www.f-schiedel-stiftung.at

12/2015 **Support scholarship**, *Faculty of Physics, TU Wien*.
www.physik.tuwien.ac.at

09/2014 **Participation**, *DPG Physics School*, Bad Honnef, Germany.
"The Physics of ITER"

12/2013 **Participation**, *Sokendai Asian Winter School*, Toki, Japan.
"Multiple Approaches in Plasma Physics and Fusion Science"

09/2013 **Participation**, *IPP Summer University*, Greifswald, Germany.
"Plasma Physics and Fusion Research"

10/2012–07/2013 **Participation**, *TUtheTOP - The High Potential Program of TU Wien*.
tuthetop.tucareer.com

2011/2012 **Austrian Handball Cup Winner**.

2010/2011 **Austrian Handball Championship Winner**.

2008/2009 **Austrian Handball Cup Winner**.

09/2006–02/2007 **Military Service**, *Military hospital*, Klagenfurt, Austria.
During this time I got the truck driving license.

07/2006 **Participation**, *GEN-AU Summer School*, Vienna, Austria.
www.ffg.at/gen-au-summerschool